



UiT The Arctic University of Norway

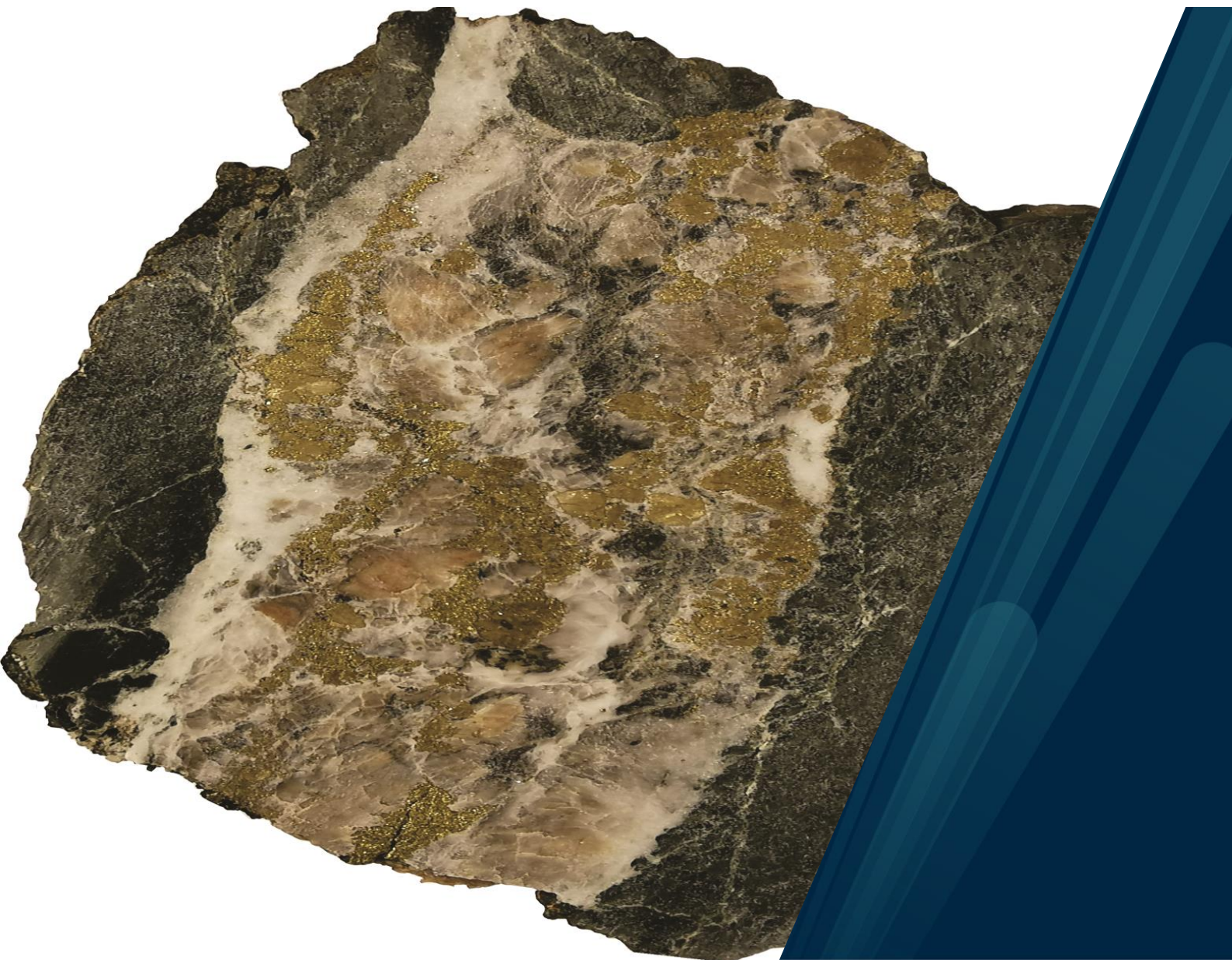
Faculty of Science and Technology

Department of Geosciences

Geochemical characteristics of sediment- and mafic rock-hosted Cu deposits in the Kåfjord area, Alta-Kvænangen Tectonic Window, Northern Norway

Sondre Stenvold Simonsen

Master's thesis in Geology, GEO-3900, June 2021



Abstract

The Precambrian Alta-Kvænangen Tectonic Window (AKTW) located in the northern part of Norway, hosts different types of copper mineralization. Some of Cu occurrences have been previously mined, but their geochemical and stable isotope characteristics have not been a subject of detailed investigations, and therefore the relevant ore-forming processes are still poorly understood. This study, brings new mineralogical, geochemical and stable isotope data collected from the sediment-hosted and the mafic rock-hosted Cu mineralization in the Kåfjord area of AKTW.

The Kåfjord area hosts Cu occurrences in sedimentary rocks of the Storviknes formation and in mafic rocks of the Kvenvik formation. Both formations are regionally folded, with Storviknes formation lying stratigraphically above Kvenvik formation. The Cu mineralization is mostly related to epigenetic quartz-carbonate veins. Considering their mineral assemblages and spatial relationship with the host rocks, the veins were subdivided into 5 different types. In the three types of sediment-hosted Cu mineralization, Cu occurs in digenite, bornite and/or chalcopyrite. In contrast, in mafic rock-hosted Cu mineralization, chalcopyrite is the only Cu-bearing mineral. In addition to the epigenetic mineralization, a syngenetic mafic rock-hosted VMS mineralization has also been identified.

The mafic rock-hosted quartz-carbonate veins show positive $\delta^{13}\text{C}$ values, indicating influences from ^{13}C -rich carbonate layers formed during the Lomagundi-Jatuli Event, while the $\delta^{13}\text{C}$ and $\delta^{18}\text{O}$ values of the sediment-hosted rocks shows a marine origin. The $\delta^{34}\text{S}$ values of sulfides from mafic rock-hosted veins indicate an influence of evaporites.

The fluid inclusion study revealed that the ore-forming fluid was highly saline with a low to moderate temperature. The high salinity controlled the capability of the fluid to transport Cu in the form of chloride complexes. The same type of highly saline fluid inclusions has been found in the sediment- and mafic rock-hosted Cu mineralization, suggesting that both types of mineralization are a product of the same ore-forming event. The study area displays geochemical characteristics typical for classical examples of sediment-hosted Cu deposits, with the Storviknes formation identified as the high-grade zone of such deposit, and the mafic rock-hosted Cu mineralization within Kvenvik formation as the low-grade zone. The mafic rocks within the Kvenvik formation are most likely the source of copper.

Acknowledgements

This project was funded by the MinExTarget project, EiT RawMaterials.

I will first of all give a big thanks to my supervisor Sabina Strmić Palinkaš and co-supervisor Harald Hansen, for all help with this thesis that would not have become any thesis without your help.

Thanks to Yulia Mun for all help and to Fredrik Sahlström for long days in the electron microscope lab. Also, a big thanks to the staff at the geological lab of UiT, to Trine, Ingvild, Karina and Matteus for analysis and guidance through sample preparations. Thanks to the University of Bergen for whole rock analysis, the University of Lausanne and the Stable Isotope Laboratory at CAGE for isotope analyses, and Hugh at GTK for laser ablation analyses. Thanks to Eirik Stokmo, especially for the help during the fieldwork where your SUV came along well.

Thanks to all the people at the red barrack (and specially Torgrim for many coffee breaks) for an enjoyable year, and a special thanks to my office partner Johan, for a good collaboration through this year with valuable talks and discussions.

Table of Contents

1	Introduction	1
1.1	Context of the study	1
1.2	Purpose of the study	2
1.3	Mining history	2
1.4	Samples and methods	5
1.4.1	Field sampling	5
1.4.2	Sample selection.....	5
1.4.3	Sample preparation.....	9
1.4.4	Analytical methods.....	12
2	Geological setting.....	17
2.1	The Fennoscandian Shield.....	17
2.1.1	The Archean domain	18
2.1.2	The Svecofennian domain.....	21
2.1.3	The Transscandinavian igneous belt	21
2.1.4	The Southwest Scandinavian domain	21
2.1.5	Alta-Kvænangen Tectonic Window.....	21
2.1.6	Raipas Supergroup	25
2.1.7	Bossekop Group	26
3	Theoretical background.....	27
3.1	Sediment-hosted copper deposits	27
3.2	Volcanogenic massive sulfide deposits (VMS).....	31
3.3	Stable isotope.....	32
3.4	Fluid inclusion studies	34
3.4.1	Microthermometric measurements.....	37
3.5	Methodology.....	41
3.5.1	LA-ICP-MS (-AES)	41

3.6	Previously work.....	43
3.6.1	Kvenvik formation	44
3.6.2	Storviknes formation	45
4	Results	47
4.1	Mineral characterization	48
4.1.1	Mafic rock-hosted Cu mineralization in the Kvenvik formation	48
4.1.2	Sediment-hosted Cu mineralization in the Storviknes formation	77
4.1.3	Sediment-hosted barren locality in the Skoadduvarri formation	94
4.2	Trace element composition of ore and accessory minerals	95
4.2.1	Geochemical signatures of sulfides	95
4.2.2	Geochemical signatures of oxides	100
4.3	Whole rock geochemistry	103
4.4	Stable isotope analysis	106
4.4.1	Stable isotope composition of carbonates	106
4.4.2	Sulfur isotope composition of sulfides	109
4.5	Fluid inclusion study	112
4.5.1	Petrographic and microthermometric description	115
5	Discussion	119
5.1	The mineral assemblages	119
5.1.1	Mafic rock-hosted Cu mineralization	122
5.1.2	Sediment-hosted Cu mineralization	129
	Mineralization east vs. west of the syncline	135
5.2	Ore-bearing fluids	135
5.3	Magnetite as an indicator of ore-forming processes	137
5.4	Ore-forming model	140
5.4.1	Syngenetic mineralization	140
5.4.2	Epigenetic mineralization	140

6	Conclusion and further work.....	146
6.1	Conclusion	146
6.2	Further work	148
	References	149
	Appendices	158
	Appendix A: Mineral abbreviations	158
	Appendix B: Additional isotope drill marks	159
	Appendix C: Mineral composition from literature.....	161
	Appendix D: LA-ICP-MS spots	163
	Appendix E: Deviations from ideal composition.....	174
	Appendix F: LA-ICP-MS raw data	178
	Appendix G: Fluid inclusion study data.....	197
	Appendix H: Correlation matrices of sulfides.....	200
	Appendix I: Magnetic anomaly and Skoadduvarri	202

1 Introduction

1.1 Context of the study

This master project is a part of a larger project entitled “MinExTarget” (Enhanced Use of Heavy Mineral Chemistry in Exploration Targeting). The project is funded by EIT (European Institute of Innovation and Technology) RawMaterials (EIT RawMaterials, 2020a). The aim of EIT RawMaterials is to: “Enable sustainable competitiveness of the European minerals, metals, and materials sector along the value chain by driving innovation, education, and entrepreneurship” (EIT RawMaterials, 2020b).

MinExTarget is oriented to the early stages of the mining value chain and covers the field of geology and mineral exploration (Figure 1). Therefore, the main goal of MinExTarget is to develop a new tool that can be used in mineral exploration to easier locate undiscovered mineral resources. The new tool is based on the concept that the targeting and qualifying of primary sources of mineralogical and geochemical anomalies can be done faster and more precisely by looking at the trace element concentration and the stable and radiogenic isotope composition of heavy minerals (MinExTarget, 2020).



Figure 1: The mining value chain.

This master thesis is one of two theses that test the MinExTarget concept on the Cu mineralization in the Alta-Kvænangen Tectonic Window (AKTW), Northern Norway (Figure 3). This thesis is focused on mineral, geochemical and stable isotope characterization of the Cu mineralization, while the thesis by Hilmo (2021) gathers the mineral, geochemical and stable isotope data from stream sediments in streams that drain the Cu mineralization in the study area.

1.2 Purpose of the study

The main goal of this master project is to determine the mineralogical, geochemical, and stable isotope characteristics of the ore mineralization, host rocks, and alteration products of the sediment-hosted and mafic rock-hosted Cu mineralization in the Kåfjord area of AKTW (Figure 3). The study combines transmitted and reflected polarized light microscopy, scanning electron microscopy coupled with an energy dispersive system (SEM-EDS), litho-geochemistry, carbon ($\delta^{13}\text{C}$), oxygen ($\delta^{18}\text{O}$) and sulfur ($\delta^{34}\text{S}$) isotope analyses, and a fluid inclusion study. In addition, laser ablation inductively coupled plasma mass spectrometer (LA-ICP-MS) has been used to identify trace element signatures of selected sulfides and oxides.

1.3 Mining history

The main outcome of the mining history is based on the book of Abrahamsen and Veiseth (1997) and Moberg (1968). Other sources are referred to in the text.

Kåfjord in Alta is known for its mining history of copper that started back in the 1800th century. It has produced thousands of tons of copper from localities in Kåfjord but also from localities farther away in Kvænangen and Raipas (Figure 2).

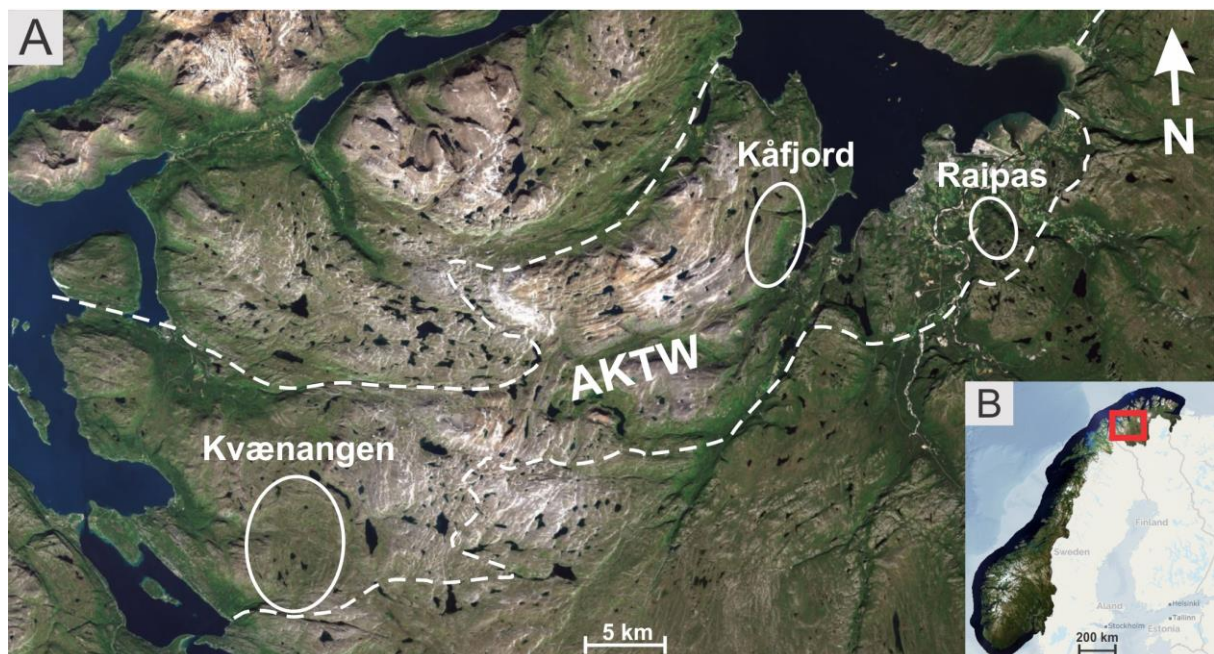


Figure 2: (A) An orthophoto showing Kvænangen, Kåfjord and Raipas laying within the AKTW (indicated by the white dashed lines). (B) Location of AKTW marked as the red square within Norway. Both orthophotos are downloaded and modified from Norge i bilder (2021).

The oldest information about prospecting in the Kåfjord area dates back to 1690s, but the mining of copper did not start until Alten Copper Mines (later “Alten Copper Works”) was established by the English merchants Henry Woodfall and John Rice Crowe in 1826. These merchants opened the mine due to promising results from another Englishman called Mitchell, who had some experience in geology and investigated the area the year before on behalf of the merchants and wrote: “the whole of this Alpine district is impregnated with Copper” (Abrahamsen & Veiseth, 1997, p. 4). In 1833, 100 workers worked in the mines of Kåfjord, and a total of 426 persons were living there. Forty-two years later, in 1875, there was a total of 2 360 persons living in Kåfjord. This mining operation was later driven by other English directors after Crowe and Woodfall ended their effort respectively in 1940 and 1944, until it was temporarily closed in 1878 due to several reasons. Among other of these reasons is described by Moberg (1968) as a general loss of energy among the people in the community. This was the main cause that ended this mining period, but trouble with infill of water in the mines and trouble of removing material as the deeper the mines got should also be pointed out, together with bad management at that time, as the mine operation was leaded from London.

In 1896, the Swedish Nils Persson bought the operation and started mining again. He also disassembled the old melting house and built a new melting house. While disassembling the old melting house, he found 32.5 tons of copper under a furnace which paid off both the rights to mine and the copper processing plant. Electricity was introduced in 1903, generated by waterpower from Møllneselva. This operation lasted until it was shut down in 1909 due to lower copper grade. Also, most known mines started to run out of material, and only smaller new deposits were discovered. Lower copper prices may also have had an effect, and this is the last period of mining in Kåfjord as of today’s date (Mørk, 1970). A total of at least 32 mines have produced copper in Kåfjord, including the mines opened during the first mining period.

Further west of the Kåfjord mines, there are, according to Zwaan and Gautier (1980), two mines called Anna and Lundstrøm that are mineralized. Any other information about the mining operation of these mines is not known, but it is likely to assume that these mines were mined simultaneously with the Kåfjord mines, or later due to their more remote location (Figure 3; Figure 4).

The processing plant in Kåfjord did also process rich copper ore material from mines in Kvænangen and Raipas during both periods of mining, also owned by Alten Copper Works. In the winter of 1851, 30 horses transported 12-15 000 kg of ore material by sleds from Kvænangen to Kåfjord over the mountain, but this was too ambitious and was later transported around the mountain.

To get the ore body into loose rocks, iron drills and explosives were used, and then the ore was detached from the barren rocks by crushing by hand (banking). This was not harmless work, and several people died in accidents related to the explosives. The ore material was then transported to the plant, where it was crushed by a crusher and then shipped by boat to England to melt it. From 1835(-36), the ore material was melted in Kåfjord as a melting house was built, and in 1836, a wet separator was installed to separate ore material from barren material after crushing it. During the second period of mining, the barren material was cast in rectangular blocks and used as a building material. These blocks are for instance covering the entrance of Kåfjord church today.

During the very first period of mining in Kåfjord, from 1827 to 1833 there were mined 3 644 tons of ore material with a value of 113 502 speciedalar, according to Moberg 1968. For the period 1843 to 1878, there were mined 61 947 tons of ore that produced 3 022 tons of copper with an average Cu grade of almost 4.9%. Of this material, “Gamla gruvan” delivered the very most material with 55 690 tons of ore material. For the second period of mining, from 1896-1909, there was produced 1 650 to 1 700 tons of copper. In total, there may have been extracted up to 6 000 tons of copper from the copper mines in Kåfjord. In addition, Kvænangen produced 6 800 tons of ore material with an average grade of 7.4% copper, and Raipas 12 500 tons with an average grade of 6.74% copper during this second period of mining, giving 1 350 tons of copper.

(Moberg, 1968; Abrahamsen & Veiseth, 1997)

1.4 Samples and methods

1.4.1 Field sampling

Field-work took place in the Kåfjord area (Figure 2) from 10th to 20th of August 2020 with the main goal to collect representative samples of the sediment-hosted and mafic rock-hosted Cu mineralization and their host rocks. At the same time, stream sediments from the streams that drain the Cu mineralization were sampled (Hilmo, 2021). In total, 78 rock samples were collected at 20 different localities. Seven of those localities were the historical mines “Innerstrømmen”, “Carl Johan”, “Wilson”, “Mitchell”, “Henning”, “Anna” and “Lundstrøm”, which can be seen in Figure 3. To get an accurate location of the different samples that were collected, a Garmin GPSMAP 64st was used. This GPS has a quad-helix antenna and a high sensitive GPS and GLONASS receiver that gives a precision of 5 to 10 meters (Garmin, 2020a, 2020b).

1.4.2 Sample selection

Thirty-two rock samples at 14 localities were selected for further mineral, geochemical and stable isotope analysis (Table 1). These localities include the historical mines and also other localities called; “Melsvik”, “Melsvik tunnel”, “Kråknes”, “Kåfjord bridge”, “Carbonate wall”, “Skoadduvarri” and “Møllnes river”, with the location of these localities and selected samples presented in Figure 3.

Table 1: All samples used in this thesis with corresponding localities, location and information about which investigation methods that have been used. Abbreviations: Carbonate isotope; Carb, Sulfur isotopes; Bn: Bornite, Dg: Digenite, Ccp: Chalcopyrite, Py: Pyrite.

Locality	Sample	Location (UTM 34W)	Thin section	Fluid inclusion	Lithogeochemistry	SEM-EDS	LA-ICP-MS	Carbonate isotope	Sulfur isotope	Isotope sample
Skoadduvarri	030	577555mE 7762159mN		x						
Melsvik	001	576831mE 7769295mN						x		001(carb)
	0012	576834mE 7769291mN						x		0012(carb)
Møllnes river	045	577539mE 7762469mN						x		045(carb)
Carbonate wall	0581	577350mE 7760588mN						x3		0581A(carb), 0581B(carb), 0581C(carb)
	042	577341mE 7760576mN						x		042(carb)
	043	577341mE 7760576mN						x		043(carb)
Lundstrøm	L2	575996mE 7763254mN	L2			x	x	x2	x	L2(bn + dg), L2A(carb), L2B(carb)
	L1	575996mE 7763254mN	L1			x				
	032	576051mE 7763339mN	032A, 032B				x (032B)	x	x	032A(carb), 032B(ccp)
	034	576006mE 7763267mN		x						
Anna	025	575339mE 7761194mN						x3		025A(carb), 025B(carb), 025C(carb)
	0221	575339mE 7761194mN	0221	x		x	x	x	x2	0221A(bn + minor ccp), 0221B(carb), 0221C(ccp + minor bn)
	0222	575339mE 7761194mN	0222				x	x2	x	0222A(carb), 0222B(ccp)
	036	575586mE 7761410mN								
	037	575611mE 7761379mN						x		037(carb)
	038	575615mE 7761370mN						x		038(carb)
	039	575632mE 7761371mN						x		039(carb)
	040	575427mE 7761092mN	040	x		x	x			
Kråknes	0045	580117mE 7767335mN						x	x	0045A(carb), 0045B(ccp)
	0046	580063mE 7767641mN			x					
Melsvik tunnel	003	577581mE 7768308mN			x					
Henning	047	578676mE 7762997mN	047			x	x		x2	047A(py), 047B(py + minor ccp)
	051	578676mE 7762997mN	051			x	x		x2	051A(py + ccp), 051B(py + ccp)
Mitchell	057	577532mE 7760660mN	057			x			x2	057(ccp + minor py), 057B(ccp + minor py)
	0571	577532mE 7760660mN	0571				x	x	x2	0571A(carb), 0571B(py + ccp), 0571C(py + ccp)
Wilson	020	577207mE 7759773mN						x		020(carb)
Carl Johan	013	577357mE 7759838mN	013A, 013B		x	x2	x2	x2	x	013A(py + minor ccp), 013B(carb), 013C(carb)
	014	577357mE 7759838mN	014				x	x		014(carb)
Innerstrømmen	060	576958mE 7758582mN	060A, 060B			x (060A)	x (060A)		x3	060A(ccp), 060B(ccp + minor py), 060C(ccp)
Kåfjord bridge	0051	578334mE 7761115mN	0051			x	x	x	x2	0051A(py), 0051B(carb), 0051C(py)
	0052	578370mE 7761187mN		x				x		0052(carb)
	0054	578334mE 7761115mN	0054		x	x	x			
	0055	578334mE 7761115mN								
Total	32		18	5	4	12	14	28	20	



Figure 3: Orthophoto of the study area with the location of studied Cu mineralization and collected samples. The orthophoto is downloaded and modified from Norge i bilder (2021).

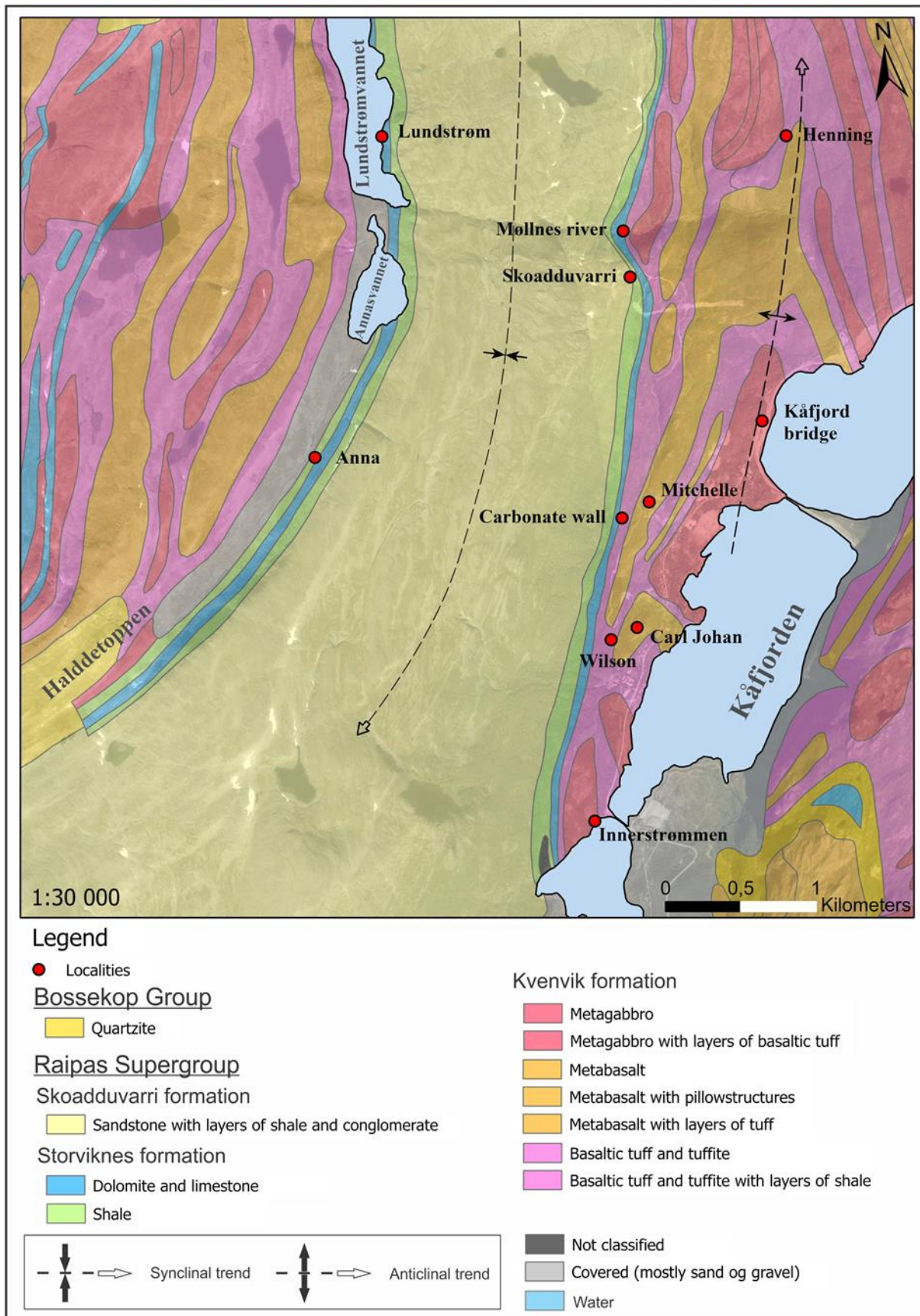
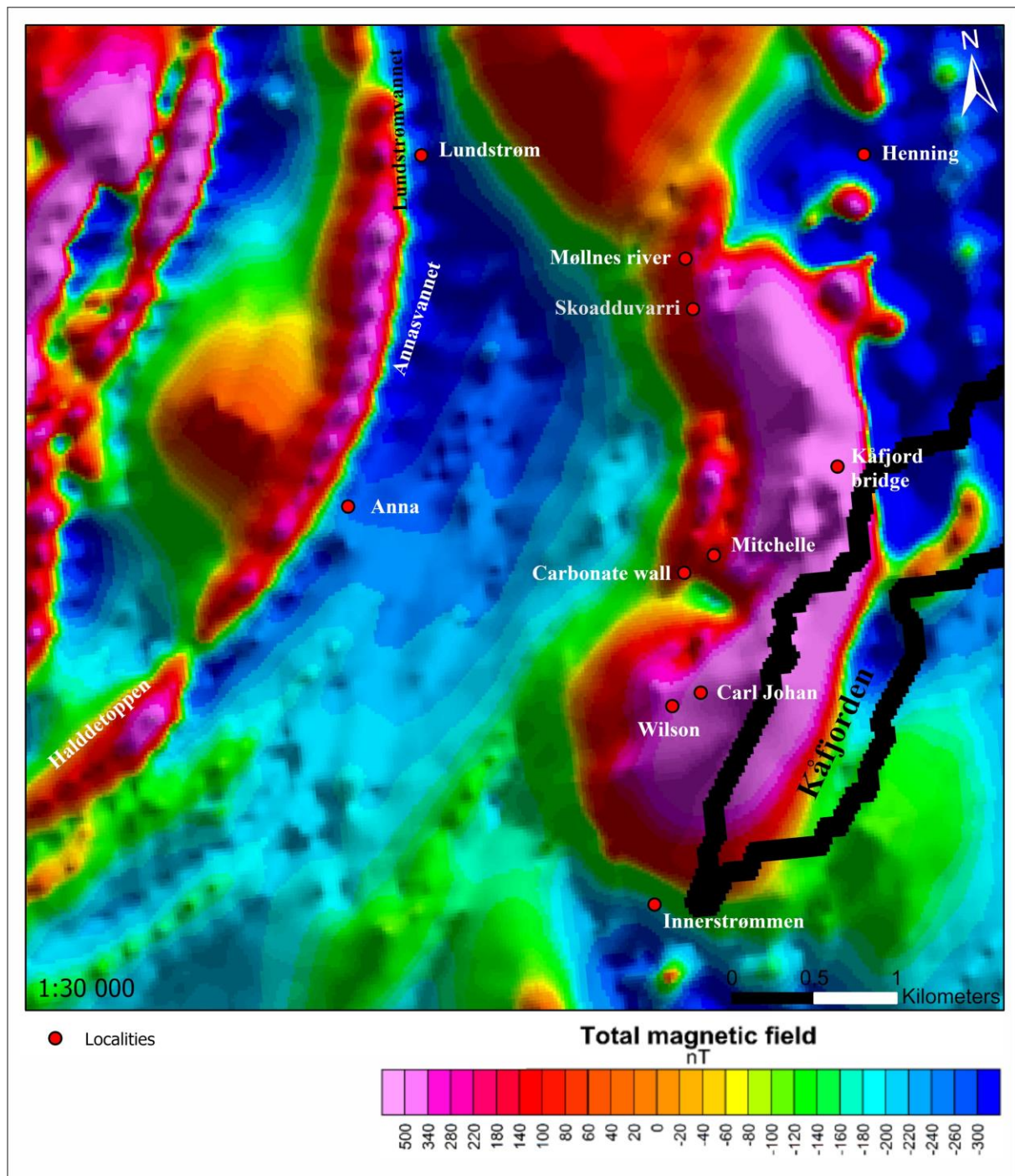


Figure 4: A 1:50 000 bedrock map from (NGU, 2021b) overlain an orthophoto from Norge i bilder (2021) with red circles indicating locations of the studied Cu mineralization. The synclinal and anticlinal trend has been added after Bergh and Torske (1988).



1.4.3 Sample preparation

The sample preparation took place in “Emilbua” at the Department of Geosciences of UiT. A MK-101 wet tile saw with a diamond blade was used for cutting the selected samples, into smaller pieces suitable for preparation of thin or thick sections, or just to open rocks to expose the texture.

A rock crusher was used for crushing four samples into <5 mm fragments for lithochemical analysis. Before the samples were crushed, they were cut into suitable pieces by the wet saw, and unwanted parts as mineralized or weathered parts were cut off. The crushed material was milled in a Retsch PM 100 agate miller, into a very fine-grained homogenous powder for lithochemical analysis.

As the carbonate and sulfur isotope analysis only requires 0.1 grams of pulverized material, a Dremel 3000 drill machine with a diamond drill head was used to extract powder of carbonate and sulfide minerals by drilling. Before drilling each sample, the drill head was cleaned by first using a paper towel to remove most of the substances. Then, the drill head was dipped in 10% hydrochloric acid (HCl) as the remaining carbonates will react with HCl and form water, carbon dioxide, and calcium chloride ($\text{CaCO}_3(\text{s}) + 2\text{HCl}(\text{aq}) \rightarrow \text{H}_2\text{O}(\text{l}) + \text{CO}_2(\text{g}) + \text{CaCl}_2(\text{aq})$). The drill head was then dried and cleaned with towel paper to ensure no substances were left on the drill head. For each drilled sample, a new paper sheet was laid underneath as a base to catch the powder and to avoid contamination. Each sample of drilled powder was put in small glasses and sent to the Stable isotope laboratory of Institute of Earth Surface Dynamics, University of Lausanne, Switzerland, for analyses of carbon ($\delta^{13}\text{C}$), oxygen ($\delta^{18}\text{O}$), and sulfur ($\delta^{34}\text{S}$) composition. In addition, two samples of sulfides ($\delta^{34}\text{S}$) were prepared for stable sulfur isotope analysis and delivered to the Stable Isotope Laboratory at CAGE – Centre for Arctic Gas Hydrate, Environment and Climate, Department of Geosciences of UiT.

Polished section preparation

The rock slabs, cut in approximately 1 x 2 x 3 cm dimensions, from selected fifteen rock samples were delivered to the geological laboratory at the Department of Geosciences, UiT, for further preparation of polished thin sections (30 μm thickness) for transmitted and reflected polarized light microscopy, SEM-EDS and LA-ICP-MS analyses. Polished thick sections (300 μm thickness) from selected six rock samples were prepared for fluid inclusion study.

Preparation for fluid inclusion study

Preparation of the double polished wafers was performed in the geological laboratory at the Department of Geosciences, UiT. Selected samples were cut into approximately 1 x 2 x 3 cm slabs. One 2 x 3 cm surface of each slab was grinded by a Logitech LP-50 with silicon carbide blades for 30 minutes and polished in a Phoenix Beta polishing machine using 6, 3

and 1-micron diamond pastes and suitable polishing cloths. The machine was set to a rotation speed of 75 rpm while the sample was manually held on the fiber mesh and turned against the rotation direction of the plate. Samples containing quartz were polished for 25-27 minutes (15 minutes with 6-micron diamond paste, 7-8 minutes with 3-micron diamond paste and 3-4 minutes with 1-micron diamond paste). Samples containing minerals softer than quartz were usually polished 15-17 minutes (10 minutes with 6-micron diamond paste, 3-4 minutes with 3-micron diamond paste and 2-3 minutes with 1-micron diamond paste). The quality of the polishing was regularly checked in a light microscope and an ultrasonic bath was also regularly used to remove particles from the surface of the wafers.

In the next step, the slab was mounted onto a standard microscopy glass with the polished part towards the glass. Crystal bond was used as an adhesive and the process was performed on a hot plate at a temperature of 120°C. After fixation, the slabs were first cut with a Struers discoplan TS wet saw and then grinded with a Struers discoplan TS grinder to the final thickness. The final thickness is usually around 250 µm but it may vary from sample to sample depending on its transparency, size of entrapped fluid inclusions, as well as on the distribution of fluid inclusion assemblages (Goldstein, 2003).

When correct thickness was obtained, the unpolished side of the sample had to be grinded by hand, by using silicon carbide with a grain size of 600K on a piece of glass as a base for about 5 minutes with water as lubricant. After the grinding was done, all the samples were polished again using the same procedure for polishing as mentioned before by the 6-micron, 3-micron and 1-micron fiber mesh with associated diamond paste.

As a final step of the process, the glass had to be removed from the samples. To do this it was put on the hot plate again and warmed up until the crystal bond melted. The sample was quickly slid off the glass into a bowl with acetone. This bowl of acetone with the thick section inside was then laid in a supersonic bath (floating on the water), and it was runned for 2 minutes as the remaining glue from the crystal bond was dissolved by the acetone. Sample by sample was checked for remaining glue and removed by spraying on acetone if necessary until all glue was removed, and the sample was clean and ready for fluid inclusion study.

1.4.4 Analytical methods

1.4.4.1 Polarized light microscopy

Characterization of micro-textures as well as identification of mineral phases were acquired from polished thin and thick sections using a Leica DMLP microscope. Transmitted light microscopy (TLM) and reflected light microscopy (RLM) were applied in the identification of transparent and opaque minerals, respectively. Photomicrographs of micro-textures and characteristic phase relationships were acquired using a Leica DMC4500 camera and the Leica Application Suite software.

1.4.4.2 Whole rock geochemistry (Major and trace element analysis by ICP-MS, ICP-AES and XRF)

The lithochemical analyses of four samples (003, 0054, 0046 and 013) were done at the Department of Geosciences of the University of Bergen. To plot the samples in diagrams, the program “R” with the package “GCD Kit” has been used (Janoušek et al., 2006).

Further preparation of samples for ICP-MS, ICP-AES, and XRF

The aliquots of 0.5 g pulverized samples were dried and heated up to 1000°C for two hours to determine the loss of ignition (LOI). For ICP-MS and ICP-AES analysis, 100 mg of the samples were weighted in 25 ml PFA Savillex beakers and digested in 3 ml concentrated HF on a heating plate at 135°C during 48 hours. The HF supernatant was evaporated to dryness and the fluoride residues were subsequently hydrolyzed in a weak solution of HNO₃ on the heating plate under sub-boiling point conditions and evaporated to dryness. The resulting nitrate salt residue was dissolved in a ca 2 ml 2N HNO₃ prior to dilution with 2% HNO₃ in 50 ml in volumetric flasks.

Major and trace element analysis by ICP-AES

A Thermo Scientific ICap 7600 Inductively Coupled Plasma Atomic Emission Spectrometer (ICP-AES) is used to measure the concentration of Al, Ca, Cu, Fe, K, Mg, Mn, Na, P, and Ti. External calibration curves from Spectrapure (certified single element solutions to prepare multi-element standard solutions) are used to do the quantification. Internal standardization of Sc is used, and samples are diluted by 2% w/v HNO₃ before analysis.

A USGS CRM BCR2 (Basalt, Columbia river) is used for quality control, with BCR2 following all steps from digestion. Repeatedly analysis of synthetic water CRM SPS-SW-2

(Spectrapure Standards AS) is done to monitor the performance during analysis and to control the calibration curves.

Trace element analysis by ICP-MS

A Thermo Scientific Element XR High-Resolution Inductively Coupled Plasma Mass Spectrometer (HR-ICP-MS) is used to measure trace element concentration of Ce, Co, Cr, Cs, Cu, Dy, Er, Eu, Gd, Hf, Ho, La, Li, Lu, Nb, Nd, Ni, Pb, Pr, Rb, Sc, Sm, Sr, Ta, Tb, Th, Ti, Tm, U, V, Y, Yb, Zn, and Zr. External calibration curves from Spectrapure (certified single element solutions to prepare multi-element standard solutions) are used to do the quantification. Internal standardization of In is used, and samples are diluted by 2% w/v HNO₃ before analysis.

A USGS CRM BCR2 (Basalt, Columbia river) is used for quality control, with BCR2 following all steps from digestion. Repeatedly analysis of synthetic water CRM SPS-SW-2 (Spectrapure Standards AS) is done to monitor the performance during analysis and to control the calibration curves.

Major element analysis by XRF

A Bruker S4 PIONEER X-ray fluorescence spectrometer is used to analyze the concentration of Si. External calibration curves from USGS based on several powdered CRMs are used for quantification. Analysis of USGS CRM BCR2 (Basalt, Columbia river) is used for quality control.

1.4.4.3 Mineral chemistry by SEM-EDS

A Zeiss Merlin Compact VP field emission scanning electron microscope (FE-SEM) with a X-Max energy dispersive system (EDS) at the Faculty of Health, UiT, was used to identify the ratio between elements in different minerals in weight percent (wt. %). Prior to the SEM-EDS analyses, polished sections were carbon-coated (10 nm) using a Leica EM ACE600 sputter coater (the first batch of analyzed samples) and a Quorum 150R ES plus coater (the second batch of analyzed samples).

A working distance (WD) of 8,5 mm between the EDS detector and the sample was used with an electron high tension of 15 kV on the first batch (thin section 040, 051, 0054, 0221, L1 and L2) and 20 kV on the second batch of samples (thin section 013A, 013B, 040, 047, 0051, 057, 060A and L1). Corrections of elements were done using Aztec analysis software from Oxford Instruments.

1.4.4.4 Trace element analyses by LA-(SC)-ICP-MS

Trace element analysis of specific minerals was done in Finland at the Geological Survey of Finland (GTK), using an Analyte 193 ArF (Photon Machines, San Diego, USA) laser-ablation (LA) system in combination with a Nu AttoM (Nu Instruments Ltd., Wrexham, UK) single collector inductively coupled plasma mass spectrometer (SC-ICP-MS).

The laser was run at a pulse energy of 5 mJ at 30% attenuation and a pulse frequency of 5 Hz to produce an energy flux of 2.17 J/cm² on the sample surface with a 25 µm spot size for oxides and a 40 µm spot size for sulfides. These two spot sizes were chosen to provide the best compromise between adequate resolution, to allow spot analysis of compositional zones determined by high contrast SEM imaging, still keeping limits of detection (LOD) as low as possible. Each analysis was initiated with a 20-second baseline measurement followed by switching on the laser for 40 seconds for signal acquisition. Analyses were made using time-resolved analysis (TRA) with continuous acquisition of data for each set of points (generally following the scheme of primary standard, quality control standard, 15 unknowns). For the analyses of oxide minerals (magnetite, hematite, ilmenite, titanite, rutile) GSE glass was used as the primary external standard, with GSD glass BHVO-2G and BCR-2G as reference materials for quality control. For the analyses of sulfide minerals (pyrite, chalcopyrite, sphalerite, bornite, digenite, tennantite, molybdenite) UQAC FeS-1 was used as the primary external standard, with USGS MASS1 as reference material for quality control. The isotope ⁵⁷Fe has been used as an internal standard. The measurements were performed on 34 isotopes for oxides and 40 isotopes for sulfides covering 34 elements for oxides and 38 elements for sulfides at low resolution ($\Delta M/M = 300$) using the fast scanning mode. Data reduction was handled using the software GLITTER TM (Achterberg et al., 2001) which allows the baseline subtraction, the integration of the signal over a selected time resolve area, and the quantification using known concentrations of the external and internal standards (GTK, 2021).

1.4.4.5 Fluid inclusion study

Petrographic and microthermometric measurements of fluid inclusions were performed at the Department of Geosciences of UiT. Six samples were selected from quartz-carbonate veins hosted by sedimentary rocks (samples 030, 034, 040 & 0221), and by gabbro (sample 060 & 0052).

Microthermometric measurements were carried out on Linkam THMS 600 stages mounted on an Olympus BX 2 microscope using 10× and 50× Olympus long-working distance objectives. Two synthetic fluid inclusion standards (SYN FLINC; pure H₂O and mixed H₂O-CO₂) were used to calibrate the equipment. The precision of the system was ±2.0°C for homogenization temperatures, and ±0.2°C in the temperature range between -60° and +10°C. The measurements were made on carefully defined fluid inclusion assemblages (FIAs), representing groups of inclusions that were entrapped simultaneously from the same fluid. The fluid inclusion assemblages were identified based on petrography prior to heating and freezing. If all fluid inclusions within the assemblage showed similar homogenization temperature, the inclusions were assumed to have trapped the same fluid and to have not been modified by leakage or necking; these fluid inclusions would thus record the original trapping conditions (Goldstein & Reynolds, 1994; Goldstein, 2001; Bodnar, 2003a).

During microthermometric measurements, the following phase transitions were recorded: the first-melting temperature (eutectic T_e); last melting temperature of hydrate (T_{hyd}); last melting temperature of ice (T_{m ice}); last melting temperature of halite (T_s); and the total homogenization temperature (T_H). Calculations of compositions, densities, and isochores were conducted applying the numerical model by Steele-MacInnis et al. (2011) for the H₂O-NaCl-CaCl₂ system and Steele-MacInnis et al. (2012) for the H₂O-NaCl system.

1.4.4.6 Stable isotope analyses

Carbon and oxygen isotope analyses of carbonates were performed at the Stable isotope laboratory of Institute of Earth Surface Dynamics, University of Lausanne, Switzerland. Measurements were carried out with an automated Thermo/Finnigan online preparation device Gas Bench II connected to a isotope ratio mass spectrometer (IRMS) using a continuous flow mode (Révész & Landwehr, 2002). Borosilicate sample bottles were washed in diluted acid, then twice in deionized water and overnight dried at 70°C. The powder samples (~250µg) were added to the vials in air, and air was removed from the sample vials by automatic autosampler-assisted flushing with He, using He flow of 100 ml/min for 5 minutes. The phosphoric acid, which is maintained at the reaction temperature (70°C for calcite and 90°C for Fe-carbonates and dolomite) was added dropwise under computer control to each individual reaction vessel. The reaction time was 60 minutes. Both the amount of the acid and the reaction time were controlled by the software.

Data was extracted to an EXCEL file by using the ISODAT NT EXCEL export utility and further calculation steps were carried out using a predefined EXCEL Worksheet. A linearity correction was applied based on the relationships between the intensity of the first sample peak (m/z 44) and $\delta^{18}\text{O}$ value of the standards. The stable carbon and oxygen isotope ratios are reported in the delta (δ) notation as per mil (‰) deviation relative to the Vienna Standard Mean Ocean Water (V-SMOW) for oxygen and Vienna Pee Dee Belemnite (V-PDB) for carbon. The analytical reproducibility was better than $\pm 0.05\text{‰}$ for $\delta^{13}\text{C}$ and $\pm 0.1\text{‰}$ for $\delta^{18}\text{O}$.

Sulfur isotope analyses were carried out at performed at the Stable isotope laboratory of Institute of Earth Surface Dynamics, University of Lausanne, Switzerland. Measurements were performed by on-line EA-IRMS system consists of a Carlo Erba 1108 elemental analyzer (EA) coupled with a continuous helium flow interface to the Thermoquest/Finnigan Mat Delta S IRMS. The EA oxidizes all sample compounds under a stream of helium and oxygen by flash combustion in a single oxidation-reduction quartz tube filled with oxidizing (tungsten trioxide) and reducing (elemental copper) agents at 1030°C . Water was removed using anhydrous magnesium perchlorate, and the gases enter a chromatographic column (Poropak QS) for separation of SO_2 which is isotopically analyzed by IRMS (Giesemann et al., 1994). The sulfur isotope values are reported in the typical δ -notation relative to V-CDT standard. The reproducibility, assessed by replicate analyses of the laboratory standard (natural pyrite, $+6.1\text{‰}$, synthetic mercury sulfide, $+15.5\text{‰}$, barium sulfate, $+12.5\text{‰}$ $\delta^{34}\text{S}$) was better than 0.2‰ .

Sulfur isotope composition of two additional sulfide minerals was performed at Stable Isotope Laboratory of CAGE, Department of Geosciences, UiT. Approximately 0.1 g of pulverized sample were loaded in Sn-capsules and were combusted in a Thermo Scientific Flash HT Plus (EA) at 1020°C after being weighed. Analysis of the combusted material was done by an IRMS (Thermo Scientific MAT253) instrument with normalization of $\delta^{34}\text{S}$ to VCDT (Vienna-Canyon Diablo Troilite) by the three international standards S1, S2, and NBS127. Uncertainty of the instrument by perfectly homogenous mixed material is a standard deviation of $\leq 0.20\text{‰}$.

2 Geological setting

2.1 The Fennoscandian Shield

The Fennoscandian Shield (Figure 6), also called the Baltic Shield, located in Norway, Sweden, Finland, and Russia is the northwestern part of the East European Craton (Gorbatshev & Bogdanova, 1993).

Gaal and Gorbatshev (1987) divided the Fennoscandian Shield into three main domains based on the age of formation: 1) the Archean domain; 2) the Svecofennian domain, and 3) the Southwest Scandinavian domain (Figure 6). The Archean domain is built up of rocks formed during the Saamian (3.1-2.9 Ga) and the Lopian orogeny (2.9-2.0 Ga) while the Svecofennian domain was formed during the Svecofennian orogeny (2.0-1.75 Ga). The Southwest Scandinavian domain was formed during the Gothian orogeny (1.75-1.50 Ga). Later orogeny's as the Sveconorwegian orogeny (1.25-0.90 Ga), and the Caledonian orogeny (600-400 Ma) have affected the western part of the Fennoscandian Shield with metamorphism and overlaying strata as the Caledonian Nappes (Gaal & Gorbatshev, 1987).

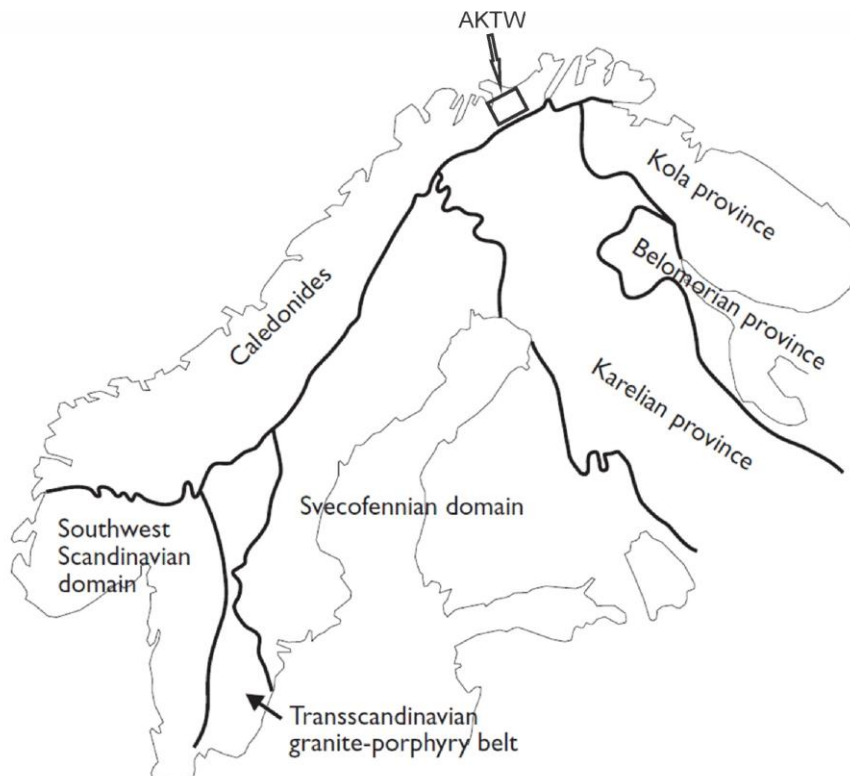


Figure 6: Overview of the Fennoscandian Shield, including the approximate location of AKTW (Alta-Kvænangen Tectonic Window), modified after Lahtinen et al. (2005), based originally on Gaal and Gorbatshev (1987).

In Norway, the Fennoscandian Shield represents the basement of the overlying Caledonian Nappes and it is exposed in several “tectonic windows” (Figure 7). These tectonic windows are a result of extension and erosion after the thrusting of the Caledonian Nappes, as nappes have glided back towards the direction of thrusting, and some places revealed the basement below with the help of erosion amplified by land uplift (Fossen et al., 2013, p. 210).

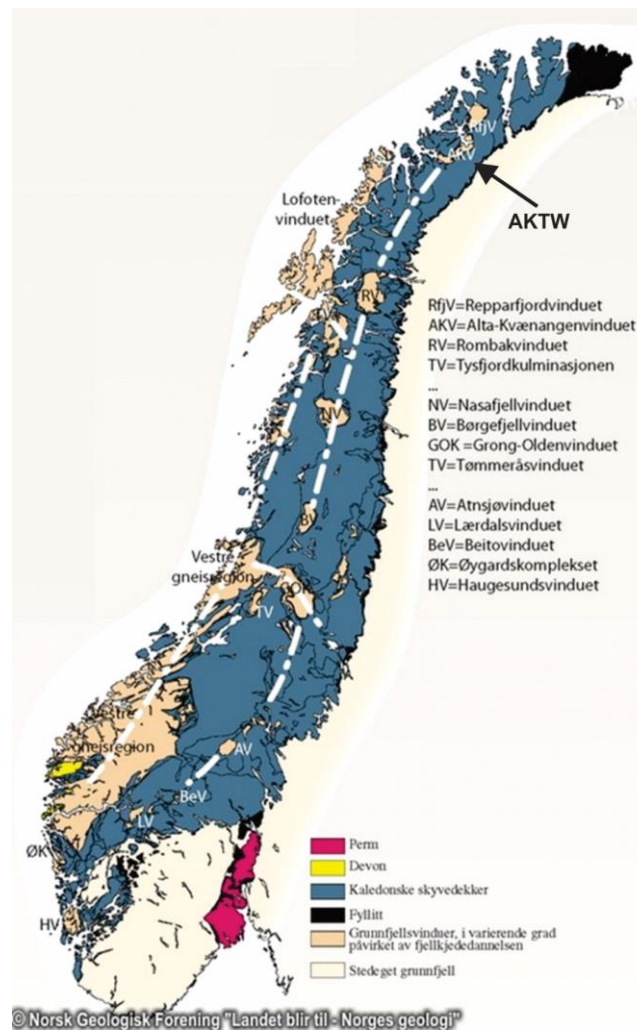


Figure 7: Tectonic windows within the Caledonian Nappes, AKTW is emphasized. Modified from Fossen et al. (2013)

The oldest rocks of the Fennoscandian Shield are gneisses found in northern Finland. These gneisses, also known as “Siuruagneiss”, have been dated to 3.5 Ga. Zircons isolated from Siuruagneiss have been dated to 3.73 Ga, suggesting the existence of even older rock in the Fennoscandian Shield (Nordgulen & Andresen, 2013, p. 71).

2.1.1 The Archean domain

The Archean domain is the northeastern-most part of the Fennoscandian Shield and has been divided into three smaller crustal provinces: the Karelian Province, the Kola Peninsula

Province, and the Belomorian Province (Figure 6; Figure 8). The majority of the Karelian Province is granite-greenstone belts, while the Kola and Belomorian Province are high-grade gneisses (Gaal & Gorbatshev, 1987).

The Karelian Province underwent several events of rifting between 2.5-1.95 Ga. It started as intracratonic rifts and developed into the opening of basins as “Kola ocean”, with the development of island arcs. This rifting resulted in volcanic activity with simultaneous erosion from the continent and sedimentation in the evolving basins, which made sequences of alternating volcanic- and sedimentary rocks (Nordgulen & Andresen, 2013, p. 71). The basement of the greenstone belts in the Karelian Province are Saamian tonalitic-trondhjemitic-granodioritic rocks (Lahtinen et al., 2005).

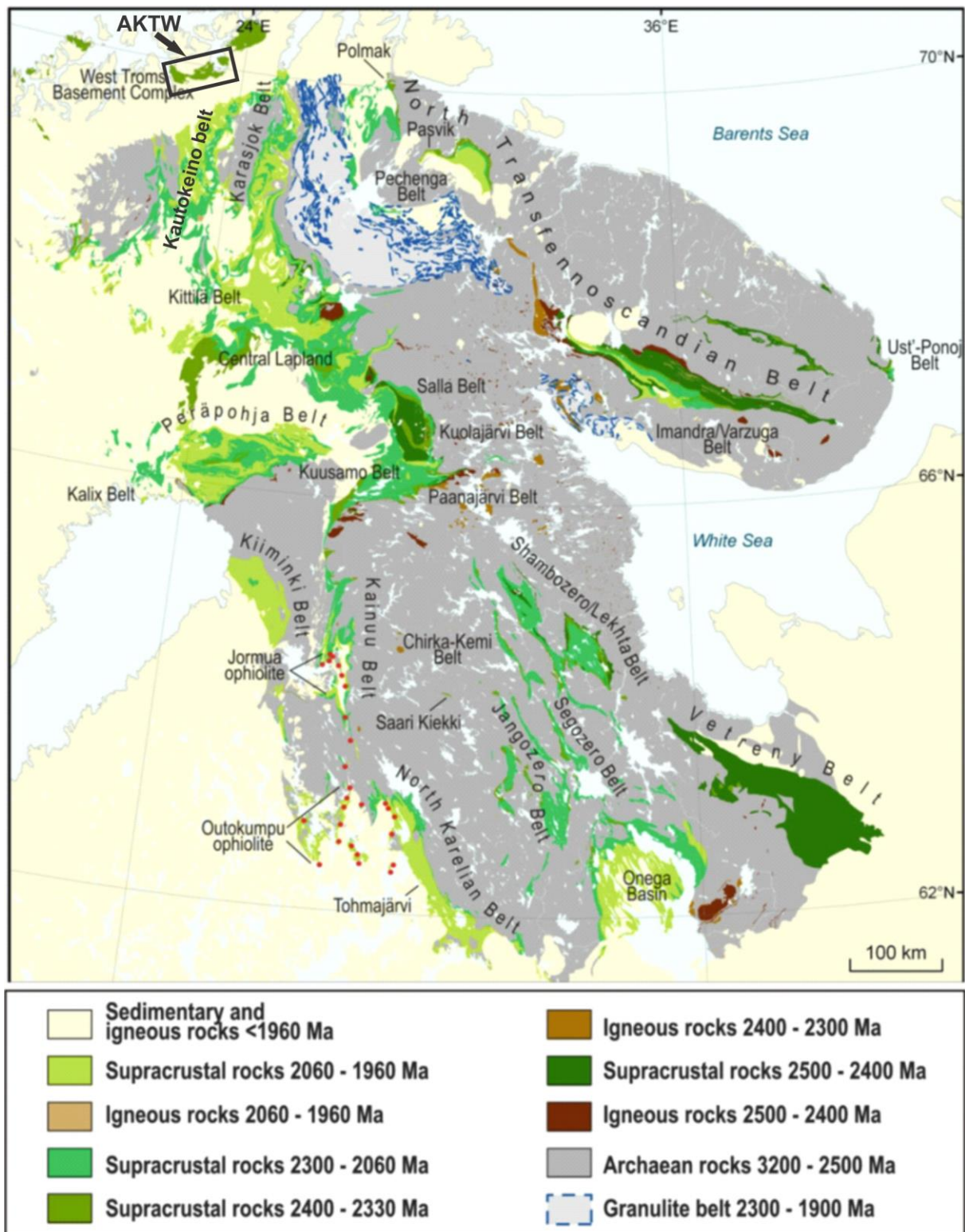


Figure 8: Northeastern-most part (Archean domain) of the Fennoscandian Shield with different types and ages of Palaeoproterozoic and Archean rocks. Alta-Kvænangen Tectonic Window (AKTW) is emphasized in the black rectangle. Modified after Melezhik et al. (2013), based originally on Koistinen et al. (2001).

2.1.2 The Svecofennian domain

The Svecofennian domain (Figure 6) is a terrain formed in the period between 1.92 to 1.79 Ga by the Svecofennian orogeny (Lahtinen et al., 2005). The orogeny occurred due to a period with compression in the western part of the Archean continent (Fennoscandian Shield), where evolved rift basins with volcanic, sedimentary, and intrusive rocks got metamorphosed and folded (Nordgulen & Andresen, 2013, p. 33, 71). Four main stages of orogenic evolution (Nironen (1997) and Lahtinen et al. (2009) within Bogdanova et al. (2015)) are; 1) Accretion of microcontinents (1.92-1.87 Ga); 2) Extension of the continent (1.86-1.84 Ga); 3) Continent-continent collision (1.84-1.79 Ga), and 4) Orogenic collapse (1.79-1.77 Ga).

2.1.3 The Transscandinavian igneous belt

At the end of the Svecofennian orogeny, huge amounts of granitic magmas started to intrude the western part of the Archean continent in the period from about 1.85 to 1.65 Ga. The remaining granites after this event are called “The Transscandinavian igneous belt” (TIB) (seen in Figure 6), and can be followed from Lofoten in the Northern part of Norway to Skåne in Southern Sweden (Nordgulen & Andresen, 2013, p. 71).

2.1.4 The Southwest Scandinavian domain

The Gothian- and Sveconorwegian orogeny are two periods of orogeneses that occurred respectively 1.75-1.55 Ga (Åhäll & Larson, 2001) and ~1.20-0.90 (Gorbatshev & Bogdanova, 1993) Ga ago in the southwestern part of the Archean continent, where rocks from several different tectonic environments got folded and metamorphosed. These rocks are now found in southern Norway and Sweden, making up the Southwest Scandinavian domain seen in Figure 6 (Nordgulen & Andresen, 2013, p. 71).

Lahtinen et al. (2005) redefined the term “Gothian orogeny” from Gaal and Gorbatshev (1987) to the term “Gothian evolution”, as it includes several events of collisions during a period of about 200Ma.

2.1.5 Alta-Kvænangen Tectonic Window

Alta-Kvænangen Tectonic window (ATKW) is in the northernmost part of the Fennoscandian Shield in northern Norway, where it lies as a tectonic window within the Caledonian Kalak Nappe Complex. The tectonic window has been revealed due to erosion of the overlaying Caledonian Nappes by land uplift, and is deformed in a low degree and metamorphosed at lower facies (Nordgulen & Andresen, 2013, p. 81).

AKTW consists of Paleoproterozoic sedimentary, magmatic, volcanic, and volcanoclastic rocks formed during rifting that later have been deformed during the Svecofennian orogeny (Figure 12; Nordgulen & Andresen, 2013, p. 71). AKTW hosts the Raipas Supergroup, which Zwaan and Gautier (1980) have divided into four formations. Kvenvik formation is the lowermost known formation which has been divided into Lower- and Upper Kvenvik formation by Vik (1985). Storviknes formation overlays Kvenvik formation, followed by Skoadduvarri formation. Luovosvarri formation completes the supergroup. The base of the Raipas Supergroup is not known, while the Bossekop Group overlays the Raipas Supergroup and appears as a quartzite in the field area (Zwaan & Gautier, 1980).

AKTW has been considered as a northwestern continuation of the Karelian province, whereas aeromagnetic geophysical maps (Figure 9) indicate a continuation from the Kautokeino greenstone belt (KGB) underneath the Caledonides to the AKTW (Melezhik et al., 2015), and also whereas KBG and AKTW show numerous lithological similarities. Both KBG and AKTW, consist partly of metamorphosed basalts and tuff/tuffites deposited in a marine basin, and the Skoadduvarri formation in the Raipas Supergroup in AKTW, is thought to be equivalent to the Carravarri formation in the KGB (Nordgulen & Andresen, 2013, p. 79, 81).

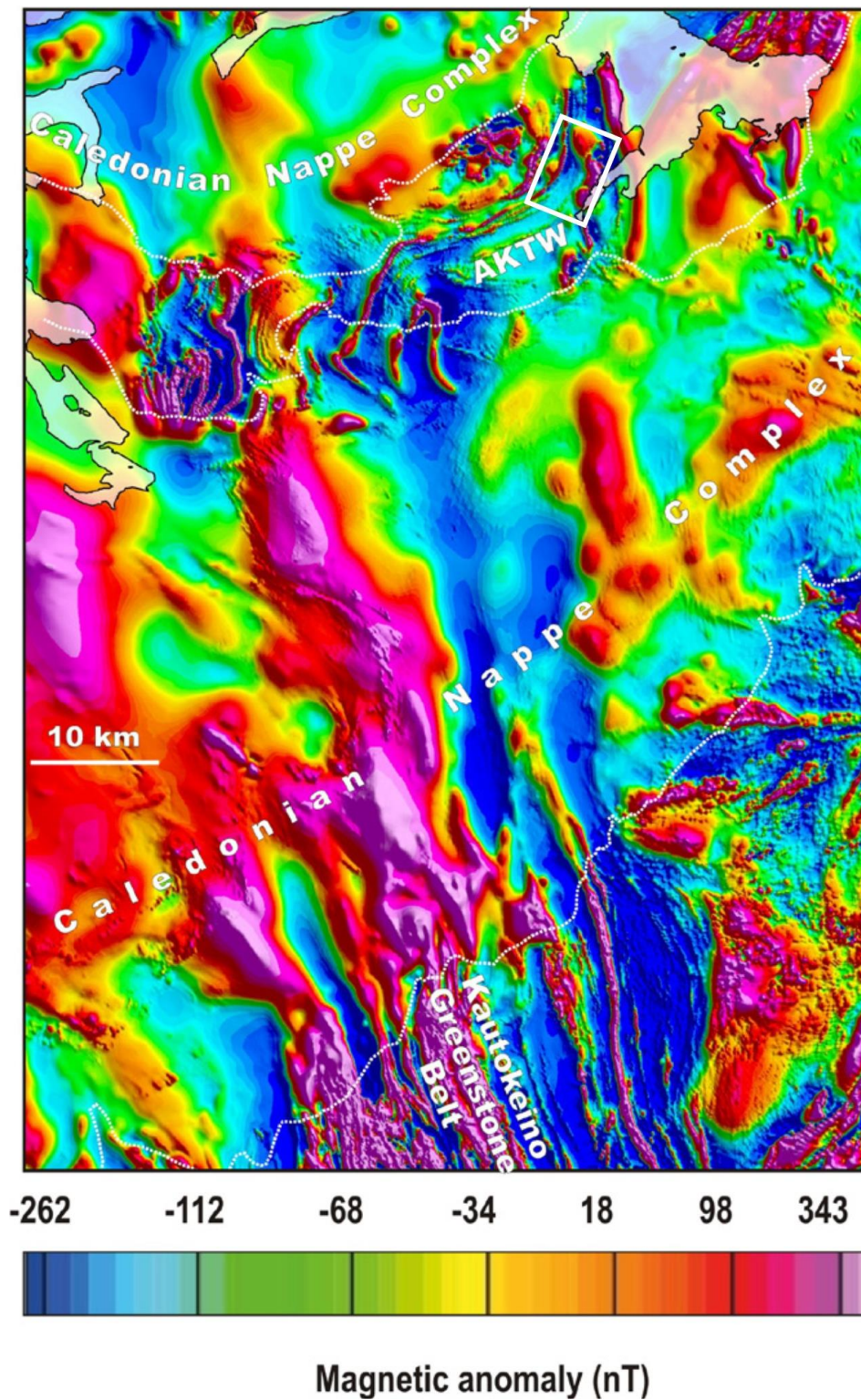


Figure 9: Aeromagnetic anomaly map, showing magnetic features from sedimentary-volcanic formations in KGB traced to AKTW underneath the Caledonian Nappe Complex (emphasized by the white dashed lines). The white rectangle indicates the location of the aeromagnetic map in Figure 5. Modified from Melezhik et al. (2015) with aeromagnetic data obtained from the MINN project database at NGU.

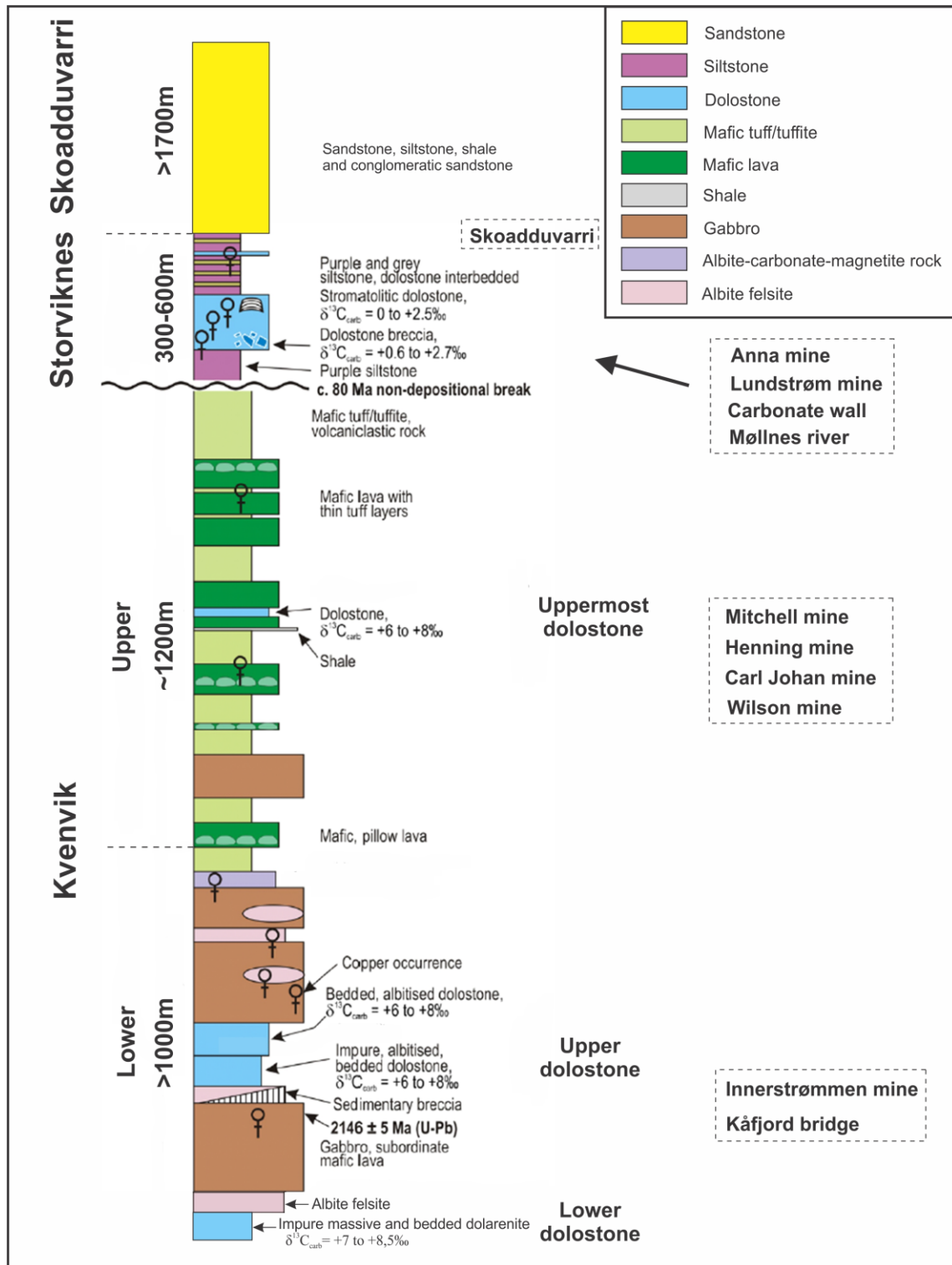


Figure 10: Stratigraphic column of the Kvenvik, Storviknes and Skoadduvarri formations within AKTW modified from Melezhik et al. (2015), based originally on Vik (1985).

2.1.6 Raipas Supergroup

2.1.6.1 Kvenvik (greenstone) formation

The Kvenvik formation is the lowermost known sequence of the Raipas Supergroup in AKTW (Figure 10). It consists of an alternating succession of gabbro, tholeiitic MORB-type basaltic lavas, pillow lava, carbonates, tuff, and tuffite, that have a thickness of at least 1500m and are metamorphosed at greenschist facies (Bergh & Torske, 1988). The carbonate has been identified as dolostones according to Melezhik et al. (2015), which divided them into three dolostone sequences, Lower dolostone, Upper dolostone and Uppermost dolostone (Figure 10). Ultramafic bodies can also be found locally in the Kvenvik formation. They are tectonically re-emplaced rocks and metamorphosed up to the greenschist facies (Gautier et al., 1979). Fifteen repetitive sequences of volcanoclastic rocks and lavas have been identified in the Kvenvik formation (Bergh & Torske, 1988). These sequences have been formed due to multiple eruptions of lava in a terrestrial to shallow-water environment, possibly during an early phase of an intracratonic rift in the Archean basement at the Fennoscandian Shields margin (Bergh & Torske, 1988).

Dating of the Kvenvik formation has been done by two studies. Gautier et al. (1979) have dated fine- and coarse-grained diabases and pillow lava to have a minimum depositional age of 1400 – 1500 Ma by $^{40}\text{K}/^{40}\text{Ar}$ dating method. Gautier et al. (1979) also suggest a formation age of 1800 – 2000 Ma for these rocks based on some of their data. Melezhik et al. (2015) have dated the gabbro hosting the Kåfjord deposits to be 2146 ± 5 Ma by the U-Pb dating method of zircons (Figure 10).

2.1.6.2 Storviknes (dolomite) formation

The Storviknes formation is laying stratigraphically above the Kvenvik formation as an unconformity with an 80 Ma non-depositional break and consists of alternating layers of siltstone and dolomites (Melezhik et al., 2015). Laminated structures of stromatolites are found in the dolomite, formed on the oceanic floor when carbonate particles attached to adhesive matters produced from algae and cyanobacteria (Nordgulen & Andresen, 2013, p. 81).

2.1.6.3 Skoadduarri (sandstone) formation

The Skoadduarri formation is the upper formation of the Raipas Supergroup (Figure 10), which has a gradual transition from the underlying Storviknes formation. Most of the Skoadduarri formation is sandstone, but siltstones, shales, and conglomeratic sandstones also

occur and have a total thickness of at least 1700m (Bergh & Torske, 1986). It is thought to have been formed as a delta in a subsiding marine basin due to evidence of tidal plain, turbidite deposits, upward coarsening, crossbedding, wave ripples, and others (Bergh & Torske, 1986).

2.1.6.4 Luovosvarri formation

The Luovosvarri formation is the uppermost formation of the Raipas Supergroup. This sequence is approximately 100m thick, consisting of alternating layers of stromatolite bearing dolomite, sandstone, and layers of shale. It is thought to be deposited in a shallow marine setting as there for instance are found wave ripple marks (Zwaan & Gautier, 1980).

2.1.7 Bossekop Group

Bossekop Group overlays the Raipas Supergroup unconformably with a basal layer of sandstone, siltstone, and shale, followed by quartzite (Zwaan & Gautier, 1980).

Ore deposits in the Fennoscandian Shield

The Fennoscandian Shield hosts various types of mineral deposits, including orogenic gold deposits, Ni-Cu±PGE deposits, VMS deposits of Zn-Cu-Pb±Ag±Au, iron oxide-copper-gold (IOCG) deposits, and Fe-Ti deposits (Weihed et al., 2005). The formation of the major orogenic gold deposits has been associated with three time periods, from 2.72-2.67 Ga, 1.90-1.86 Ga, and 1.85-1.79 Ga, all related to shortening of the crust. Ni-Cu ± PGE deposits have been deposited in seven different geological environments during a period from 2.74 to 1.88 Ga. These are in Archaean (2.74 Ga) and Palaeoproterozoic (2.20-2.05 Ga) greenstone belts, mafic layered intrusions (2.49-2.45 Ga), ultramafic volcanism (1.97 Ga), Palaeoproterozoic ophiolite complexes (1.97 Ga), mafic and ultramafic intrusions (1.88 Ga) and minor deposits related to dykes of diabase formed in post-orogenic regimes. Between 1.97-1.88 Ga, all the major VMS deposits in the Fennoscandian Shield were formed in an extensional regime. IOCG deposits were formed related to magmatism at 1.88 Ga ago and during the period of 1.80-1.77 Ga. Larger Fe-Ti deposits were formed at 930-920 Ma hosted by anorthositic magma (Weihed et al., 2005).

3 Theoretical background

3.1 Sediment-hosted copper deposits

Sediment-hosted copper deposits or sediment-hosted stratiform copper deposits, represent copper and copper-iron sulfide mineralization hosted by sedimentary rocks such as carbonates, siltstones, shales, or sandstones (Figure 11; Kirkham, 1989). The mineralization is often associated with the original bedding of the host rock (Boynton, 1984), but mineralization can also occur oblique to the original bedding, as sediment-hosted copper deposits can form in different settings and are thought to be of epigenetic origin (Brown, 1997). This means that mineralization is happening after deposition of the host rock, with copper minerals sometimes replaces earlier syngenetic mineralization of iron sulfides (Brown, 1997). The thickness of these mineralized layers is generally less than 30 meters and often less than 3 meters (Hitzman et al., 2010). The deposition most commonly occurs in shallow-marine basins often related to passive continental margins, failed arms of triple junction, or intracontinental rifts with a high rate of evaporation (Cox et al., 2003).

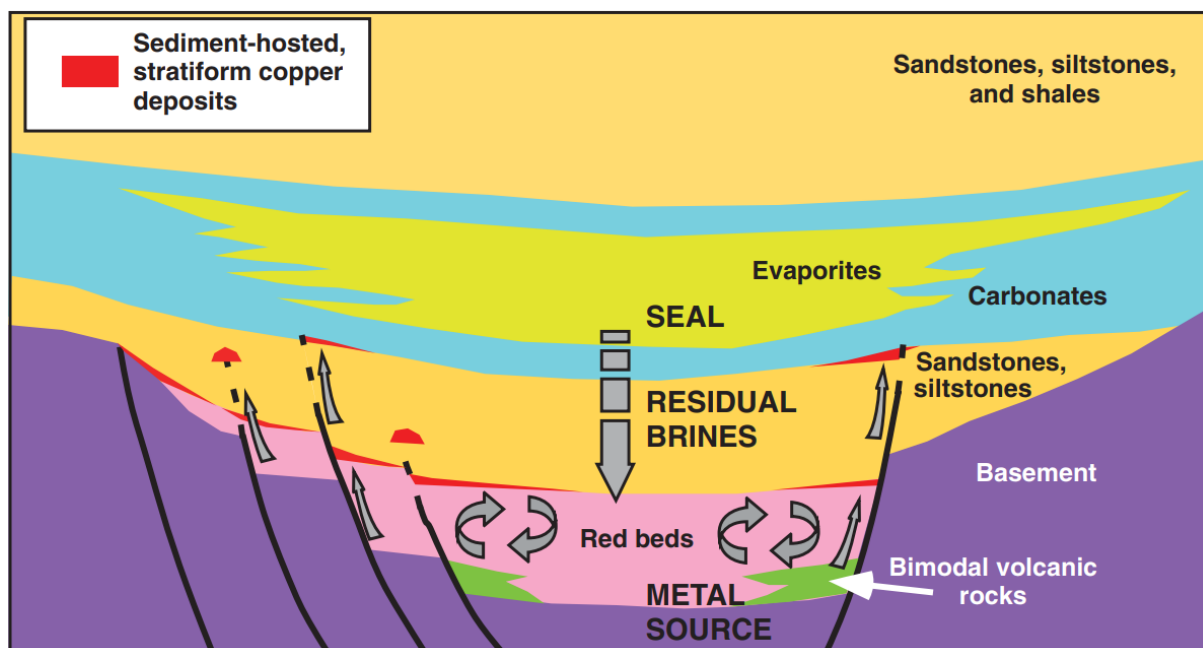


Figure 11: Cross-section of a typical setting of an intracratonic sediment-hosted copper deposit within a closed basin, from Hitzman et al. (2010).

Figure 11 shows a typical sediment-hosted copper deposit in an intracontinental setting with an underlying basement that is filled with red beds and bimodal (felsic and mafic) volcanic rocks formed during rifting of the continental crust. Marine siltstones, shales, and sandstones that locally can be organic-rich overlays. Marine carbonates with a thick sequence of evaporites are deposited above these siliciclastic sediments, which are succeeded by

continental to shallow marine siliciclastic sediments. This sedimentary sequence can have a thickness from a few kilometers up to >10 km, which makes highly saline brines from the evaporitic sequence move down into the oxidized red beds. Convection of the brines is initiated from burial pressure and sometimes igneous activity, whereas this brine-fluid picks up metals from both the red beds (which also oxidizes the fluid) and the underlying basement. The metal-rich oxidized brine circulates up and hits organic material, which acts as a reductant in the siliciclastic sediments, and copper sulfides are precipitated. Precipitation of copper can also occur at higher levels by being transported in faults, but in most cases, the evaporitic layer has a function as an uppermost seal of the hydrologic system (Hitzman et al., 2010).

Subtypes

United States Geological Survey (USGS) collected information about 785 sediment-hosted copper deposits around the world and divided this type of deposit into three subtypes (Cox et al., 2003): 1) reduced-facies Cu deposits; 2) redbed Cu deposits; and 3) Revett-type Cu deposits. These three subtypes vary in both the type of reductant rock (often host rock to mineralization), the reducing ability, and the tonnage and the ore grade.

- 1) Reduced-facies Cu deposits are characterized by an organic matter-rich (high capacity of reducing fluids) fine-grained sediment (e.g. siltstone, shale, mudstone) as a reductant rock occurring in 41 percent of this type of deposit investigated, often with stromatolites and other tidal evidence from lacustrine or marine origin.
- 2) Redbed Cu deposits are characterized by having an organic matter-poor (low capacity of reducing fluids) coarse-grained sediment (e.g. sandstone, quartzite or conglomerate) with minor patches of organic debris as reducing medium within the coarser-grained sediment, which is the case for 85 percents of this type of deposit.
- 3) The Revett-type Cu deposits have a reductant rock that varies and has a low capacity of reducing fluids. The host rock is coarse-grained sedimentary rocks in 77 percent of this type of deposit, whereas sandstone is the most abundant sediment type. In Phanerozoic deposits, the reducing medium is often fluids of sulfide-rich sour gas or hydrocarbons (Cox et al., 2003).

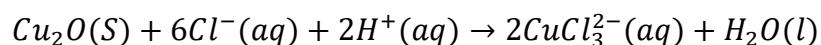
For the reduced-facies Cu deposits, tectonism is an important factor that drives fluid flow and controls ore deposition (Cox et al., 2003). Some deposits have basalt flows as a source rock of copper as in the sediment-hosted Kennecott-type of deposits in the Wrangler Mountains of

Alaska. Here, the underlying greenstones are supposed to host the high-grade copper (ore grade of 13 wt.% Cu) occurring as massive CuS-minerals in the border between the greenstone composed mainly of basalt flows, and the overlying limestone (MacKevett et al., 1997).

Formation criteria's

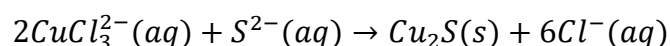
Four conditions to form a sediment-hosted copper deposit are required according to Cox et al. (2003), whereas all of them must be fulfilled to form this type of deposit.

1. The first condition is the presence of an oxidized source rock that is used as a source to leach out copper. This source rock must be a mafic rock, or a rock that contains ferromagnesian minerals such as subaerial volcanic rocks, shales, conglomerates, or red sandstones, and it must also be hematite stable. Marine volcanic rocks are therefore most likely to be unsuitable as a source rock as it has not degassed the volatiles and contain therefore reduced sulfur, which excludes the formation of a hematite-stable environment. The marine volcanic rocks are also not exposed to oxygen in the same degree as subaerial volcanic rocks.
2. The second condition requires a media to mobilize the copper, and this is often brines or evaporites that pick up and transports copper by chloride complexes as they are enriched in sodium and chlorite. Leaching of copper from an oxidized source rock with chlorite complexes can be seen in Equation 1 below.



Equation 1: Copper transported by chlorite complexes.

3. The third condition requires a reduced fluid or rock to precipitate copper. This fluid rich in reduced sulfur can be formed by sulfate-reducing bacteria under anaerobic conditions that are commonly produced in carbonate rocks or organic-rich shales. The reduced host rocks contain often disseminated mineralization of pyrite as fluids in equilibrium with pyrite also can form reduced fluids. Chalcocite is produced when reduced sulfides react with chlorite complexes, as seen in Equation 2 below.



Equation 2: Formation of chalcocite from chlorite complexes

4. The fourth condition is that there must be a condition for fluids to mix in the host rock, which primarily is a sedimentary rock, but sometimes this mixing happens in

volcanic rocks. The host rock needs to have a good ability to transport fluids (high permeability) to allow fluid mixing, which often is related to folding, faults, and graben structures, making way for fluid to circulate and interact. Compaction is also an important factor for fluid mixing. Less permeable shales within the host rock promote conditions for bedding-parallel mixing of fluids and related bedding-parallel mineralization (Cox et al., 2003).

Circulation of fluids in sediment-hosted copper deposits due to a salinity contrast is supposed by Koziy et al. (2009) to be an important mechanism of fluid mixing and transport of deeper-seated copper from igneous basement rocks. This was tested in the Zambian Copperbelt as copper from underlying red beds has been thought to not be a sufficient source of copper by Hitzman (2000), due to too small amounts of and too low copper grade in the available red beds. Koziy et al. (2009) found that even in low permeable rocks, fluid circulation sufficient to leach out elements in igneous basement rocks would occur due to this salinity contrast. When the effect of salinity was removed, the fluid circulation dropped significantly even in permeable rocks containing permeable faults (Koziy et al., 2009).

Ore mineral characteristics

According to Cox et al. (2003), characteristic ore minerals formed in sediment-hosted Cu deposits are pyrite, chalcopyrite, bornite, different types of CuS-minerals as chalcocite and digenite, and minor amounts of sphalerite and galena. Silver in native form is common, and copper in native form is found where the sulfide content is low. Some of these minerals were found in different zones of the deposits, as pyrite was found close to reduced rocks while chalcocite was found close to an oxidized source rock. Based on different ore minerals occurring at different places in the deposit, it can be divided into a high-grade copper zone and a low-grade copper zone. The high-grade zone is characterized by the appearance of chalcocite and bornite with pyrite as a trace element. The low-grade zone is characterized by appearances of pyrite and chalcopyrite, with a negative correlation of pyrite and the copper grade. For reduced-facies, mineralization is characterized by a zonation from chalcocite to bornite to chalcopyrite to pyrite towards the underlying source rock of copper. Cox et al. (2003) also mentioned that in 10 deposits, which nearly all of them are “important” deposits, they contain different arsenic minerals such as tennantite. These arsenic minerals occur together with chalcopyrite and represent a later hydrothermal overprint in the high-grade zone, overprinting earlier epigenetic mineralization of bornite-chalcocite (Cox et al., 2003).

Examples of sediment-hosted deposits

Well-known sediment-hosted copper deposits are the Permian Kupferschiefer deposits in Central Europe and the Neoproterozoic Zambian Copperbelt deposits in Congo, Africa. The oldest known sediment-hosted copper deposits are the Udokan deposit in Russia, with an age of 2.2-1.8 Ga, according to Abramov (2008) within Hitzman et al. (2010). Deposition of the sediments occurred between ~2.2 to 2.06 Ga and mineralization at ~1.9 Ga related to a collision between two domains that also metamorphosed (mostly at greenschist facies) and inverted the metasedimentary basin according to Perello et al. (2016).

3.2 Volcanogenic massive sulfide deposits (VMS)

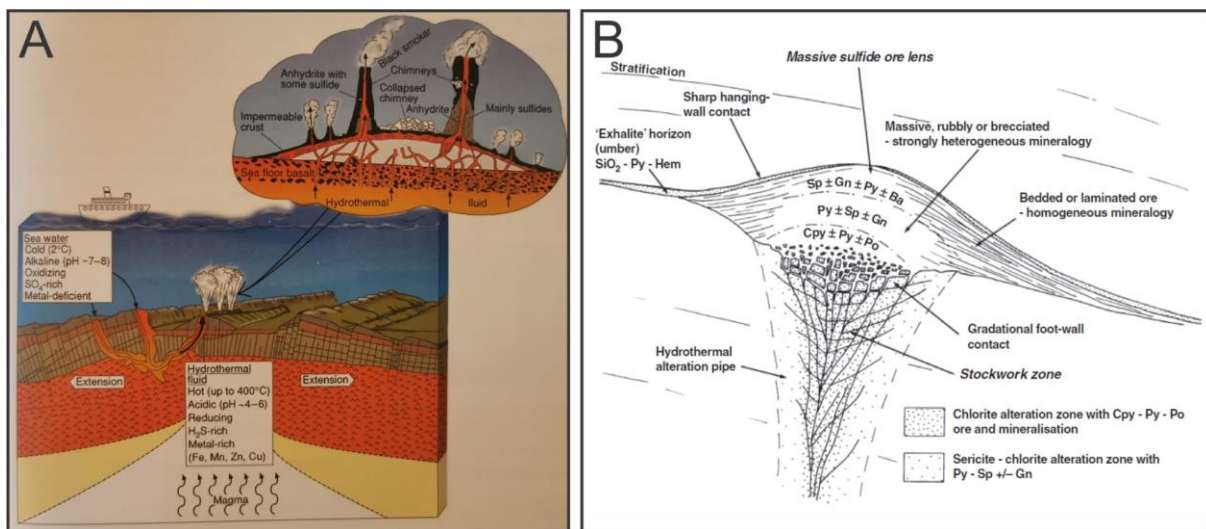


Figure 12: (A) Cross-section of a mid-oceanic ridge environment with formations of black smokers due to fluid circulation, with characteristics of fluids also listed. From Laurence (2020, p. 197) based originally on Lydon (1998) and Scott (1997); (B) Lenticular shaped VHMS deposit with ideally structure and associated ore mineralization from Sawkins (1976). Cpy: Chalcopyrite, Py: Pyrite, Po: Pyrrhotite, Sp: Sphalerite, Gn: Galena, Ba: Barite, Hem: Hematite.

VMS deposits, also called volcanic hosted massive sulfide (VHMS) deposits are deposits typically enriched in Cu and Zn that have been formed from hydrothermal fluids circulating in volcanic active submarine environments (Laurence, 2020, p. 195). Black and white smokers are undersea chimneys associated with VMS deposits forming today, especially around mid-oceanic ridges (Figure 12A). A magma source related to volcanic activity heats the fluids as they travel down towards the magma, elements in the surrounding rocks are picked up, and fluids start to ascend at a certain temperature and pressure. On the way up, the hot hydrothermal fluids are concentrated in channels within the stockwork zone shown in Figure 12B above and escape through chimneys into seawater (Laurence, 2020, p. 196, 197). Precipitation of minerals occurs mainly due to a drop in temperature on the way up, building the chimney itself, the mound around by settlement of particles and chimney collapse, and

mineralization occurs by replacement processes within the mound itself (Lydon, 1998). This mound is, according to Sawkins (1976), characterized by a stratiform zonation of minerals as different elements have a temperature-dependent solubility. This temperature does usually evolve from colder to hotter temperatures as the deposit evolves, with Cu being significantly more soluble at higher temperatures from around 250°C, and Fe in pyrite at even higher temperatures (Laurence, 2020, p. 201, 202). The mineral assemblages in Figure 12B above shows this zonation, with chalcopyrite, pyrite, and pyrrhotite forming the base of the deposit (at a later stage), above the stockwork zone which contains disseminated sulfides (Sawkins, 1976).

Ancient VMS deposits have been exposed to different plate tectonic processes, which most likely have destroyed chimneys, but associated mounds of a stratiform massive sulfide mineralization can be preserved (Figure 12B; Sawkins 1976).

3.3 Stable isotope

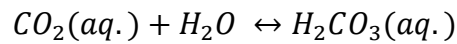
Isotopes are atoms with the same amounts of protons but different amounts of neutrons. Stable isotopes are isotopes of an element that does not change the number of neutrons over time. In contrast, unstable or as also called radiogenic isotopes, do change this number of neutrons over time. As neutrons have a significant weight in atoms, different isotopes of the same element have different weights (Hoefs, 2018, p. 1).

The different weights of isotopes make the lighter isotopes more readily to interact in chemical processes than heavier isotopes as less dissociation energy is needed to break bonds due to the vibrational frequency and energy are higher in lighter isotopes (Tiwari et al., 2015, p. 68). Different geological processes can affect the distribution of the heavier and lighter isotopes of the same element between coexisting phases by isotopic fractionation, and therefore can stable isotope ratios be used to trace back those processes. The two main types of isotopic fractionation processes are, according to Tiwari et al. (2015, p. 68), equilibrium fractionation and kinetic fractionation.

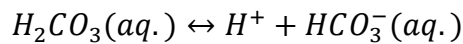
Equilibrium fractionation

The equilibrium fractionation implies that there is an equilibrium between the light and the heavy isotopes in coexisting phases, and changes in this equilibrium are only caused by isotope exchanges (Tiwari et al., 2015, p. 68, 69). The equilibrium depends mostly on the temperature, with higher temperature giving less fractionation and opposite, but it is also to

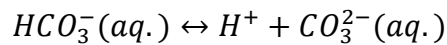
some degree depending on the pressure in the system (Hoefs, 2018, p. 6). Evaporation-condensation processes are an example that can lead to variation in isotopic composition by pressure change, as lighter isotopes will preferentially be in the vapor phase and heavier in the liquid phase (Hoefs, 2018, p. 8, 9). Formation of carbonates enriched in ^{13}C is usually caused by equilibrium fractionation as inorganic carbon from the atmospheric CO_2 enters the seawater, as seen in the equations below (Hoefs, 2018, p. 62).



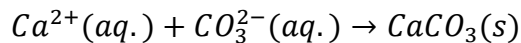
Equation 3: Carbon dioxide reacts with H_2O forming carbonic acid in equilibrium (Hoefs, 2018, p. 62).



Equation 4: Carbonic acid forming H^+ and bicarbonate in equilibrium (Hoefs, 2018, p. 62).



Equation 5: Bicarbonate forming H^+ and carbonate ion in equilibrium (Hoefs, 2018, p. 62).



Equation 6: Calcium and carbonate ions forming calcite (Hoefs, 2018, p. 62).

What also can be formed in addition to calcite is dolomite if magnesium (Mg^{2+}) is available in the system or ankerite if an addition of iron (as Fe^{2+}) and manganese (Mn^{2+}) are available.

Kinetic fractionation

The kinetic fractionation can also cause isotopic fractionation and is mainly based on the rate of reactions in molecules that forms no isotopic equilibrium (Tiwari et al., 2015, p. 69).

Diffusion is one process that can give rise to kinetic fractionation as there will be a fractionation between light and heavy isotopes, as lighter isotopes will travel faster than heavier ones (Hoefs, 2018, p. 10, 12). Organic carbon is typically isotopic light ($\sim -25\%$) enriched in ^{12}C by kinetic fractionation effects during complex reactions when carbon dioxide is transformed into oxygen by photosynthesis in both terrestrial and aquatic plants (Hoefs, 2018, p. 64-66). Marine carbonates have in general a $\delta^{13}\text{C}$ value of $\sim 0\%$, which can be disturbed by infiltration of light organic carbon if production and burial of organic matter are high. The organic matter enriches the marine carbonates in lighter ^{12}C , which moves the $\delta^{13}\text{C}$ into a lighter composition (Hoefs, 2018, p. 65, 66).

Delta notation

$$\delta^{18O} = \left(\frac{\frac{18O}{16O} \text{ sample} - \frac{18O}{16O} \text{ standard}}{\frac{18O}{16O} \text{ standard}} \right) \times 1000\text{‰}$$

Equation 7: Calculation of delta oxygen 18, modified from Pat Shanks III (2014).

The delta notation (Equation 7) is used to express the differences in isotopic composition between the sample and the relevant standard. The expression for δ^{18O} is shown in the equation by using 18O and 16O , but other elements as carbon by 13C and 12C or sulfur with 34S and 32S are also usually applied, getting a result in per mil (‰) as the differences in the isotopic composition is very small. If the measured sample has a heavier isotopic composition than the standard reference composition used, a positive value will be calculated, while a negative value indicates the opposite (Pat Shanks III, 2014, p. 60).

International standards

The original standard used for 18O and 2H in water are SMOW (Standard Mean Oceanic Water) after Craig (1961), but IAEA (International Atomic Energy Agency) replaced this standard with the now international used V-SMOW (Vienna-SMOW) standard, obtained from distilled seawater which differs slightly from SMOW. PDB (Pee Dee Formation) was introduced to use as a standard for both 18O and 13C in carbonates by Craig (1957). This has later been used as the standard for all compounds of carbon. IAEA introduced VPDB (Vienna-PDB) not long after PDB, which is nearly identical to PDB and has been accepted to be used internationally (Clark & Fritz, 1997, p. 8-10).

Lomagundi-Jatuli Event

The Lomagundi-Jatuli Event is a global event of positive δ^{13C} isotope values in sedimentary carbonates during a period of Palaeoproterozoikum (Melezhik & Fallick, 2010), that have been formed due to an increased burial of organic carbon initiated by an increase of oxygen in the atmosphere (Bachan & Kump, 2015). The period of deposition of these sedimentary carbonates has been suggested by Karhu (1993) to be formed with a δ^{13C} peak of $10 \pm 3\text{‰}$ at 2.1-2.2 Ga ago in the Fennoscandian Shield. Melezhik et al. (2007) suggested the minimum age of this event to be 2058 ± 2 Ma by using zircons in sedimentary rocks as a dating method.

3.4 Fluid inclusion studies

Fluid inclusions (FIs) are small inclusions mostly between 1-10 μm , rarely larger than 1mm (Roedder, 1984) of solid, liquid and/or vapor phases that have been trapped within a mineral

at liquid phase (Bodnar, 2003a) during the growth of the mineral as primary or pseudosecondary inclusions, or later as secondary inclusions (Roedder, 1984). Primary inclusions are trapped in defects during mineral growth, while pseudosecondary inclusions are trapped during healing of fractures also during mineral growth and secondary inclusions are trapped later after mineral growth, during healing of fractures, seen in Figure 13 (Roedder, 1984). A fourth type of fluid inclusions is those that are identified as indeterminable inclusions (Goldstein, 2003).

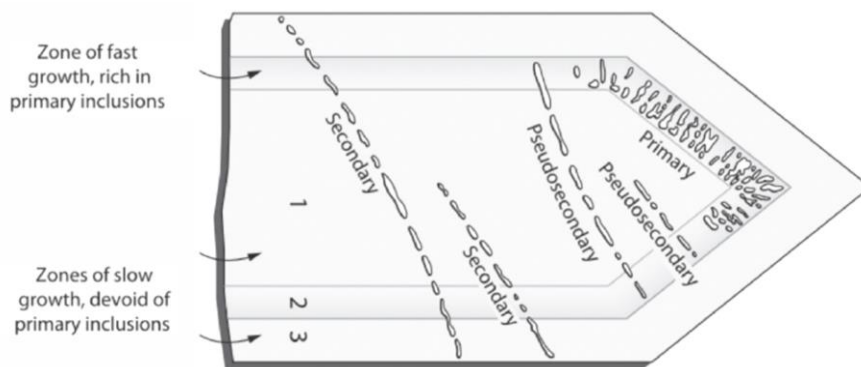


Figure 13: Illustration of primary, secondary and pseudosecondary fluid inclusions within a mineral, from Lambrecht and Diamond (2014).

These inclusions cannot be assigned with confidence to any of those three origins that are mentioned. The fluid which is the source of these inclusions can be of various origin, forming different types of fluid inclusions (Figure 14). This fluid can be a liquid, a vapor, or a supercritical fluid (Bodnar, 2003a), forming these different phases in the fluid inclusions seen in Figure 14. The composition among the fluid inclusions depends on what fluid have been present when the fluids were trapped. As described by Bodnar (2003a), this fluid composition can include: “pure water, brines of various salinity, gas or gas-bearing liquids, and silicate, sulfide or carbonate melts, among others” (Bodnar, 2003a, p. 1).







Inclusion types		
Monophase liquid (L) 	Monophase vapor (V) 	Monophase solid (S) 
Liquid-rich, two phase (L+V) 	Vapor-rich, two phase (V+L) 	Multiphase solid (S+L±V) 

Figure 14: Selected fluid inclusion types, modified after Shepherd et al. (1985). Abbreviations: L: Liquid, V: Vapor, S: Solid.

Fluid inclusion assemblage

Fluid inclusion assemblages (FIAs) are described by Goldstein and Reynolds (1994) within Bodnar (2003a, p. 5) as: “a group of fluid inclusions that were all trapped at the same time”. As FIA are trapped at the same time, it is also assumed to have been trapped in a fluid of the same composition and under the same pressure and temperature conditions (Bodnar, 2003a). The time of trapping is relative, as this time varies from the type of deposit it has been formed in and could potentially last for a longer period, with for instance in deeper metamorphic deposits where the pressure and temperature condition can remain the same for many years (Bodnar, 2003a). Fluid inclusions formed in a mineral within an immiscible fluid will most likely not represent the overall composition of the fluids by only measure one fluid inclusion, and it is therefore necessary to identify fluid inclusions within FIAs to get a better indication of the system (Goldstein & Reynolds, 1994). FIAs need to be identified by petrography, which is most commonly done with a transmitted light microscope but also with CL (cathodoluminescence) and BSE (backscattered-electron) (Goldstein, 2003).

Roedders Rules

When an FIA has been assigned by petrography, Roedders Rules needs to be verified before microthermometric measurements can start. Roedders Rules are, according to Bodnar (2003a), three rules that must be verified by either petrography and/or microthermometric analysis to check if fluid inclusions still provide the original trapping conditions and not have been reequilibrated by later processes (Bodnar, 2003a).

- 1) The first rule is that the inclusion must be trapped as a single homogenous phase.
- 2) The second rule is that the volume of the inclusion must not have been changed after trapping (must represent an isochoric system).
- 3) The third rule is that it must represent the original inclusion with nothing added or removed after trapping (Bodnar, 2003a).

Similar petrographic properties such as phase proportions and microthermometric behavior as homogenization temperature indicate that the fluid inclusions most likely meet Roedders Rules (Bodnar, 2003a).

3.4.1 Microthermometric measurements

Homogenization temperature

When performing a fluid inclusion study, one measure and identifies several different properties of fluid inclusions to obtain data as pressure, density, salinity and composition. This is done by petrography and also microthermology, which is the study of phase changes in fluid inclusions during heating and cooling, allowing for the determination of temperatures making phase changes (Goldstein & Reynolds, 1994). In the study of ore deposits, fluid inclusions can for instance be used to estimate the temperature of the ore-forming fluids in hydrothermal deposits (Bodnar et al., 2014). Fall and Bodnar (2018) developed an acceptable range of homogenization temperature from fluid events in different deposits, suggesting that a difference in temperature of $>20^{\circ}\text{C}$ within one FIA should be checked.

To estimate the temperature of the ore-forming fluids, the homogenization temperature (T_h) needs to be measured (Figure 15), which is the measured temperature when for example a two-phase fluid inclusion at room temperature forms one single phase when being heated up at higher temperatures (Bodnar et al., 2014). The reason for the formation of a two-phase fluid inclusion at lower temperatures can be explained as described by Roedder (1984). He explains that cooling of a newly formed host mineral and trapped fluid inclusions will make the fluids within the inclusion shrinking more than the host mineral, and by this forcing a bubble to form at a lower temperature than the formation temperature (usually observed at room temperature), as a response to weight up for the increased pressure formed within the inclusion (Roedder, 1984). Heating the sample up from what usually is room temperature to the formation temperature, will make the bubble disappear and form a homogeneous fluid again as the pressure decreases, and this is what is called the homogenization temperature (Roedder, 1984). If the fluid inclusions are primary inclusions, this temperature will represent the temperature of the fluids when the mineral was formed (Bodnar et al., 2014), while secondary inclusions will provide temperature data about fluids in the system at a later time.

As some fluid inclusions also occur as single-phase inclusions at room temperature, the homogenization temperature measured by these inclusions is the minimum temperature at when they were formed, and a pressure correction must therefore be done to obtain the correct trapping temperature (Bodnar, 2003b).

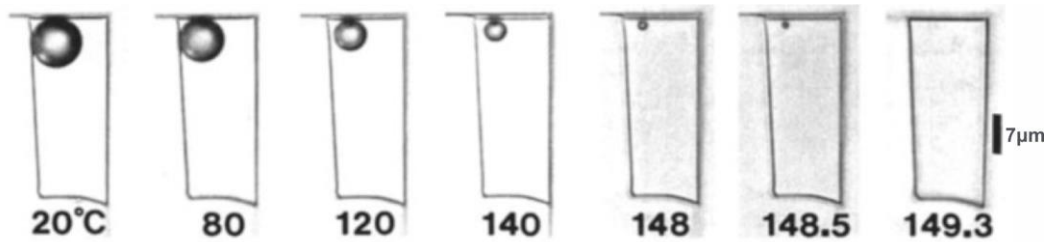


Figure 15: Heating of a vapor bubble in a fluorite inclusion from 20 to 149.3°C, indicating T_h at 149.3°C by a total homogenization. Modified from Goldstein and Reynolds (1994).

To assign the homogenization temperature as the original fluid temperature, the inclusions must be entrapped within an immiscible or boiling fluid system with no indications of changes after entrapment (Bodnar et al., 2014). Two-phase L+V inclusions indicate being entrapped within an immiscible or boiling fluid and T_h can therefore already be used as the temperature of the fluid. It is important to do the heating of the sample first as cooling can make the fluid inclusions stretch and may decrepitate due to volume expansion (Lawler & Crawford, 1983). As noted by Bodnar (2003c), decrepitation of fluid inclusions happens when fractures develop due to an increasing change in size or shape of the inclusions and all fluid escapes, making them unusable for fluid inclusion study, which is more common to occur during cooling but can also happen during heating (Bodnar, 2003c).

First melting temperature

By performing microthermometry on aqueous inclusions by cooling below 0°C, one can according to Goldstein and Reynolds (1994), among other properties, predict the composition of the fluid and also suggest which phase diagram should be applied for the specific fluid inclusion assemblages. The composition of the fluid is determined by measuring the first melting temperature (T_e), or as also called the eutectic temperature. This is the temperature at which the solid (frozen) phase starts to melt (Goldstein & Reynolds, 1994).

The first melting temperature can in some settings be difficult to determine exactly, as in for instance small hydrohalite crystals in low salinity fluids (Goldstein & Reynolds, 1994). In such cases, a temperature that is the lowest observed temperature during melting but still higher than the first melting temperature can be determined by looking at movements or changes in the outlines of the crystal, which will be sufficient enough to be used for the assignment of many system compositions that are not too close to each other (Goldstein & Reynolds, 1994). The composition of fluids are also very complex, especially in aqueous sedimentary fluid inclusions, which implies that the determination of a system composition

based on first melting temperature does not consider all components in the fluid (Goldstein & Reynolds, 1994).

H₂O-NaCl & H₂O-NaCl-CaCl₂ systems

When the first melting temperature is determined, it can be assigned to a system composition of for example H₂O-NaCl if the first melting temperature occurs at ~-21°C and H₂O-NaCl-CaCl₂ if it occurs at ~-52°C, because NaCl will be the principal dissolved salt at ~-21°C and NaCl and CaCl₂ will be the principal dissolved salts at around -52°C (Borisenko, 1977). This is demonstrated in Figure 16 below, which shows that the first melting temperature for the H₂O-NaCl system composition occurs at -21.2°C with a salinity of 23.3 wt.% NaCl when it is heated up from ice and hydrohalite forming liquid and ice.

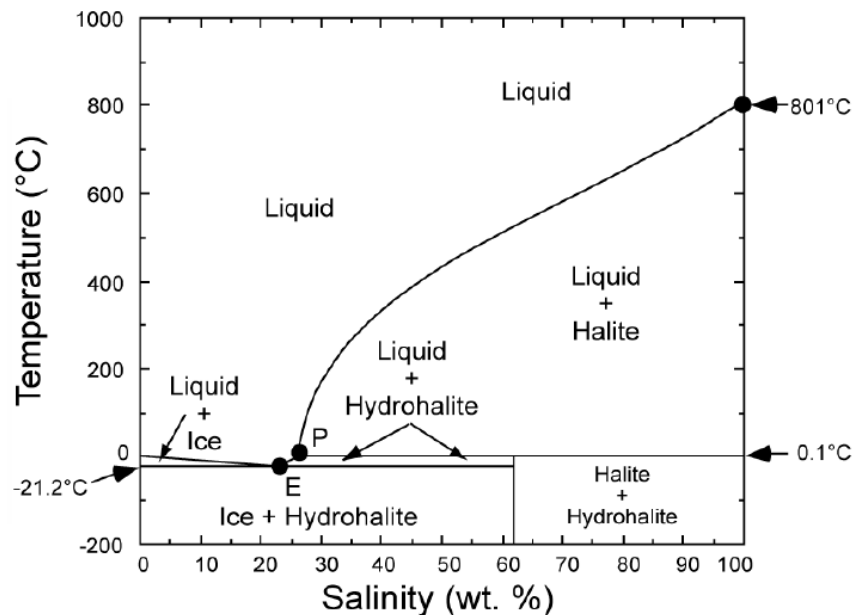


Figure 16: Projection of temperature and salinity in a vapor-saturated H₂O-NaCl system, from Bodnar (2003b) that is based on data from Hall et al. (1988), Sterner et al. (1988) and Bodnar et al. (1989). E: Eutectic (-21.2°C, 23.2wt.% NaCl).

For all aqueous system compositions, there also occurs an immiscibility field that depends on the salinity of the fluid at a certain pressure and the temperature conditions. This immiscibility field (Figure 17) for the H₂O-NaCl system indicates that a lower salinity vapor phase and a higher salinity liquid phase occur in equilibrium within the pressure and temperature conditions of the shaded area, but this area is smaller for less saline fluids (Bodnar, 2003b). Inclusions formed at P-T conditions outside this immiscibility field will be single-phase vapor or liquid depending on the pressure and temperature (Bodnar, 2003b).

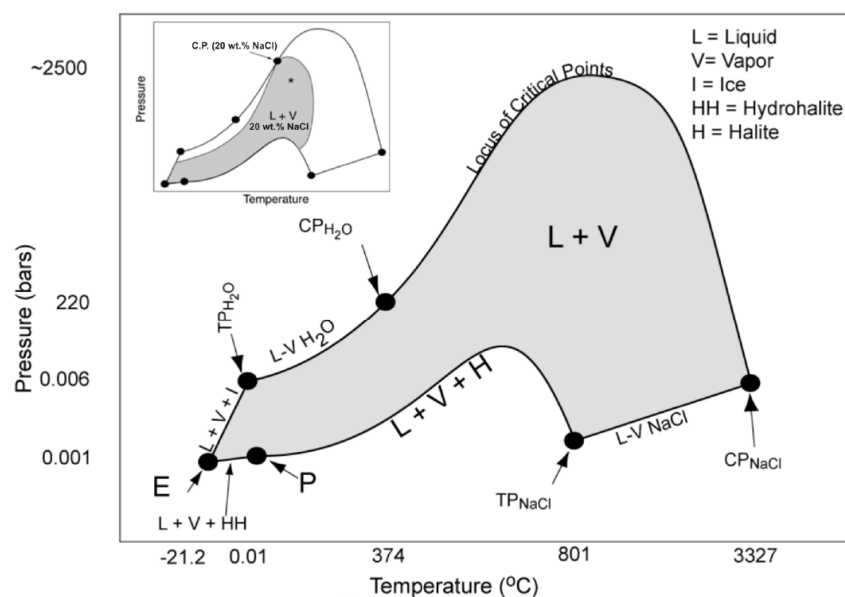


Figure 17: Pressure and temperature projection for the H₂O-NaCl system. The shaded area represents a fluid immiscibility between a high salinity liquid and a low salinity vapour phase, with the smaller inset figure showing a system with a salinity of 20 wt.% NaCl. From Bodnar (2003b). Abbreviations: TP: triple point, CP: critical point, E: eutectic point, P: peritectic point.

In two-phase (liquid + vapor) aqueous fluid inclusions, the final ice melting temperature (T_m ice) can be used to determine the bulk salinity of the entrapped fluid (Goldstein & Reynolds, 1994). If the fluid contains halite daughter minerals, the final melting temperature of halite (T_s) shall be used to calculate the salinity of the fluid as T_s are proportional to the wt.% of NaCl, and the solubility of NaCl at different temperatures are known (Shepherd et al., 1985).

$$\text{Wt. \% NaCl} = 26.242 + 0.4928x + 1.42x^2 - 0.223x^3 + 0.04129x^4 + 0.006295x^5 - 0.001967x^6 + 0.0001112x^7$$

Equation 8: Calculation of the salinity of a fluid by T_s , where x is equal to $T^\circ\text{C}/100$ with $0.1 \leq T^\circ\text{C} \leq 801^\circ\text{C}$, from Sterner et al. (1988).

This equation can only be applied in an H₂O-NaCl system if halite dissolves at the same time when liquid and vapor homogenizes, meaning on the L+V+H curve in Figure 17. The density of a fluid which is depending on the homogenization temperature, can be calculated by combining the homogenization temperature and the composition of the fluid with thermodynamic data, in for example in the H₂O-NaCl system (Archer, 1992). With a known density, the pressure in the system can be calculated by isochores, given that the volume of the fluid inclusions have remained constant after trapment. The slop of isochores, which are a linear relationship between the pressure and temperature in a system, has been constructed for the H₂O-NaCl system by Bodnar and Vityk (1994), using the homogenization temperature, salinity,

Fluid inclusion characteristics from Repparfjord tectonic window

Fluid inclusion characteristics from the Repparfjord tectonic window (RTW), located ~80 km NE of AKTW (Figure 7) have recently been published (Mun et al., 2020). RTW hosts a succession of mafic metavolcanic and sedimentary carbonate-siliciclastic rocks with two Cu deposits, “Nussir” and “Ulveryggen”, hosted in dolomitic marble and metasiliciclastic rocks. FI characteristics from the Nussir deposit show homogenization temperatures ranging between 135 to 350°C and 102-520°C at the Ulveryggen deposit, with salinity ranging from 0.35 to 36 wt.% NaCl equ. Cu-sphalerite geothermometry combined with fluid inclusion data indicates that the Cu mineralization at Nussir was formed at 330-340°C and a pressure of 1.1 to 2.7 kbars (Mun et al., 2020).

3.5 Methodology

3.5.1 LA-ICP-MS (-AES)

LA-ICP-MS (Laser Ablation - Inductively Coupled Plasma - Mass Spectrometer) is an instrument (Figure 18) that combines several different techniques to get a highly precise isotopic and elemental composition of major and trace elements, down to parts per billion by single solid mineral spots and also in bulk analyses of powder (Fryer et al., 1995). For geological sciences are LA-ICP-MS used a lot due to the low detection limit and spatial resolutions on the μm scale, where it among other things can determine concentrations of rare earth elements within mineral phases, and in the subject of ore-forming processes, it can identify elements occurring in fluid inclusions (Günther & Hattendorf, 2005). It can also be used for bulk rock geochemistry by ablation of a solid sample or a powder (Yongsheng et al., 2013).

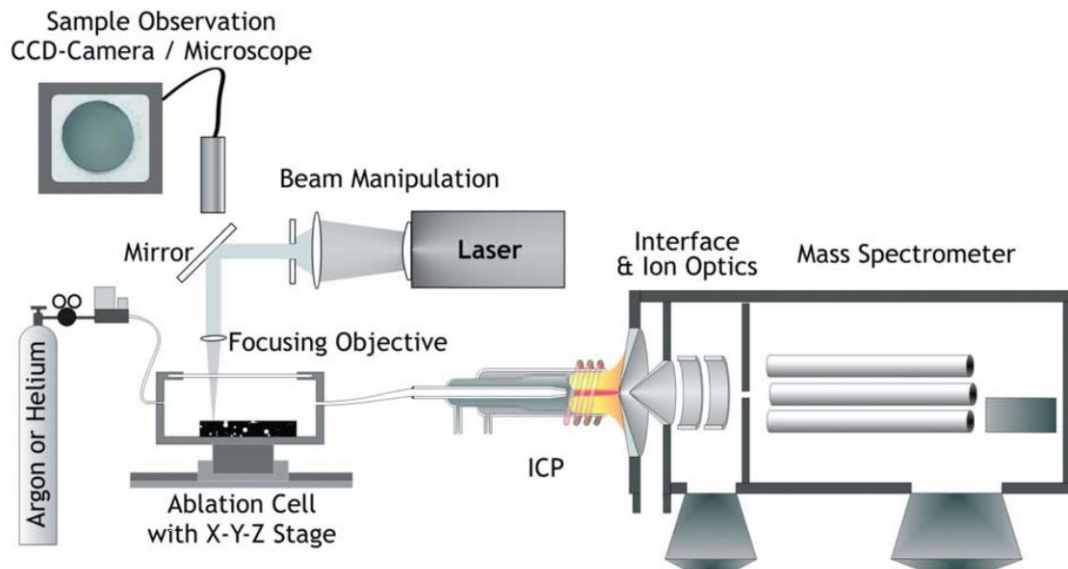


Figure 18: The main components of a LA-ICP-MS system. From Günther and Hattendorf (2005).

LA-ICP-MS is a relatively fast method, with the analysis of one spot done within 3 minutes as there is no need for sample digestion (Yongsheng et al., 2013). The process starts with adjusting the area of interest in position, and a focused laser beam ablates a given spot size of the sample into aerosol particles. These aerosol particles are then transported to the ICP module by inert gasses like helium and argon (Koch & Günther, 2011). In the ICP module are the particles ionized at high temperatures by a bombardment of electrons before it travels through the mass spectrometer, where a magnet separates the ionized elements and related isotopes due to differences in the mass to charge ratio, as lighter elements and isotopes of elements are more attracted by the magnet. These ionized elements are collected in faraday collectors, often three collectors in newer instruments but single collectors (SC) are also used where the signal from the ions are converted to electrical impulses, and sent to an amplifier and interpreted by a data program (Hoefs, 2018, p. 28, 29).

Accuracy

The accuracy of the analysis depends on many factors within the instrument itself but also on an external reference material and an internal standard used. The internal standard, which is the known concentration of at least one element in a sample, is used together with the external reference sample for corrections of differences between the sample and the external reference during ablation, and the external sample is also used to calibrate the instrument itself before ablation (Fryer et al., 1995). These external reference materials are standard materials in different types, such as the USGS GS reference glasses, which includes the GSC-1G, GSD-1G and GSE-1G that contains major and trace elements of basalt, in the concentration ranges

4-5 ppm, 40-50 and 400-500 ppm, respectively (Yongsheng et al., 2013). Element fractionation is one of the main disadvantages of the LA-ICP-MS method, which makes problems with the instrument's calibration as different suites of elements behave similarly during ablation (Fryer et al., 1995).

To improve the accuracy and precision of the analysis, and to also reduce the detection limit, using a larger spot size will help (Yongsheng et al., 2013). However, this larger spot size is not possible to obtain in every setting as mineral grains contain in many circumstances impurities or are intergrown, and many grains are also very small. UV wavelengths are used in the ablation process due to the advantages of using shorter wavelengths over longer wavelengths such as IR (Günther & Hattendorf, 2005), as a shorter wavelength will reduce the thermal alteration of the ablated material (Outridge et al., 1997).

ICP-AES

ICP-AES (Inductively Coupled Plasma Atomic Emission Spectroscopy) uses the light rays produced from the ICP-module to identify up to 70 different elements in the AES-module by their characteristic light rays. The concentration of each element is measured down to parts per billion (ppb) from samples in both solid, liquid and gaseous phases (Neikov & Yefimov, 2018, p. 94).

3.6 Previously work

The geology of the Kåfjord area has been studied by Bergh and Torske in several papers. Bergh and Torske (1988) presented a model for the deposition of the Kvenvik formation. This model suggests a deposition related to a volcanic active rift system where volcanic lavas and volcanoclastic material was deposited continuously in a shallow water to subaerial setting with a spasmodically subsidence. The volcanic activity decreased, and the Storviknes and Skoadduvarri formation was deposited. Bergh and Torske (1986) worked with the Skoadduvarri formation and suggested it was deposited in a subsiding marine basin, with the Alta area deposited on a delta as fluvio-marine sequences.

Mørk (1970), Vik (1985) and Melezhik et al. (2015) among others, were working more specifically on the Cu mineralization and/or its host rocks. Their main findings are summarized in the text below.

3.6.1 Kvenvik formation

The basis of the Kvenvik formation in Kåfjord is a metagabbro (Mørk 1970). Melezhik et al. (2015) classified the metagabbro (2146 +/- 5Ma) to be a coarse-grained leucocratic and homogenous gabbro containing calcite-chalcopyrite veinlets. They classified the texture as an unfoliated ophitic texture with laths of plagioclase embedded in an interstitial matrix of amphibole where epidote, chlorite, and calcite replace mafic minerals. Accessory magnetite and chalcopyrite were also identified in the gabbro (Melezhik et al., 2015).

Mørk (1970) proposed that all mineralization in Kåfjord are related to a big shear zone, either laying in the shear zone or next to it with mineralization related to infill in cracks in the greenstone. Brittle thrusting makes the biggest distance of mineralization from the shear zone hard to determine (Mørk, 1970). Melezhik et al. (2015) have identified copper sulfides in AKTW in general within Kvenvik formation occurring in quartz-carbonate veins hosted by volcanic rocks and as disseminations in albite felsites.

Melezhik et al. (2015) found enrichment of $\delta^{13}\text{C}$ in all dolostone units (Lower, Upper and Uppermost) in the Kvenvik formation, which is linked to the global isotopic event Lomagundi-Jatuli. All $\delta^{13}\text{C}$ values are varying between +5.4‰ to +8.5‰ except one at +1,7‰. The $\delta^{18}\text{O}$ values of the same dolostone units are low, varying between +13‰ to +23.3‰. Any significant correlation between the $\delta^{13}\text{C}$ and the $\delta^{18}\text{O}$ values, with SiO_2 or Na_2O abundance or Mn/Sr or Mg/Ca ratio was not found. For the upper dolostone unit, which is the only dolostone investigated in the area of Kåfjord, 11 samples gave a range of value for $\delta^{13}\text{C}$ between +7.3‰ to +8.3 ‰ and $\delta^{18}\text{O}$ between +13.9‰ to +15.1‰ (Melezhik et al., 2015).

Carl Johan mine

The Carl Johan mine is, according to Mørk (1970), one of the first areas with Cu mineralization found in Kåfjord. It is divided into two mines that are not connected on the surface, with mineralization occurring as infill in cracks in strongly tectonized greenstone. The biggest of these mines is “Store Carl Johan”, which is approximately 150m long at the surface, striking 30 degrees with a dip of 60 degrees towards west, with gangues in the northern part, oriented E-W. “Lille Carl Johan” is approximately 60-70m long, striking 18 degrees and dipping vertically. Numerous smaller veins with various directions occur at both Store and Lille Carl Johan. The average thickness of the Carl Johan deposit is less than 1m, and core drilling in 1967 indicated that the mineralized gangues got thinner the deeper it was drilled (Mørk, 1970).

Mitchell's mine

The Mitchell's mine is the westernmost mine of the Kåfjord mines with a length of about 300 meters and an average thickness of 1-1.5 meters, oriented with a strike of 0-15 degrees dipping steeply towards east. The Cu-mineralization occurs in the main vein and also in minor veins with various orientations (Mørk, 1970).

Henning mine

The Henning mine occurs in tectonized graphite-rich schist hosting mineralization of pyrite and chalcopyrite, which is mainly related to infill of quartz and carbonate in cracks. This mine was a test mine that is nearly mined empty with several smaller prospects north of this mine (Mørk, 1970).

3.6.2 Storviknes formation

The Storviknes formation has a base of a reddish laminated calcareous siltstone, followed by three thin layers of massive dolomite and quartz, which alternates within a green-colored siltstone, according to Vik (1985). These sedimentary layers of dolomites and siltstones are deposited in a shallow-marine tidal environment with various thicknesses. At Melsvik, the total thickness of Storviknes formation is 100 meters, containing five thinner dolomite layers (0.3-5 m) alternating within a green to grey-colored siltstone (Vik, 1985).

Vik (1985) has found Cu mineralization in several stratigraphic levels related to epigenetic and sedimentary structures occurring in dolomites and hematite-rich red- and grey-colored siltstones. Melezhik et al. (2015) has identified copper sulfides in AKTW in general within Storviknes formation occurring in sediment-hosted deposits as cement in breccias and disseminated in shales and dolomites.

The Anna and Lundstrøm mines are two historical mines that lay on the mountain west of Kåfjord in the western limb of the synclinal, within Storviknes formation. The sedimentary layers hosting these two mines are dipping steeply towards west, and Mørk (1970) suggests that they are tectonically affected by a zone that is parallel with the strike of these layers, giving rise to the mineralization (Mørk, 1970).

Anna mine

The Anna mine is, according to Vik (1985), hosted by a grey-colored siltstone with a general weak foliation but a well-developed schistosity (and crenulation) in the lower part of the stratigraphy. This siltstone alternates with three thin dolomite layers that contain spread

copper-mineralization in all layers, but the mining operation has mostly been concentrated in the middle layer by a 50m underground entrance and a 50m underground mine.

Mineralization is related to displacement by coarse-grained quartz, calcite, dolomite, and baryte in the fine-grained laminated dolomite layers. Pyrite and chalcopyrite are the main ore minerals, with chalcopyrite and accessory galena occurring in cracks in the quartz (Vik, 1985).

Lundstrøm mine

At the Lundstrøm mine, three dolomite layers alternate within a green-colored siltstone that has its color due to the influx of clay minerals and dolomite, according to Vik (1985). The main mined area lies below the lower/westernmost dolomite layer close to Lundstømvannet as two shafts, in a strongly tectonized siltstone that is mineralized. The mineralized area indicates later deformation by brecciation and folding with mineralization related to quartz-carbonate infill with bornite as the main ore mineral but also digenite, covellite, chalcopyrite, and tenorite. Tenorite is a copper oxide that occurs as small individual balls with the shape of yarn. A linarite-mineral (oxidation of galena and copper sulfides) and an unknown white-grey-colored mineral with a reflectance of 30% is also identified in minor amounts (Vik, 1985).

Melezhik et al. (2015) got $\delta^{13}\text{C}$ values of carbonates in the Storviknes formation varying between -3.1‰ to +2.7‰ and $\delta^{18}\text{O}$ values varying between +14.7‰ to +26.4‰. None of these samples were collected from the Kåfjord area, but from Borrås, Raipas, and Viknes, where the Storviknes formation also is occurring (Melezhik et al., 2015).

4 Results¹

¹ *“The use of the prefix “meta” will be omitted in the text using only the protolith name (e.g. gabbro, basalt). According to NGU (2021b), claystone is identified in Kvenvik formation but will hereafter be called shale, and the dolostone (Melezhik et al., 2015) will be called carbonate. In Storviknes formation, the rock hosting the carbonate layers have been called siltstone according to Vik (1985) and NGU (2021a), and claystone according to NGU (2021b) but will hereafter be called shale. The carbonate layers are identified as dolomite by Vik (1985), and dolomite and limestone according to NGU (2021a) and NGU (2021b), but a general term “carbonate layers” will be used hereafter.”*

“Mineral abbreviations are from Whitney and Evans (2010) (Appendix A). The term major for elements in minerals is defined as >1 wt.%, minor 0.1 – 1 wt.%, and trace <0.1 wt.%. Minerals identified in thin sections have been described as major minerals if they constitute for >10% of the host rock or vein within the host rock, minor 1 – 10%, and accessory <1%.”

4.1 Mineral characterization

4.1.1 Mafic rock-hosted Cu mineralization in the Kvenvik formation

4.1.1.1 The Kåfjord bridge area



Figure 19: The Kåfjord bridge area; (A) Outcrop showing the host gabbro and a quartz-carbonate vein; (B) Hand sample 0054 with the marked location of the relevant thin section; (C) Hand sample 0051 with the marked location of thin section by the black rectangle and three circles indicating the drilling for isotope analysis (0051A, 0051B, 0051D, and 0051E); (D) Hand sample 0052 with red circles indicating the drilling spots for carbonate isotope analyses (0052 and 0052B).

The Kåfjord bridge locality is located approximately 500 meters NW of the Kåfjord bridge, in a roadcut where the old E6 takes off from the new E6 (Figure 4). This locality is hosted by the lowermost part of the Kvenvik formation and it has not been mined. The mineralization, hosted by a massive gabbro (2146 ± 5 Ma; Melezhik et al. (2015)), occurs in the form of quartz-carbonate veins (Figure 19A). Four samples (0054, 0051, 0052 & 0055) have been collected from this location.

Hand sample description

Sample 0054 (Figure 19B) represents the host rock homogenous gabbro with a grain size of around 1000 microns (1 mm). The sample shows weak sulfide dissemination and is rich in magnetite.

Sample 0051 (Figure 19C) represents a sulfide-bearing quartz-carbonate vein hosted by the gabbro. The main sulfide mineral is pyrite with crystals up to 5 mm across (Appendix B).

Sample 0052 (Figure 19D) represents a nearly barren quartz-carbonate vein. It predominantly consists of calcite (identified by white-colored rhombohedral-shaped crystals and a strong reaction with HCl) with minor amounts of quartz.

Sample 0055 (Appendix B) represents a sulfide-bearing quartz-carbonate vein. Pyrite has been recognized as the main sulfide mineral.

Petrography and mineral chemistry

Thin section 0054

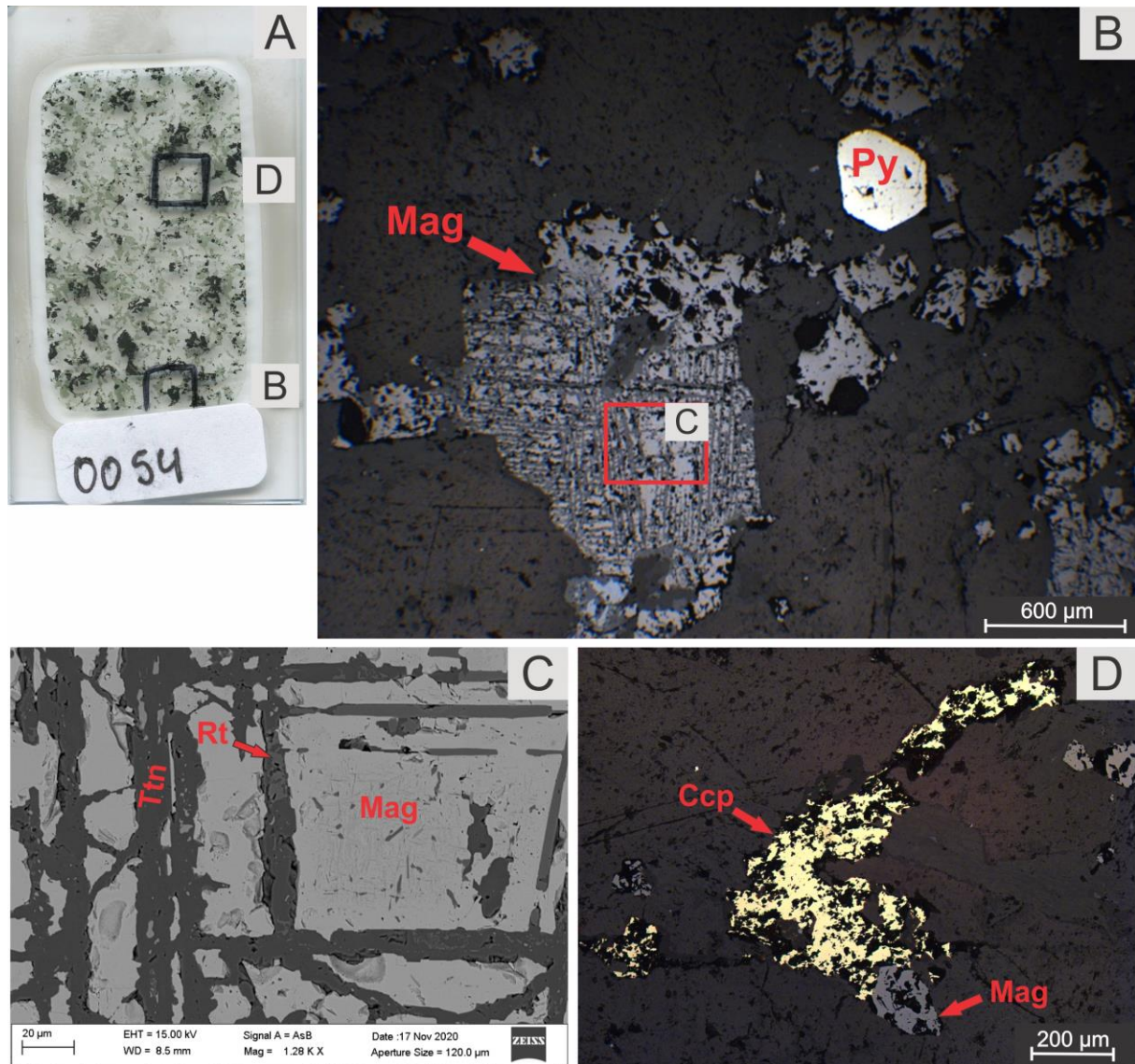


Figure 20: Thin section 0054; (A) A picture of the whole thin section with two black quadrants indicating the area of Figures B and D; (B) RLM (reflected light microscopy) PPL (plane polarized light) picture showing the grey-colored mineral magnetite and the light yellowish-colored pyrite with the area of Figure C marked by the red rectangle; (C) A backscattered electron image of lamellae-rich magnetite with infill of titanite and rutile; (D) RLM PPL picture of the yellow-colored chalcopyrite and the grey-colored magnetite. Abbreviations: Mag: Magnetite, Py: Pyrite, Rt: Rutile, Ttn: Titanite, Ccp: Chalcopyrite.

Thin section 0054 (Figure 19B) has been analyzed by polarized light microscopy and the SEM-EDS technique (Table 2). The main mineral phases are plagioclases, pyroxenes, amphiboles, magnetite, quartz and chlorites. A hydrothermal overprint resulted in a partly sericitization of plagioclases. Magnetite is an abundant mineral in the gabbro (Figure 20B). Some magnetite grains are massive, but magnetite often shows a presence of exsolution lamellae (Figure 20C). The massive upper part of the magnetite grain (Figure 20B) has the approximate ideal composition of magnetite (Table 2; Appendix C), while the lower lamellae-

rich part contains titanium and manganese corresponding to a lower iron content (Table 2) than the ideal composition. The lamellae predominantly consists of titanite associated with minor amounts of rutile (Figure 20C & Table 2). Disseminated euhedral grains of pyrite are found in minor amounts within the host rock, while only accessory amounts of chalcopyrite have been recorded in tiny veinlets with a thickness of ~15 cm across (Figure 20B & Figure 20D).

Table 2: Element composition (in wt.%) of the main sulfide and oxide mineral phases found in sample 0054. The composition has been determined by the SEM-EDS technique.

Thin section 0054		Fe	S	Ti	O	Mn	Si	Al	Ca
Ore minerals	Pyrite	45.2- 46.8	53.2- 54.8						
Host rock minerals	Massive magnetite	74.8- 75.1			24.9- 25.2				
	Magnetite with exsolution lamellae	64-70		3-7	27	1-2			
	Titanite	0-1.5		24-26	39-40		14-15	0.5	20
	Rutile	1		60	39				

Thin section 0051

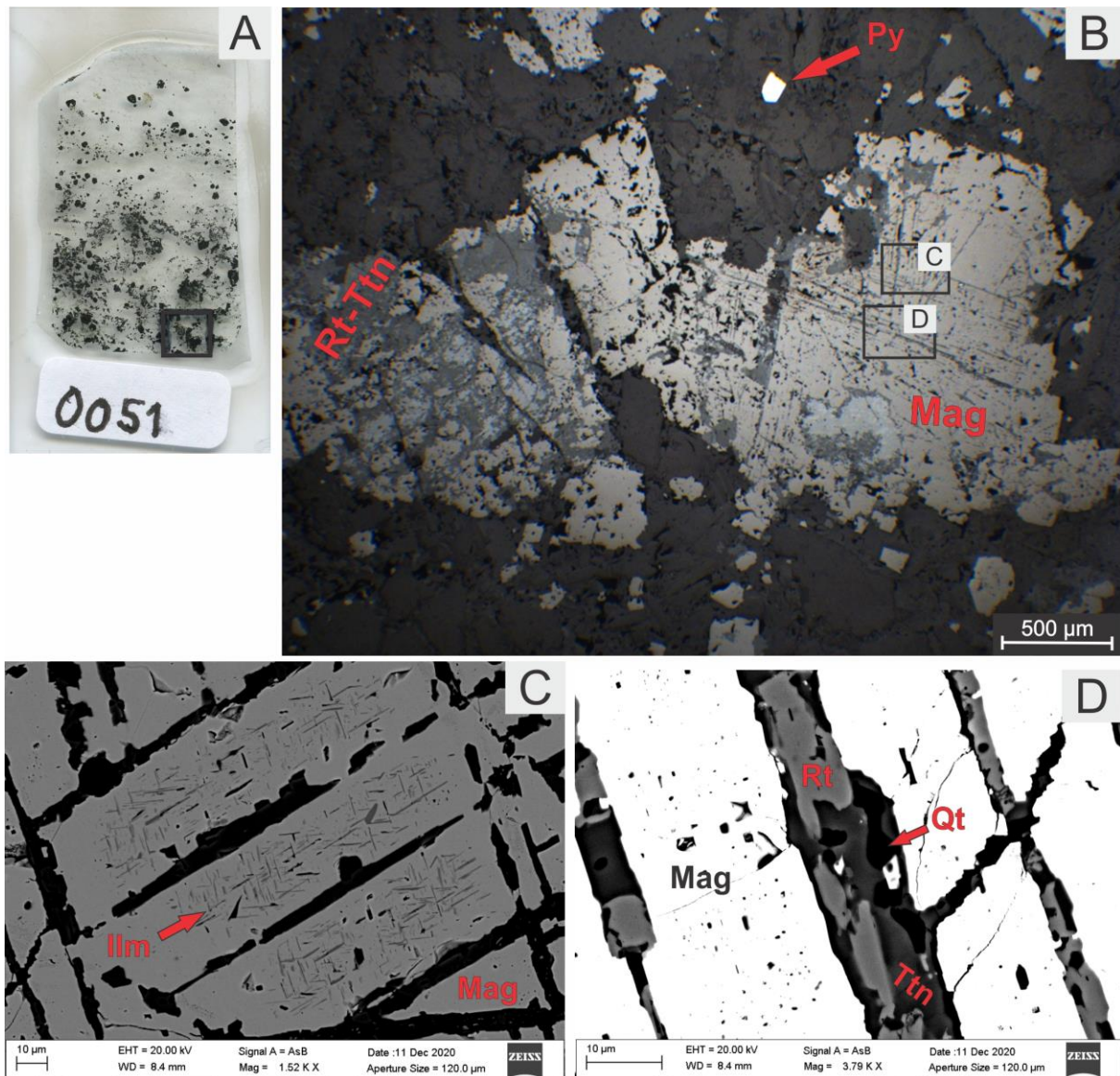


Figure 21: Thin section 0051; (A) Whole thin section with the area of Figure B marked by the quadrant; (B) RLM PPL picture showing magnetite and pyrite. Figures C and D are indicated by two rectangles; (C) A backscattered electron image of magnetite with ilmenite lamellae marked; (D) A backscattered electron image of magnetite with lamellae composed of titanite, rutile and quartz. Abbreviations: Py: Pyrite, Mag: Magnetite, Rt: Rutile, Ttn: Titanite, Qt: Quartz.

Thin section 0051 from sample 0051 (Figure 19C) consists of gabbro in the lowermost part and quartz-carbonate vein in the uppermost part. The gabbro predominantly consists of pyroxene and albite. Magnetite and minor amounts of Mn-rich calcite have been identified as well (Table 3). The quartz-carbonate vein is mineralized by pyrite and minor amounts of magnetite. No chalcopyrite has been found within the vein. The transition from the gabbroic part to the quartz-carbonate vein is characterized by an increase of magnetite towards the gabbro and an increase in pyrite towards the quartz-carbonate vein. Massive and lamellae-rich magnetite can also be observed in this thin section (Figure 21B). The lamellas are infilled

with approximately equal amounts of titanite and rutile, and minor amounts of quartz (Figure 21D). Ilmenite has also been identified as exsolution lamellar within the lamellae-rich magnetite (Figure 21C).

Table 3: Element composition (in wt.%) of the main mineral phases found in sample 0051. The composition has been determined by the SEM-EDS technique.

Thin section 0051		Fe	S	Ti	O	Mn	Si	Al	Na	Ca	Mg
Ore minerals	Pyrite	47	53								
Gangue mineral	Calcite				13-22	1.5				77-86	
Host rock minerals	Magnetite with exsolution lamellae	74.5		0.5	25						
	Rutile	1		60	39					0.5	
	Titanite			25	40		15	0.6		20	
	Ilmenite	41-50		17-22	28-31	6					
	Pyroxene	7			43		27	9			12
	Albite				46		34	11	8		

4.1.1.2 The Innerstrømmen mine

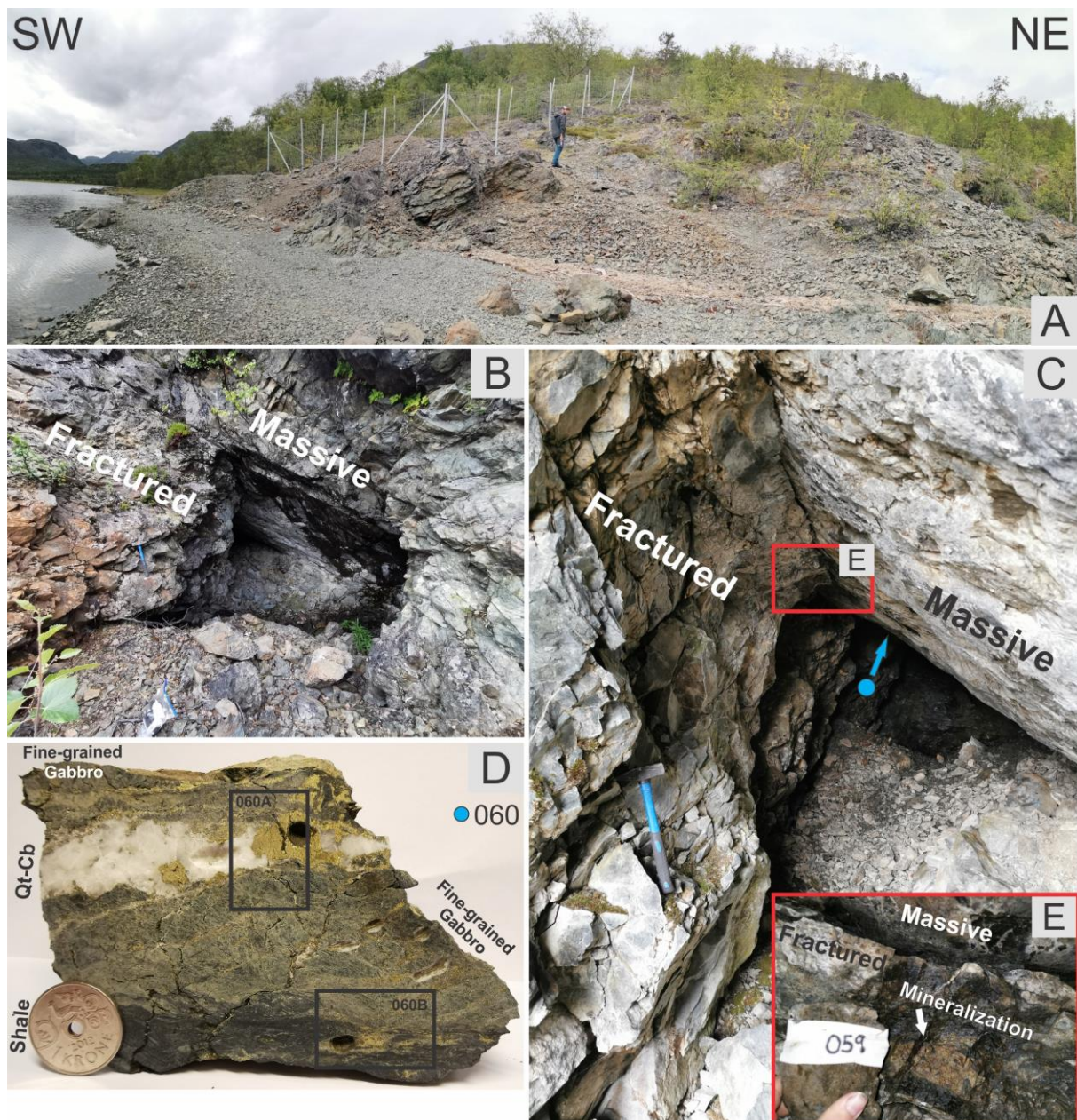


Figure 22: The Innerstrømmen mine; (A) Overview of the locality; (B) Entrance to the mine with a massive upper rock and a lower fractured rock; (C) Inside the mine with the location of sample 060 as the blue circle and a red rectangle indicating the area of Figure (E); (D) Hand sample 060 with the marked area of thin section 060A and 060B; (E) Massive sulfide mineralization inside the mine (sample 059). Abbreviations: Qt-Cb: Quartz-Carbonate.

Innerstrømmen is a locality in the Kvenvik formation that previously has been a subject of copper mining (NGU, 2021d). It is the southernmost mine of the Kåfjord mines, located 200 meters SW from the bridge of the old E6 (Figure 4). According to NGU (2021a), it is hosted by gabbro. Two mine entrances were found, whereas one of them, the westernmost (Figure 22B) was explored. Mineralization occurred in a brittle shear zone below a massive wall, dipping approximately 30 degrees towards NNE (see Figure 22C). The mining operation has

been in a small scale as this mine has only been excavated for about seven meters. Two samples (059 and 060) were collected from inside the mine.

Hand sample description

Sample 059 (Figure 22E) is from a mineralization within the brittle shear zone, close to the massive wall. This mineralization is 3 cm thick and identified to be mainly chalcopyrite hosted by shale. There has not been done any other investigation of the sample than a visual inspection.

Sample 060 (Figure 22D) is also collected in the brittle shear zone, a bit further inside the mine. The upper green part of the sample is fine-grained gabbro which borders to a dark-colored shale in the lowermost part of the sample. A quartz-carbonate vein cut through the fine-grained gabbro and is the sulfide-richest part of the sample. Minor amounts of sulfides do also occur disseminated within the fine-grained gabbro and the shale.

Petrography and mineral chemistry

Thin section 060A

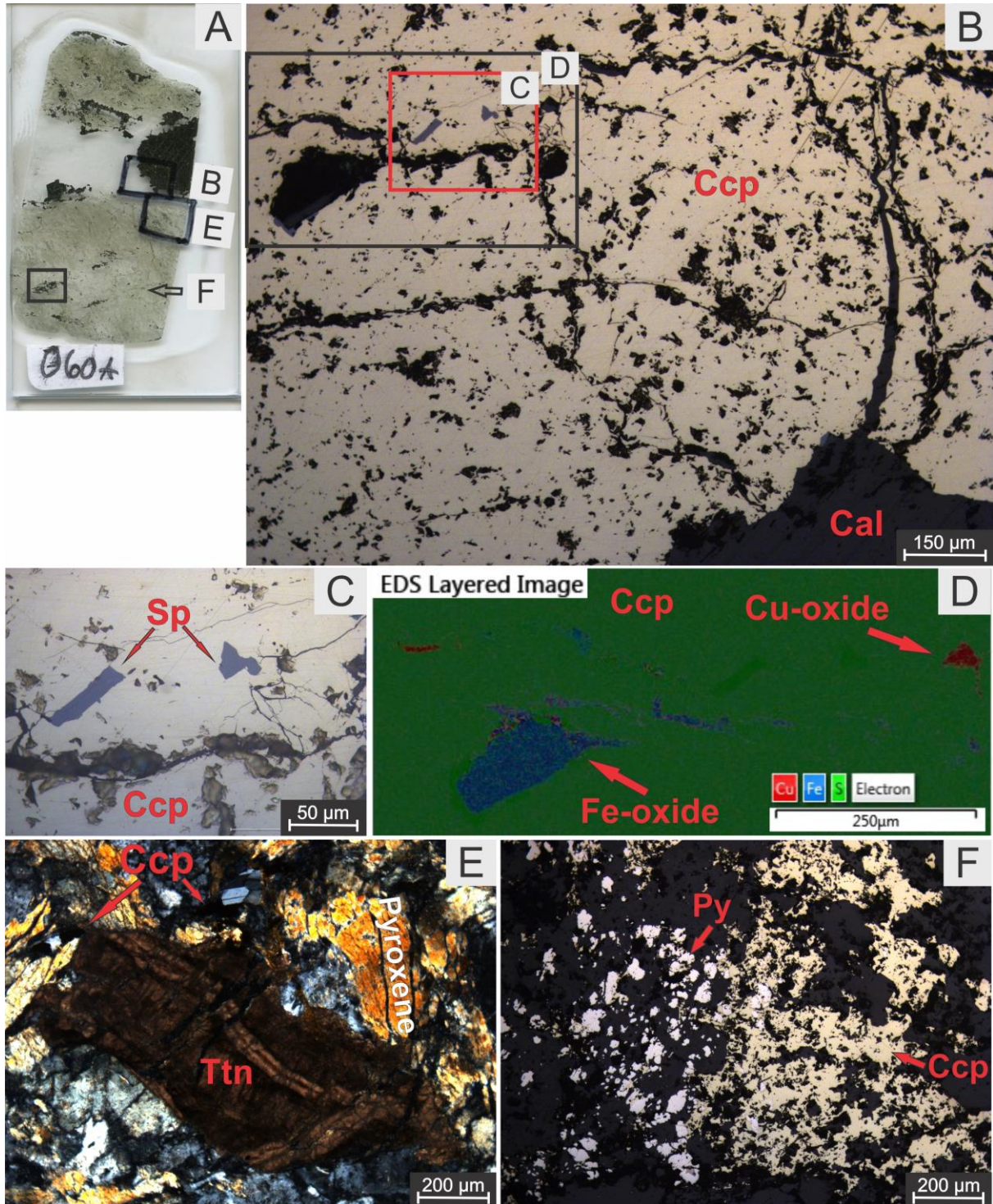


Figure 23: Thin section 060A; (A) Thin section 060A with the location of Figures B, E, and F marked; (B) RLM PPL picture of the mineralized vein with a red rectangle indicating the area of Figure C, and a black rectangle indicating the area of Figure D; (C) RLM PPL picture within Figure B showing sphalerite clasts embedded in chalcopyrite; (D) An image from the EDS mapping showing Fe-oxide (blue color) and Cu-oxide (red color) within chalcopyrite; (E) Transmitted light microscopy (TLM) PPL picture showing the host rock minerals titanite and pyroxene within a matrix of quartz and plagioclases. Chalcopyrite is also marked (black color); (F) RLM PPL picture of pyrite and chalcopyrite within the fine-grained gabbro. Abbreviations: Ccp: Chalcopyrite, Cal: Calcite, Sp: Sphalerite, Ttn: Titanite, Py: Pyrite.

Thin section 060A (Figure 23A) is from the upper part of sample 060 (Figure 22D). It consists of a mineralized quartz-carbonate vein (Figure 23B) and a fine-grained gabbro (Figure 23E & Figure 23F). The vein consists predominantly of calcite with minor amounts of quartz (Figure 23B; Table 4). Sulfides found in the vein are mainly chalcopyrite with accessory amounts of sphalerite embedded within chalcopyrite (Figure 23C). Copper- and iron oxide occurs as infill in fractures and bigger defects in the chalcopyrite (Figure 23D).

Minor amounts of chalcopyrite and pyrite are also found in the fine-grained gabbro. Chalcopyrite occurs as infill in fractures between host rock minerals and as dissemination together with pyrite (Figure 23E & Figure 23F). There can be seen a transition from chalcopyrite to the right that gradually shifts to pyrite to the left (Figure 23F). Minerals as pyroxenes, plagioclases, quartz, and bigger clasts of titanites up to 800 µm in diameter have been identified in the fine-grained gabbro (Figure 23E & Table 4). Pyroxenes occur as smaller grains up to 400 µm, while the quartz and plagioclases have grain sizes up to 200 µm (Figure 23E).

Table 4: Element composition (in wt.%) of the main mineral phases found in sample 060A. The composition has been determined by the SEM-EDS technique.

Thin section 060A		Fe	Cu	Zn	S	O	Ti	Si	Mn	Mg	Al	Ca	Mg
Ore minerals	Chalcopyrite	30.7	34.7		34.6								
	Sphalerite	5-6	1	58-61	32	1							
	Cu-oxide	4	66		1	28-30						0.4	
	Fe-oxide	21				45		13	0.2	9	11		
Gangue mineral	Calcite					32-47						53-68	
Host rock minerals	Titanite	0-2				40	23	15		0.5	1	20	
	Pyroxene	14-21				39-41		20-26			2-7	4-9	8

Thin section 060B

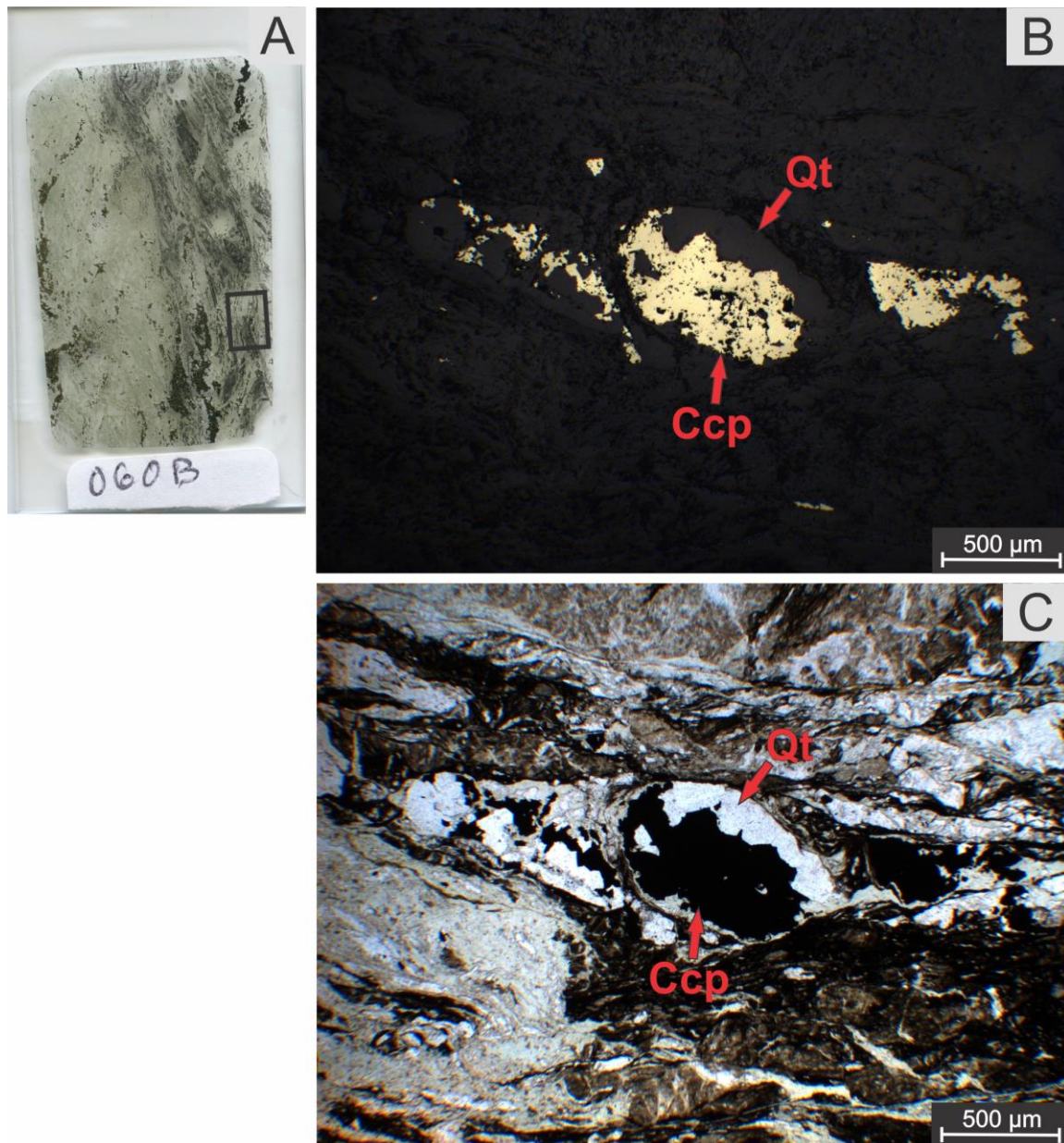


Figure 24: Thin section 060B; (A) Thin section 060B with the area of Figures B and C marked; (B) RLM PPL picture showing clasts of chalcopyrite and quartz; (C) TLM PPL picture of the same area as Figure B showing the host rock minerals chlorite (light green) and amphibole (dark green). Abbreviations: Qt: Quartz, Ccp: Chalcopyrite.

Thin section 060B (Figure 24A), is a section of the lower part of sample 060 (Figure 22D). It consists of fine-grained gabbro and shale, with the shale in the right part of the thin section (Figure 24A). Identification of individual mineral grains of the host rock has been difficult as the shale is deformed and very fine-grained (Figure 24C). The green color in transmitted light has been used to interpret possible mineral phases as chlorite (light green) and amphibole (dark green). Clasts of more competent minerals as quartz with associated chalcopyrite have been identified within shale, sometimes brecciated into several smaller clasts (Figure 24B & C).

4.1.1.3 The Carl Johan mine

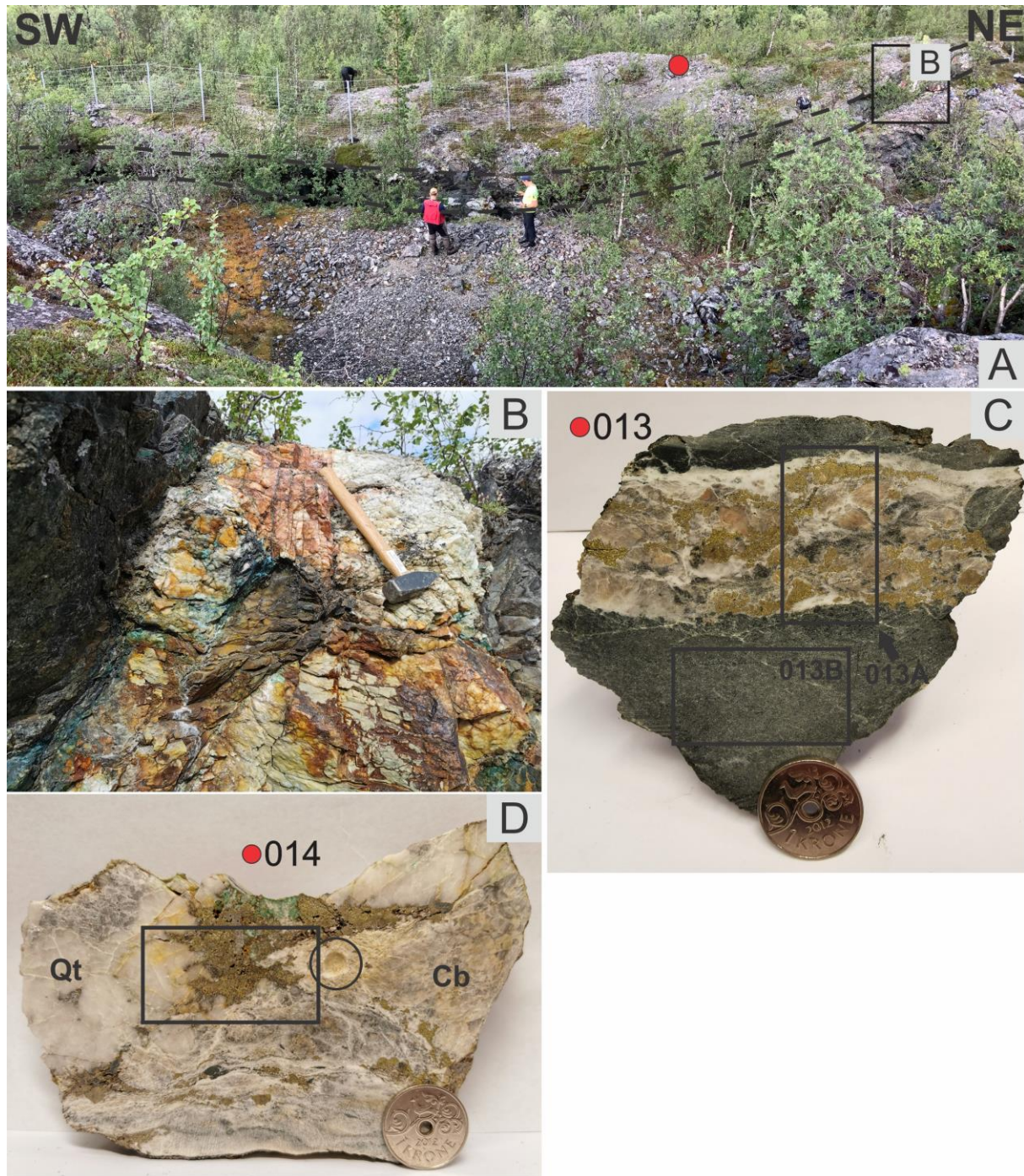


Figure 25: The Carl Johan mine; (A) Overview of the Carl Johan mine with two black dashed lines emphasizing the mineralization, which could easily be followed for ~100 m. The location of samples 013 and 014 are marked by the red circle, and the black quadrant shows the area of Figure B; (B) Main mineralized quartz-carbonate vein; (C) Hand sample 013 with two rectangles indicating the location of thin sections 013A and 013B; (D) Hand sample 014 with a rectangle indicating the area of thin section 014 and circle showing the drilling of isotope sample 014. Abbreviations: Qt: Quartz, Cb: Carbonate mineral.

Carl Johan is a locality that previously has been mined for copper, located behind a small hill approximately 150 meters west of the old E6 (Figure 4). The investigated area is thought to be “Store Carl Johan” (Mørk, 1970). This mine has an opening of about 1-2m close to the

surface that gets thinner until it ends some few meters into the ground, with a gentle slope. An underground continuation of the mine has also be observed with an entrance to the right in Figure 25A. The main mineralization is a 1 m thick quartz-carbonate vein hosted in basalt (Figure 25B). Two samples (013 & 014) were collected from the tailings.

Hand sample description

Sample 013 (Figure 25C) represents a basalt hosted, sulfide-bearing quartz-carbonate vein collected from the tailings (Figure 25B). The vein is 3 cm thick with mineral grains stretching along with the direction of the vein.

Sample 014 (Figure 25D) also represents a sample from the mine tailings. It consists of one part that is mainly carbonate (marked Cb in Figure 25), one part dominated by quartz (marked Qt), and an interlying part that is massive sulfides. The lower part of the sample represents a carbonate-rich part with planar structures and associated mineralization.

Petrography and mineral chemistry

Thin section 013A

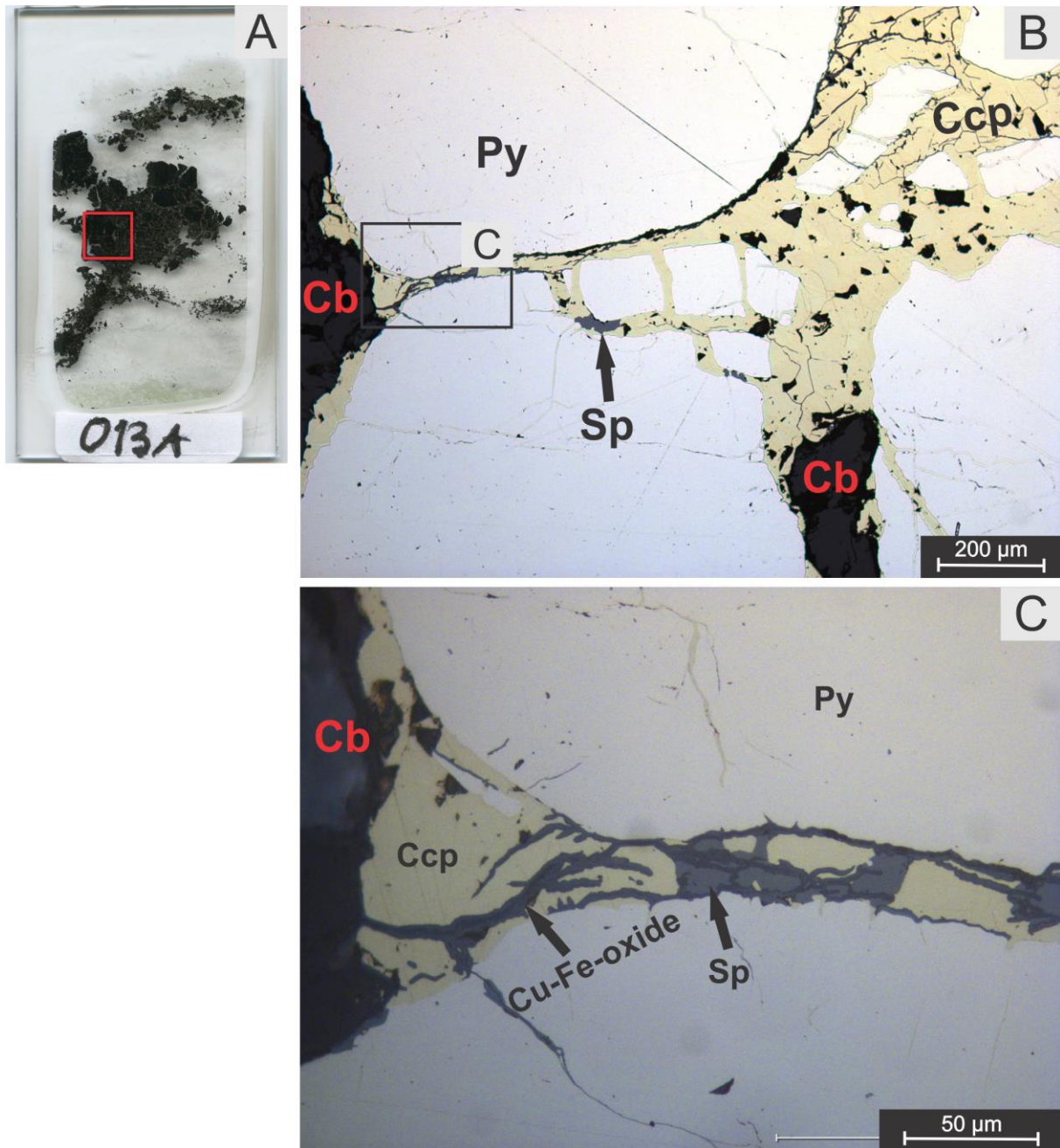


Figure 26: Thin section 013A; (A) Thin section 013A with the area of Figure B marked by the red quadrate; (B) RLM PPL picture showing pyrite, chalcopyrite, sphalerite and a carbonate mineral with the area of Figure C marked by the black rectangle; (C) RLM PPL picture showing Cu-Fe-oxide veins (dark grey) and sphalerite (light grey) occurring within the chalcopyrite. Abbreviations: Py: Pyrite, Ccp: Chalcopyrite, Cb: Carbonate mineral, Sp: Sphalerite.

Pyrite and chalcopyrite with minor amounts of sphalerite are the main ore minerals within the mineralized quartz-carbonate vein in thin section 013A. Pyrite occurs as brecciated subhedral clasts up to 1500 µm in diameters, while chalcopyrite occurs as infill around and inside the pyrite grains (Figure 26B). Sphalerite occurs together with the chalcopyrite (Figure 26C).

Chalcopyrite, sphalerite and pyrite are infiltrated by Cu-Fe-oxides (Figure 26C; Table 5). Gangue minerals are carbonates and quartz, with carbonates as the predominantly gangue mineral. The carbonate is almost pure calcite but contains minor amounts of manganese and magnesium in some clasts (Table 5).

Table 5: Element composition (in wt.%) of the main mineral phases found in sample 013A. The composition has been determined by the SEM-EDS technique.

Thin section 013A		Fe	Cu	Zn	S	O	Mn	Mg	Ca
Ore minerals	Pyrite	47			53				
	Chalcopyrite	31.1	33.4		35.5				
	Sphalerite	3		64	33				
	Cu-Fe-oxide	10	59		8	24			
Gangue mineral	Carbonate mineral					40-51	0-0.7	0-0.3	45-51

Thin section 013B

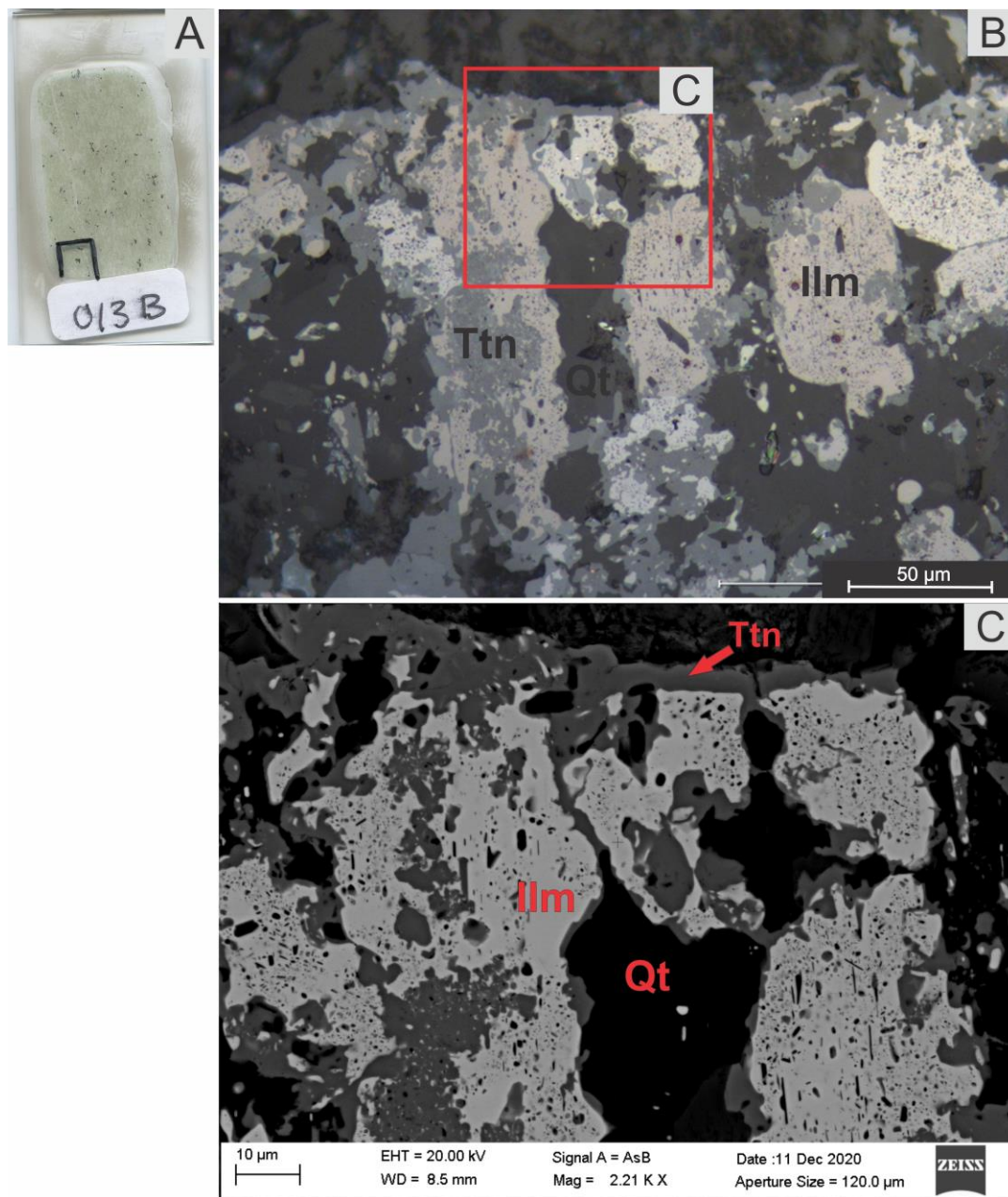


Figure 27: Thin section 013B; (A) Thin section 013B with the area of Figure B marked; (B) RLM PPL picture showing ilmenite, titanite and quartz. The area of Figure C is marked by the red quadrant; (C) A backscattered electron image showing the same as in Figure B, but with a more defined border between the mineral phases. Abbreviations: Ttn: Titanite, Ilm: Ilmenite, Qt: Quartz.

Thin section 013B (Figure 27A) is basalt from sample 013 (Figure 25C). The basalt is very fine-grained, deformed, and banded with grains not bigger than 100 µm in diameter. The main minerals are pyroxenes (Table 6), amphiboles, quartz, plagioclases, and sanidine type of K-feldspar (identified by sanidine twinning). A carbonate mineral (Table 6) and seritization bands are also observed within the basalt. Mineral grains up to ~300 µm of a two-phase mineral consisting of ilmenite and titanite have also been identified as the black clasts within

the basalt (Figure 27A). One of these clasts has been investigated (Figure 27B & C), where ilmenite is the brighter main mineral phase with titanite occurring around. Quartz is identified within this two-phase mineral. In addition, accessory amounts of disseminated chalcopyrite within the basalt have been found.

Table 6: Element composition (in wt.%) of the main mineral phases found in sample 013B. The composition has been determined by the SEM-EDS technique.

Thin section 013B		Fe	Ti	O	Si	Mn	Mg	Al	Ca
Gangue mineral	Carbonate mineral			22-23			0.2-0.3		76-77.5
	Ilmenite	31	33			7			
Host rock minerals	Titanite		24	39	14			0.5	22
	Pyroxene	22.5		41	14		11	12	

4.1.1.4 The Wilson mine

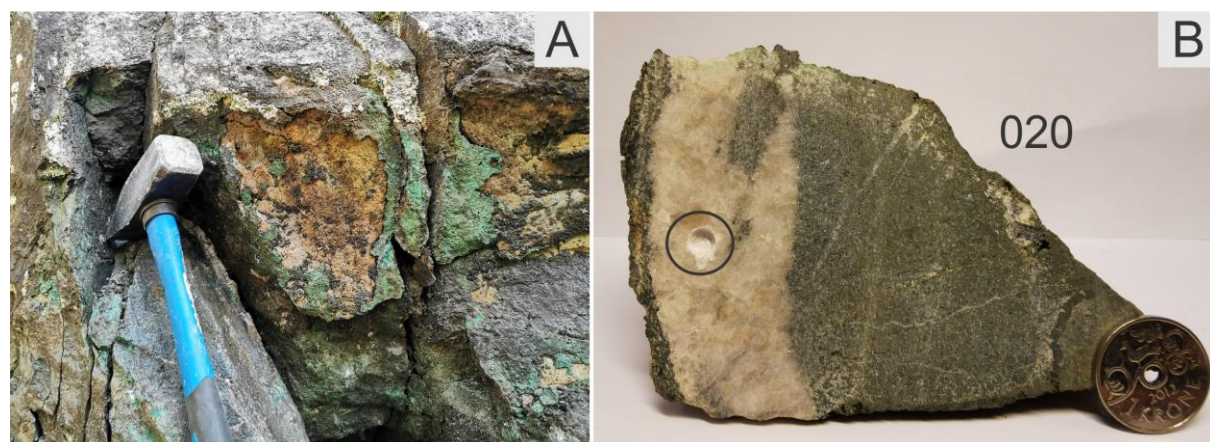


Figure 28: The Wilson mine; (A) A thin (3cm) mineralized vein hosted by basalt and covered by green-colored malachite; (B) Sample 020 representing a quartz-carbonate vein hosted in basalt. The black circle indicates the location of the carbonate sample 020.

The Wilson mine is located approximately 250m SW of Carl Johan mine. Based on field observations, it looks like this mine has been mined for copper on a larger scale than the Carl Johan mine. Outcrop of the main ore(s) could not be found, only smaller quartz-carbonate veins (Figure 28A). Sample 020 (Figure 28B) is one of these veins, covered by green-colored malachite on the outside, but no mineralization within the vein could be identified. A weak chalcopyrite dissemination was observed in the basalt.

4.1.1.5 The Mitchell mine

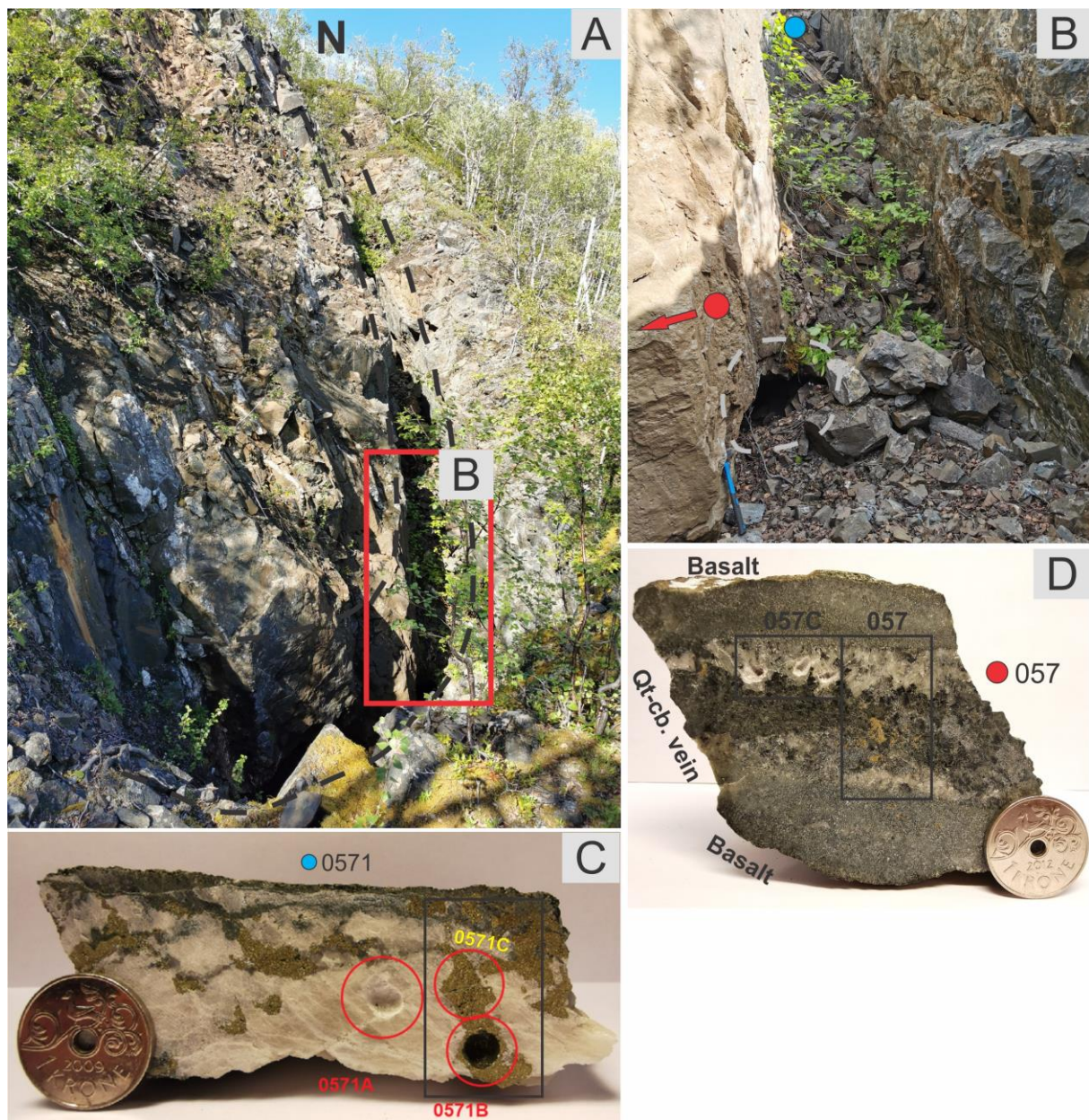


Figure 29: The Mitchell mine; (A) Overview of the mine with two dashed lines emphasizing the open cut; (B) Inside the mine with a dashed circle showing the mine entrance for the underground continuation. Red and blue circles show the location of samples 057 and 0571; (C) Hand sample 0571 with rectangle indicating the area of thin section 0571. Three red circles indicate isotope drill marks of 0571A, 0571B, and 0571C; (D) Hand sample 057 with horizontal rectangle indicating isotope drilling of carbonate (057C) and vertical rectangle indicating the area of thin section 057. Abbreviations: Qt-cb: Quartz-carbonate.

The Mitchell mine is the westernmost mine of the Kåfjord mines (Mørk, 1970), located in between the Henning and Carl Johan/Wilson mines (Figure 4). In this area, several other mines do also occur (NGU, 2021d), but the description of the mines from Vik (1985) and maps from Mørk (1970) indicates that this is Mitchell mine. The investigated part of the mine is the lowermost part of the ore body (Figure 29A & B), where an inaccessible underground continuation of the mine is indicated. Only minor mineralization hosted by smaller (~3 cm)

quartz-carbonate veins could be found as the main ore body has been exhausted at the surface. Two samples have been collected, samples 057 and 0571 (location indicated in Figure 29B).

Hand Sample description

Sample 057 (Figure 29D) is collected from the wall of the mine, just out of the picture in Figure 29B. The sample is a 2.5 cm thick quartz-carbonate vein hosted by basalt. Sulfides are found in both the vein and as disseminations in basalt, with the vein hosting most of the Cu mineralization.

Sample 0571 (Figure 29C) is collected from the tailings inside the mine. The sample represents a 3 cm thick mineralized quartz-calcite vein hosted by basalt (basalt part is detached). The majority of the sulfides are in the vein but were also present as disseminations in the basalt.

Petrography and mineral chemistry

Thin section 057

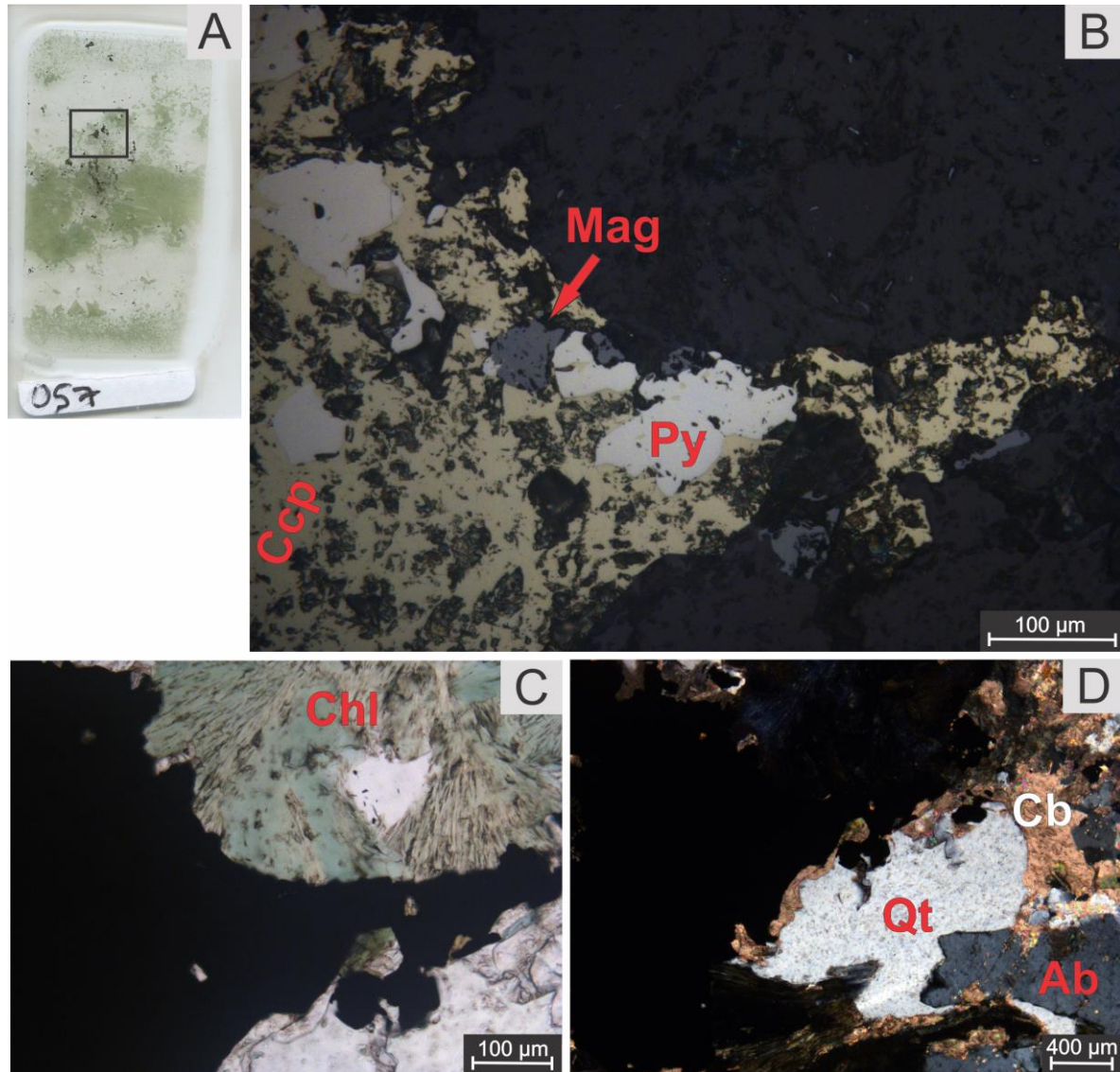


Figure 30: Thin section 057; (A) Thin section 057 with a rectangle indicating the area of Figures B, C, and D; (B) RLM PPL picture of the ore minerals pyrite and chalcopyrite, including magnetite; (C) TLM PPL picture showing chlorite as gangue mineral (same area as Figure B); (D) TLM XPL (cross polarized light) picture showing quartz, carbonates and albite in an area just below Figures B and C. The opaque minerals are pyrite, chalcopyrite and magnetite. Abbreviations: Mag: Magnetite, Py: Pyrite, Ccp: Chalcopyrite, Chl: Chlorite, Cb: Carbonate mineral, Qt: Quartz, Ab: Albite.

Thin section 057 (Figure 30A) is from hand sample 057 (Figure 29D). Chalcopyrite is the main ore mineral with small inclusions (~100 μm) of anhedral shaped pyrite and (~50 μm) magnetite embedded within the chalcopyrite (Figure 30B). Gangue minerals are mainly calcite, quartz, albite, and chlorite (Figure 30C & D; Table 7), with albite showing lamellar twinning. Chlorite (Figure 30C) is green-colored, occurring as fibrous (light green) and massive (dark green) interbedded grains. The fibrous part contains minor amounts of Hg (Table 7).

Table 7: Element composition (in wt.%) of the main mineral phases found in sample 057. The composition has been determined by the SEM-EDS technique.

Thin section 057		Fe	S	Cu	O	Si	Mg	Na	Al	Ca	Hg
Ore minerals	Pyrite	46.7-47	53-53.3								
	Chalcopyrite	30.9	34.4	34.6							
Gangue minerals	Plagioclase - albite				46.6-48.3	32.1-33.6		8.8	11		
	Chlorite	20			44	14	11		11		(0.1-0.2)
	Calcite				57	0.3	0.5			42	
	Magnetite	74			25	1					

Thin section 0571

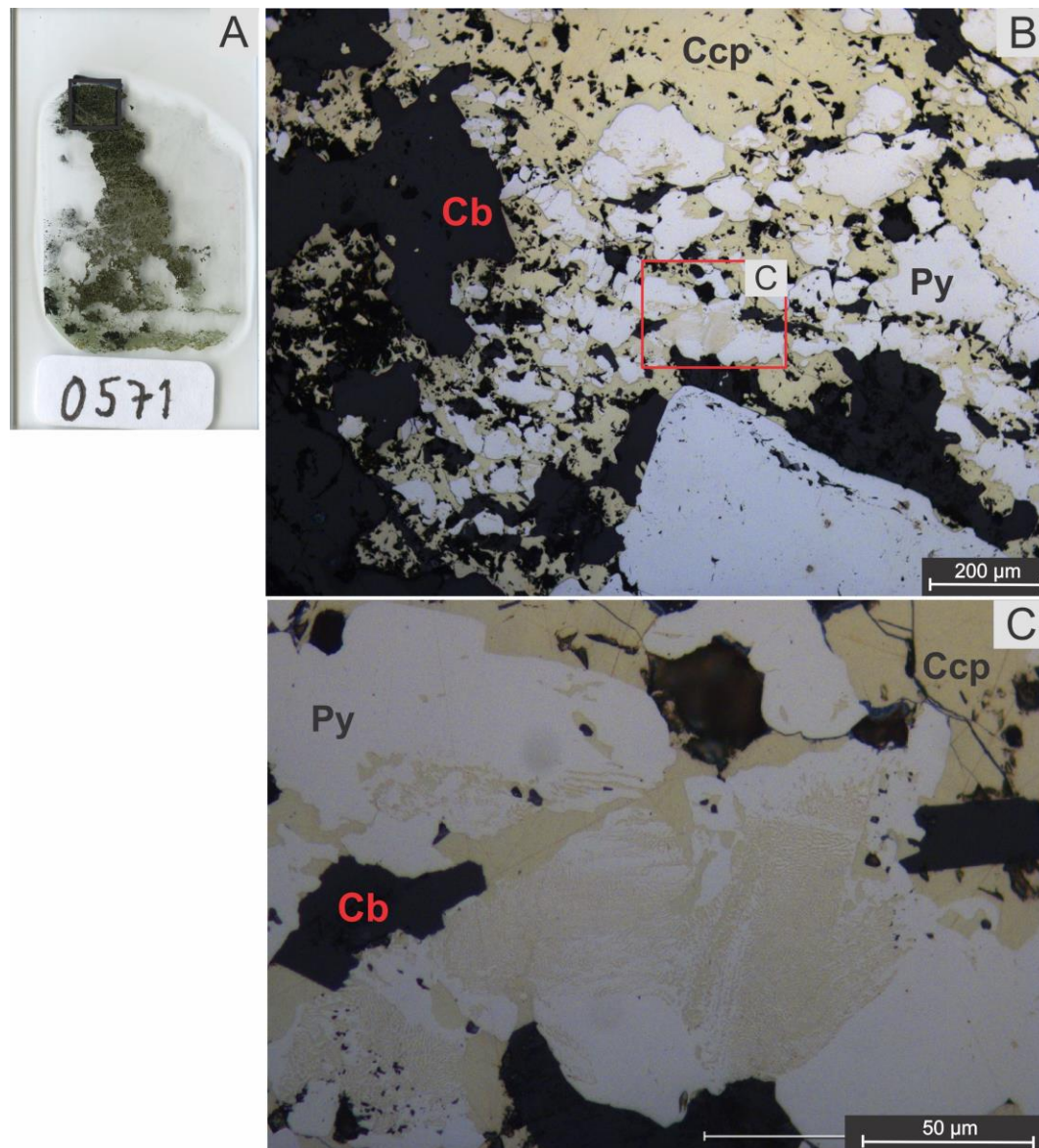


Figure 31: Thin section 0571; (A) Thin section 0571 with the quadrant (upper part of thin section) indicating Figures B and C; (B) RLM PPL picture showing the main ore minerals pyrite and chalcopyrite with a rectangle

indicating Figure C. The black mineral grains are mainly quartz and carbonate; (C) RLM PPL picture showing an exsolution texture between pyrite and chalcopyrite, with grey-colored iron-oxide infiltrating the chalcopyrite. Abbreviations: Ccp: Chalcopyrite, Py: Pyrite, Cb: Carbonate mineral.

Thin section 0571 from hand sample 0571 (Figure 29C) represents the mineralization in the vein. It consists mostly of pyrite and chalcopyrite (Figure 31B). Pyrite occurs as anhedral-shaped inclusions embedded within chalcopyrite, some places occurring with an exsolution type of texture with chalcopyrite (Figure 31C). The chalcopyrite is infiltrated by iron oxides (Figure 31C).

4.1.1.6 The Henning mine

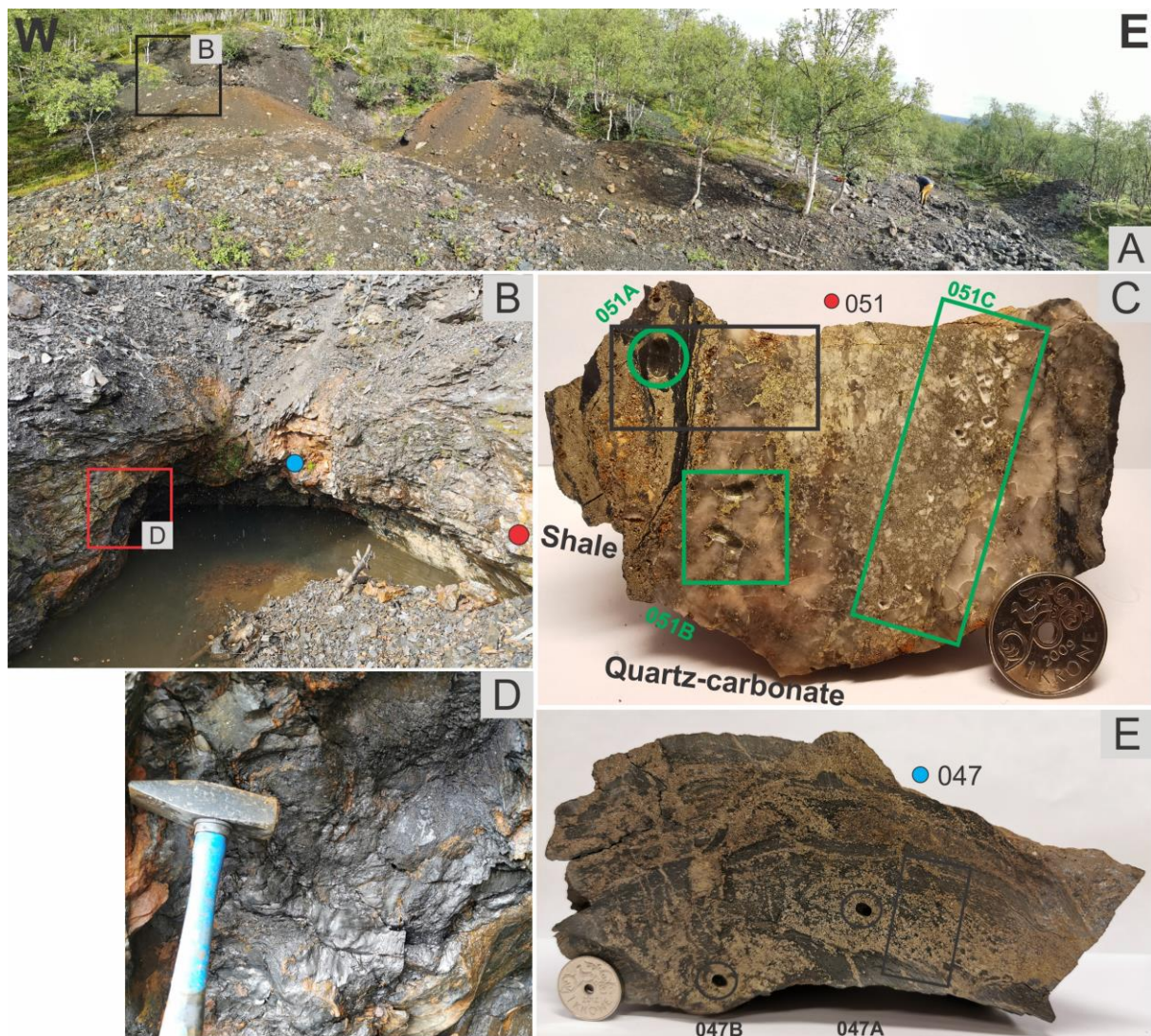


Figure 32: The Henning mine; (A) Overview of the mine with a quadrat indicating Figure B; (B) The mine entrance with the location of samples 047 and 051 as blue and red circles. Quadrat indicates Figure D; (C) Hand sample 051 with thin section 051 marked as the black rectangle. Green circle, quadrat, and rectangle shows the location of isotope samples 051A, 051B and 051C; (D) Nearly pure graphite was observed close to the mineralization in sample 047 and 051; (E) Hand sample 047 with the location of thin section 047 marked by a black rectangle. Circles indicate isotope samples 047A and 047B.

Henning mine lies in the northernmost part of the Kåfjord mines (Figure 4), approximately 550 meters north of the bend of Møllnes river. The site is vegetated with forests and overburden covering the ground. Only the upper part of the mine opening is exposed as the whole mine is flooded. The host rock is basaltic tuff and tuffite with layers of shale (NGU 2021b), containing graphite exposed in the mine opening (Figure 32B & D). The locality shows two styles of mineralization, a stratiform mineralization (Figure 32E; sample 047) and a mineralization related to quartz-carbonate veins (Figure 32C; sample 051).

Hand sample description

Sample 047 (Figure 32E) is collected from the center of the mine opening (Figure 32B). It represents stratiform layers of pyrite hosted in basaltic tuff/tuffite as the main sulfide mineralization. Minor amounts of chalcopyrite have also been identified locally with pyrite.

Sample 051 (Figure 32C) is also collected from the mine opening (Figure 32B). It represents a 7 cm thick quartz-carbonate vein that is hosted in shale. Sulfide mineralization occurs in both the quartz-carbonate vein and the shale, with massive mineralization in the shale and disseminated mineralization in the quartz-carbonate vein. The mineralization in the shale is controlled by planar structures.

Petrography and mineral chemistry

Thin section 047

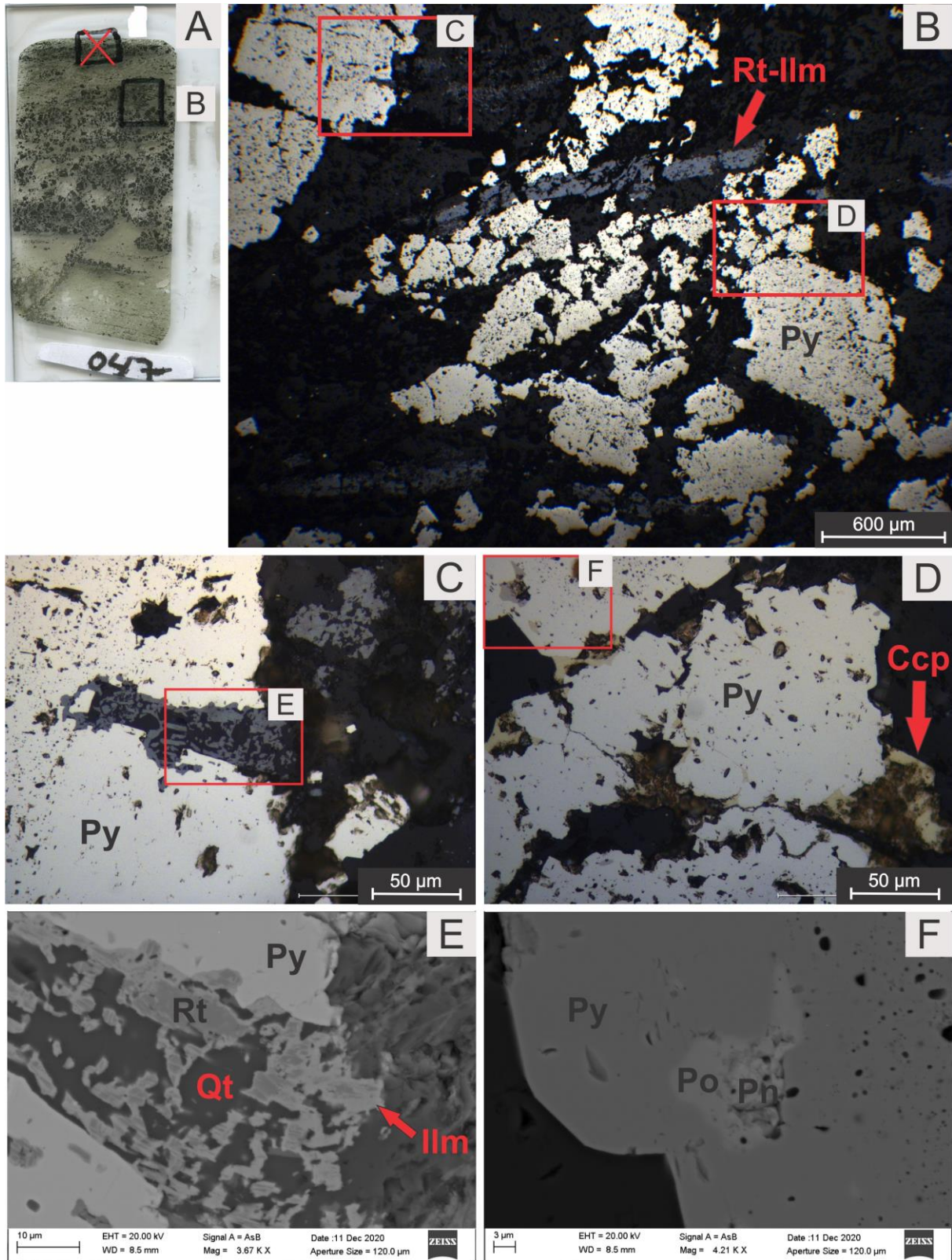


Figure 33: Thin section 047; (A) The whole thin section with Figure B marked; (B) RLM PPL picture showing pyrite grains and rutile-ilmenite band with Figures C and D marked; (C) RLM PPL picture showing the interaction between pyrite and the rutile-ilmenite bands. Figure E is marked; (D) RLM PPL picture showing chalcopyrite

embedded around pyrite with Figure F marked; (E) A backscattered electron image showing the zonation between rutile (dark grey) and ilmenite (light grey), with quartz also appearing; (F) A backscattered electron image showing pentlandite and pyrrhotite within pyrite. Abbreviations: Rt-Ilm: Rutile-Ilmenite, Py: Pyrite, Ccp: Chalcopyrite, Qt: Quartz, Pn: Pentlandite, Po: Pyrrhotite.

Thin section 047 (Figure 33A) is from sample 047 (Figure 32E) and shows the stratiform sulfide mineralization within the tuff/tuffite. Pyrite is the only major sulfide mineral with subhedral-shaped grains up to 1000 μm across. Chalcopyrite, pyrrhotite, and pentlandite are accessory minerals. Chalcopyrite occurs both at the rims and as exsolution within the pyrite (Figure 33D & Appendix D). Pyrrhotite occurs as less than 10 μm grains within pyrite, sometimes intergrown with pentlandite (Figure 33F). Minor amounts of stratiform layered rutile-ilmenite bands are present (Figure 33B), with rutile as the main phase and ilmenite at the rims of the rutile (Figure 33E). Quartz occurs within the rutile-ilmenite bands and within the host rock as well, in addition to chlorite and biotite. The chlorite appears as needle-shaped fibrous grains with a greenish color. An unknown mineral showing high interference colors has also been found within the host rock and analyzed (Table 8). All host rock minerals have a grain size smaller than 100 μm .

Table 8: Element composition (in wt.%) of the main mineral phases found in sample 047. The composition has been determined by the SEM-EDS technique.

Thin section 047		Fe	Cu	Ni	S	O	Ti	Si	Mn	Mg	Al	K
Ore minerals	Pyrite	46.5			53.5							
	Chalcopyrite	35	34		34							
	Pyrrhotite	61			39							
	Pentlandite	34-53		8-28	35-39							
Host rock minerals	Rutile	1.5				37	61					
	Ilmenite	31				34	32	2.5-3	1			
	Chlorite	33				38		13		4	9	
	Unknown					40		26			17	8

Thin section 051

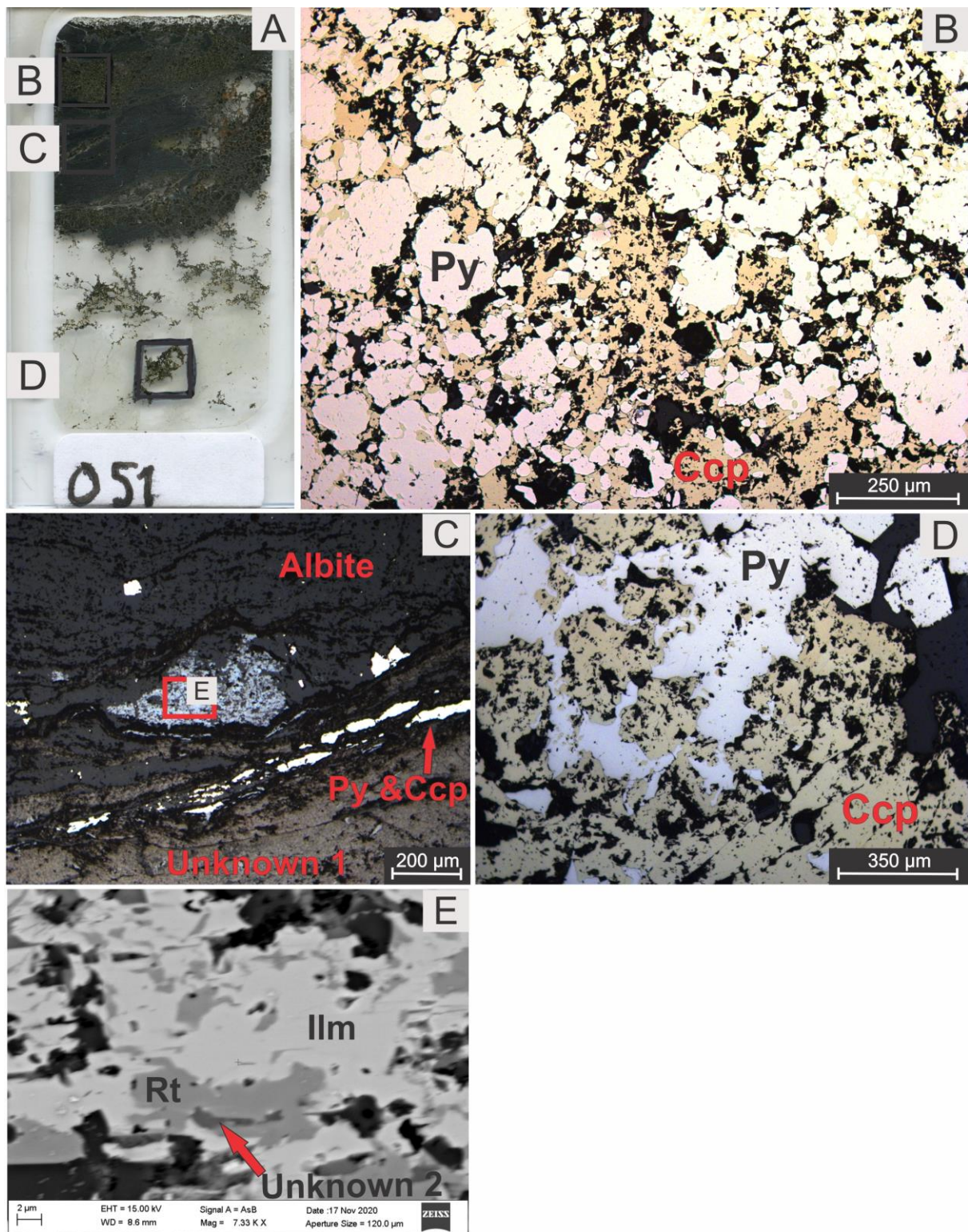


Figure 34: Thin section 051; (A) Whole thin section with the area of Figures B, C, and D marked; (B) RLM PPL picture showing pyrite embedded within chalcopyrite; (C) RLM PPL picture showing pyrite and chalcopyrite occurring in the zone between two host rock minerals (albite and an unknown mineral (unknown 1)). The area of Figure E is marked; (D) RLM PPL picture showing pyrite embedded within chalcopyrite; (E) A backscattered electron image showing a three-phase mineral of ilmenite, rutile and an unknown mineral (unknown 2). Abbreviations: Py: Pyrite, Ccp: Chalcopyrite, Rt: Rutile, Ilm: Ilmenite.

Thin section 051 (Figure 34A) from sample 051 (Figure 32C) represents a mineralized shale in contact with a quartz-carbonate vein. Coexisting pyrite (anhedral to subhedral) and chalcopyrite are the main ore minerals, both in the shale (massive) and the quartz-carbonate vein (disseminated), (Figure 34B and D). The shale is very fine-grained and deformed, consisting of mainly two minerals which have been identified to be albite and an unknown mineral (unknown 1), (Figure 34C; Table 9). Albite have inclusions of a three-phase mineral (Figure 34E; Table 9).

Table 9: Element composition (in wt.%) of the main mineral phases found in sample 051. The composition has been determined by the SEM-EDS technique.

Thin section 051		Fe	S	O	Ti	Si	Mn	Mg	Al	Na	K
Host rock minerals	Ilmenite	36		30	32		1				
	Rutile			37-38	60-60.5						
	Albite			47		34			11	8.5	
	Unknown 2	17-27		36-40	0-14	5-7.5		4.5-6			0-7
	Unknown 1	3-20	0-2	28-41		24.5-40		0-4.7	9-11.5	5-7.5	

4.1.1.7 The Melsvik tunnel area



Figure 35: The Melsvik tunnel area; (A) Overview of the locality with rectangle indicating Figure B; (B) Outcrop where sample 003 (Figure C) is collected; (C) Hand sample 003 showing a homogeneous basalt.

Locality Melsvik tunnel (Figure 3) is located just above the westernmost tunnel opening of the Melsvik tunnel (Figure 35A) in Kvenvik formation (NGU 2021a). The well-exposed

bedrock is massive basalt (Figure 35B and C), with no earlier mining activity, only clearance of overburden related to the building of the tunnel.

Hand sample description

Sample 003 represents a homogenous fine-grained basalt. It contains accessory amounts of disseminated fine-grained sulfides identified by hand sample.

4.1.1.8 The Kråknes area

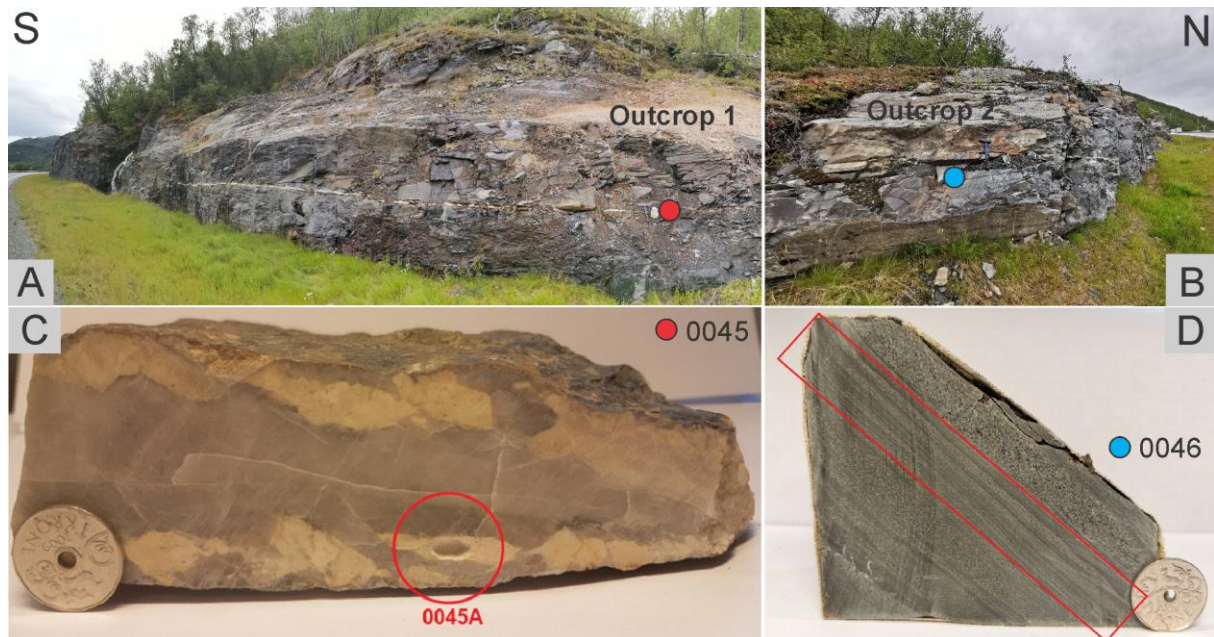


Figure 36: The Kråknes area; (A) Outcrop 1 with a red circle indicating sample 0045; (B) Outcrop 2 with a blue circle indicating sample 0046; (C) Hand sample 0045 showing a brecciated quartz-carbonate vein with a circle indicating carbonate isotope sample 0045A; (D) Hand sample 0046 showing a tuff/tuffite with a rectangle indicating the area of whole rock analysis.

Locality Kråknes is divided into two outcrops. Both outcrops are in a roadcut at E6 close to the exit of the road to Kråknes (Figure 3), within the Kvenvik formation (NGU, 2021a).

Outcrop 2 (Figure 36B) is located 300 meters from the eastern tunnel opening of Melsvik tunnel, while Outcrop 1 (Figure 36A) is located further 300 meters along E6. The bedrock is tuff/tuffite, hosting a quartz-carbonate vein at outcrop 1. Two samples have been collected from this locality (Figure 36C & D).

Hand sample description

Sample 0045 (Figure 36C) represents a part of the light-colored quartz-carbonate vein (Figure 36A). The sample shows brecciated clasts of carbonate minerals at the border of the vein with massive quartz in the middle. The vein hosts minor amounts of chalcopyrite.

Sample 0046 (Figure 36D) represents a tuff/tuffite collected at outcrop 2 (Figure 36B). The rock shows planar structures consisting of layers with different thicknesses and grain sizes. Chalcopyrite occurs mostly within coarser-grained layers.

4.1.2 Sediment-hosted Cu mineralization in the Storviknes formation

4.1.2.1 The Anna area

Outcrop 1

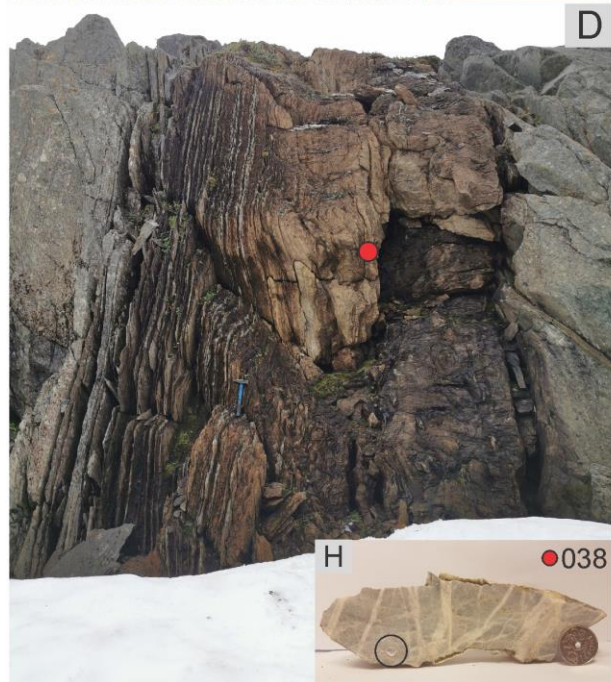
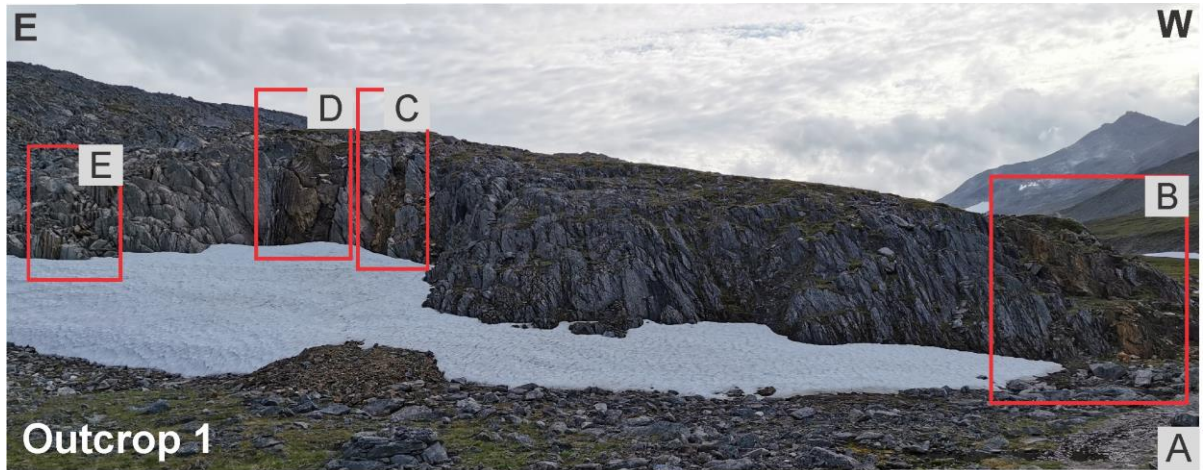


Figure 37: Outcrop 1 at the Anna area; (A) Overview of the outcrop showing four carbonate layers indicated with rectangles; (B) Layer 1 (westernmost), approximately 5m thick with the location of sample 036; (C) Layer 2, approximately 1.5 m thick with the location of sample 037; (D) Layer 3, approximately 4 m thick with the location of sample 038; (E) Layer 4 (easternmost) with the location of sample 039; (F) Sample 036 representing a layered carbonate with isotope sample 036 marked; (G) Sample 037 representing a massive carbonate with isotope sample 037 marked; (H) Sample 038 representing an infiltrated massive carbonate with isotope sample 038 marked; (I) Sample 039 representing a massive carbonate with isotope sample 039 marked.

Locality Anna is located on the mountain west of Kåfjord, approximately 2 km NE of the Halde northern light observatory at Halde mountain. The locality is spread out on three main outcrops, all of them in Storviknes formation. This first outcrop shows four carbonate layers interlayered with a grey-colored shale (Figure 37A). Vik (1985) reported three carbonate layers at this location. All layers strike NE-SW with a nearly vertical dip towards NW. The fourth layer (Figure 37E) differs from the three first layers as it consists of at least six thinner layers of carbonates, with each layer not thicker than 20cm. The first three layers contain chlorite-rich tuff and quartz veins. Both types of veins are 1-2 cm thick and stand out from the carbonate due to the difference in resistance to weathering. In general, the chlorite-rich tuff follows the strike of the carbonate layers, while the quartz veins are oriented perpendicular to the strike (Figure 41C).

Outcrop 2

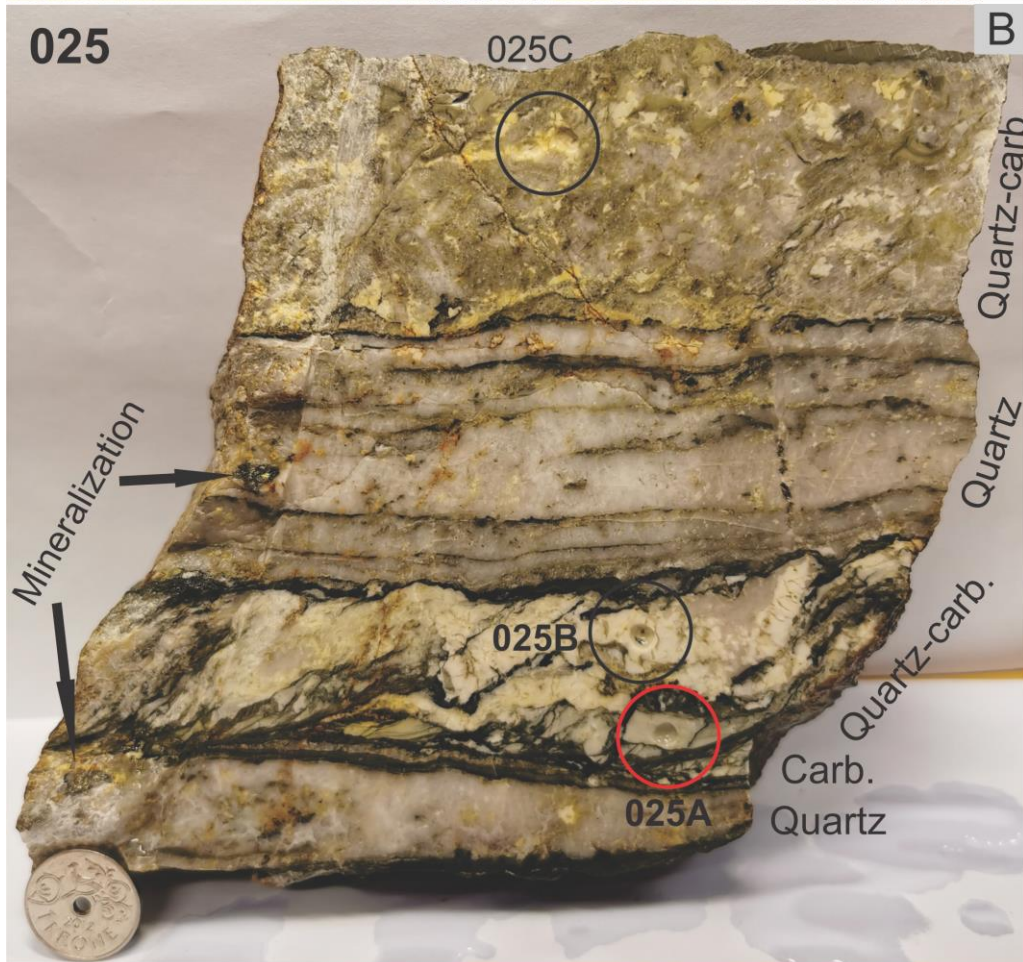


Figure 38: Outcrop 2 at the Anna area; (A) Tailings from Anna mine with the entrance of the mine marked, which starts in the shale west of the first carbonate layer. Haldde mountain is the highest mountain in the background; (B) Hand sample 025 with isotope samples 025A, 025B, and 025C marked. From bottom to top of the sample: shale, quartz with minor amounts of carbonate, shale, carbonate, shale, quartz-carbonate, shale, quartz with minor amounts of carbonate alternating with thinner layers of shale, shale, and quartz-carbonate; (C) A picture of hand sample 0222 with the black rectangle marking the approximate location of thin section 0222.

Outcrop 2 (Figure 38A) represents the tailings from the historic Anna copper mine located ~300 m SW of outcrop 1. Samples 025, 0222, (Figure 38B & C) and 0221 (Appendix B) are from the tailings.

Hand sample description

Sample 025 (Figure 38B) represents alternating layers of quartz, carbonate, quartz-carbonate, and shale. Minor amounts of chalcopyrite occur in the two quartz-rich layers.

Sample 0222 (Figure 38C) is characterized by several chalcopyrite-bearing veins cutting through a massive carbonate host rock.

Sample 0221 (Appendix B) is similar to hand sample 0222, but the ore minerals within the veins have a darker color.

Petrography and mineral chemistry

Thin section 0222

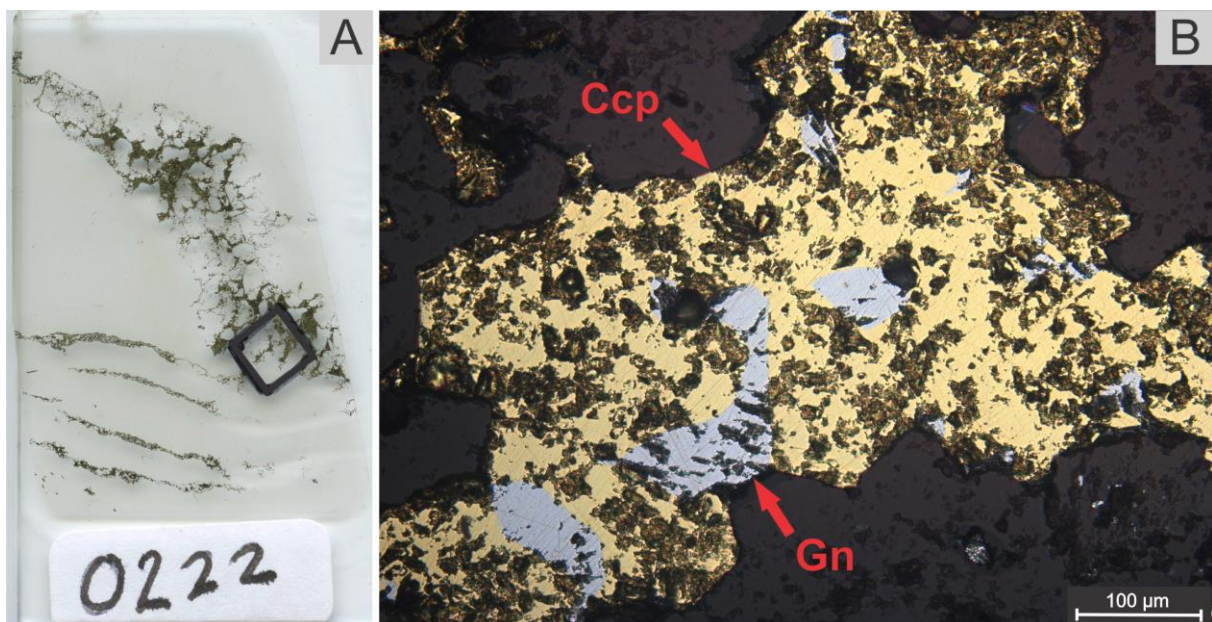


Figure 39: Thin section 0222; (A) The whole thin section with quadrant indicating Figure B; (B) RLM PPL picture showing the main ore mineral chalcopyrite with inclusions of the light-greyish-colored galena. Abbreviations: Ccp: Chalcopyrite, Gn: Galena.

Thin section 0222 (Figure 39A) is from hand sample 0222 (Figure 38C) and contains chalcopyrite as a major ore mineral with inclusions of accessory galena. Galena has mainly

been identified by its characteristic triangular-shaped marks (not seen in this picture). Quartz is the main gangue mineral with minor amounts of carbonates. No host rock minerals have been identified in the very fine-grained (~10 µm) matrix, but it is assumed to be identical to sample 0221.

Thin section 0221

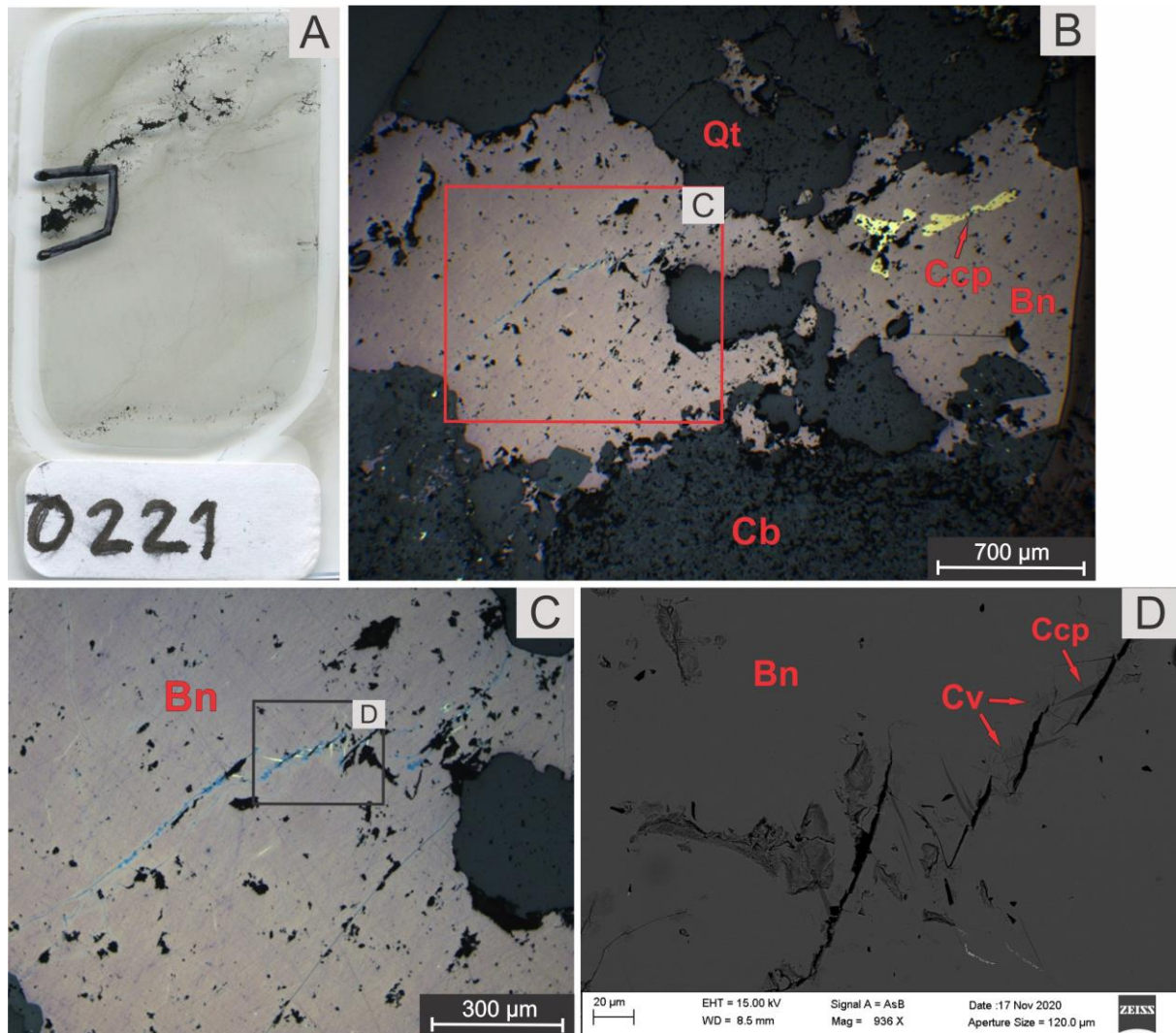


Figure 40: Thin section 0221; (A) The whole thin section with the area of Figure B indicated; (B) RLM PPL picture showing the main ore minerals, the orange-brownish-colored bornite and chalcopyrite with Figure C marked by a quadrant; (C) RLM PPL picture showing the yellow-colored chalcopyrite and blue-colored covellite within bornite, with Figure D marked by a rectangle; (D) A backscattered electron image showing the triangular-shaped chalcopyrite and irregular-shaped covellite related to fractures in bornite. Abbreviations: Qt: Quartz, Ccp: Chalcopyrite, Bn: Bornite, Cb: Carbonate mineral, Cv: Covellite.

Thin section 0221 (Figure 40A) from hand sample 0221 (Appendix D) contains three ore minerals within a quartz-carbonate vein (predominantly quartz) that is hosted by a carbonate rock. Bornite is the main ore mineral occurring in major amounts (Figure 40B). Chalcopyrite occurs in minor amounts as inclusions within bornite (Figure 40B), as infill related to

fractures in bornite (Figure 40C & D), and it also occurs together with bornite (Appendix D). Chalcopyrite does not occur inside the fractures but next to them as small triangular-shaped veins. Covellite occurs in accessory amounts next to the fractures with an irregular shape (Figure 40C & D). The host rock has a fine-grained grain size from 3 to 25 μm . The mineral chemistry of this carbonate host rock and ore minerals can be found in Table 10.

Table 10: Element composition (in wt.%) of the main mineral phases found in sample 0221. The composition has been determined by the SEM-EDS technique.

Thin section 0221		Fe	Cu	S	O	Mn	Mg	Ca
Ore minerals	Bornite	11	63.5	25				
	Chalcopyrite	30	35	34				
	Covellite	2-11	63-67.5	26-29				
Host rock mineral	Carbonate mineral				50	1	15	28

Outcrop 3

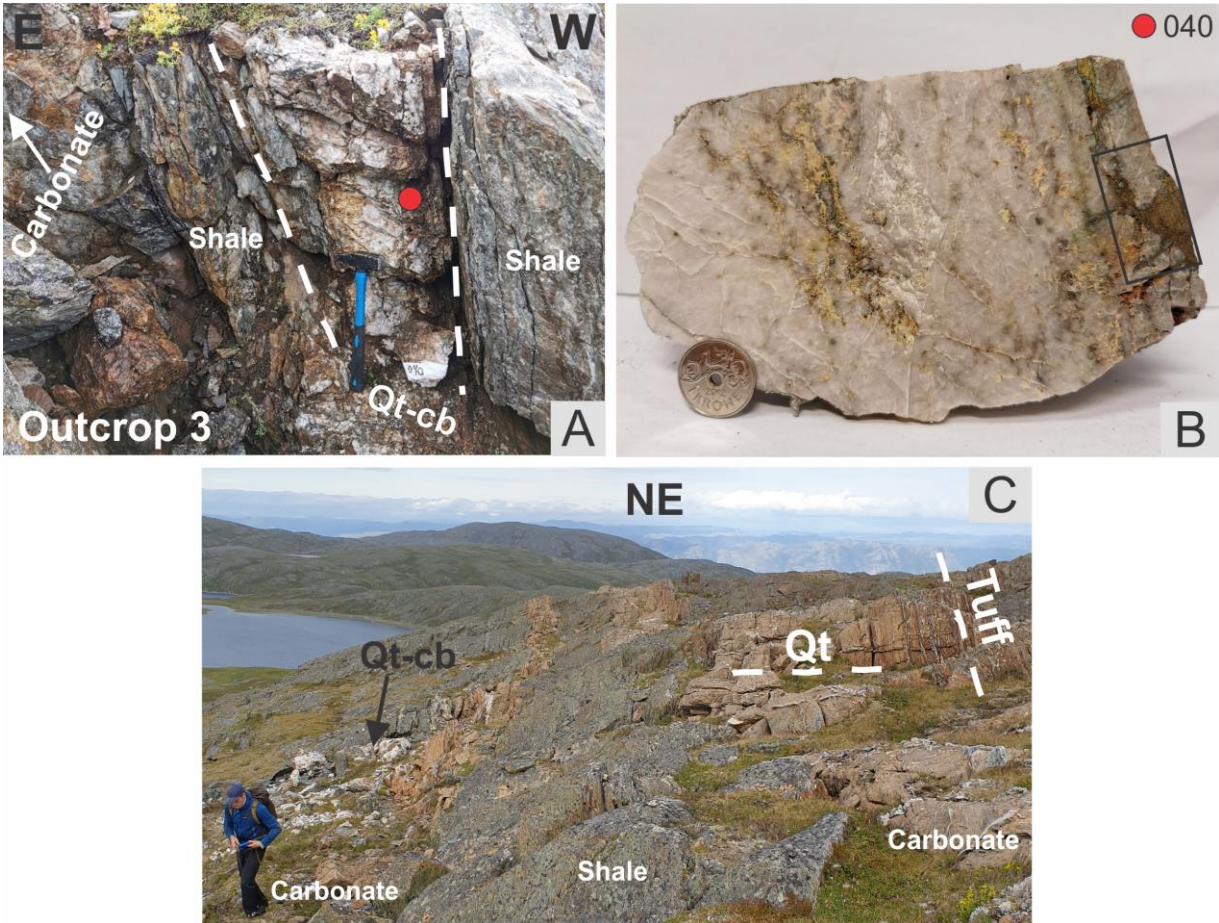


Figure 41: Outcrop 3 at the Anna area; (A) Overview of the outcrop, with a red circle indicating sample 040. Dashed white lines indicate quartz-carbonate vein hosted by shale; (B) Hand sample 040 showing a mineralized quartz-carbonate rock with rectangle indicating thin section 040; (C) Overview showing the quartz-carbonate and

tuff following the strike of the carbonate layers (layer 2 to the left and 3 to the right) while the quartz is oriented perpendicular to the strike. Abbreviations: Qt-cb: Quartz-carbonate.

Outcrop 3 at Anna is a test pit located close to carbonate layer 2. A mineralized quartz-carbonate vein hosted in shale occurs 1 m west of this carbonate layer (Figure 41A). Sample 040 has been collected from this locality (Figure 41B).

Hand sample description

Sample 040 (Figure 41B) represents a quartz-rich vein that also contains minor amounts of a yellow-colored carbonate mineral. Sulfides are more enriched in the right part of the sample (which was in contact with the shale), but it is also disseminated within the quartz-carbonate, mainly related to the carbonate.

Petrography and mineral chemistry

Thin section 040

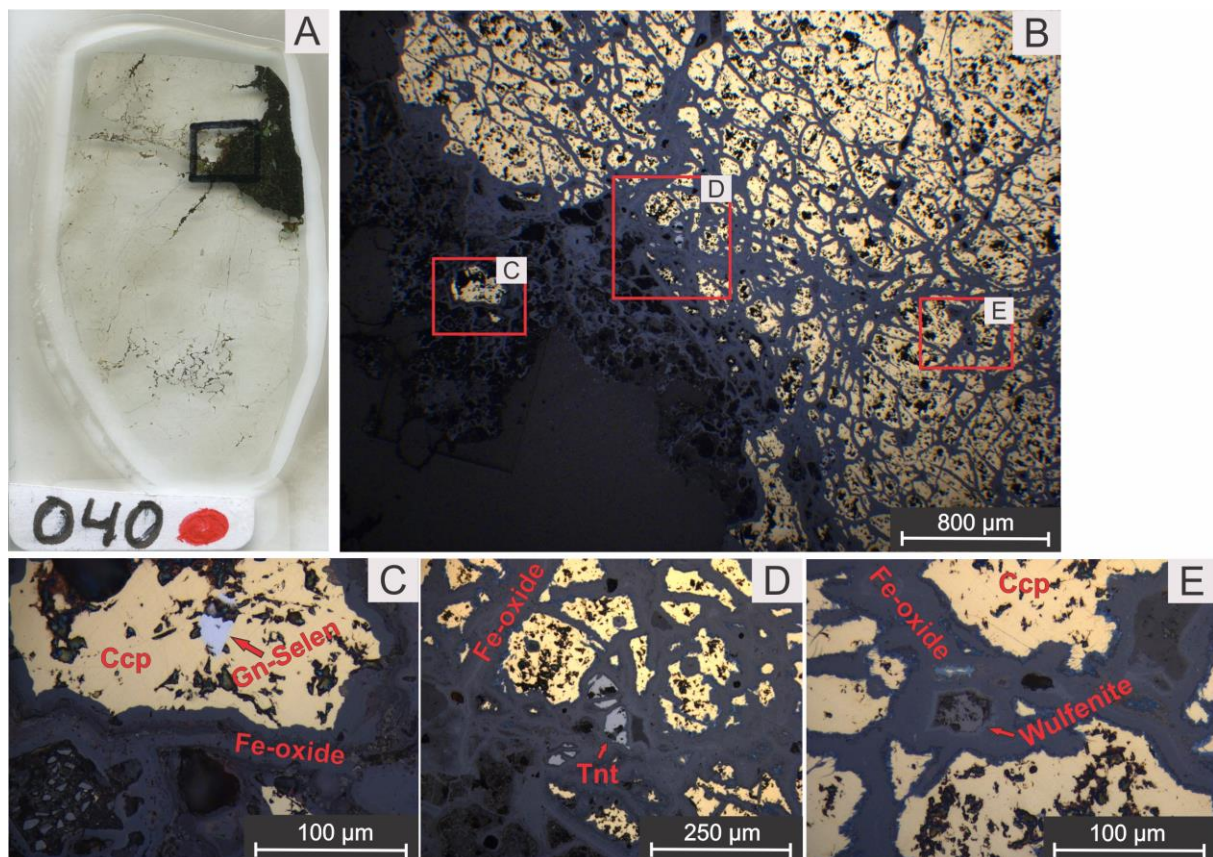


Figure 42: Thin section 040; (A) The whole thin section with black quadrat indicating the area of Figure B; (B) RLM PPL picture showing the main mineralization of chalcopyrite infiltrated by the grey-colored iron-oxide. Three red squares indicate Figures C, D, and E; (C) RLM PPL picture showing inclusion of a white-colored selenium-rich galena within chalcopyrite; (D) RLM PPL showing tennantite embedded in iron-oxide. (E) A RLM PPL picture showing dark-grey-colored wulfenite embedded in iron-oxide. Abbreviations: Gn-Selen: Selenium-rich Galena. Ccp: Chalcopyrite, Tnt: Tennantite.

Thin section 040 (Figure 42A) from sample 040 (Figure 41B) consists mostly of quartz as gangue mineral containing chalcopyrite as sulfide phase (Figure 42B). Chalcopyrite is infilled with or later oxidized to iron oxide, and it contains inclusions of selenium-rich galena (Figure 42C). Tennantite ($\text{Cu}_{12}\text{As}_4\text{S}_{13}$) is found in accessory amounts within iron-oxide (Figure 42D). The last ore mineral identified in this thin section is wulfenite (PbMoO_4) (Figure 42E). Wulfenite has been identified in accessory amounts within the iron oxide (Figure 42E) and as inclusions within chalcopyrite. The mineral chemistry of all minerals can be found in Table 11.

Table 11: Element composition (in wt.%) of the main sulfide and oxide mineral phases found in sample 040. The composition has been determined by the SEM-EDS technique.

Thin section 040		Fe	Cu	S	Pb	As	Mo	Zn	Se	O	Si
Ore minerals	Chalcopyrite	31	35	34							
	Fe-oxide	42-51	7-17		2-10	0-3.3				29-34	1.5-2
	Gn-selen			7	80				11	0.8	
	Tennantite	5	42	28		20		4		1	
	Wulfenite	1			57.5		25.5			15	

4.1.2.2 The Lundstrøm mine

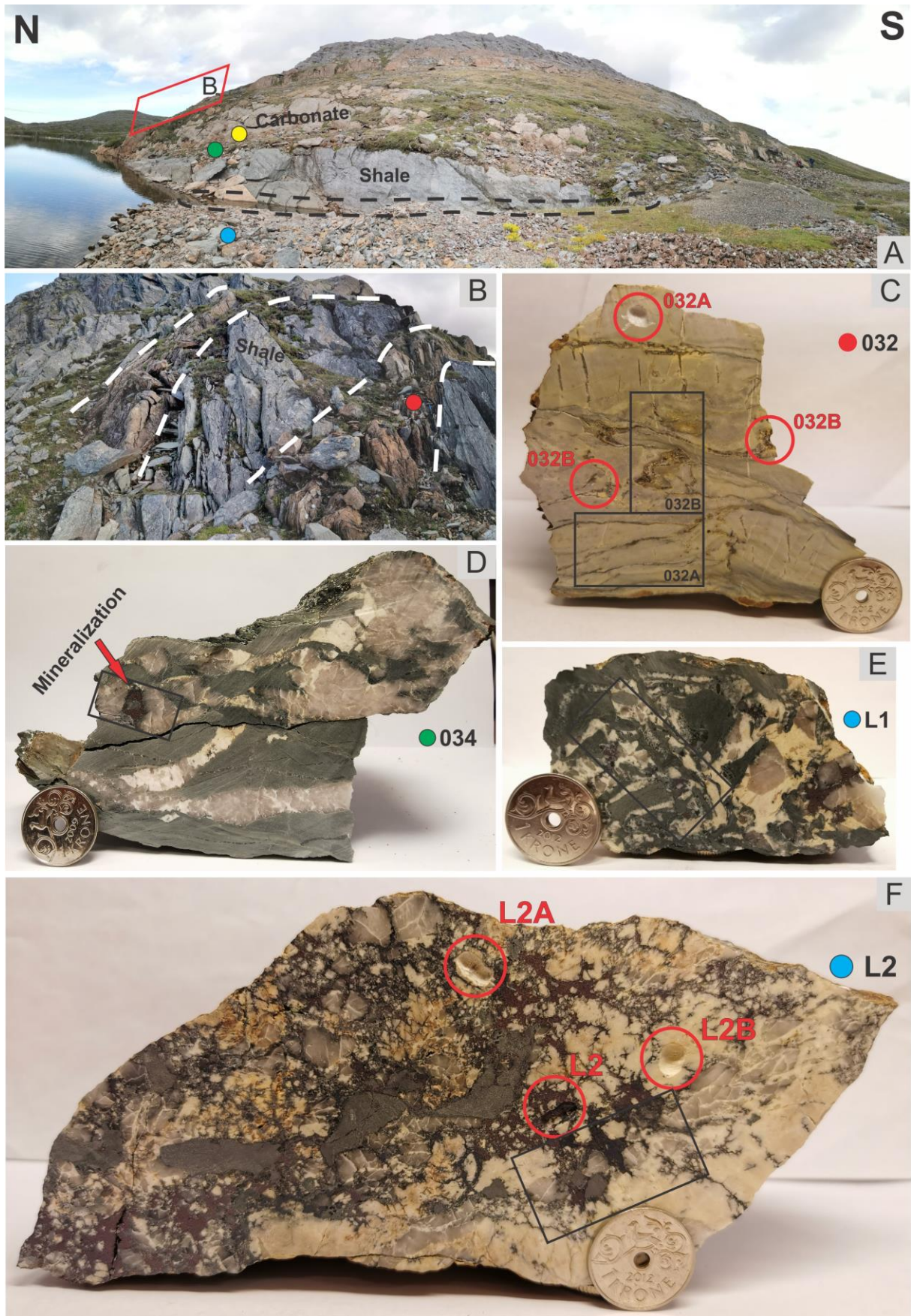


Figure 43: The Lundstrøm mine; (A) Overview of the locality with a parallelogram indicating Figure B. Blue circle indicates sample L1 and L2 (Figures E and F), while green circle indicates sample 034 (Figure D), and yellow circle indicates sample 033 (Figure 44). Dashed lines indicate the main mine opening; (B) Second and third carbonate layers marked with dashed lines. The red circle in the second carbonate layer indicate sample 032 (Figure C); (C) Hand sample 032 showing a ductile deformed and mineralized carbonate with three circles indicating isotope samples 032A and 032B (032B was drilled at two spots to get enough material). The horizontal and vertical rectangle indicates thin sections 032A and 032B, respectively; (D) Hand sample 034 showing a mineralized sample with rectangle marking area for fluid inclusion study; (E) Hand sample L1 showing a mineralized brecciated sample with the location of thin section L1 marked by a rectangle; (F) Hand sample L2 showing a mineralized brecciated sample with circles indicating isotope samples (L2, L2A, L2B). Thin section L2 is marked with a rectangle.

The historic Lundstrøm mine is located at the shoreline of Lundstrøm lake, approximately 2.2 km NE of the Anna mine. The carbonate horizon found at Anna can be followed all the way to Lundstrøm (Figure 4). Tailings, a water-filled mine opening, and a winze are still present. Mining activity has been concentrated in the shale west of the first carbonate layer, which is now filled with water (Figure 43A). This carbonate layer has a thickness of approximately 3-4 meters, while the second and third has a thickness of about 1,5 meters and are also interlayered with shale (Figure 43B), with all carbonate layers showing lateral variation due to folding. Five samples were collected at this locality (Figure 43A & B).

Hand sample descriptions

Samples L1 and L2 (Figure 43E and F) are brecciated with clasts of quartz and shale, infilled with carbonate and dark-blue-colored ore minerals. L2 shows two different colors of the carbonate, a weathered skin-colored (carbonate isotope L2A), and an unweathered white-colored carbonate (carbonate isotope L2B).

Sample 032 (Figure 43C) was collected from the second carbonate layer at Lundstrøm (Figure 43B). It represents a massive carbonate that contains ductile deformed sulfide-bearing layers.

Sample 033 (Figure 44) is from the first carbonate layer, close to the shale (Figure 43A). It is brecciated with clasts of quartz enclosed by carbonates. The quartz was easily seen on weathered surfaces as white-colored out-sticking clasts within the brown-colored weathered carbonate. Bornite and digenite are the main ore minerals and occurs as disseminations within the carbonate.

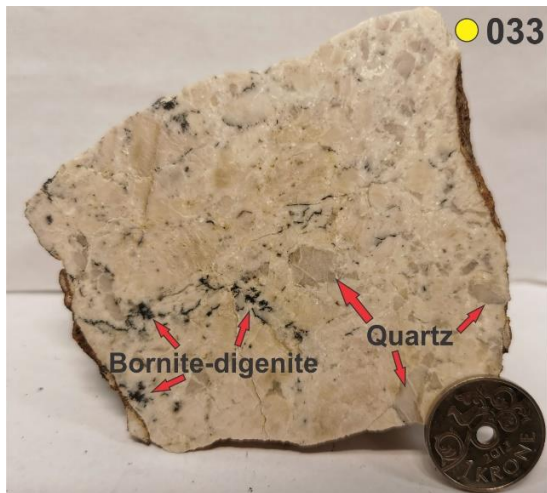


Figure 44: Hand sample 033 showing disseminated bornite and digenite within brecciated quartz-carbonate.

Sample 034 (Figure 43D) was collected on top of the shale (Figure 43A). It shows indications of brecciation in the upper part of the sample by clasts of shale occurring within the quartz-carbonate infill. Dark-blue-colored bornite and digenite are associated with the breccia matrix. Massive shale infiltrated by two quartz-carbonate veins makes up the lower part of the sample, with mineralization occurring within the quartz and carbonate.

Petrography and mineral chemistry

Thin section L2

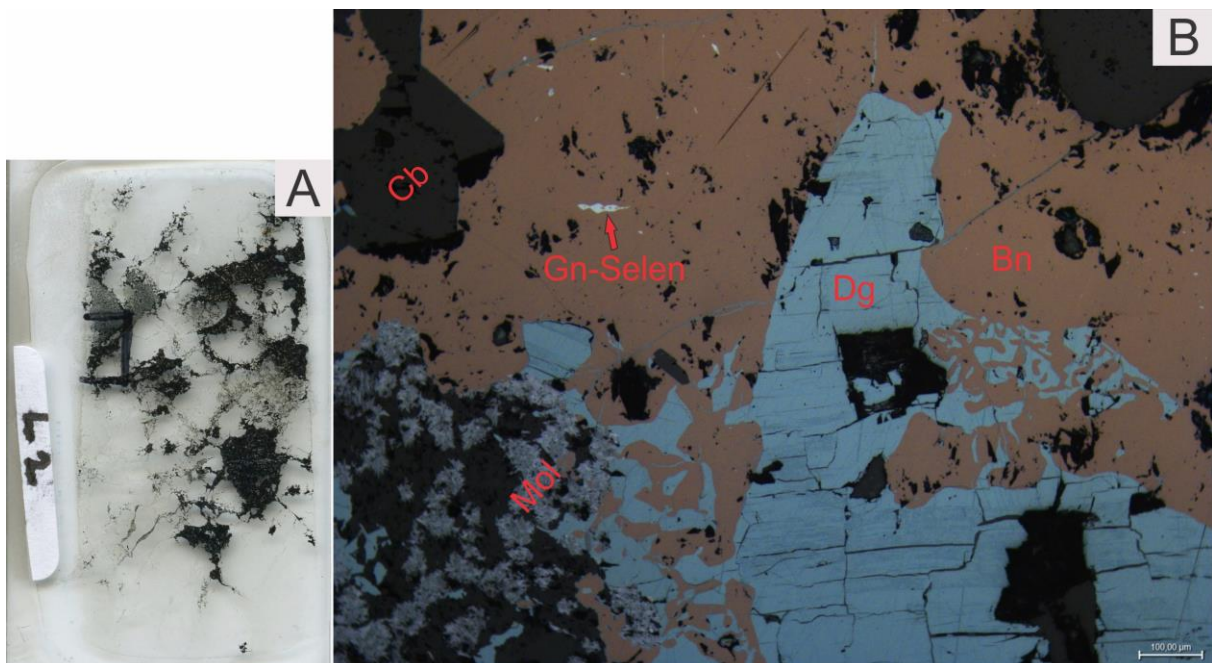


Figure 45: Thin section L2; (A) Whole thin section with the area of Figure B marked; (B) RLM PPL picture showing the relation between the ore minerals. Bornite is the orange-brownish-colored mineral, while digenite is the blue-colored fractured mineral. Selenium-rich galena is the pale-yellow-colored mineral within bornite, and molybdenite is the light-bluish-colored mineral appearing as “balls of yarn” within carbonate. Abbreviations: Cb: Carbonate mineral, Gn-Selen: Selenium-rich galena, Mol: Molybdenite, Dg: Digenite, Bn: Bornite.

Thin section L2 (Figure 45) from sample L2 (Figure 43F) contains bornite and digenite as the major ore minerals. Digenite occurs mostly within bornite, where it sometimes forms exsolution-textures with bornite (Figure 45B). Fractures in the digenite are filled with copper-oxide (Table 12), and digenite also occurs as massive grains. Digenite could be djurleite as the copper and sulfur composition is slightly closer to djurleite (Table 12; Appendix C & discussed in Appendix E). Accessory selenium-rich galena occurs as dissemination within the bornite (Figure 45B). Molybdenite is the last ore mineral identified. It appears in accessory amounts as “balls of yarn” at edges of bornite-digenite within carbonates (Figure 45B). Quartz and Fe-Mn-rich carbonates are the main gangue minerals. The mineral chemistry of the carbonate mineral, including the ore minerals, can be found in Table 12 below.

Table 12: Element composition (in wt.%) of the main mineral phases found in sample L2. The composition has been determined by the SEM-EDS technique.

Thin section L2		Fe	Cu	S	Pb	Mo	Zn	Se	O	Mn	Mg	Ca
Ore minerals	Bornite	11	64	25								
	Digenite		78.8-79.3	20.7-21.2								
	Gn-Selen		3	8	78.5			9-10	0.8-0.9			
	Molybdenite		2	36-37		59-60			2			
	Cu-oxide		74-79	1					20-26			
Gangue mineral	Carbonate mineral	5							52	1.5	13	26

Thin section 032B

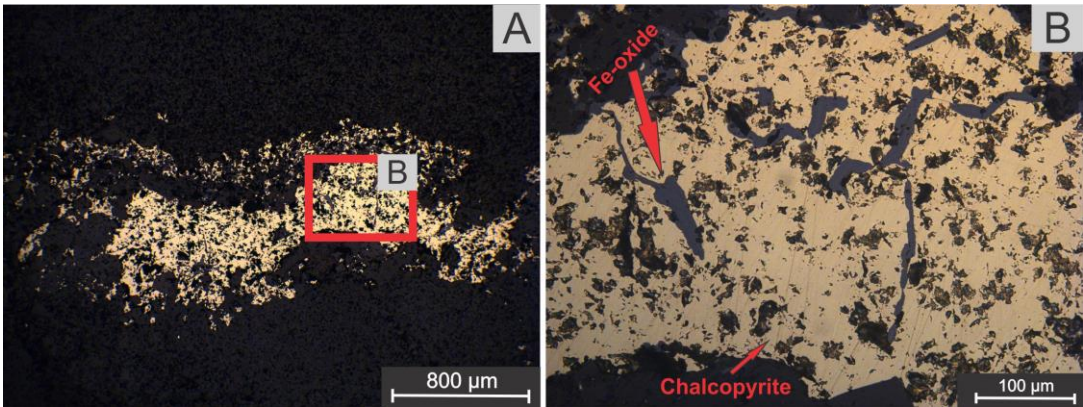


Figure 46: Thin section 032B; (A) RLM PPL picture showing chalcopyrite (yellow-colored) within a quartz-carbonate vein hosted in carbonate with the area of Figure B marked; (B) RLM PPL showing chalcopyrite with related Fe-oxide (grey-colored).

Thin section 032B (Figure 46) from sample 032 (Figure 43C) contains chalcopyrite as the only ore mineral with infill of iron-oxide identified to be hematite.

Thin section L1

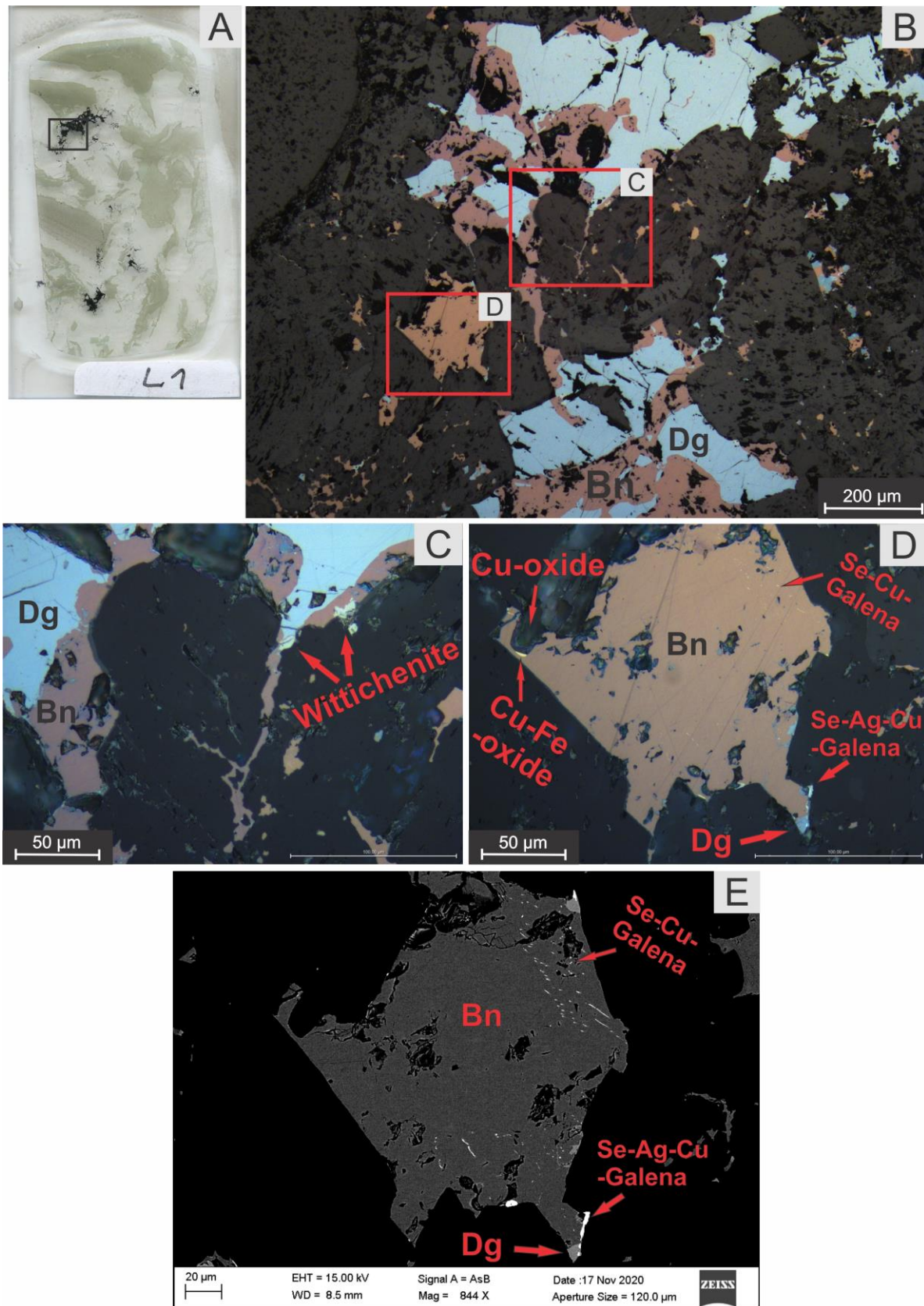


Figure 47: Thin section L1; (A) Whole thin section with a square indicating the area of Figure B; (B) RLM PPL picture showing the main ore minerals bornite (orange-brownish-colored) and digenite (light-blue-colored) with squares indicating the area of Figures C and D; (C) RLM PPL picture showing the pale-yellow-colored

wittichenite; (D) RLM PPL picture showing a bornite clast with yellow-colored Cu-Fe-oxide and Se-Cu-Galena, and bright-blue-colored Se-Ag-Cu-Galena, and blue colored digenite; (E) A backscattered electron image showing the same area as Figure D, with Se-Ag-Cu-Galena as the very bright mineral phases. Digenite and disseminated Se-Cu-galena are the light-grey mineral phases. Abbreviations: Bo: Bornite, Dg: Digenite, Ccp: Chalcopyrite, Se-Cu-Galena: Selenium- and copper-rich galena, Se-Ag-Cu-Galena: Selenium-, silver-, and copper-rich galena.

Thin section L1 (Figure 47) from hand sample L1 (Figure 43E) contains bornite and digenite as the major ore minerals (Figure 47B). Digenite occurs as fractured and massive grains, mainly within bornite, where it some places forms exsolution textures. Digenite could be chalcocite as the copper and the sulfur content is closer to chalcocite (Table 13, Appendix C & discussed in Appendix E). The sample also contains accessory copper-bismuth called wittichenite (Cu_3BiS_3) (Figure 47C; Table 13), which is found in contact with bornite and digenite. Cu-Fe-oxide has also been identified and occurs at the edges of bornite (Figure 47D). It changes gradually from pure Cu-oxide to more iron-rich towards the bornite. Accessory selenium and copper-rich galena (Se-Cu-Galena) occurs as fine-grained ($\sim 1 \mu\text{m}$) dissemination within bornite (Figure 47D and E). Selenium, silver and copper-rich galena (Se-Ag-Cu-Galena) also occurs in accessory amounts related to edges of bornite-digenite (Figure 47D & E). Gangue minerals are carbonate minerals (dolomite or ankerite) and quartz, including an unknown mineral. The mineral chemistry of all ore minerals, including the carbonate and the unknown gangue mineral can be found in Table 13.

Table 13: Element composition (in wt.%) of the main mineral phases found in sample L1. The composition has been determined by the SEM-EDS technique.

Thin section L1		Fe	Cu	S	Pb	Mo	Se	O	Ag	Te	Mn	Mg	Si	Al	Ca
Ore minerals	Bornite	11	64	25											
	Digenite		78.8-79.3	20.7-21.2											
	Cu-Fe-oxide		3	8	78.5			9-10	0.8-0.9						
	Wittichenite		2	36-37		59-60			2						
	Se-Cu-Gn		74-79	1	15		4		20-26						
	Se-Ag-Cu-Gn		8-11	4	47-58		18-19		8-15	2.5-5.6					
	Cu-oxide	2.7	62.5	2					32.6						
Gangue mineral	Carbonate mineral	6-7						47-49			2	11.5			28-30
	Unknown	15						43				15	15	12	

4.1.2.3 The Carbonate wall locality

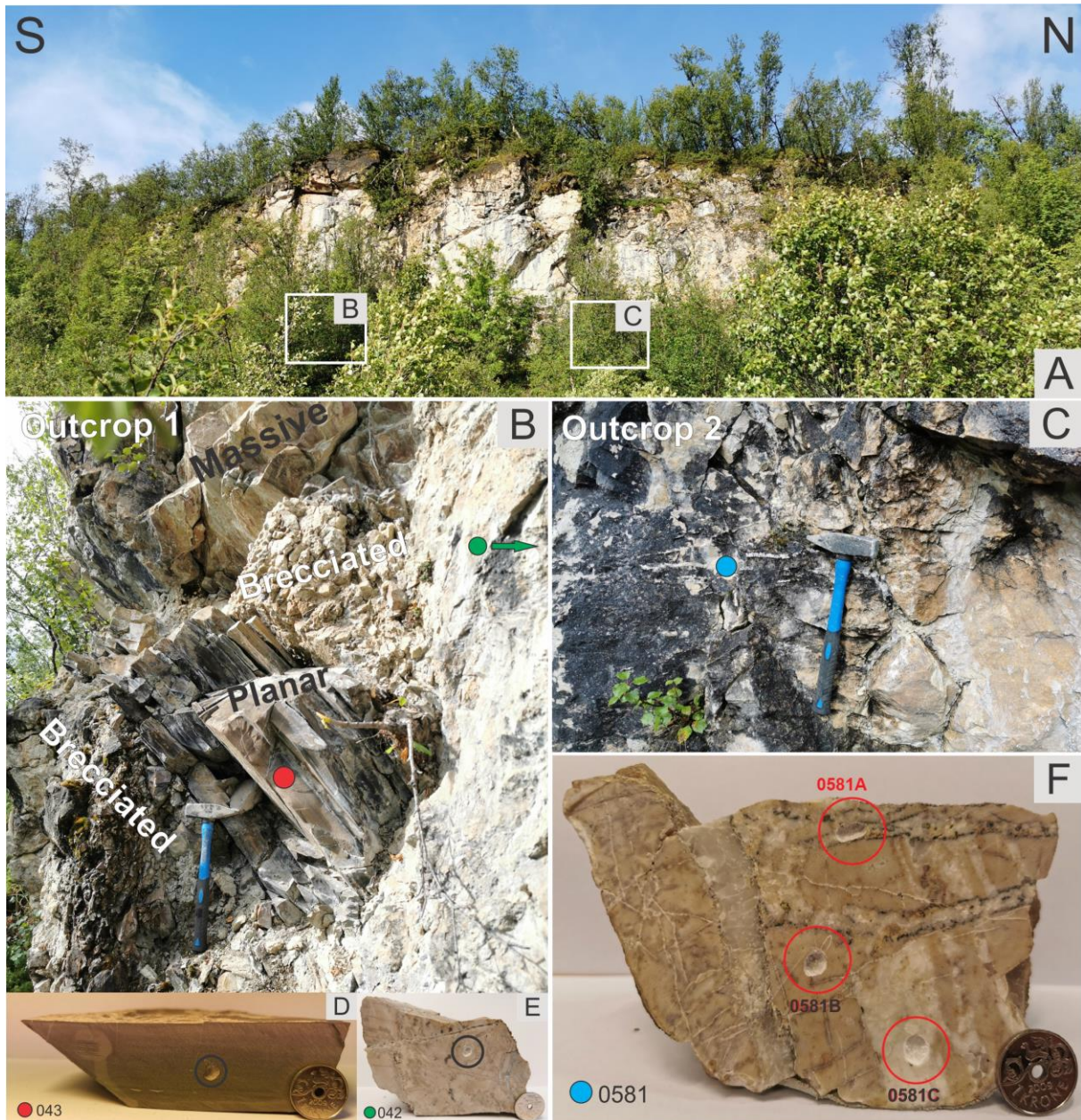


Figure 48: The Carbonate wall locality; (A) Overview of the locality with red quadrants indicating outcrop 1 (Figure B) and outcrop 2 (Figure C); (B) Outcrop 1 showing massive, brecciated and planar carbonate rocks, with samples 042 and 043 marked by the green and red circle; (C) Outcrop 2 showing veins in the massive with sample 0581 marked; (D) Hand sample 043 showing a calcareous shale with isotope sample 043 marked; (E) Hand sample 042 showing a massive carbonate with isotope sample 042 marked; (F) Hand sample 0581 showing a carbonate infiltrated by veins, with circles indicating the isotope samples 0581A, 0581B, and 0581C.

The Carbonate wall locality (Figure 48A) is a part of the Storviknes formation, situated 300 m SW of the Mitchell mine. It lays on the eastern limb of the syncline and is a continuation of the carbonate layers at Anna and Lundstrøm mines (Figure 4). The upper part of the carbonate wall is more weathered with a distinct brown color, while the lower, less weathered part of the cliff face has been investigated at two outcrops (Figure 48B & C). Outcrop 1 shows a zone of calcareous shale with a layering dipping around 50 degrees towards SW. The calcareous shale

is located between two brecciated zones with a massive carbonate layer on the top (Figure 48C). At outcrop 2, the massive carbonate was infiltrated by quartz-carbonate veins. Only smaller amounts of sulfides could be observed in the quartz-carbonate veins (sample 0581). Three samples were collected from this locality (Figure 48B & C).

Hand sample description

Sample 042 represents a massive carbonate, while sample 043 is of the calcareous shale (Figure 48E & D). Sample 0581 is a massive carbonate that is infiltrated by three generations of quartz-carbonate veins with different ratios of quartz and carbonate (Figure 48F). One vein was mineralized with chalcopyrite while the two others were barren.

4.1.2.4 The Møllnes river locality

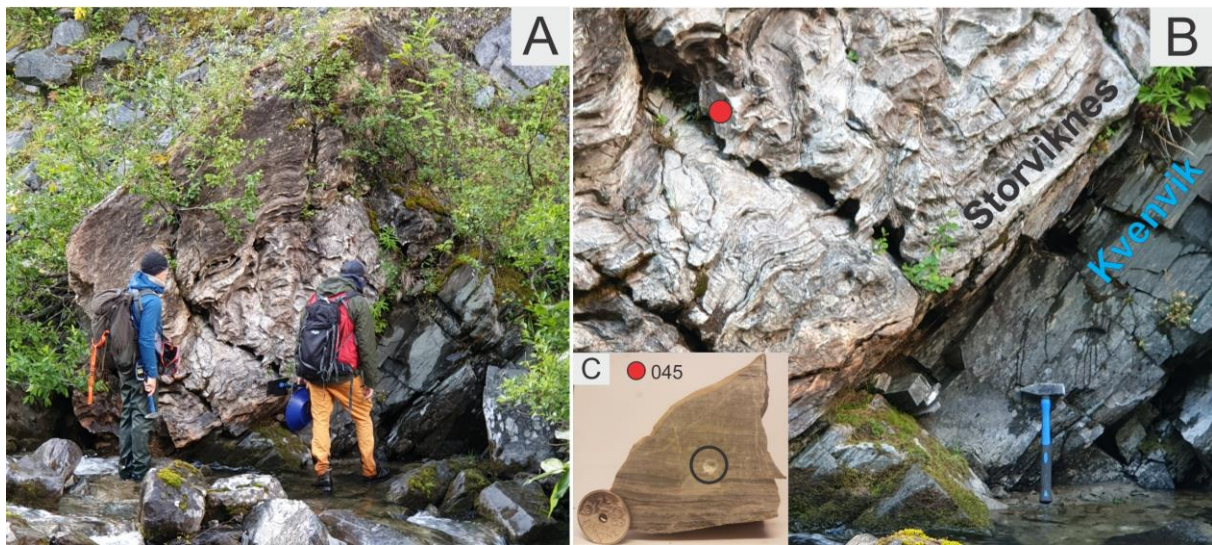


Figure 49: The Møllnes river locality; (A) Overview of the locality; (B) Kvenvik formation in the right part of the picture and Storviknes in the left part, with the red circle marking sample 045; (C) Hand sample 045 showing a layered carbonate with a circle indicating isotope sample 045.

The Møllnes river locality is situated at the contact between the carbonate of Storviknes formation and the underlying basaltic tuff and tuffite of the Kvenvik formation (Figure 4), approximately in the middle part of Møllnes river. This contact can be seen in Figure 49B and is likely to represent the bedrock, but it could also be a bigger block that has been moved and tilted.

Hand sample description

Sample 045 (Figure 49C) represents a barren carbonate of the Storviknes formation east of the syncline (Figure 4).

4.1.2.5 The Melsvik locality



Figure 50: The Melsvik locality; (A) Overview of the locality with red and blue circles indicating sample 0012 and 001; (B) Hand sample 0012 shows a mineralized layered carbonate with a circle indicating isotope sample 0012; (C) Hand sample 001 shows a barren layered carbonate with infilled veins. A circle indicates isotope sample 001.

The Melsvik locality (Figure 50A) is in a roadcut on E6 close to the road to Melsvik (Figure 3). It is situated in the Storviknes formation (NGU, 2021a). The roadcut shows two carbonate layers hosted by shale, with boudinage observed in the upper layer. Two samples were collected.

Hand sample description

Sample 001 (Figure 50C) is from the lower carbonate layer, representing a layered carbonate with small zones (~5mm) of mineralization occurring along with the layering.

Sample 0012 (Figure 50B) is from the upper carbonate layer, representing a barren layered carbonate with veins oriented perpendicular to the layering.

4.1.3 Sediment-hosted barren locality in the Skoadduvarri formation

4.1.3.1 The Skoadduvarri locality

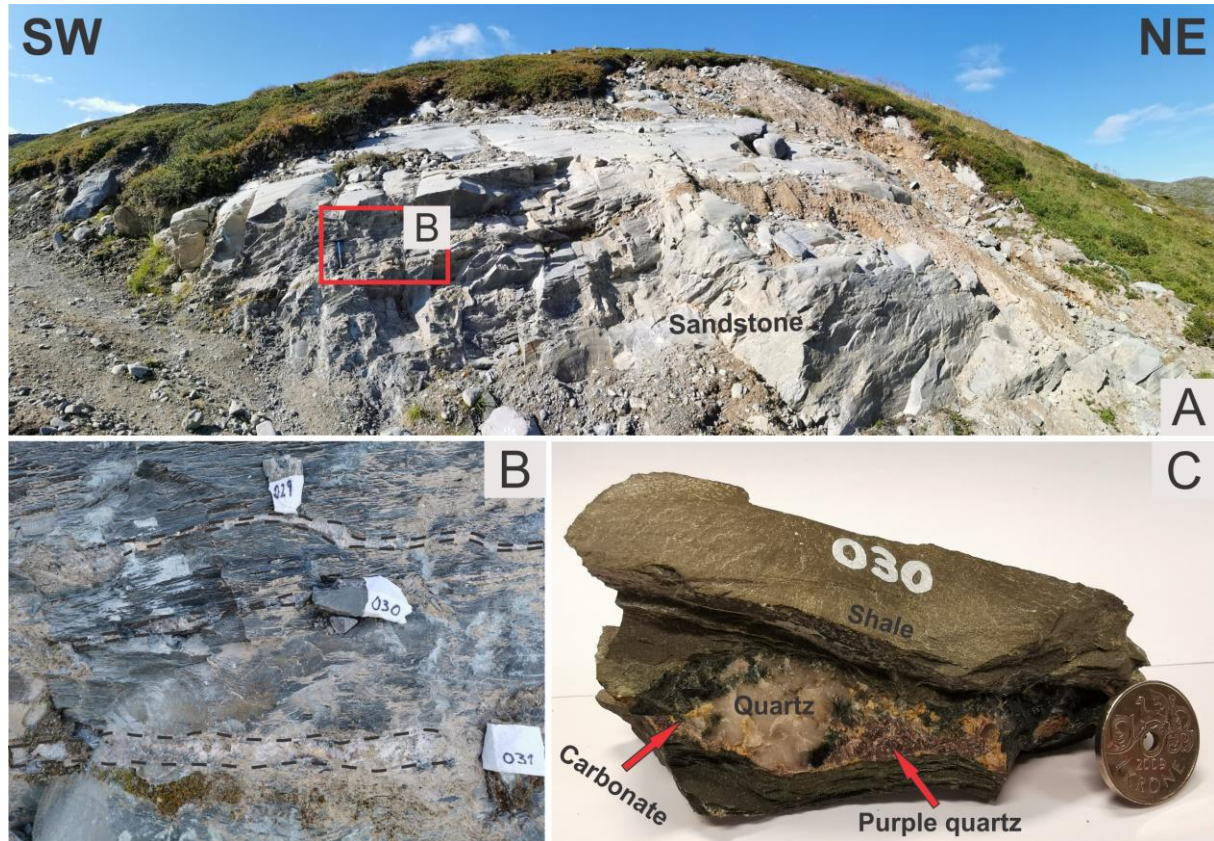


Figure 51: The Skoadduvarri locality; (A) Overview of the locality with rectangle indicating Figure B; (B) Three quartz-carbonate veins with the location of samples 029, 030 and 031; (C) Hand sample 030 showing a quartz-carbonate vein hosted by shale.

The Skoadduvarri (Figure 51A) lies in the Skoadduvarri formation, close to the shale of the Storviknes formation (NGU, 2021b). This locality is exposed in a roadcut just above the tree line. Three barren quartz-carbonate veins were investigated (Figure 51B), hosted by shale very close to the veins and sandstone at some distance away.

Hand sample description

The middle quartz-carbonate vein (sample 030; Figure 51C) has been a subject of fluid inclusion study. This sample contains purple and white-colored quartz occurring together with a yellow-colored carbonate mineral, with no mineralization observed.

4.2 Trace element composition of ore and accessory minerals

Utilizing the LA-ICP-MS technique, a total of 40 elements have been analyzed in sulfides, and 34 elements have been analyzed in oxides (Appendix F). Concentrations of the most relevant elements are presented in boxplot diagrams in Figure 52 and Figure 53.

4.2.1 Geochemical signatures of sulfides

Chalcopyrite is the only mineral occurring in both the mafic rock-hosted (including the stratiform mineralization) and the sedimentary hosted Cu mineralization. In general, a similar distribution of trace elements in chalcopyrite from the mafic rock-hosted and the stratiform Cu mineralization has been observed (Figure 52). Chromium is an exception and its concentration in stratiform chalcopyrite exceeds those found in quartz-carbonate veins hosted by mafic rocks. Comparing to the mafic rock-hosted chalcopyrite, chalcopyrite found in sediment-hosted quartz-carbonate veins shows a depletion in Zn, Ni, Sb, and Cd (Figure 52). Outliers in the mafic rock-hosted veins show some high values of Co and Te in chalcopyrite compared to the rest of the mafic rock and the sediment-hosted chalcopyrite (Figure 52).

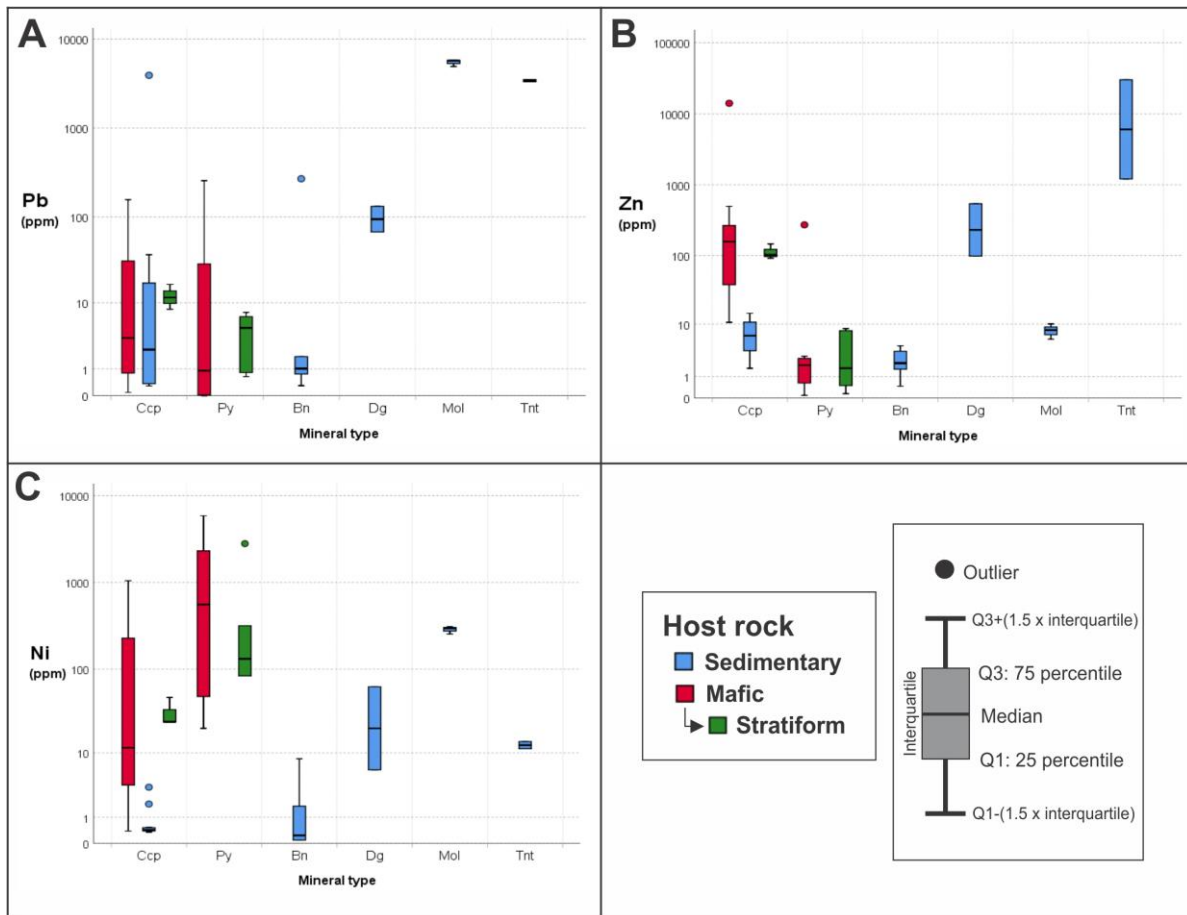


Figure 52: Boxplots presenting trace element concentrations (in ppm) for sulfides sorted by mineral type and related host rock. "Stratiform" is mafic rock-hosted and contains only sample 047. Based on a total of 79 spots from LA-ICP-MS (Appendix F). 22 spots in mafic rock-hosted Ccp, 12 spots in sediment-hosted Ccp, 3 spots in stratiform Ccp, 18 spots in mafic rock-hosted Py, 5 spots in stratiform Py, 2 spots in Sp, 6 spots in Bn, 2 spots in Dg, 3 spots Mol and 2 spots in Tnt. All values below detection limit are presented as $\frac{1}{2}$ of detection limit, and "zero values" (detection limit and spot value are zero) are presented as zero. Abbreviations: Ccp: Chalcopyrite, Py: Pyrite, Sp: Sphalerite, Bn: Bornite, Dg: Digenite, Mol: Molybdenite, Tnt: Tennantite.

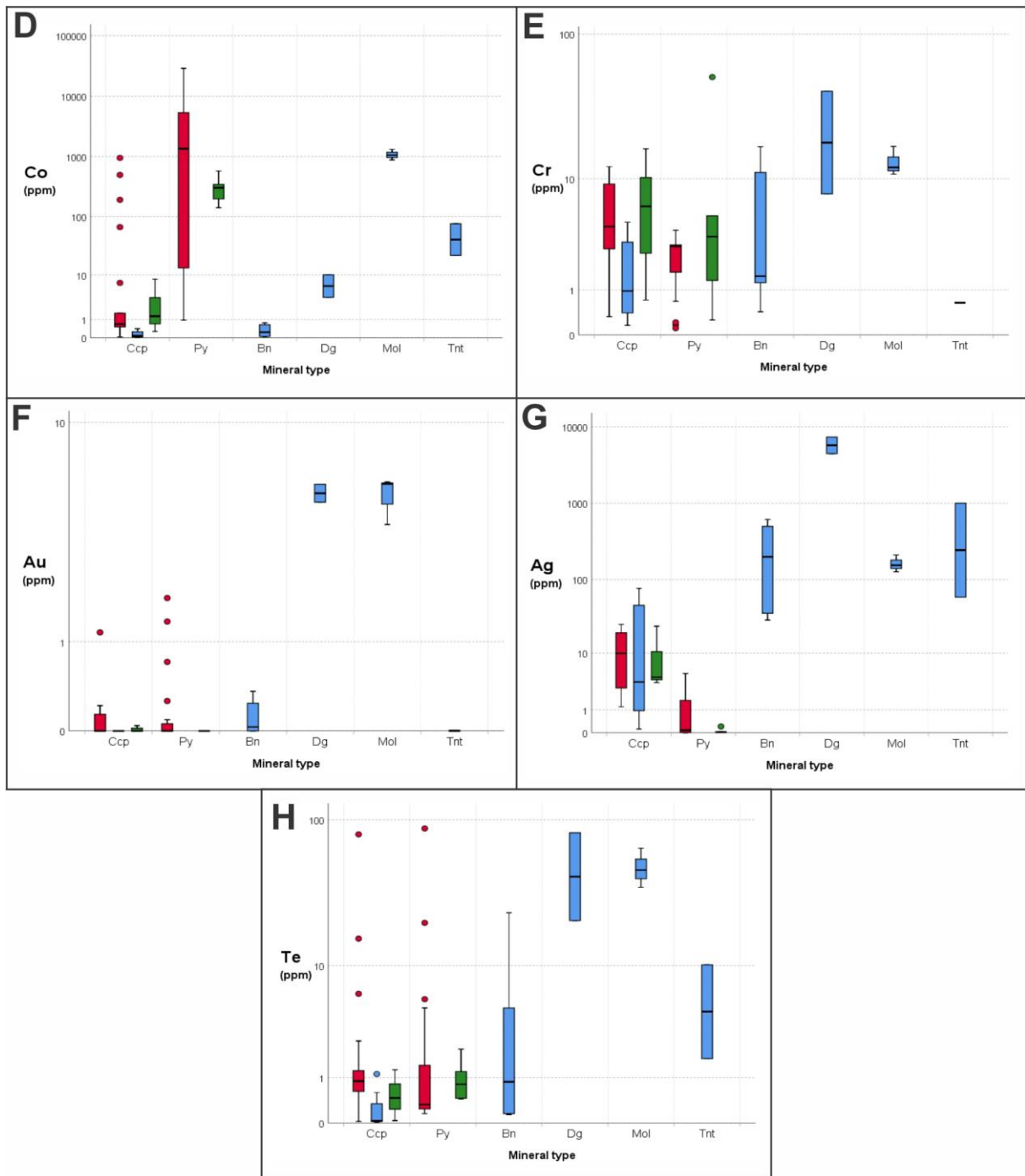


Figure 52: Continued.

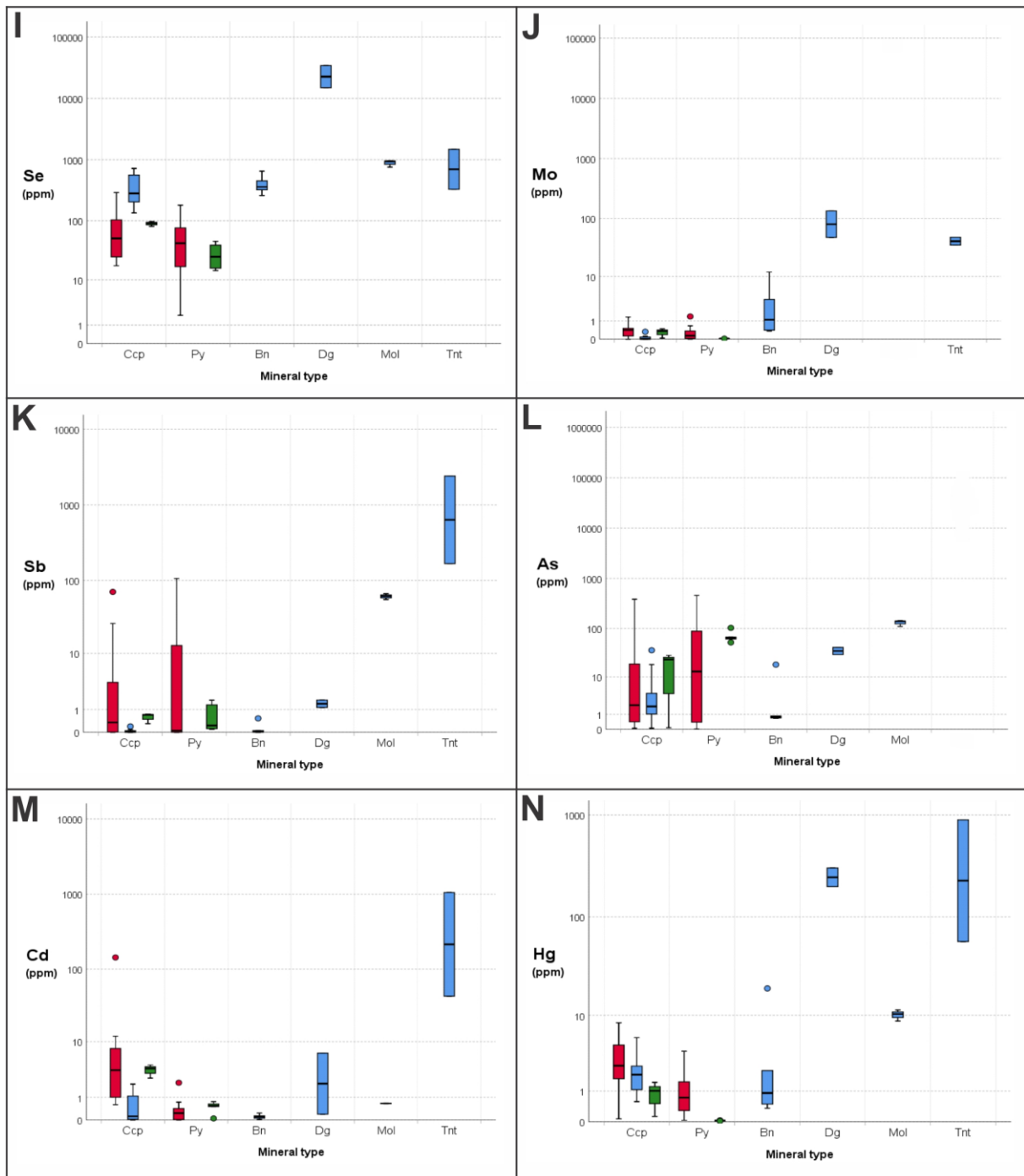


Figure 52: Continued

Chalcopyrite is the only mineral occurring in both the mafic rock-hosted (including the stratiform mineralization) and the sedimentary hosted Cu mineralization. In general, a similar pattern for all elements in chalcopyrite within the mafic rock-hosted (red color) and the stratiform sample (green color) have been observed. Chromium is an exception where the Cr concentrations in stratiform chalcopyrite exceed those found in quartz-carbonate veins in mafic rocks. A depletion in Zn, Ni, Sb, and Cd can be seen in the sediment-hosted chalcopyrite relative to the mafic rock-hosted chalcopyrite. A weak depletion in Cr is also

observed. Outliers in the mafic rock-hosted veins show some high values of Co and Te in chalcopyrite compared to the rest of the mafic rock- and the sediment-hosted chalcopyrite.

Pyrite has only been identified in mineralized quartz-carbonate veins and the stratiform mineralization in the mafic rock-hosted deposits. Pyrite from the stratiform type of the mineralization contains < detection limit of Au, 0.0056 (half detection limit) to 0.209 ppm Ag, 52.39 to 102.94 ppm As, 0.09 to 1.65 ppm Sb, 0.02 (half detection limit) to 0.035 (half detection limit) ppm Hg, and 141.86 to 575.5 ppm Co. Pyrite associated with quartz-carbonate veins hosted by mafic rocks contains 0 to 1.81 ppm Au, 0 to 4.94 ppm Ag, 0.0145 (half detection limit) to 457.92 ppm As, 0.00125 (half detection limit) to 106.36 ppm Sb, 0.035 (half detection limit) to 3.91 ppm Hg, 0.96 to 8856.63 ppm Co (Appendix F).

Pyrite hosted in quartz-carbonate veins shows a range from 3626 to 5867 ppm Ni (thin section 013A), while the host rock pyrite shows a range from 20.1 to 21.52 ppm Ni (thin section 0054). Cobalt in the host rock pyrite (thin section 013A) shows a concentration from 9678 to 28830 ppm, while pyrite in veins shows a concentration from 681 to 1104 ppm Co.

Bornite, digenite, molybdenite and tennantite have been found only in sediment-hosted deposits. Bornite contains < detection limit to 0.36 ppm Au, 28.85 to 615.26 ppm Ag, 0.77 to 18.33 ppm As, < detection limit to 0.527 ppm Sb, 0.36 to 19.18 ppm Hg, and 0.045 to 0.78 ppm Co. Digenite contains 4.92 to 5.8 ppm Au, 4464.83 to 7364.13 ppm Ag, 29.7 to 41.52 ppm As, 1.13 to 1.66 ppm Sb, 198.47 to 302.75 ppm Hg, and 3.67 to 10.05 ppm Co. Molybdenite shows enrichment in Pb, Co, Ni, Sb and As compared to bornite and digenite, while tennantite is characterized by higher concentrations of Zn, Sb, As and Cd compared to bornite, digenite and molybdenite (Appendix F, Figure 52).

4.2.2 Geochemical signatures of oxides

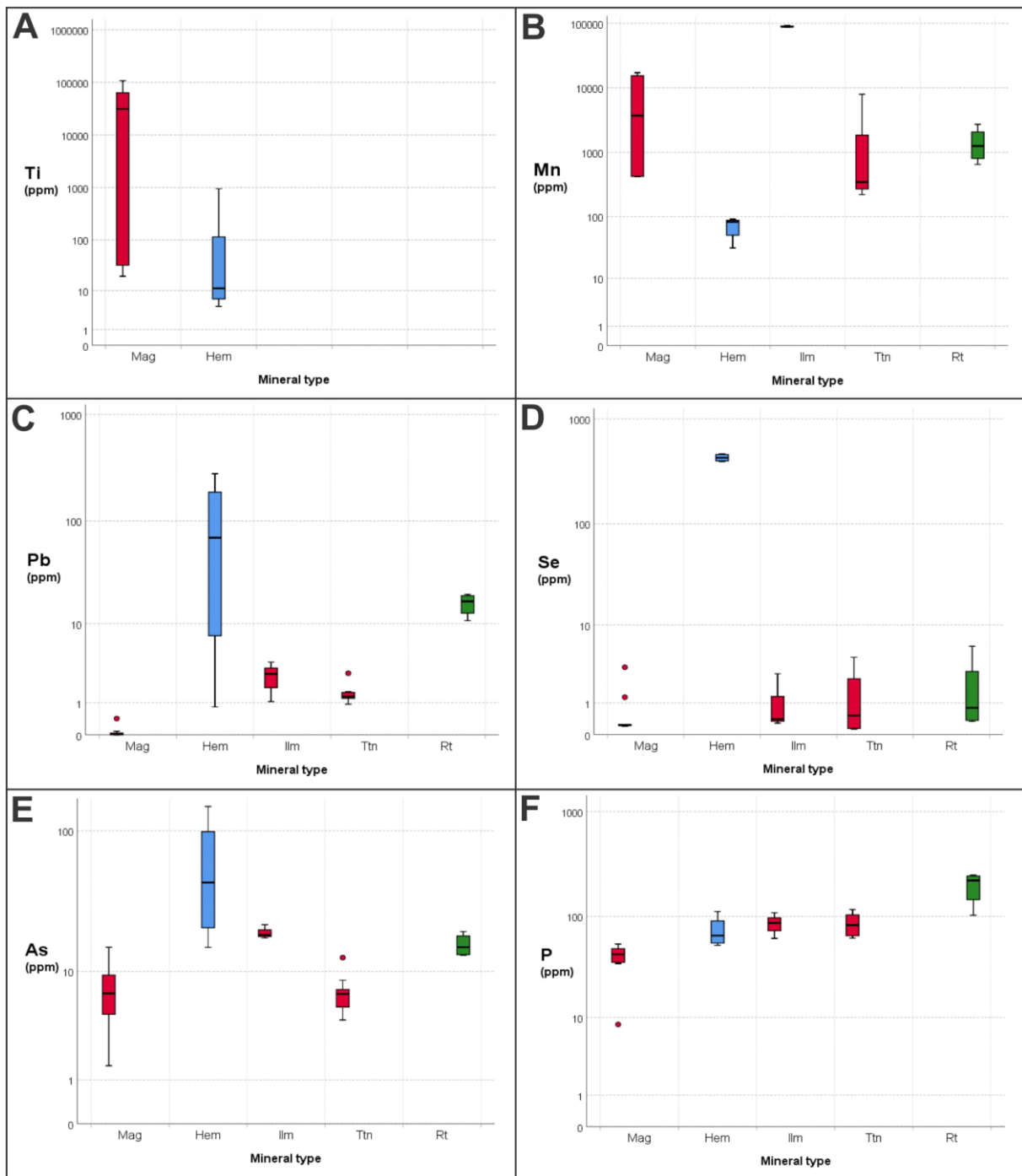


Figure 53: Boxplots presenting trace element concentrations (in ppm) for oxides sorted by mineral type and related host rock. “Stratiform” is mafic rock-hosted and contains only sample 047. Based on a total of 29 spots from LA-ICP-MS seen in Appendix F. 9 spots in Mag, 4 spots in Hem, 3 spots in Ilm, 9 spots in Ttn and 4 spots in Rt. All values below detection limit are presented as $\frac{1}{2}$ of detection limit, and “zero values” (detection limit and spot value are zero) are presented as zero. Abbreviations: Mag: Magnetite, Hem: Hematite, Ilm: Ilmenite, Ttn: Titanite, Rt: rutile.

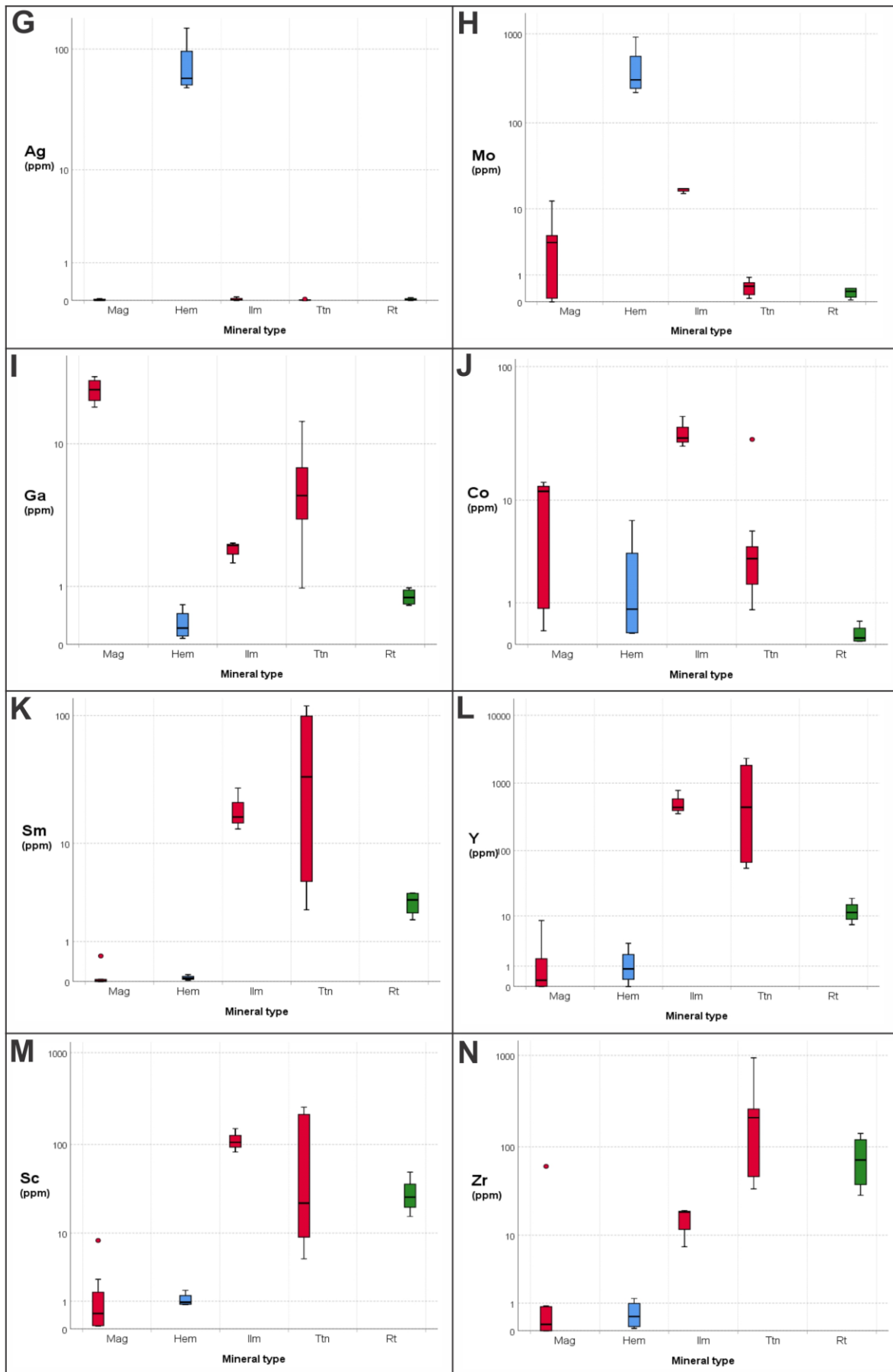


Figure 53: Continued.

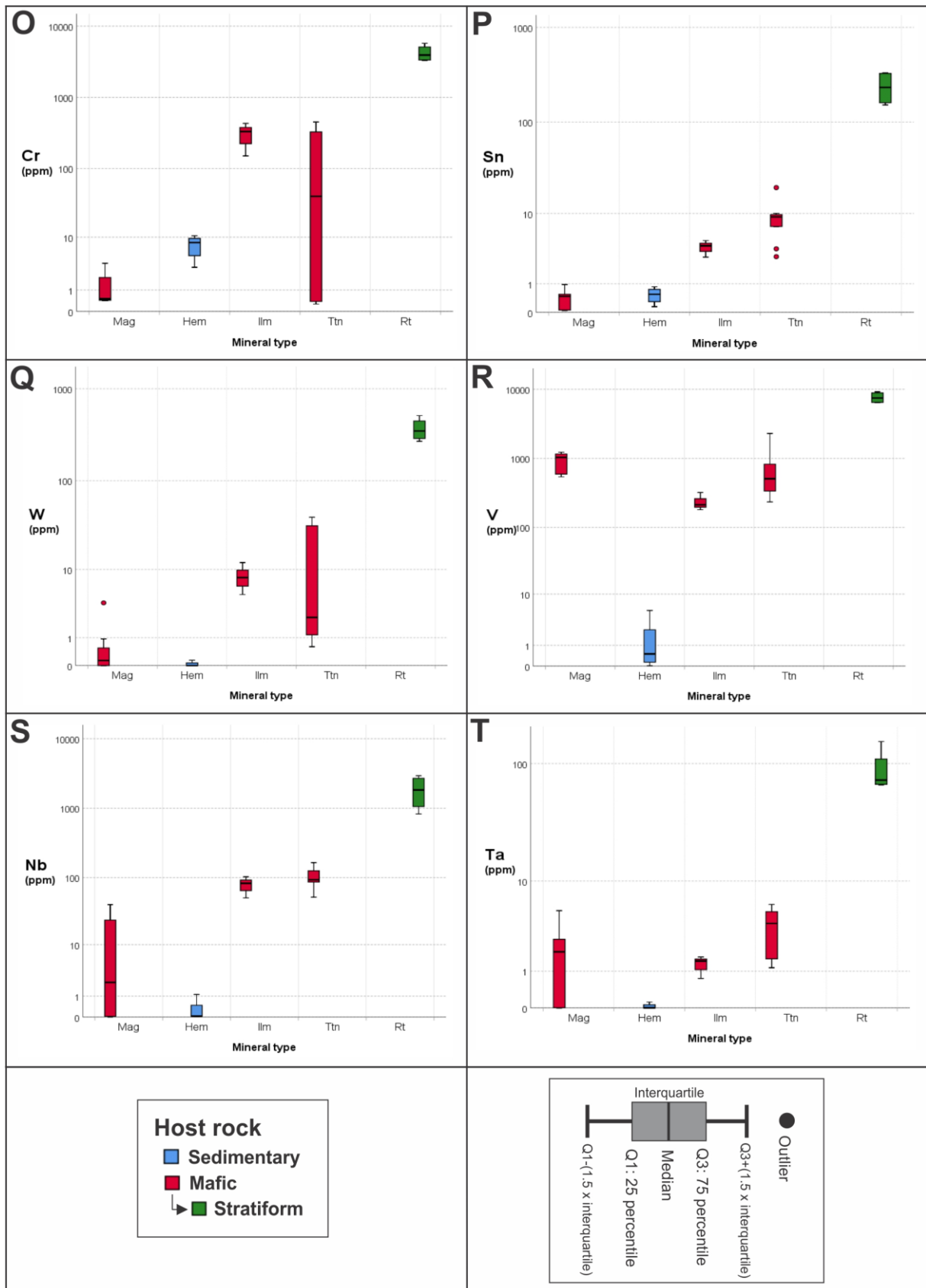


Figure 53: Continued.

Mafic rock-hosted magnetite hosted from locality Kåfjord bridge, shows enrichment in Ti compared to hematite and Ga compared to all other oxides. Ilmenite from locality Carl Johan is enriched in Mn, Pb, As, Mo and Co compared to magnetite and titanite. Compared to all oxides are ilmenite enriched in Mn and Co. Titanite shows enrichment of Sm, Y and Zr compared to all other oxides. Titanite as infill in the magnetite (thin section 0054), around ilmenite (thin section 013B), and as titanite clasts (thin section 060A) shows that Cr is under detection limits in 0054, from 328 to 452 ppm in 013B and 26 to 74 ppm in 060A. P, W and As are enriched in 013B (32 to 40 ppm) compared to 0054 and 060A. Rutile from the stratiform mineralization shows enrichment of elements as of P, Cr, Sn, W, V, Nb compared to the other oxides.

Hematite from the sediment-hosted locality Lundstrøm is enriched in Pb (0.832 to 278.08 ppm), Se (392.77 to 465.28 ppm), As (15.1 to 146.98 ppm), Ag (48.58 to 147.08 ppm) and Mo (219.44 to 917.89 ppm) compared to all other oxides.

All oxides have similar concentrations of As (~10 ppm), P (~100 ppm) and Mn (~1000 ppm). Silver and Mo are enriched in the sediment-hosted oxides, and very depleted in the mafic rock-hosted. Arsenic, Pb and Se are more enriched in the sediment-hosted comparing to Fe-oxides from the mafic rock-hosted deposits (Figure 53).

4.3 Whole rock geochemistry

Lithochemical analyses of major and trace elements, including rare earth elements (REE) have been carried out on four mafic rock samples from the Kvenvik formation. The analyzed samples can be subdivided into two categories: 1) intermediate host rocks for the Cu mineralization (samples 013 & 0054) and 2) mafic lithologies barren of Cu mineralization (samples 003 & 0046). The sample localities and their lithological character is listed in (Table 14).

Table 14: List of the mafic rocks selected for the whole rock geochemical analyses.

Sample	013	0054	0046	003
Rock type	Basalt	Gabbro	Tuff/tuffite	Basalt
Host/country	Host rock	Host rock	Country rock	Country rock
Locality	Carl Johan	Kåfjord bridge	Kråknes	Melsvik tunnel

Table 15: Major element oxide concentrations (in wt.%) of representative mafic rocks from the Kvenvik formation.

Sample	Na ₂ O	MgO	Al ₂ O ₃	SiO ₂	P ₂ O ₅	K ₂ O	CaO	TiO ₂	MnO	Fe ₂ O ₃	%LOI	Total
003	4.00	9.22	14.97	46.61	0.05	0.08	7.46	1.10	0.26	13.59	3.77	101.11
013	2.65	10.04	15.18	44.66	0.03	0.12	4.81	0.92	0.32	14.45	7.92	101.10
0046	4.85	6.89	14.03	47.76	0.07	0.09	2.48	2.68	0.14	18.73	3.26	100.97
0054	5.49	3.84	9.60	47.88	0.19	0.12	5.24	2.11	0.15	24.05	0.45	99.11

Table 16: Trace element concentrations (in ppm) of representative mafic rocks from the Kvenvik formation. Corrected for LOI (Loss on ignition). * Analyzed by ICP-AES.

Sample	Li	Sc	V	Cr	Co	Ni	Cu	Zn	Rb	Sr	Y	Zr	Nb	Cs	Ba	Hf	Ta	Pb	Th	U	%LOI	Correction factor
003	46.96	44.03	303.8	250.3	46.86	106.1	58.02	96.90	1.80	58.65	19.02	36.57	3.61	0.225	21.50	1.32	0.240	0.411	0.311	0.083	3.77	0.9623
013	20.75	42.32	242.4	679.1	32.87	55.04	13.21	88.23	3.67	18.36	21.41	21.71	2.32	0.245	9.19	0.715	0.151	0.830	0.284	0.158	7.92	0.9208
0046	22.55	40.99	381.3	308.3	63.37	133.0	14.16	105.6	1.56	29.87	23.59	136.6	10.84	0.192	26.07	3.93	0.714	0.967	1.22	0.278	3.26	0.9674
0054	7.52	43.43	319.3	0.60	48.49	6.86	277.4*	15.14	1.98	13.03	37.21	53.95	6.74	0.049	9.98	2.03	0.431	0.832	0.587	0.353	0.45	0.9955

Table 17: Rare earth elements concentrations (in ppm) of representative mafic rocks from the Kvenvik formation. Corrected for LOI (Loss on ignition).

Sample	Y	La	Ce	Pr	Nd	Sm	Eu	Gd	Tb	Dy	Ho	Er	Tm	Yb	Lu	%LOI	Correction factor
003	18.13	3.45	8.58	1.38	7.01	2.26	0.861	3.00	0.540	3.56	0.764	2.17	0.308	1.94	0.284	3.77	0.9623
013	20.14	10.36	20.94	2.83	12.33	2.73	0.684	3.20	0.580	3.90	0.862	2.46	0.340	1.96	0.241	7.92	0.9208
0046	22.16	6.12	16.18	2.80	14.86	5.10	2.05	5.81	0.947	5.66	1.09	2.88	0.393	2.41	0.334	3.26	0.9674
0054	36.45	4.67	12.71	2.19	11.70	4.05	1.56	5.73	1.08	7.24	1.57	4.55	0.655	4.08	0.579	0.45	0.9955

The whole rock geochemistry reveals concentrations of 2.65 wt. % Na₂O, 0.12 wt.% K₂O and 44.66 wt.% SiO₂ in sample 013. Sample 0054 contains 5.49 wt. % Na₂O, 0.12 wt.% K₂O and 47.88 wt.% SiO₂, while sample 0046 contains 4.85 wt. % Na₂O, 0.09 wt.% K₂O and 47.76 wt.% SiO₂. The last sample, sample 003 contains 4.00 wt. % Na₂O, 0.08 wt.% K₂O and 46.61 wt.% SiO₂.

Tas-plot

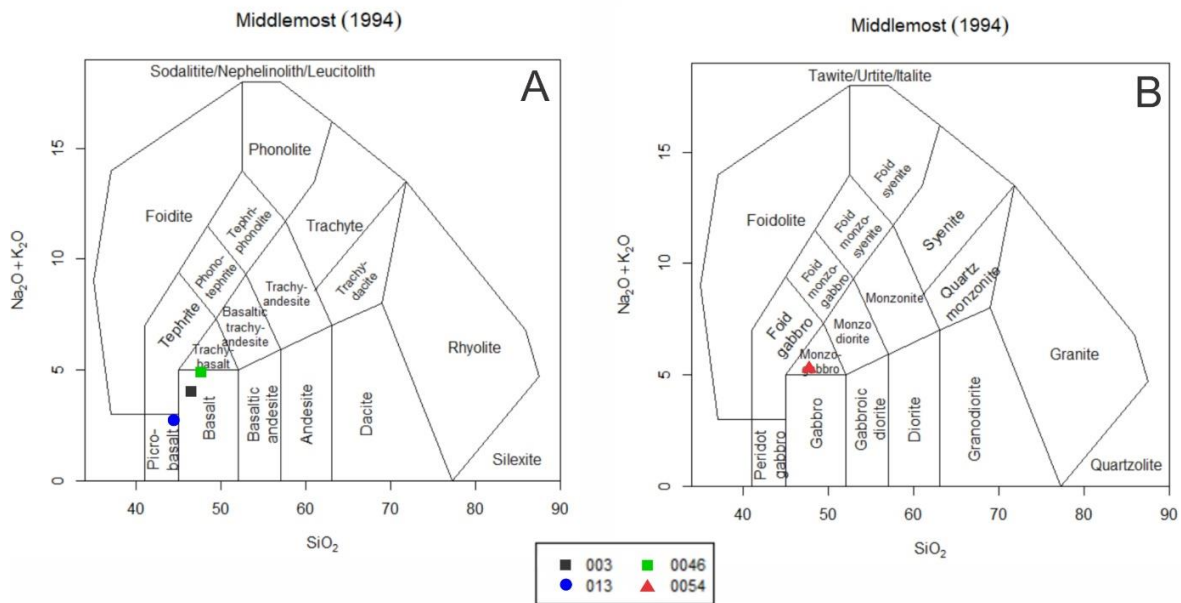


Figure 54: Two TAS plots from Middlemost (1994); (A) TAS plot for volcanic rocks with three samples plotted; (B) TAS plot for plutonic rocks with one sample plotted. 003: Basalt, 013: Picrobasalt, 0046: Basaltic tuff/tuffite, 0054: Monzogabbro.

The TAS classification shows that samples 003 and 0046 have a basaltic composition, while 013 have been classified as an ultramafic rock called picrobasalt, due to a lower SiO_2 content. Sample 0054 has been classified as a monzogabbro due to a relatively high content of Na_2O and K_2O .

4.4 Stable isotope analysis

4.4.1 Stable isotope composition of carbonates

A total of 28 spots from 20 carbonate-rich samples at ten different localities have been drilled for carbonate isotope ($\delta^{13}\text{C}$ & $\delta^{18}\text{O}$) analyses. All carbon and oxygen isotope samples are from dolomite or calcite, collected from host rocks or quartz-carbonate veins in mafic rock-hosted (Kvenvik formation) and sediment-hosted (Storviknes formation) deposits. All eight samples from the Kvenvik formation are from veins, while seven of nineteen samples from the Storviknes formation are from veins, and the rest is from the host rocks (Table 18).

Table 18: All carbon and oxygen isotope samples with associated locality, type, mineralogy, and isotopic composition. $\delta^{13}\text{C}$: delta 13 carbon, $\delta^{18}\text{O}$: delta 18 oxygen, $\delta^{18}\text{O}$ -dolomite: delta 18 oxygen corrected for dolomite, VPDB: Vienna Pee Dee Belemnite, VSMOW: Vienna Standard Mean Ocean Water.

	Locality	Sample	Type	Mineralogy	$\delta^{13}\text{C}$ (VPDB)	$\delta^{18}\text{O}$ (VPDB)	$\delta^{18}\text{O}$ (VSMOW)	$\delta^{18}\text{O}$ - dolomite (VSMOW)	
Sediment-hosted	Anna	025A	Barren quartz-carbonate vein	Dolomite	0.0	-14.4		16.1	
		025B	Barren quartz-carbonate vein	Dolomite	-0.4	-14.5		15.9	
		025C	Barren quartz-carbonate vein	Dolomite	-0.6	-15.3		15.1	
		0221B	Host rock dolomite	Dolomite	0.1	-14.9		15.6	
		0222A	Host rock dolomite	Dolomite	0.0	-14.8		15.6	
		037	Host rock dolomite (2. layer)	Dolomite	0.8	-13.5		17.0	
		038	Host rock dolomite (3. layer)	Dolomite	0.1	-14.1		16.3	
		039	Host rock dolomite (4. layer)	Dolomite	-2.9	-15.5		14.9	
	Lundstrøm	L2A	Mineralized brecciated quartz-carbonate vein	Dolomite	-3.7	-11.2		19.3	
		L2B	Mineralized brecciated quartz-carbonate vein	Dolomite	-3.5	-11.6		18.9	
		032A	Host rock dolomite	Dolomite	0.7	-13.8		16.7	
	Carbonate wall	0581A	Mineralized quartz-carbonate vein	Calcite	-0.6	-9.5	21.1		
		0581B	Massive dolomite	Dolomite	0.9	-9.3		21.4	
		0581C	Barren quartz-carbonate vein	Calcite	0.7	-10.0	20.6		
		042	Massive dolomite	Dolomite	1.3	-8.3		22.3	
		043	Barren calcareous shale	Calcareous shale	0.7	-9.8	20.8	20.8	
	Møllnes river	045	Barren layered dolomite	Dolomite	0.7	-14.8		15.7	
	Melsvik	001	Barren layered dolomite	Dolomite	1.3	-13.3		17.2	
		0012	Mineralized layered dolomite	Dolomite	0.5	-15.2		15.2	
	Mafic hosted	Kråknes	0045A	Mineralized brecciated quartz-carbonate vein	Dolomite	3.6	-16.8		13.6
		Mitchell	0571A	Mineralized calcite vein	Calcite	3.1	-18.3	12.0	
Wilson		020	Barren quartz-carbonate vein	Calcite	5.8	-18.4	12.0		
Carl Johan		013B	Mineralized quartz-carbonate vein	Calcite	5.6	-18.0	12.4		
		014	Mineralized quartz-carbonate vein	Calcite	5.9	-17.9	12.5		
		013C	Mineralized quartz-carbonate vein	Dolomite	5.7	-18.9		11.5	
Kåfjord bridge		0051B	Mineralized quartz-carbonate vein	Calcite	8.8	-18.1	12.3		
		0052	Nearly barren quartz-carbonate vein	Calcite	2.0	-18.0	12.4		

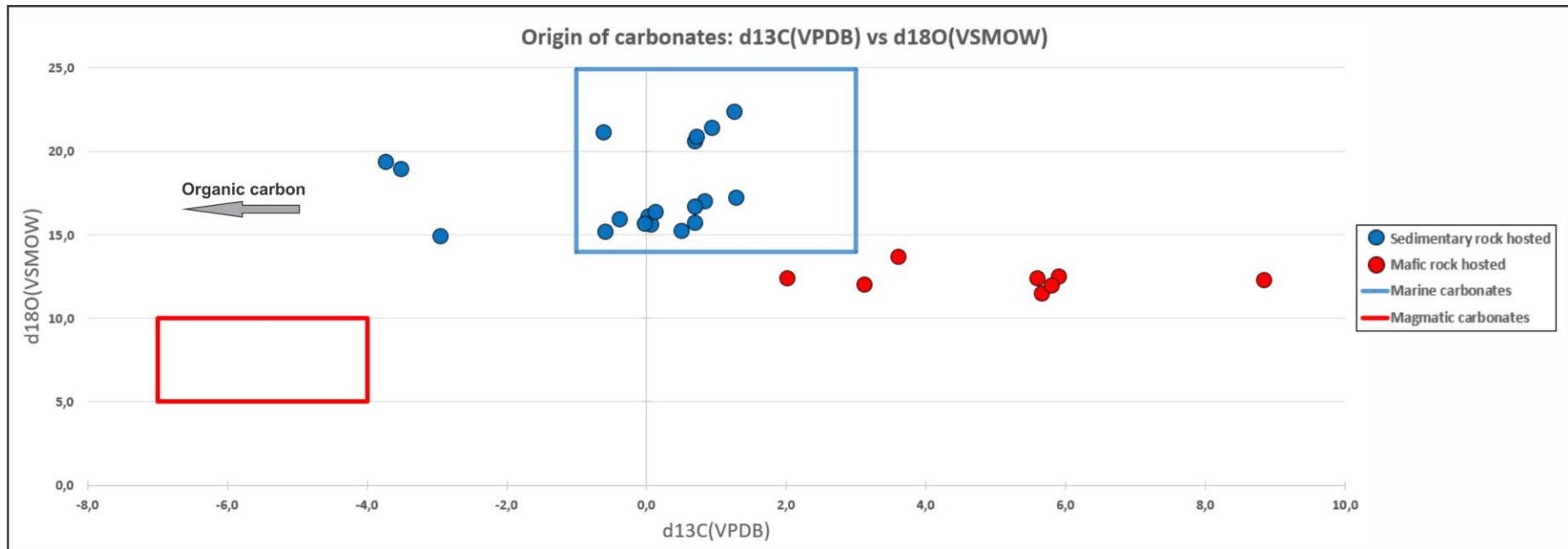


Figure 55: The $\delta^{18}\text{O}$ (VSMOW) vs. $\delta^{13}\text{C}$ (VPDB) plot. Typical values for marine carbonates are presented by the area of the blue box (data from Veizer and Hoefs (1976)), while magmatic carbonates usually overlap with the values represented by the red box (data from Stakes and O'Neil (1982)). The grey arrow indicates an influence of organic matter. VSMOW: Vienna Standard Mean Ocean Water, VPDB: Vienna Pee Dee Belemnite.

Quartz-carbonate veins hosted by mafic rocks of the Kvenvik formation contains carbonates characterized by relatively high $\delta^{13}\text{C}$ values (+2.0 to +8.8 ‰ VPDB; the mean value at +5.07 ‰ VPDB) and $\delta^{18}\text{O}$ values between +11.5 to +13.5 ‰ VSMOW with a mean value at +12.34 ‰ VSMOW.

Host rock carbonates in the Storviknes formation has $\delta^{13}\text{C}$ values ranging from -2.9 to +1.3 ‰ VPDB with a mean value at +0.4 ‰ VPDB, and $\delta^{18}\text{O}$ values from +14.9 to +22.3 ‰ VSMOW with a mean value at +19 ‰ VSMOW. Carbonates hosted in quartz-carbonate veins have $\delta^{13}\text{C}$ values from -3.7 to +0.7 ‰ VPDB with a mean value at -1.2 ‰ VPDB, and $\delta^{18}\text{O}$ values from +15.1 to +21.1 ‰ VSMOW with a mean value at 18.2 ‰ VSMOW.

4.4.2 Sulfur isotope composition of sulfides

A total of 20 spots from 12 sulfide-bearing samples at eight different localities have been drilled for sulfur isotope ($\delta^{34}\text{S}$) analyses. The sulfur isotopes are from different sulfides from mafic rock-hosted and sediment-hosted deposits (Table 19).

Table 19: All samples with delta 34 sulfur values in VDCT (Vienna-Canyon Diablo Troilite). Analysis of sulfur isotopes have been done in the lab in Switzerland except for two samples marked with * that have been analyzed at the Stable Isotope Laboratory of CAGE. These two samples from the lab at CAGE were analyzed by using 4 replicas of each sample (4x057B and 4x0571C). The average value ($\delta^{34}\text{S}$ -average) and standard deviation ($\delta^{34}\text{S}$ -STD) was calculated from these four replicas for both samples. Abbreviations: Bn: Bornite, Ccp: Chalcopyrite, Dg: Digenite, Py: Pyrite.

	Locality	Sample	Type	Mineralogy	$\delta^{34}\text{S}$ -average	$\delta^{34}\text{S}$ -STD
					per mil vs VCDT	
Sediment-hosted	Anna	0221A	Quartz-carbonate vein	Bn + minor Ccp	-7.08	0.10
		0221C	Quartz-carbonate vein	Ccp + minor Bn	-6.93	0.08
		0222B	Quartz-carbonate vein	Ccp	1.40	0.19
	Lundstrøm	L2	Brecciated quartz-carbonate vein	Bn + Dg	-7.09	0.03
		032B	Quartz-carbonate vein	Ccp	3.71	0.25
Mafic-hosted	Kråknes	0045B	Quartz-carbonate vein	Ccp	5.38	0.13
	Henning	047A	Shale	Py	-16.10	0.33
		047B	Shale	Py + minor Ccp	-16.27	0.52
		051A	Shale affected by mineralized qz-cb vein	Py + Ccp	5.13	0.11
		051B	Quartz-carbonate vein	Py + Ccp	3.72	0.40
	Mitchell	057	Quartz-carbonate vein	Ccp + minor Py	22.90	0.11
		0571B	Quartz-carbonate vein	Py + Ccp	16.88	0.36
		057B*	Quartz-carbonate vein	Ccp + minor Py	24.16	0.50
		0571C*	Quartz-carbonate vein	Py + Ccp	17.00	0.40
	Carl Johan	013A	Quartz-carbonate vein	Py + minor Ccp	9.57	0.03
	Innerstrømmen	060A	Quartz-carbonate vein	Ccp	13.34	0.47
		060B	Basalt	Ccp + minor Py	9.88	0.01
		060C	Shale	Ccp	9.58	0.24
	Kåfjord bridge	0051A	Quartz-carbonate vein	Py	2.18	0.27
		0051C	Quartz-carbonate vein	Py (pure crystal)	3.76	0.18

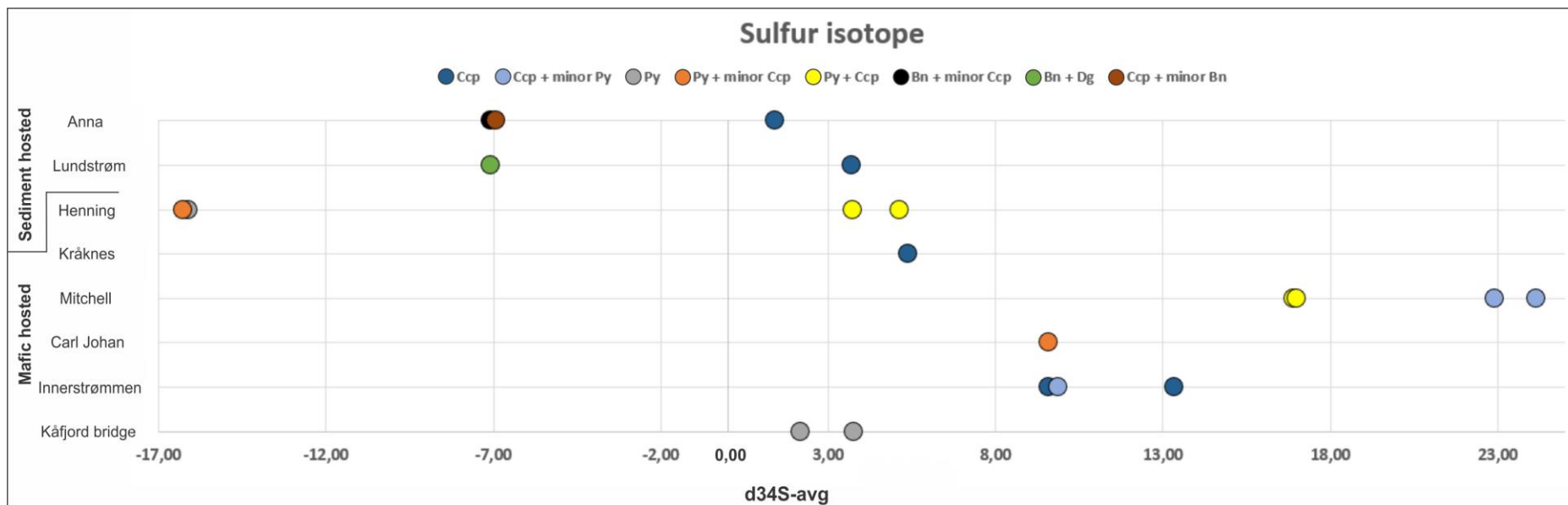


Figure 56: $\delta^{34}\text{S}$ (VCDT) of different minerals plotted against different localities. Some points are of two minerals which are due to intergrowth. Abbreviations: Ccp: Chalcopyrite, Py: Pyrite, Bn: Bornite, Dg: Digenite.

All sulfides hosted by mafic rocks of the Kvenvik formation related to quartz-carbonate veins have positive $\delta^{34}\text{S}$ values, with an average value of +11.04 ‰ VCDT. Sample 0051A from locality Kåfjord bridge has the lightest $\delta^{34}\text{S}$ composition with values of +2.18 and +3.76 ‰ VCDT. The Mitchell mine has the heaviest $\delta^{34}\text{S}$ composition (sample 057 & 057B) with values of +22.90 and +24.16 ‰ VCDT, respectively. Two other samples from the same locality (0571B & 0571C) are also significantly heavy with $\delta^{34}\text{S}$ values of +16.88 and +17.00 ‰ VCDT, respectively.

The stratiform type of Cu mineralization (sample 047; the Henning mine) is characterized by a strong depletion in ^{34}S . The analyzed samples (047A and 047B) of pyrite, and pyrite with minor amounts of chalcopyrite, shows values of -16.10 and -16.27 ‰ VCDT, respectively. Sulfides hosted by a quartz-carbonate at the same locality (samples 051B & 051A) reflect significantly higher $\delta^{34}\text{S}$ values (+3.72 and +5.13 ‰ VCDT, respectively).

Sulfides from the sediment-hosted localities (all within quartz-carbonate veins) show a wide span of their sulfur isotope compositions. The obtained values range from -7.08 to +3.71 ‰ VCDT with an average of -3.20 ‰ VCDT (Table 19; Figure 56).

4.5 Fluid inclusion study

Five representative samples for fluid inclusion studies were selected to identify the properties of the ore-forming fluids. This included one sample from Kvenvik formation, three samples from Storviknes formation, and one sample from Skoadduvarri formation. The samples were selected with care as many samples were unsuitable, mainly due to low transparency (milky quartz and carbonates). A total of 87 fluid inclusions within 23 fluid inclusion assemblages (Appendix G) have been analyzed within these five samples.

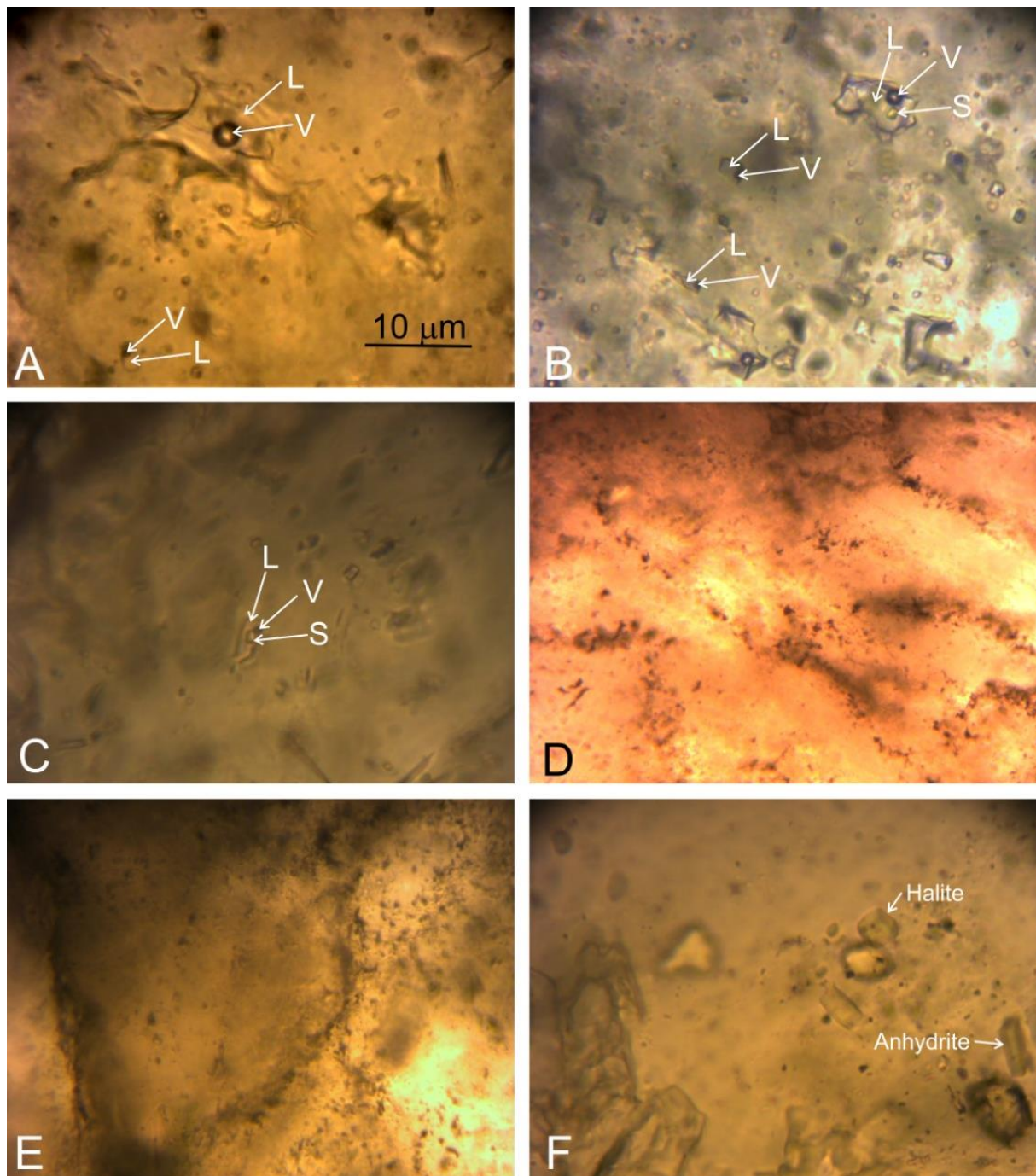


Figure 57: (A) Two-phase, L+V, fluid inclusions hosted by quartz (and carbonate) at sediment-hosted locality Anna (sample 040); (B) Coexisting two-phase, L+V, and three-phase, L+V+S, fluid inclusions hosted by quartz (and carbonate) at the sediment-hosted locality Lundstrøm (sample 034); (C) Three-phase, L+V+S, fluid inclusions hosted by calcite at the gabbro-hosted locality Kåfjord bridge (sample 0052); (D) Irregular inclusions with decrepitation haloes in sediment-hosted quartz-carbonate veins in Skoadduvarri formation (sample 030); (E) Irregular inclusions with decrepitation haloes hosted by quartz (and carbonate) at the sediment-hosted locality Anna (Sample 0221); (F) Solid inclusions of predominantly halite and anhydrite hosted by quartz (and carbonate) at the sediment-hosted locality Anna (sample 0221). The scale in figure A is the same for all figures. Abbreviations: L: liquid, V: vapor, S: solid.

Table 20: A summary of the results from the fluid inclusion study shown by minimum and maximum recorded values. One fluid inclusion in a fluid inclusion assemblage*. Abbreviations: L+S/L+V: Changed phase to L+S or L+V during heating, T_e : First melting temperature, $T_{m\text{ ice}}$: Final ice melting temperature, T_s : Final halite temperature, T_h : Homogenization temperature

Formation	Locality	Sample	Fluid inclusion type	Phases (room temp.)	T_e (°C)	Compositi-on	Salinity (wt.% NaCl equ.)	NaCl / (NaCl+ CaCl ₂)	Density (g/cm ³)	$T_{m\text{ ice}}$ (°C)	T_s (°C)	T_h (°C)	Homogeniza-tion mode	dP/dT (bar/°C)
Skoaddu-varri	Skoaddu-varri	030	1	L+V	-52	NaCl-CaCl ₂ -H ₂ O	27.1-27.5	0.62-0.66	~1.1	-24.5 to -25.5	+5.6 to +16	215-225	L+V → L	18.34-18.86
					-21	NaCl-H ₂ O	26.3	1	~1.1	-	+5 to +15	122-200	L+V → L	19.66-24.50
			3	-	-	-	-	-	-	-	-	-	-	-
Storviknes	Lundstrøm	034	1	L+V	-52	NaCl-CaCl ₂ -H ₂ O	27.1-27.4	0.64-0.65	~1.1	-25	+3.5 to +15	217-222	L+V → L	18.44-18.70
					-21	NaCl-H ₂ O	5-7.9	1	~1.0	-3 to -5	-	125-135	L+V → L	19.16-20.37
			2	L+V+S	-52	NaCl-CaCl ₂ -H ₂ O	33.5-40.2	-	1.1 – 1.2	-	+230 to +315	217-230	L+V+S → L+S → L (L+V+S → L)*	18.40*
			3	-	-	-	-	-	-	-	-	-	-	-
	Anna	0221	1	L+V	-21	NaCl-H ₂ O	6.4-6.7	1	~1.0	-4 to -4.2	-	118-122	L+V → L	20.40-20.64
			2	L+V+S	-52	NaCl-CaCl ₂ -H ₂ O	29.5-30.1	-	~1.1	-	+145 to +160	192-212	L+V+S → L+V → L	19.05-20.03
			3	-	-	-	-	-	-	-	-	-	-	-
			4	-	-	-	-	-	-	-	-	-	-	-
		040	1	L+V	-23	NaCl-H ₂ O	26.3-26.5	1	~1.1	-	+10 to +25	212-230	L+V → L	18.01-18.99
			2	L+V+S	-52	NaCl-CaCl ₂ -H ₂ O	29.7-29.9	0.71-0.72	~1.1	-25	+150 to +155	230-235	L+V+S → L+V → L	18.00-18.23
Kvenvik	Kåfjord bridge	0052	2	L+V+S	-52	NaCl-CaCl ₂ -H ₂ O	31.9-34.7	-	~1.1	-	+200 to +247	212-225	L+V+S → L+S/L+V → L	L+S: 19.45-20.91 L+V: 18.66-19.06

4.5.1 Petrographic and microthermometric description

The petrographic study revealed the following types of fluid inclusions, based on their phase relationship at room temperature: 1) Type 1 – two-phase L+V fluid inclusions; 2) Type 2 – three-phase L+V+S fluid inclusions; 3) Type 3 – fluid inclusions that reflect post-entrapment re-equilibration, particularly decrepitation and the formation of relict inclusions arranged on linear arrays together with trails of neonates and; 4) Type 4 – solid monophasic inclusions, where L stands for liquid, V for vapor and S for solid (Figure 57; Table 20).

4.5.1.1 Sediment-hosted

Sample 030

Sample 030 (Figure 57D; hand sample Figure 51C) from the Skoadduvarri sandstone is a barren quartz-carbonate vein associated with chlorites. Quartz hosts numerous trails with decrepitated fluid inclusion as well as clusters of two-phase, L+V, inclusions that mostly occur within isolated clusters. The two-phase inclusions show irregular shapes and range in size up to 15 μm . Upon freezing at -60°C , fluid inclusions became light brownish with a vaguely granular texture. According to their first melting (T_e) temperatures, fluid inclusions can be subdivided into two subgroups: 1) Fluid inclusions with T_e around -52°C and 2) Fluid inclusions with T_e around -21°C .

The first melting around -52°C suggests NaCl and CaCl_2 as the principal dissolved salts (Borisenko, 1977). In this subgroup of inclusions, the final ice melting ($T_{m\text{ ice}}$) is recorded in the temperature interval between -24.5 and -25.5°C . Hydrohalite is transformed to halite around 0°C , and the final halite temperature (T_s) is recorded between $+5.6$ and $+16^{\circ}\text{C}$. The bulk salinity ranges between 27.1 and 27.5 wt.% NaCl equ., with the $\text{NaCl}/(\text{NaCl}+\text{CaCl}_2)$ ratio between 0.62 and 0.66. Homogenization to the liquid phase occurs between 215 and 225°C . The calculated bulk density is $\sim 1.1\text{ g/cm}^3$.

The first melting around -21°C suggests NaCl as the principal dissolved salt (Borisenko, 1977). In this subgroup of inclusions, hydrohalite is also transformed to halite around 0°C and the final halite temperature (T_s) is recorded between $+5$ and $+15^{\circ}\text{C}$, suggesting the bulk salinity around 26.3 wt.% NaCl equ. Homogenization to the liquid phase occurs between 122 and 200°C , and the calculated density is $\sim 1.1\text{ g/cm}^3$.

Sample 034

Sample 034 (Figure 57B; hand sample Figure 43D) is a mineralized quartz-carbonate vein associated with chlorites and hosted by dolomite at the Lundstrøm Cu deposit. The main Cu minerals are bornite and digenite. Quartz hosts numerous trails with decrepitated fluid inclusion and clusters of three-phase, L+V+S, and two-phase, L+V, fluid inclusions.

The three-phase fluid inclusions show T_e around -52°C , suggesting the NaCl-CaCl₂-H₂O system with NaCl and CaCl₂ as principal dissolved salts. In some larger inclusions of this type, the transition from hydrohalite to halite is visible around 0°C . During the heating experiments, the vapor bubbles disappear in the temperature range between 217 and 230°C , and the total homogenization by halite crystal dissolution is recorded between 230 and 315°C . The bulk salinity spans from 33.5 and 40.2 wt.% NaCl eq. The calculated density varies between 1.1 and 1.2 g/cm³. One inclusion shows simultaneous disappearance of vapor and solid phases at 230°C (L+V+S \rightarrow L).

According to their T_e , the two-phase inclusions can be subdivided into two subgroups: 1) Fluid inclusions with T_e around -52°C and 2) Fluid inclusions with T_e around -21°C . The inclusions with T_e around -52°C (NaCl-CaCl₂-H₂O) have $T_{m\text{ ice}}$ and T_s recorded at -25.0°C and between $+3.5$ and 15°C , respectively, reflecting the bulk salinity of 27.1 - 27.4 wt.% NaCl equ. and the NaCl/(NaCl+CaCl₂) ratio of 0.64 to 0.65 . The total homogenization into the liquid phase occurs between 217 and 222°C . The calculated bulk density is ~ 1.1 g/cm³. The fluid inclusions with T_e around -21°C (NaCl-H₂O) are characterized by $T_{m\text{ ice}}$ between -3.0 and -5.0°C , corresponding to the bulk salinity between 5.0 and 7.9 wt.% NaCl equ. The homogenization to the liquid phase is recorded in the temperature range between 125 and 135°C . The calculated density is ~ 1.0 g/cm³.

Sample 0221

Sample 0221 (Figure 57E & F; hand sample Figure 38C) is represented by a mineralized quartz-carbonate vein hosted by dolomite at the Anna Cu deposit. The main Cu minerals are bornite and chalcopyrite. Trails of decrepitated fluid inclusions are common in quartz and carbonates. Clusters of three-phase, L+V+S, and two-phase, L+V, fluid inclusions are often associated with solid halite inclusions.

The two-phase fluid inclusions can be assigned the NaCl-H₂O system composition based on the first melting temperature occurring at -21°C , suggesting NaCl as the principal dissolved

salt. Homogenization temperature for two-phase L+V fluid inclusions occurs between 118 to 122°C with a $T_{m\ ice}$ ranging from -4 to -4.2°C, salinity is ranging from 6.4 to 6.7 wt.% NaCl equ. and the calculated density is $\sim 1.0\text{ g/cm}^3$.

The first melting temperature for three-phase fluid inclusions is at -52°C, which can assign NaCl and CaCl₂ as the principal dissolved salts. Homogenization temperature for three-phase L+V+S fluid inclusions is 192 to 212°C. Salinity ranges from 29.5 to 30.1 wt.% NaCl equ. Final halite temperature (T_s) occurs between 145 to 160°C, and the calculated density is $\sim 1.1\text{ g/cm}^3$.

Sample 040

Sample 040 (Figure 57A; hand sample Figure 41B) is represented by a mineralized quartz (-carbonate) vein at the sediment-hosted locality Anna. Two types of fluid inclusions were identified in this sample. These two types are two-phase L+V fluid inclusions and three-phase L+V+S fluid inclusions.

First melting temperature for the two-phase inclusions occurs at -23°C, which means it can be assigned NaCl as the principal dissolved salt. T_s occur between 10 to 25°C with a homogenization temperature between 212 to 230°C. Salinity is ranging between 26.3 to 26.5 wt.% NaCl equ. and the density is calculated to be $\sim 1.1\text{ g/cm}^3$.

First melting temperature for the three-phase inclusions occurs at -52°C, which assigns it to NaCl and CaCl₂ as principal dissolved salts. The final ice melting temperature ($T_{m\ ice}$) occurs at -25°C. Homogenization temperature is measured to be between 230 to 235°C with a final halite temperature (T_s) at 150 to 155°C. NaCl/(NaCl+CaCl₂) is calculated to a ratio between 0.71-0.72 and a salinity of 29.7 to 29.9 wt.% NaCl equ. Density is calculated to be $\sim 1.1\text{ g/cm}^3$.

4.5.1.2 Mafic rock-hosted

Sample 0052

Sample 0052 (Figure 57C; hand sample Figure 19D) is represented by a nearly barren calcite vein hosted by gabbro at the Kåfjord bridge locality. One type of fluid inclusion could be observed based on petrography and is three-phase L+V+S fluid inclusions.

First melting temperature occurs at -52°C, which suggests NaCl and CaCl₂ as the principal dissolved salts. T_s , final halite temperature occurs between 200 to 247°C. Salinity is ranging

between 31.9 to 34.7 wt.% NaCl equ. Density is calculated to be $\sim 1.1 \text{ g/cm}^3$, and the homogenization temperature occurs between 212-225°C.

In addition to this sample, another sample in the Kvenvik formation from locality Innerstrømmen was prepared for the fluid inclusion study. This is sample 060 (Figure 22D) representing a mineralized quartz-carbonate vein hosted by basalt, but no measurements were obtained as there were only observed decrepitated fluid inclusions.

5 Discussion

5.1 The mineral assemblages

The Cu mineralization in the Kåfjord area has been found in the Kvenvik and Storviknes formations (Figure 4). The mineralization occurs predominately in forms of quartz-carbonate veins. In the Kvenvik formation, the mineralized quartz-carbonate veins are hosted by basaltic tuffs and tuffites, basalts and gabbro, and therefore this type of mineralization has been classified as the mafic rock-hosted Cu mineralization. In addition to the quartz-carbonate veins, a basaltic tuff/tuffite hosted stratiform mineralization was found at the Henning mine (Figure 32, Figure 4). Sedimentary lithologies (carbonates and shales) of the Storviknes formation, which stratigraphically lies above the Kvenvik formation, also host mineralized quartz-carbonate veins. This type of mineralization has been classified as the sediment-hosted Cu mineralization. As summarized in Figure 58, the mafic rock-hosted and sediment-hosted types of Cu mineralization show a significant difference in their mineral assemblages.

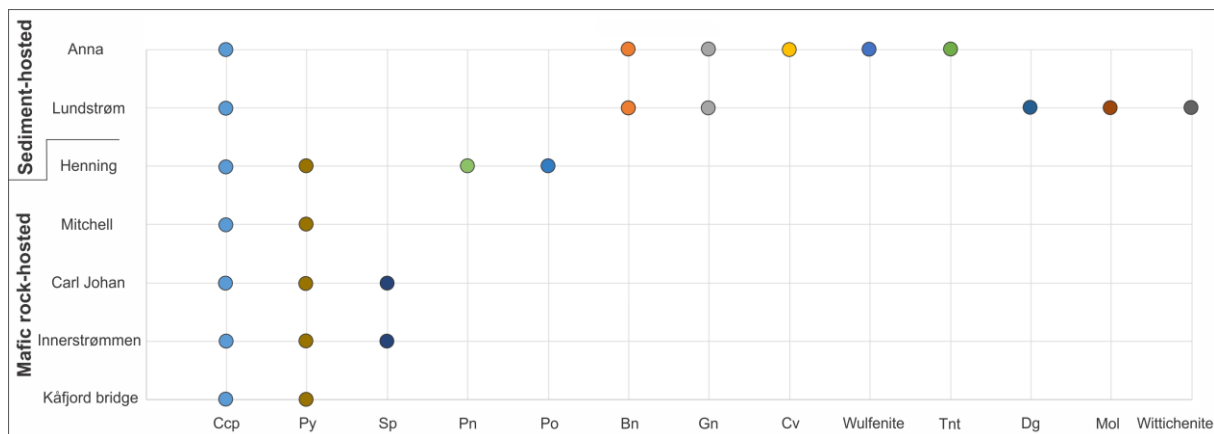


Figure 58: Ore mineral distribution at different localities in the study area. Abbreviations: Ccp: Chalcopyrite, Py: Pyrite, Sp: Sphalerite, Pn: Pentlandite, Po: Pyrrhotite, Bn: Bornite, Gn: Galena, Cv: Covellite, Tnt: Tennantite, Dg: Digenite, Mol: Molybdenite.

Chalcopyrite is the only ore mineral found in both types of mineralization. Pyrite is relatively abundant in mafic rock-hosted mineralization, but it is absent from the sediment-hosted mineral assemblages. Sphalerite is found in association with two mafic rock-hosted localities (Carl Johan & Innerstrømmen), and pentlandite and pyrrhotite have been found only in the stratiform mineralization (Henning mine; sample 047). In contrast to the mafic rock-hosted mineralization, the sediment-hosted localities are characterized by more complex sulfide mineral assemblages that often contain bornite, digenite, galena, covellite, wulfenite, tennantite, molybdenite, and wittichenite (Figure 58).

In addition to the different composition of their mineral assemblages, the mafic-rock hosted and the sediment-hosted mineralization differs in their major element composition (Figure 59).

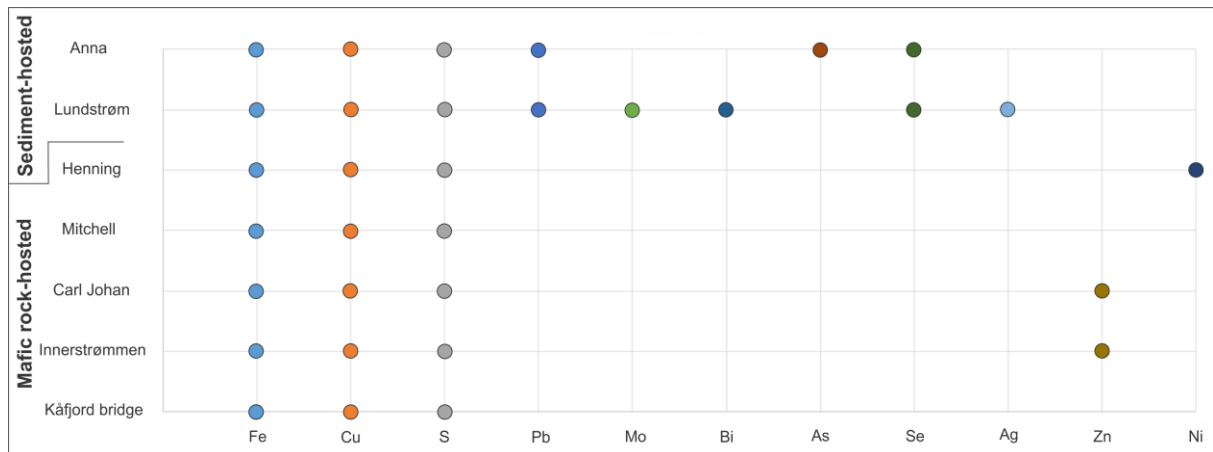


Figure 59: Elements associated with selected minerals identified at different localities in the study area, from Figure 58. Fe, Mo, and Ni are siderophile elements, while Cu, S, Pb, Bi, As, Se, Ag, and Zn are chalcophile elements.

Iron, Cu, and S are abundant elements in both mafic rock-hosted and sediment-hosted types of mineralization. Zinc and Ni are restricted to mafic rock-hosted localities only, with Zn related to quartz-carbonate veins and Ni related to the stratiform mineralized sample. Lead, Mo, Bi, As, Se and Ag are restricted to sediment-hosted deposits.

Combining the characteristics of Cu-bearing mineral assemblages and their spatial and temporal relationship with their host rocks, the mineralization in the Kåfjord area, AKTW, can be divided into 6 main types of mineralization.

- 1) Syngenetic mineralization of a stratiform type associated with basaltic tuff/tuffite of the Kvenvik formation (the Henning mine; sample 047) predominantly composed of pyrite, chalcopyrite, pyrrhotite and pentlandite (Figure 60A; Figure 32).
- 2) Epigenetic quartz-carbonate veins hosted by gabbro of the Kvenvik formation (the Kåfjord bridge locality; sample 0051), with pyrite as the main sulfide mineral (Figure 60B; Figure 19).
- 3) Epigenetic quartz-carbonate veins hosted by basaltic tuffs/tuffites, basalts and gabbro of the Kvenvik formation (localities of Innerstrømmen, Carl Johan, Mitchell & Henning mines; samples 060, 013, 014, 057, 0571 & 051) with pyrite and chalcopyrite as the main sulfide phases and variable amounts of sphalerite (Figure 60C).

- 4) Epigenetic quartz-carbonate veins hosted by carbonates of the Storviknes formation (the Anna & Lundstrøm mines; samples 0221, 0222 & 032) with chalcopyrite as the main sulfide phase and variable amounts of bornite, covellite and galena (Figure 60D; Type 4.1). Most of the quartz-carbonate veins of this subtype reflect a brittle regime during their emplacement, but locally ductile deformed bedding-parallel quartz-carbonate veins are found (Figure 60E; Type 4.2).
- 5) Epigenetic quartz-carbonate veins hosted by shale of the Storviknes formation (the Anna mine; sample 040) with chalcopyrite, selenium-rich galena, tennantite and wulfenite (Figure 60F).
- 6) The brecciated epigenetic mineralization hosted by carbonates and shales of the Storviknes formation (the Lundstrøm mine; samples L1 & L2) with digenite, bornite, molybdenite, wittichenite, Se-rich galena, Se-Cu-rich galena and Se-Ag-Cu-rich galena (Figure 60G).

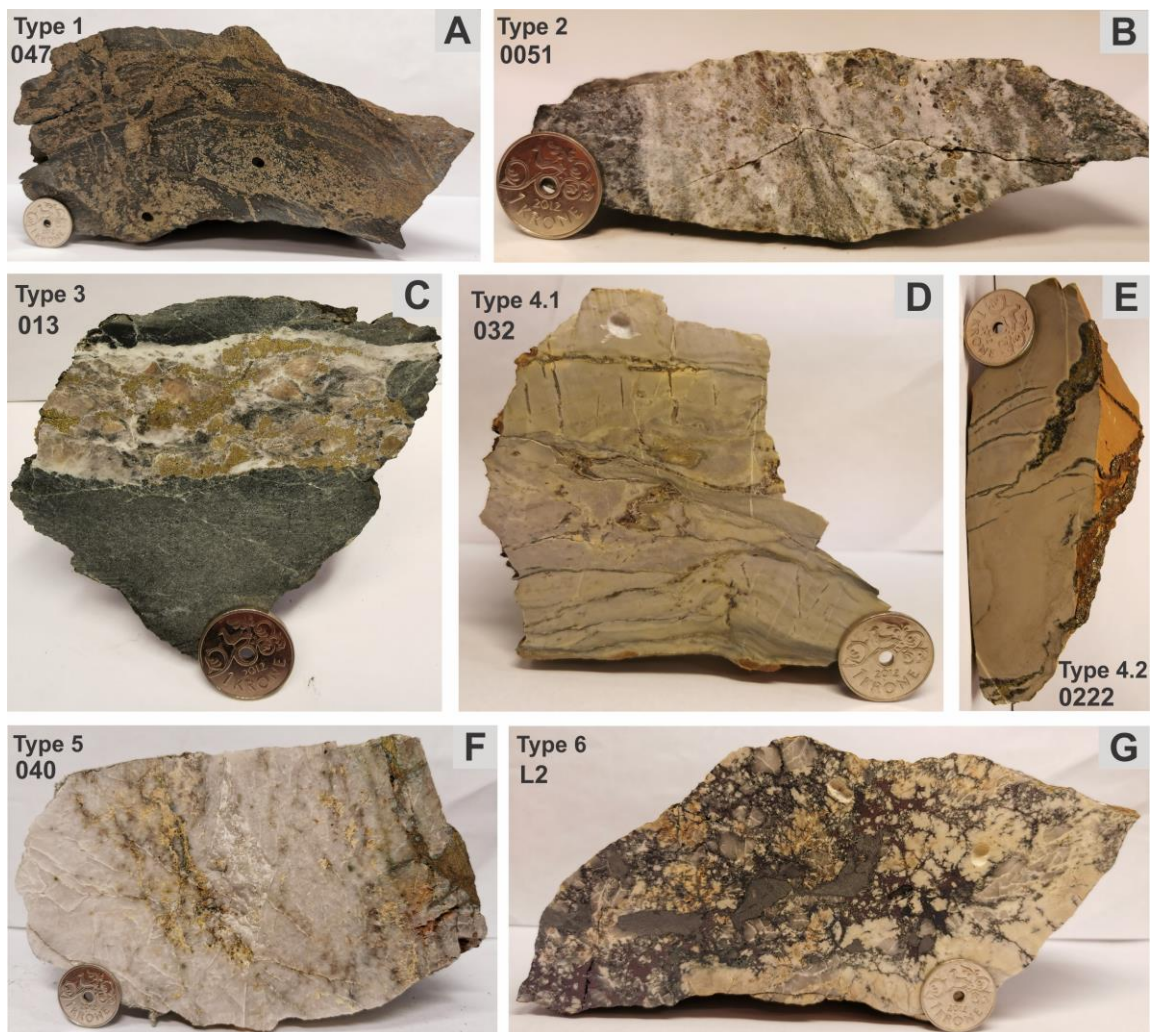


Figure 60: Different types of the Cu mineralization in the Kåfjord area of AKTW. (A) Type 1 stratiform pyrite+chalcopyrite+pyrrhotite+pentlandite mineralization; (B) Type 2 pyrite mineralization in qt-cb vein; (C) Type

3 pyrite+chalcopyrite±sphalerite mineralization in qt-cb vein; (D) Type 4.1 bedding-parallel chalcopyrite mineralization in qt-cb vein; (E) Type 4.2 chalcopyrite+bornite±covellite±galena mineralization in qt-cb vein; (F) Type 5 chalcopyrite+Se-rich galena+tennantite+wulfenite mineralization in qt-cb vein; (G) Type 6 digenite+bornite±molybdenite±wittichenite±Se-rich-galena±Se-Cu-rich galena±Se-Ag-Cu-rich galena mineralization in brecciated qt-cb vein. Abbreviations: Qt-cb: Quartz-carbonate vein.

All Cu mineralization found in the Kvenvik and Storviknes formations, with the exception of the stratiform mineralization found at the Henning mine, is related to quartz-carbonate veins with varying amounts of quartz and carbonates. Some veins are nearly only composed of carbonates, while others contain mostly quartz. The variations in the quartz-carbonate relationship are to some extent, stratigraphically controlled. Veins composed predominantly of carbonates are associated with the stratigraphically lowermost units (the Kåfjord bridge locality & Innerstrømmen mine). Veins composed of approximately equal amounts of quartz and carbonates are found at the Carl Johan mine (sample 014), Kråknes locality and Henning mine i.e. within the stratigraphically middle part of the mineralized complex. Veins composed mostly of quartz are found at the Anna mine, Lundstrøm mine (sample 032) and the Skoadduvarri locality i.e. they are spatially associated with the stratigraphically uppermost units (Figure 10).

5.1.1 Mafic rock-hosted Cu mineralization

5.1.1.1 Stratiform mafic rock-hosted Cu mineralization

The stratiform mineralization associated with basaltic tuff/tuffites and shales of the Kvenvik formation (the Henning mine locality; Sample 047, Figure 32E) has a syngeneic character which indicates that this type of Cu mineralization was deposited simultaneously with the mafic rocks of the Kvenvik formation. The Kvenvik formation has been recognized as a product of multiple eruptions of basaltic lava in a terrestrial to shallow-water environment during an intracratonic rifting phase in the Archean basement at the Fennoscandian Shields margin (Bergh & Torske, 1988).

The new lithogeochemical data obtained from basalts and gabbro in the Kvenvik formation (Table 15) are in agreement with previously published studies (Bergh & Torske, 1986, 1988), reflecting their tholeiitic character (Figure 61).

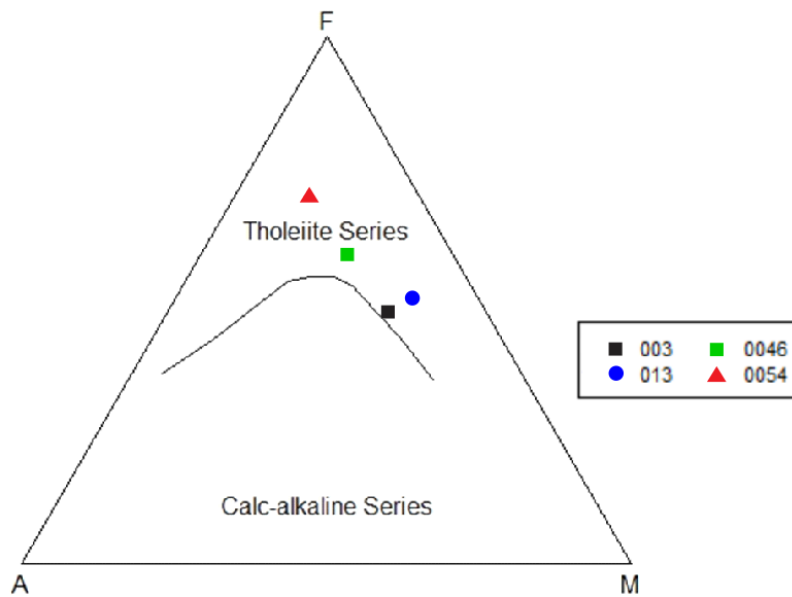


Figure 61: AFM plot from Irvine and Baragar (1971) with four samples plotted. A: Na₂O + K₂O, F: FeO, M: MgO, 003: Basalt, 013: Picrobasalt, 0046: Basaltic tuff/tuffite, 0054: Monzogabbro.

As the study area has undergone a low-grade greenschist metamorphism that could have affected the original elemental composition of the analyzed mafic rocks, a set of discriminant diagrams based on immobile elements have been used to estimate a primary geotectonic setting of the Kvenvik formation. The Th/Nb vs. La/Yb and Ti vs. V diagrams revealed the MORB character of all four analyzed samples (Figure 62).

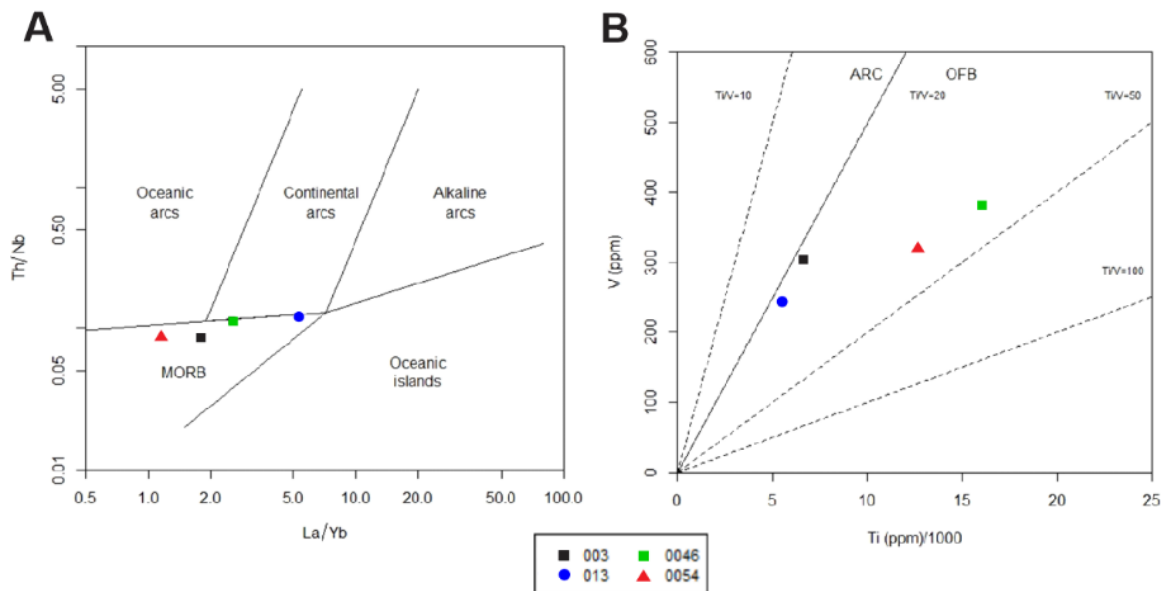


Figure 62: (A) Th/Nb vs. La/Yb plot from Hollocher et al. (2012) with four samples plotted. (B) Ti vs. V plot from Shervais (1982) with four samples plotted. OFB: Ocean floor basalt (MORB), ARC: Island arc. 003: Basalt, 013: Picrobasalt, 0046: Basaltic tuff/tuffite, 0054: Monzogabbro.

In addition, geotectonic plots based on the logarithmic ratio of five immobile high-field-strength elements (La, Sm, Yb, Nb, & Th) proposed by Agrawal et al. (2008) also classified all analyzed rocks to the MORB field (Figure 63).

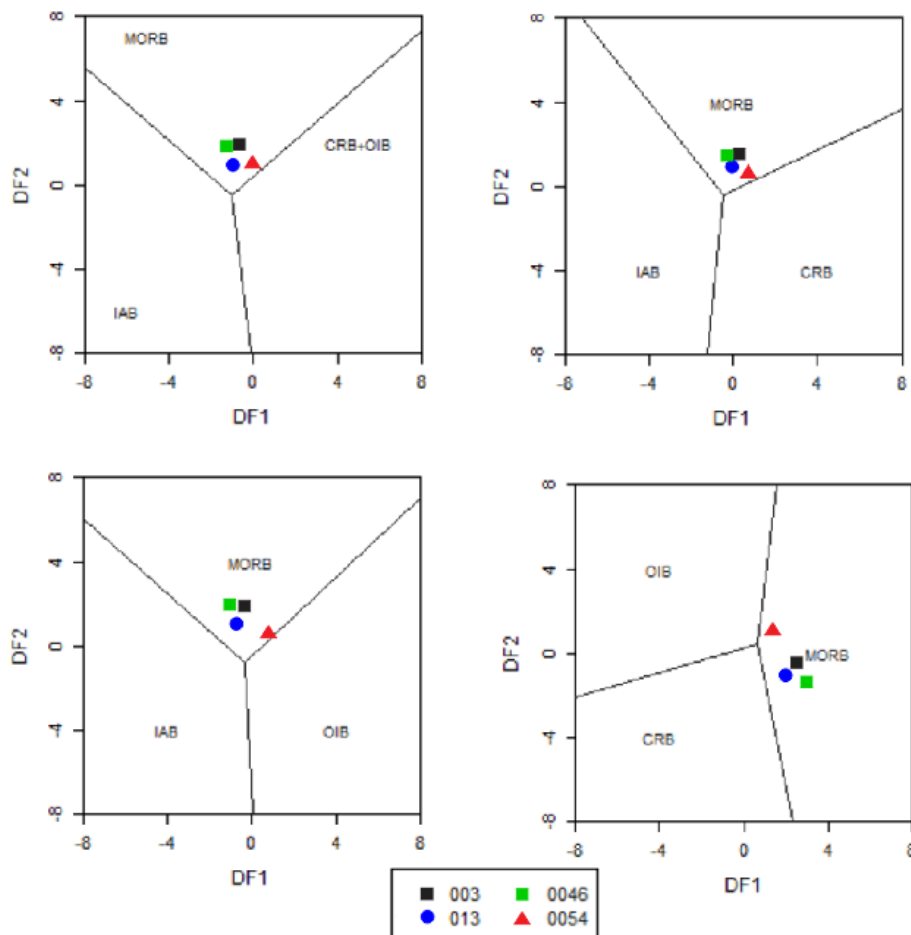


Figure 63: Four geotectonic plots from Agrawal et al. (2008) with four samples plotted. IAB: Island-arc basic rock, CRB: Continental rift basic rock, OIB: Ocean island basic rock, MORB: Mid-oceanic ridge basic rock, 003: Basalt, 013: Picrobasalt, 0046: Basaltic tuff/tuffite, 0054: Monzogabbro

A spider plot of Boynton (1984) has been used to reveal different REE patterns (Figure 64). Samples 003 and 0046 (barren country rocks) show nearly flat patterns. The barren basalt (sample 003) is slightly enriched in LREE (light rare earth elements) comparing to HREE (heavy rare earth elements). In contrast, the barren tuff/tuffite sample (sample 0046) shows a slight depletion in LREE compared to HREE, which is a common MORB pattern. Sample 0054 (host gabbro) has a positive slope of LREE and a negative slope of HREE, and a pronounced positive Eu anomaly. Sample 013 (host basalt) is characterized by a high LREE/HREE ratio indicating hot spot origin, and a strong negative Eu anomaly. All analyzed samples display a weak negative Ce anomaly. The general depletion of Ce can be explained by an enrichment of Ce in ferromanganese nodules on the seafloor (Nath et al., 1994). The

positive Eu anomaly in sample 0054 (gabbro) is controlled by a high abundance of Ca-plagioclases (Lesnov, 2010, p. 209), while the negative Eu anomaly in sample 013 (basalt) reflects that crystallization of the basalt followed the fractional crystallization of Ca-plagioclase.

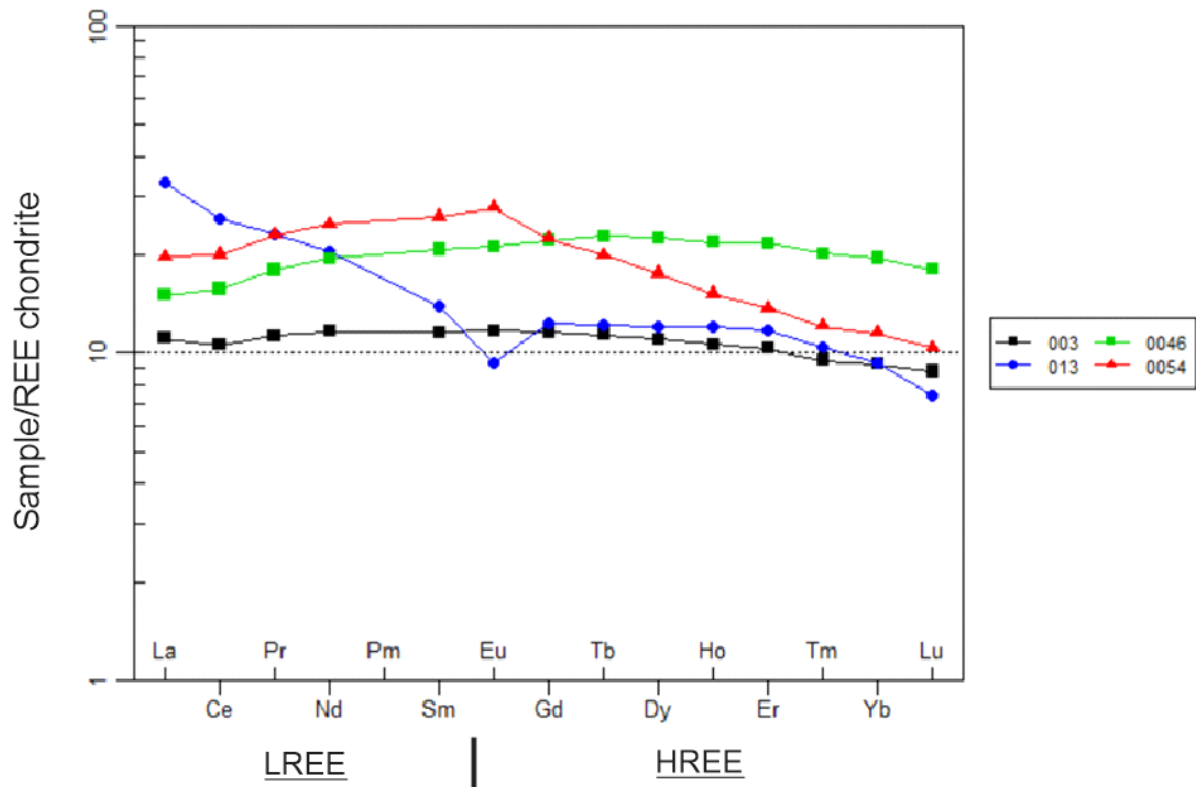


Figure 64: Spider-plot modified from Boynton (1984) with concentrations of REE on the y-axis and the different REE on the x-axis. 003: Basalt, 013: Picobasalt, 0046: Basaltic tuff/tuffite, 0054: Monzogabbro.

Pyrite is the most abundant ore mineral in the studied stratiform mineralization. It is accompanied by variable amounts of chalcopyrite, pyrrhotite and pentlandite. Minor amounts of rutile and ilmenite have also been recorded (Figure 33B, D & E). Pentlandite intergrowth with pyrrhotite and pyrite has been found as a common feature (Figure 33F).

Trace elements of stratiform chalcopyrite are similar to chalcopyrite found in the epigenetic quartz-carbonate veins (Figure 52), with an exception for Cr which shows a slight enrichment in the stratiform chalcopyrite (up to 16.39 ppm) comparing to epigenetic chalcopyrite (up to 12.22 ppm). Trace elements in stratiform pyrite show similar characteristics of Pb, Ni, Co, Te, Se and Cd compared to mafic rock-hosted epigenetic pyrite. A slight enrichment in Zn, Cr and As, and a depletion in Hg, Sb, Au and Ag are also observed. Trace element characteristics of rutile show a general enrichment of many elements compared to the mafic rock-hosted quartz-carbonate veins in the boxplots (Figure 53). These elements include P, Nb, Sn, Cr, W,

V and Ta. The elements Pb, Zn, Co, Ni, Se and As in the stratiform mineralization follow the range within the mafic rock-hosted quartz-carbonate veins while Hg, Ag, and Au are slightly depleted. As seen, Cr is also enriched in rutile, which gives a trend for enrichment of Cr in general in chalcopyrite, pyrite and rutile compared to all other mafic rock-hosted deposits.

The stratiform mineralization at the Henning mine is characterized by negative $\delta^{34}\text{S}$ values (Table 19), reflecting a strong enrichment in ^{32}S . These negative values suggest an influence of sulfate-reducing bacteria that reduced isotopically heavy marine sulfate to light hydrogen sulfide by the process of kinetic fractionation (Seal, 2006). The stratiform mineralization textures indicate that sulfide minerals could have been deposited simultaneously with bacterial activity (Figure 32E). The rutile-ilmenite occurs as “bands”, and does also follow this stratiform pattern of pyrite (Figure 33B).

Textural, mineralogical and stable isotope features, accompanied by the lithogeochemical character of the host rocks, suggest that the stratiform mineralization at the Henning mine belongs to a group of volcanogenic massive sulfide (VMS) ore deposits (Figure 12A; Laurence, 2020). VMS deposits have not been recognized so far in AKTW, but they are a well-known type of mineralization in the Fennoscandian Shield (Weihed et al., 2005). Anyhow, the major episode of deposition of VMS deposits in the Fennoscandian Shield occurred between 1.97-1.88 Ga (Weihed et al., 2005). This does not correspond to the age of the stratiform mineralization in the studied area, which has been formed between ~ 2220 and 2146 ± 5 Ma according to the Lomagundi-Jatuli Event recorded in the carbonates of the Kvenvik formation and dating of the gabbro (Melezhik et al., 2015).

5.1.1.2 Epigenetic mafic rock-hosted Cu mineralization

The great majority of Cu mineralization in the Kvenvik formation occurs in the form of epigenetic quartz-carbonate veins that are hosted by gabbro, basalts and basaltic tuffs and tuffites (Figure 25A & B; Figure 29A & B; Figure 36A).

Although chalcopyrite has been found at all studied localities in the Kåfjord area, it must be emphasized that the quartz-carbonate veins hosted by gabbro at the Kåfjord bridge locality are generally lacking chalcopyrite. Anyhow, chalcopyrite is relatively abundant in the host gabbro, where it mostly occurs along grain boundaries of host rock minerals (sample 0054; Figure 20D). Trace element composition of this chalcopyrite and chalcopyrite grains disseminated in basalts at the Carl Johan mine (sample 013B; Figure 25C) show enrichment

in Se and depletion in Pb compared to chalcopyrite found in different quartz-carbonate veins in the study area (Figure 66).

The quartz-carbonate veins hosted by basalts and basaltic tuffs and tuffites may contain two different types of chalcopyrite (Figure 65):

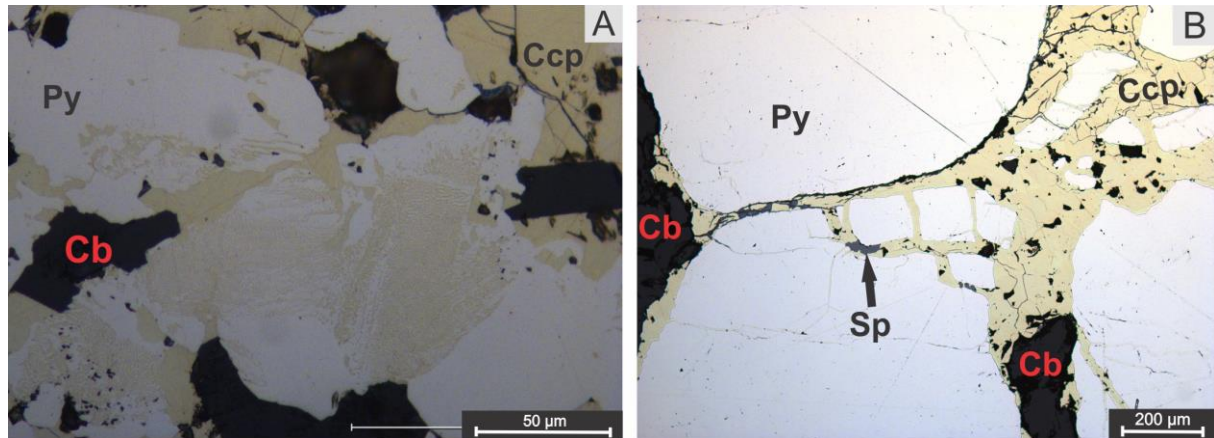
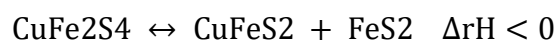


Figure 65: (A) Type 1 chalcopyrite showing an immiscible texture formed by pyrite and chalcopyrite interaction (from thin section 0571, Mitchell); (B) Type 2 chalcopyrite showing brecciated clasts of pyrite (from thin section 013A, Carl Johan). Abbreviations: Py: Pyrite, Ccp: Chalcopyrite, Sp: Sphalerite, Cb: Carbonate mineral.

- Type 1 chalcopyrite occurs as exsolution with anhedral-shaped pyrite crystals (Figure 31C; Figure 65A).
- Type 2 chalcopyrite infiltrates and cements brecciated clasts of anhedral to subhedral-shaped pyrite (Figure 26B; Figure 65B).

The observed textural characteristics indicate that Type 1 chalcopyrite is a product of exsolution from an originally Cu-rich sulfide phase that became unstable due to cooling (Equation 9) and/or due to an increase in sulfur fugacity in the system (Equation 10).



Equation 9: Cu-rich phase in equilibrium with chalcopyrite and pyrite.



Equation 10: Cu-rich phase in equilibrium with chalcopyrite and pyrite.

Type 2 chalcopyrite represents a later generation of chalcopyrite that clearly overprints earlier formed and brecciated pyrite. The trace element composition does not reveal any significant difference between the two different types of chalcopyrite (Appendix F). Eventually only Ag, Pb and Se show some variations (Figure 66). Type 1 chalcopyrite is enriched in Se, but depleted in Ag and Pb comparing to Type 2 chalcopyrite.

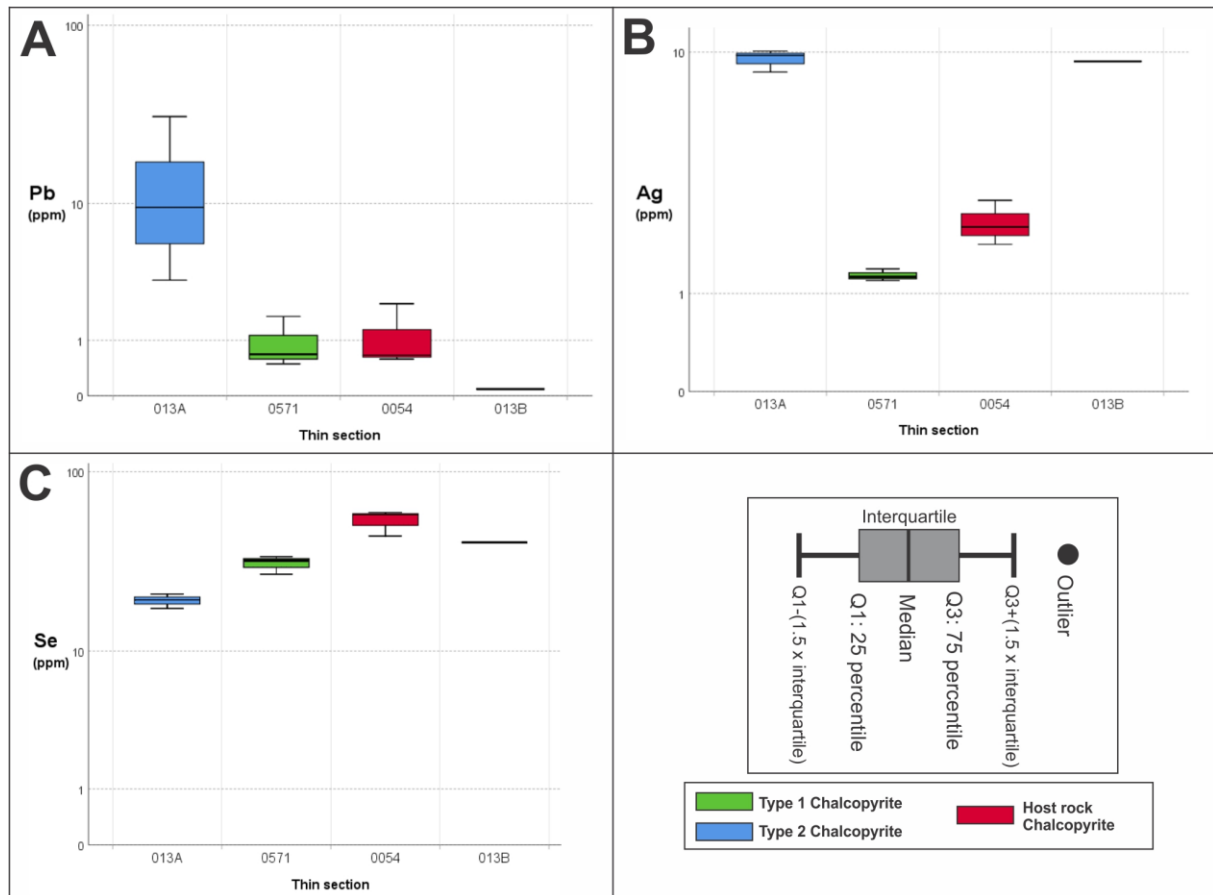


Figure 66: Boxplots presenting trace element concentrations (in ppm) for sulfides sorted by type of chalcopyrite. Based on 3 spots in each thin section. Silver in chalcopyrite from thin section 0571 ranges from 1.19 to 1.38 ppm, and 8.56 to 10.08 ppm in thin section 013A. Lead ranges from 0.49 to 1.69 ppm in thin section 0571, and 3.23 to 31.42 ppm in thin section 013A. Selenium ranges from 27.43 to 34.32 ppm in thin section 0571, and 17.62 to 21.26 ppm in thin section 013A. Chalcopyrite in thin sections 0054 and 013B shows selenium values ranging from 41.14 to 59.85 ppm, silver values from 1.83 to 9.3 ppm and lead from 0.089 to 2.15 ppm.

The chalcopyrite hosted in gabbro (Figure 20D) and basalt (Appendix D; spot 013B-ccp) plotted in Figure 66, show a slight enrichment in Se compared to Type 1 and 2 chalcopyrites, but follows mainly the same pattern as chalcopyrite in veins.

Sphalerite is also present in the quartz-carbonate veins hosted by mafic rocks of the Kvenvik formation. It usually occurs in minor amounts within Type 2 chalcopyrite (sample 013A at the Carl Johan mine; Figure 26C) or related to massive chalcopyrite mineralization in some of the quartz-carbonate veins (e.g. sample 060A at the Innerstrømmen locality; Figure 23C).

In the Kvenvik formation, pyrite occurs in the quartz-carbonate veins (e.g. Figure 26B and Figure 30B) and as disseminations in the mafic host rock (Figure 20B). The vein-hosted pyrite is generally anhedral to subhedral, while disseminated pyrite is usually euhedral. Pyrite hosted in veins is significantly enriched in Ni (3626 to 5867 ppm Ni) compared to the host rock pyrite (20.1 to 21.52 ppm Ni). A noticeable enrichment in Se, Sb and Pb and a weak

enrichment in Ag and Mo have also been found in vein-type pyrite. In contrast, Co is more enriched in the host rock pyrite (9678 to 28830 ppm) compared to the pyrite in the veins (681 to 1104 ppm; Appendix F).

The epigenetic Cu mineralization hosted by mafic rocks of the Kvenvik formation is associated with carbonates enriched in ^{13}C (Figure 55), which corresponds to the values of Melezhik et al. (2015). This enrichment can be explained by a high water-rock ratio (Banner & Hanson, 1990) and/or carbonate deposition during the Lomagundi-Jautli Event (Melezhik et al., 2015). The epigenetic mineralization also shows a positive $\delta^{34}\text{S}$ composition reflecting thermochemically reduced marine sulfates and/or evaporite as the main source of sulfur. The isotopically heaviest $\delta^{34}\text{S}$ composition has been recorded at the Mitchell mine (+16.88 to +24.16 ‰), indicating a contribution of evaporites enriched in ^{34}S (Banner & Hanson, 1990; Hoefs, 2018).

The source of copper of the mineralization in the Kvenvik formation is most likely to be gabbro and basalts. Trace elements in chalcopyrite in the host rocks (Figure 66) can however not be used to assign the chalcopyrite as primary. Sulfides have also been observed in the coarse-grained layers of tuff/tuffite, which could also be a primary source of copper, but it can also represent sulfidation associated with a later circulation of hydrothermal fluids and associated remobilization of metals.

5.1.2 Sediment-hosted Cu mineralization

The sediment-hosted Cu mineralization located within the Storviknes formation recorded both brittle and ductile regimes. The brecciated samples (e.g. samples L1, L2, 033 & 034 from the Lundstrøm mine; Type 6 mineralization, Figure 60G) clearly indicate a brittle setting, while ductile deformed carbonate layers have been observed at the Lundstrøm and Anna mines (e.g. sample 032; Type 4.1 mineralization, Figure 60D) from Lundstrøm showing ductile deformation of the carbonate and related mineralized quartz-carbonate vein. The bedding-parallel mineralization suggests that it was formed as an early epigenetic type by an increase in pressure, leading to circulation of fluids with mineralization restricted to layers with different permeability. This is the common type of Cu mineralization found in numerous sediment-hosted Cu deposits (Hitzman et al., 2010). The folding of the area must have come after the deposition and can probably be linked to the brecciated type of mineralization, which most likely was brecciated due to infiltration of hydrothermal fluids along with the carbonate-shale contact (Figure 43A).

The sediment-hosted Cu deposits have more complex mineralogy than the mafic rock-hosted occurrences (Figure 58). The mineralization is generally related to quartz-carbonate veins, but these veins show different styles of mineralization (Types 4-6; Figure 60D, E, F & G) as a result of different structural settings (brittle vs. ductile) and variations in host sedimentary lithologies (carbonate vs. shale).

Most trace elements in chalcopyrite from different subtypes of sediment-hosted Cu mineralization do not show a significant difference, with the exception of Pb, Ag, Se, Sn and Zn (Table 21; Figure 67). Sample 032 (a carbonate-hosted, bedding-parallel ductile deformed vein) is enriched in Ag and Zn compared to sample 0221 and 0222 (carbonate-hosted veins), and depleted in Pb and Sn.

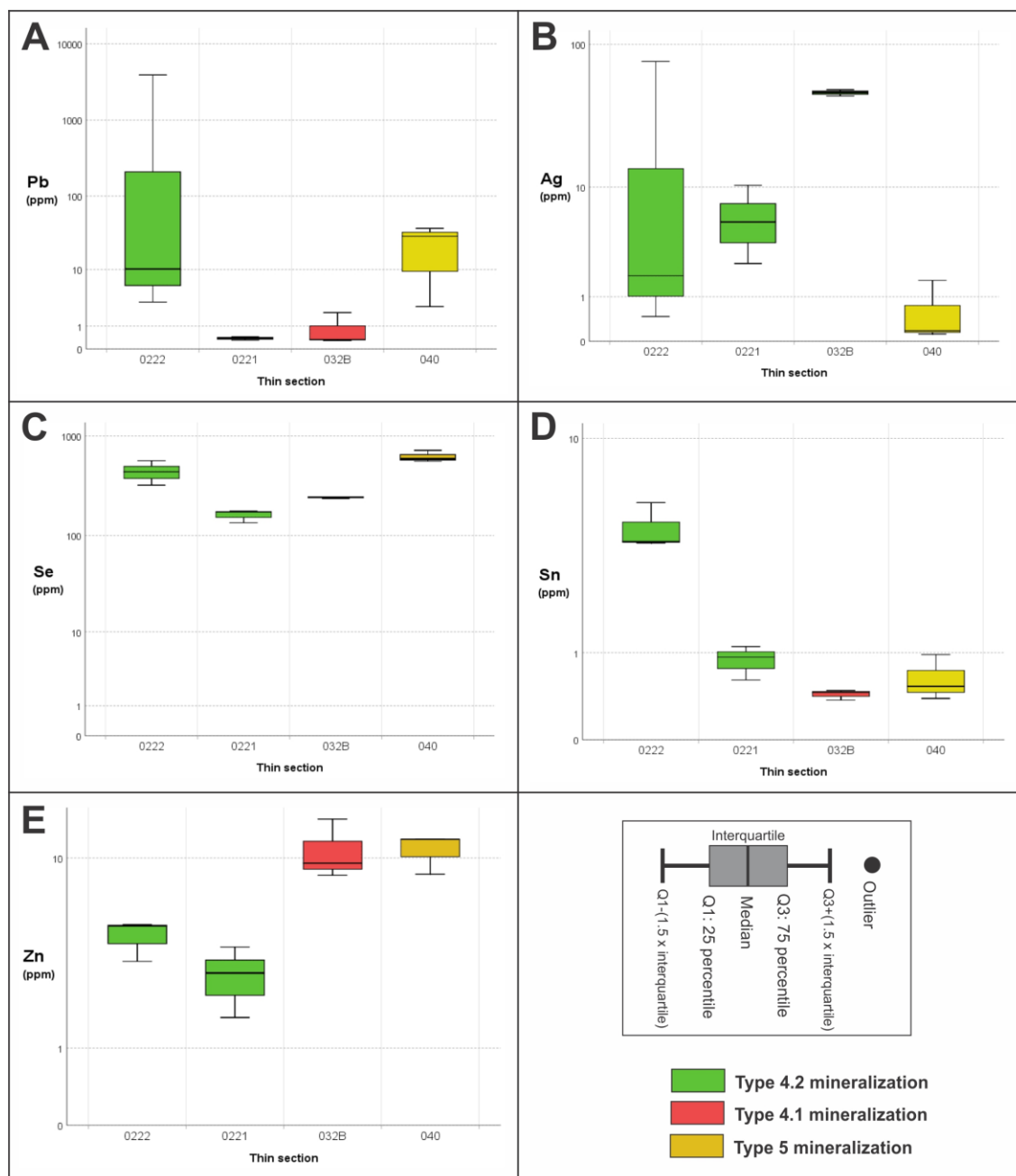


Figure 67: Boxplots presenting trace element concentrations (in ppm) for chalcopyrite. Based on 3 spots in each thin section.

Boxplots in Figure 67 are associated with Table 21.

Table 21: Minimum and maximum values for selected trace elements within chalcopyrite (Figure 67), from Appendix F.

	Zn		Se		Ag		Sn		Pb	
Sample	Min	Max	Min	Max	Min	Max	Min	Max	Min	Max
032	8.42	14.59	236.62	246.16	0.156	0.42	0.372	0.48	0.288	2
0221	1.63	3.95	134.49	176.11	2.35	10.31	0.61	1.1	0.306	0.439
0222	3.35	5.05	321.62	566	0.47	76.41	3.78	5.6	3.12	3912.51
040	8.51	12.03	556.8	718.92	0.119	1.58	0.39	0.97	2.6	37.09

Chalcopyrite from quartz-carbonate veins hosted by shale (sample 040) is enriched in Se and depleted in Ag comparing to chalcopyrite in the other carbonate-hosted veins (Table 21; Figure 67). Other trace element concentrations are similar, which suggests chalcopyrite could have formed from the same fluid with a slightly different character. Anyhow, sample 040 records a presence of As-tennantite in the association with chalcopyrite (Figure 42D). According to Cox et al. (2003) the presence of As-minerals (such as tennantite) in association with chalcopyrite in sediment-hosted deposits may reflect a later hydrothermal overprint. Tennantite shows enrichment in trace elements as Zn, Sb and Cd compared to other sediment-hosted sulfides (Figure 52).

Molybdenite found in association with bornite and digenite (e.g. sample L2, Figure 45B) shows enrichment in Pb, Ni, Co, Au and Te compared to other sediment-hosted sulfides (Figure 56). Bornite found in carbonate-hosted quartz-carbonate veins (e.g. sample 0221; Figure 40A) and the brecciated type of mineralization (e.g. samples L1, L2, 032 & 034) indicates the high-grade zone of a sediment-hosted deposit (Cox et al., 2003). The brecciated type of mineralization is characterized by abundant digenite (Figure 45B; Figure 47B). Digenite occurs mostly within bornite and shows a general enrichment in several elements (as Zn, As, Se, Ag & Mo) compared to the bornite, which contains approximately the same trace element amounts in sample L2 from Lundstrøm and 0221 from Anna (Table 22; Figure 68). This can indicate that the bornite at Lundstrøm and Anna were formed from the same fluid.

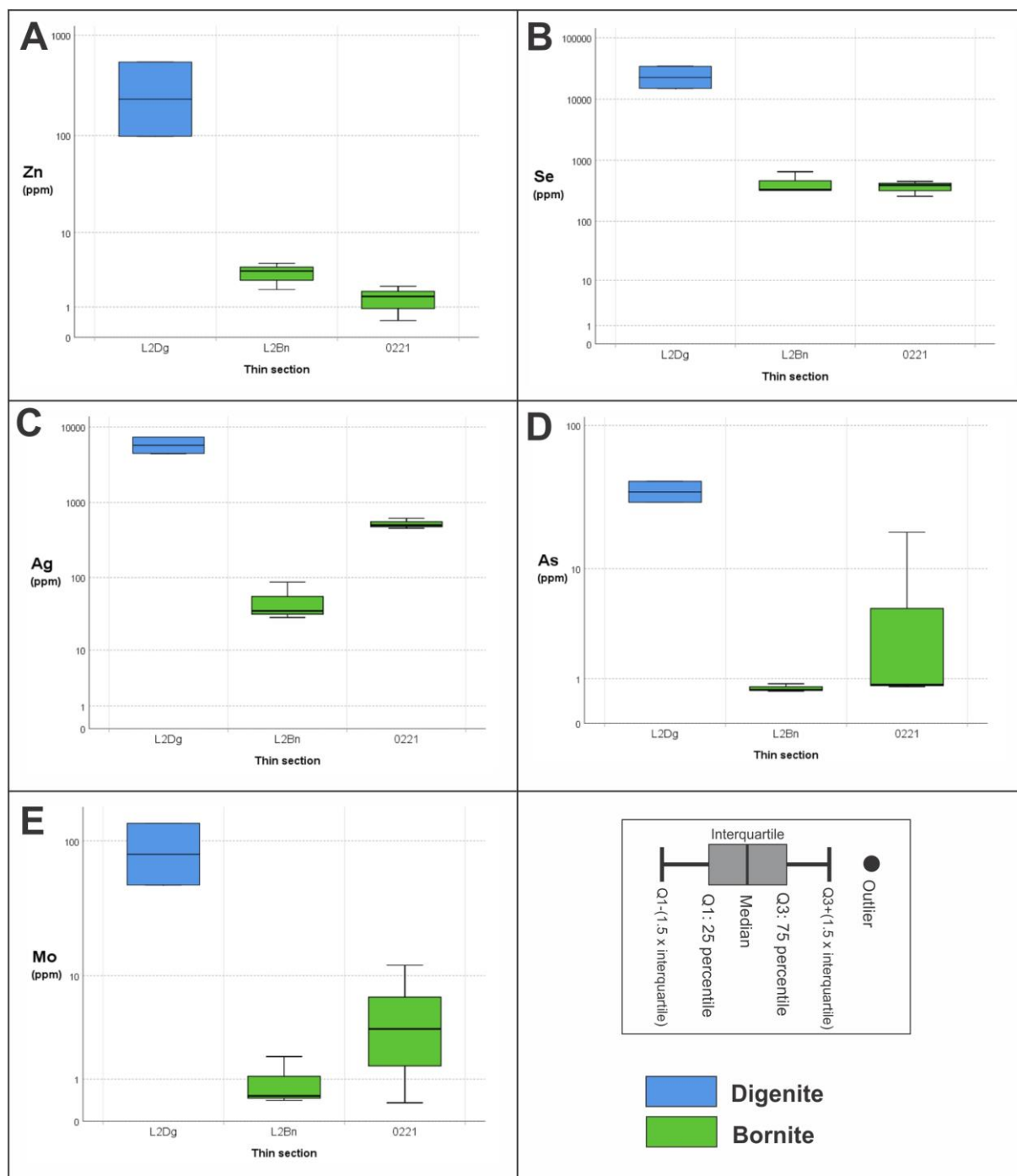


Figure 68: Boxplots presenting trace element concentrations (in ppm) for bornite and digenite. Based on 2 spots in digenite and 6 spots in bornite.

Boxplots in Figure 68 are associated with Table 22.

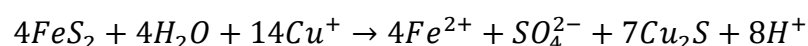
Table 22: Minimum and maximum values for selected trace and minor elements (Figure 68), from Appendix F.

	Zn		As		Se		Ag		Mo	
Sample	Min	Max	Min	Max	Min	Max	Min	Max	Min	Max
L2 (Digenite)	98.44	541.04	29.7	41.52	14945.56	34301.64	4464.83	7364.13	47.89	133.82
L2 (Bornite)	1.99	4.44	0.65	0.85	321.5	649.69	28.85	86.93	0.41	1.9
0221 (Bornite)	0.47	2.22	0.77	18.33	259.34	451.19	454.16	615.26	0.36	12.05

The main source of Cu in the Storviknes formation is most likely related to remobilization of Cu from mafic rocks of the underlying Kvenvik formation. Trace element distribution in chalcopyrite hosted in sedimentary rocks shows enrichment of Se compared to mafic rock-hosted Cu mineralization (Figure 52). Lead, Ag, As, and Hg follow the same concentrations in sediment-hosted and mafic rock-hosted chalcopyrite, while Zn, Ni, Cr, Sb and Cd are depleted in the sediment-hosted chalcopyrite compared to the mafic rock-hosted chalcopyrite (Figure 52). This can suggest the same fluid with trace elements affected by different host rocks. Sedimentary rocks within Storviknes formation may be the source of Se, while Kvenvik formation are the source of Zn, Ni, Cr, Sb and Cd, including Cu. Trace elements in oxides in sediment-hosted mineralization reveal an enrichment of Pb, Se, As, Ag and Mo compared to the mafic rock-hosted mineralization (Figure 53). This supports that at least Se has its source from sedimentary rocks within Storviknes formation. Correlation matrices (Appendix H) also indicate this, with a good correlation between Se in digenite in the sediment-hosted mineralization, while it has a poor correlation with all sulfides in mafic rock-hosted mineralization.

The more exotic minerals, such as for instance tennantite, wulfenite and wittichenite (arsenic, molybdenum and bismuth minerals), together with molybdenite and Se-rich galena are commonly associated with the Cu mineralization hosted by the shale of the Storviknes formation. Shale within Storviknes formation could therefore be the source of at least Se but also Pb, As, Ag and Mo.

The noticeable lack of pyrite in the sediment-hosted deposits (Figure 58) is also mentioned for other sediment-hosted deposits in Norway and Sweden, including AKTW (Sandstad & Torgersen, 2019; Mun et al., 2020). This lack of pyrite corresponds to the sediment-hosted model of Cox et al. (2003), with pyrite only observed in trace amounts in the high-grade zone of the sediment-hosted Cu deposits. The lack of pyrite in sediment-hosted deposits (in the high-grade zone) can be described by the replacement of pyrite by chalcocite and other CuS minerals (Sverjensky, 1987):



Equation 11: Pyrite replaced by chalcocite, from Sverjensky (1987)

Carbon and oxygen isotope analyses (Table 18) revealed that most of the sedimentary-hosted carbonate samples have an isotope composition similar to marine carbonates (Figure 55), and

correspond to the isotope values from Melezhik et al. (2015). The exceptions are two samples from the brecciated rock (L2; $\delta^{13}\text{C}$ of -3.5 & -3.7 ‰) at Lundstrøm and one carbonate layer at the Anna mine (039; $\delta^{13}\text{C}$ of -2.9 ‰). All three of these samples are depleted in ^{13}C , reflecting a contribution of isotopically light organic components.

Sulfur isotope analyses discriminated two types of sulfides in the Storviknes formation according to their $\delta^{34}\text{S}$ composition (Figure 56). One type, which all three samples are related to bornite or digenite, has a $\delta^{34}\text{S}$ composition close to -7.00 ‰, while the other type related to two samples of chalcopyrite has a $\delta^{34}\text{S}$ composition at +1.40 and +3.71 ‰. This difference in $\delta^{34}\text{S}$ between types of ore minerals can be caused by different bond strengths in sulfides during cooling of the fluid. Chalcopyrite will have a higher $\delta^{34}\text{S}$ composition than bornite and the CuS minerals chalcocite/digenite due to its higher bond strength between elements that preferably enriches ^{34}S over ^{32}S (Donald, 1969).

Mineralization east vs. west of the syncline

Localities Carbonate wall and Møllnes river (east of syncline) are supposed to be a continuation of the carbonate layers at Anna and Lundstrøm (west of syncline, Figure 4), which also the carbonate isotope study suggests (Figure 55). However, mineralization is mainly restricted to only one quartz-carbonate vein in sample 0571 (Figure 48), and some smaller mineralization observed at the Møllnes river locality. No mining activity related to this carbonate east of the syncline also suggests the lack of mineralization. The lack of mineralization here could be related to that there are reported both lateral and vertical zonations of ore minerals in some sediment-hosted Cu deposits (Cailteux et al., 2005). Maybe this eastern part can be the lateral limit, but structurally, this eastern part should not be a lateral limit as it lies just above the Cu-rich Kvenvik formation. A more likely cause could be the absence of a reducing medium to precipitate copper (Cox et al., 2003), but carbonates in general are a good reducing source (Hitzman et al., 2010). The lack of mineralization here is most likely to be structurally controlled because the main mineralization west of the syncline is related to brecciated zones and quartz-carbonate veins displace carbonates and shale, making room for mineralization. This has not been observed east of the syncline.

5.2 Ore-bearing fluids

The fluid inclusion study was carried out on five samples selected with an aim to identify physicochemical characteristics of the fluids associated with the deposition of mineralized quartz-carbonate veins hosted by mafic rocks of the Kvenvik formation, and sedimentary

rocks of the Storviknes formation, as well as with the deposition of barren quartz-carbonate veins in the study area (Table 20; Appendix E).

The two-phase (L+V) fluid inclusion and numerous decrepitated post-entrapment re-equilibrated inclusions have been found in both barren and mineralized veins. According to the recorded eutectic temperatures (T_e), two-phase type of the inclusions can be subdivided in two groups: 1) NaCl-CaCl₂-H₂O inclusions (with T_e around -52°C) and 2) NaCl-H₂O inclusions (with T_e around -21°C). The two-phase NaCl-CaCl₂-H₂O inclusions are characterized by a salinity ranging from 27.1 to 27.5 wt.% NaCl equ. and homogenization temperatures (T_h) between 215 to 225°C. The two-phase NaCl-H₂O inclusions revealed two distinct groups of salinity and homogenization temperatures. One group ranging with a salinity from 5 to 7.9 wt.% NaCl equ. and T_h between 118 and 135°C, and the another one with a salinity between 26.3 and 26.5 wt.% NaCl equ. and T_h between 195 and 200°C.

In contrast, the multi-phase (L+V+S) and solid inclusion have been found only in the mineralized quartz-carbonate veins. Any significant difference between inclusions found in mafic rock hosted and sediment-hosted mineralized veins have not been recorded (NaCl-CaCl₂-H₂O; salinity = 29.7-40.2 wt.% NaCl equ.; T_h = 192-235°C), indicating that the same ore-forming fluid was circulating through the Kvenvik and Storviknes formations and depositing mineralized quartz-carbonate veins of the epigenetic character. The high salinity recorded for the multi-phase inclusions together with the presence of solid halite inclusions (Figure 57F), suggests the ore-forming fluids were highly saline and that this high salinity was the main driving mechanism for mobilization of Cu in the form of Cu-chloride complexes.

The absence of indication for mixing of two or more fluids suggests that metals and sulfur were transported by the same fluid. Such transporting mechanism requires an oxidizing character of ore-forming fluid sufficient to keep S in the sulfate form. Similar mechanisms have been recognized in sediment-hosted Cu deposits elsewhere (Hitzman, 2000; Cox et al., 2003; Hitzman et al., 2010).

Fluid inclusion characteristic compared to the Cu mineralization in RTW

The fluid inclusions from RTW have homogenization temperatures between 135 to 350°C at the Nussir deposit and 102-520°C at the Ulveryggen deposit (Mun et al., 2020). The homogenization temperature from this study falls more or less within these ranges, but

sphalerite geothermometry at the Nussir deposit suggested the Cu mineralization occurring at 330-340°C (Mun et al., 2020). Such high temperatures have not been obtained in this study. Fluids with a salinity ranging from 0.35 to 36 wt.% NaCl equ. is present in the RTW (Mun et al., 2020), which is slightly lower than the highest observed salinity in Kåfjord.

5.3 Magnetite as an indicator of ore-forming processes

At locality Kåfjord bridge, the magnetite grains that were identified within the gabbro can be used to link the hydrothermal alteration of magnetite to the fluids bringing the Cu mineralization. The magnetite can be divided into three types: 1) massive pure magnetite, 2) massive pure magnetite stuck together with lamellae-rich magnetite, and 3) lamellae-rich magnetite stuck together with massive magnetite (Figure 69).

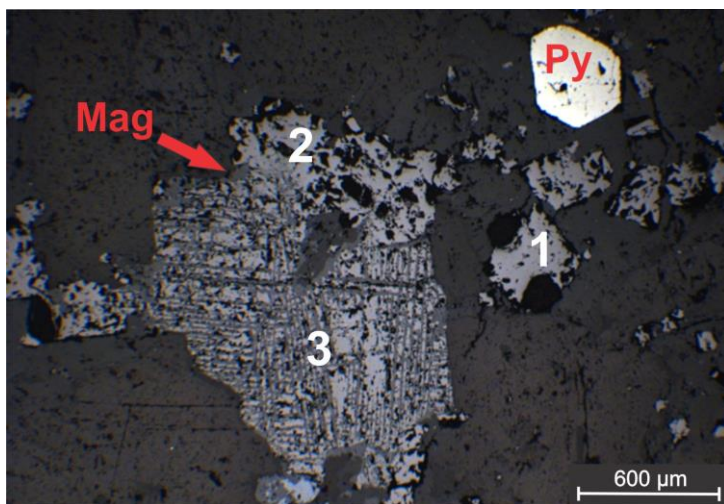
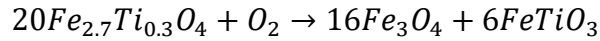


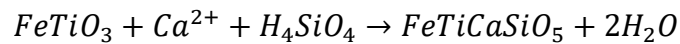
Figure 69: Type 1, 2 and 3 magnetite. Abbreviations: Mag: Magnetite, Py: Pyrite.

The massive type 1 and 2 magnetite had a composition from SEM-EDS that was close to the ideal composition of magnetite, while the lamellae-rich magnetite deviated a bit and contained in addition to iron and oxygen, some titanite and manganese. Lamellae in the magnetite were infilled by titanite and rutile, and there have also been identified exsolution textures of ilmenite within the lamellae-rich type 3 magnetite. According to Ivanyuk et al. (2017), ilmenite can form lamellae's oriented along crystallographic planes (111 & 100) in magnetite when the original mineral titanomagnetite, is exposed to a higher oxygen fugacity during cooling of the magma. These crystallographic planes of ilmenite correspond well to the observed pattern of ilmenite in magnetite seen in Figure 21C, where two distinct planes can be seen (also see Figure 69 for lamellae-rich pattern). The reaction forming magnetite and ilmenite during cooling of newly formed titanomagnetite with a high oxygen fugacity available can be seen in Equation 12 below.



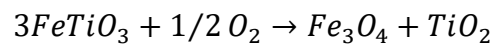
Equation 12: Transformation from titanomagnetite to magnetite and ilmenite, from Ivanyuk et al. (2017).

After ilmenite has formed in magnetite during the cooling of the magma, it is most likely that the gabbro has been hydrothermal altered. The presence of cross-cutting quartz-carbonate veins in the gabbro enhances this possibility of hydrothermal alteration including the observed seritization. This hydrothermal fluid was probably rich in calcium that may have come from the breakdown of plagioclase (Shau et al., 2000). It was also silica-rich (in the form of H_4SiO_4), which may have altered ilmenite into titanite, seen in Equation 13 below.



Equation 13: Hydrothermal alteration of ilmenite to titanite.

The same fluid may also have had an oxidizing character which can explain why rutile is found together with titanite (Figure 20C & Figure 21D). There is evidence of this possible oxidizing character of the fluid as anhydrite is found as solid inclusions in quartz-carbonate veins from the fluid inclusion study. Anhydrite ($CaSO_4$) needs four oxygen atoms to form, and this suggests that the fluid could be the source to carry oxygen and form anhydrite. On the other hand, anhydrite could potentially have been formed under evaporitic conditions before the fluid started to circulate, and by this only have been transported by the fluid which then didn't need to be oxygen-rich. Fluid traveling in such conditions with lots of anhydrite present, would on the other hand, probably contain some oxygen in the solution from dissolved anhydrite that could readily interact with ilmenite and form rutile.



Equation 14: Ilmenite forming magnetite and rutile.

It is likely to assume that at least the lamellae-rich magnetite in the gabbro at Kåfjord bridge have originated from titanomagnetite, that during cooling of the magma formed exsolution texture of ilmenite with a later hydrothermal fluid that transformed ilmenite into titanite and rutile, still keeping the same two distinct planes. This hydrothermal alteration may occurred during one fluid circulation event, but it could also have happened by two or more events by the circulation of different fluids with various properties. If the origin of the massive magnetite is titanomagnetite is more difficult to explain, but it is most likely to assume that it originated from magnetite and has behaved as an immobile mineral during hydrothermal

alteration. What should have been investigated is if there can be seen an increased abundance of lamellae-rich magnetite in the veins compared to in the host rock.

To get an indication of what type of magnetite that is present at locality Kåfjord bridge, data from the LA-ICP-MS analysis have been plotted in a plot from Dare et al. (2014), which differentiates magmatic magnetite from hydrothermal magnetite (Figure 70).

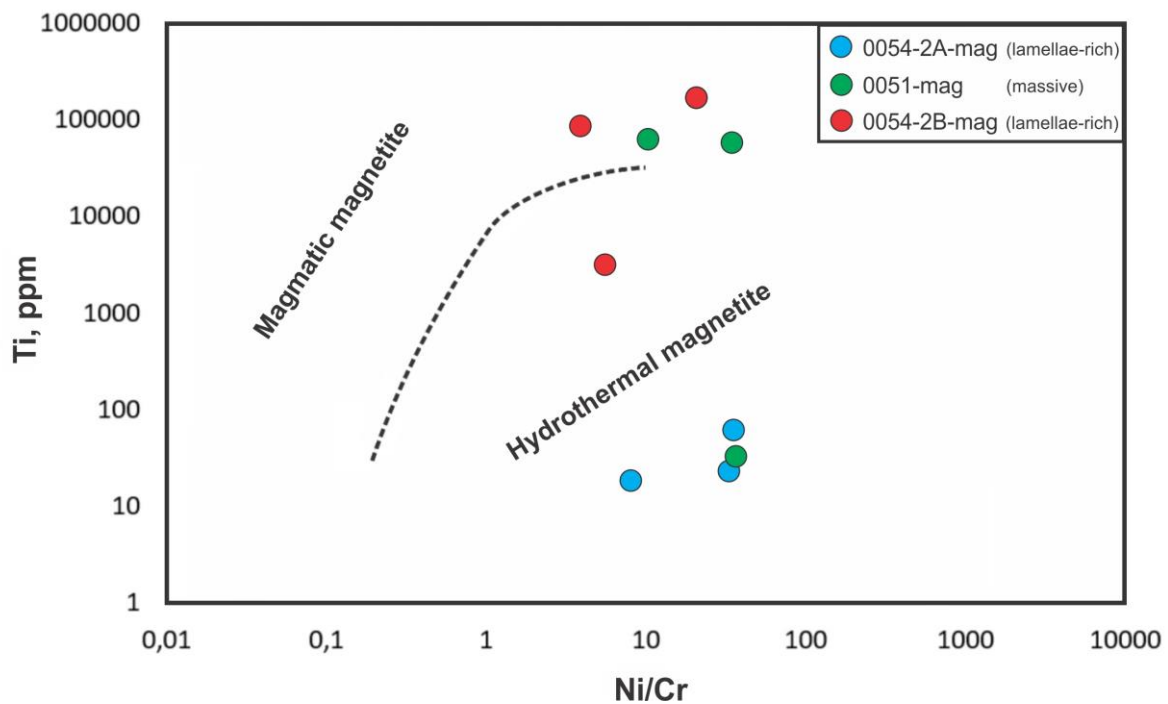


Figure 70: Ti vs Ni/Cr plot, modified from Dare et al. (2014).

Both magmatic magnetite and hydrothermal magnetite have been identified from this plot by three spot clusters in two samples at locality Kåfjord bridge. Sample 0054, a gabbro collected distant from a quartz-carbonate vein, suggests hydrothermal magnetite by the blue-colored circles, which is one spot from the massive type 2 magnetite and two spots from the massive type 1 magnetite. This indicates no differences in origin between these two types of massive magnetite. The red circles from the lamellae-rich magnetite within the same thin section indicate a magmatic origin in two spots and hydrothermal origin in one spot. These three spots are type 3 lamellae-rich magnetite, which is believed to originally be titanomagnetite that has been hydrothermal altered. The green spots also show two spots in the magmatic origin and one spot in the hydrothermal, but this is from the massive type 2 magnetite collected close to a quartz-carbonate vein. By this, there cannot be seen any correlation in origin between the massive and the lamellae-rich magnetite, but the hydrothermal alteration of ilmenite can be linked to the ore-forming fluid.

In the paper of Ilton and Eugster (1989), magnetite within a chlorite-rich fluid was used to predict the exchange of Fe with Mn, Zn, Cu and Cd. The result suggested that these elements would preferentially form deposits distal to the hydrothermal mineralization of magnetite, with Cu and Cd being very enriched in the fluid compared to in the magnetite. This could explain to some degree why copper is absent within the quartz-carbonate veins close to the gabbro.

5.4 Ore-forming model

5.4.1 Syngenetic mineralization

The syngenetic stratiform mineralization, classified as a VMS deposit (sample 047), has most probably been deposited on the seafloor during rifting (Bergh & Torske, 1988) when the Kvenvik formation was formed (~ 2220 to 2146 ± 5 Ma; Melezhik et al., 2015). A ~ 80 Ma sedimentation break followed before deposition of the Storviknes and Skoadduvarri formation (Melezhik et al., 2015). At some time after deposition of these formations, the whole sequence was most probably exposed to a compressional force that folded the area and initiated circulation of fluids and remobilization of metals, including Cu.

5.4.2 Epigenetic mineralization

Field observations indicate that the epigenetic Cu-mineralization in the Kvenvik and Storviknes formation could be related to fold hinges as the strike of the major Cu-mineralized quartz-carbonate veins are oriented nearly parallel to the regional folds supposed by Bergh and Torske (1988). The Kvenvik formation lies within an anticlinal fold (Bergh & Torske, 1988) with Cu mineralization in larger quantities, which indicates that the major mineralization could be most concentrated in the anticline fold hinge, which is approximately the surface exposed in Kåfjord today, where most mineralization already have been discovered and mined in the 1800th and 1900th century. Storviknes formation has its limbs exposed, showing mineralization in smaller quantities than Kvenvik formation.

The epigenetic ore mineralization within Kvenvik and Storviknes formation share many common features with sediment-hosted Cu deposits known worldwide (MacKevett et al., 1997; Hitzman, 2000; Cox et al., 2003; Hitzman et al., 2010). Geochemical signatures for sediment-hosted Cu deposits are also present. These are according to Cox et al. (2003), mainly characterized by the presence of Cu, Ag, Pb and Zn, but with a noticeable lack of Au. Copper, Ag, Pb and Zn are relatively concentrated in chalcopyrite in both types of deposits in

Kvenvik and Storviknes formation, and a general lack of gold is also observed (Figure 52). Silver-, lead- and zink-rich mineral phases are also present (e.g. Se-Ag-Cu-rich galena & sphalerite).

The source rock of the Cu mineralization is most likely the basalt in the Kvenvik formation. These rocks are suitable of hosting copper and most probably exhibit oxidizing conditions with the formation of a hematite stable oxidized environment (Cox et al., 2003), as the Kvenvik formation is deposited in a spasmodically subsiding basin under subaerial to shallow water (Bergh & Torske, 1988). The rock may therefore, most probably have been periodically exposed to air during deposition. The gabbro which intruded at 2146 ± 5 Ma (Melezhik et al., 2015) after the deposition of the basalt, may also have contributed as a source of copper, but the formation of a hematite-stable oxidized environment is not as clear. The unknown bedrock beneath Kvenvik formation may also have acted as a source rock of copper.

It is most likely to assume that the source of the fluids comes from the sedimentary rocks in the Storviknes formation laying stratigraphically above the greenstone in Kvenvik formation, following the sediment-hosted model of Hitzman et al. (2010). This also the main model for the Kennecott-type of deposits in Alaska (MacKevett et al., 1997), with fluids descending from the overlying limestones and marine sedimentary rocks into the “Niklai Greenstone”. The fluid inclusion study revealed that the quartz-rich samples collected from Skoadduvarri formation have the same characteristics as the samples from Kvenvik and Storviknes formation, which suggests that Skoadduvarri formation may also have contributed with fluids. Connate water in the dolostones occurring in the Kvenvik formation (Melezhik et al., 2015) is also likely to have contributed to the fluid, resulting in a high salinity fluid.

This high salinity recorded in the mineralized veins, is most probably related to dissolution of evaporites associated with the carbonate layers within Kvenvik formation, as halite casts in this carbonate have been found, which indicates presence of evaporites (Melezhik et al., 2015). Highly saline fluids are associated with sediment-hosted Cu deposits as the Kipushi Zn-Cu deposit (Heijlen et al., 2008) in the central African Copperbelt (Cailteux et al., 2005) and the nearby Nussir and Ulveryggen deposit in RTW (Mun et al., 2020). Storviknes formation may also have contributed with highly saline fluids due to the presence of solid halite inclusions (Figure 57F). At the same time, evaporates within Kvenvik formation could have provided significant amounts of sulfur in the sulfate form (Melezhik et al., 2015), which is related to the known increase in sulfate precipitation from seawater during the Lomagundi-

Jatuli carbon excursion (Bekker & Holland, 2012). This highly saline fluid is capable to leach out copper occurring in igneous basement rocks with a low permeability Koziy et al. (2009), which is the case for the Kennecott-type of deposits in Alaska (MacKevett et al., 1997), where the underlying greenstone is supposed to be the source rock of copper. The same is most likely to also have occurred in Kåfjord. By the presence of this highly saline fluid, copper has most likely been transported as chloride complexes (Cox et al., 2003).

Host rocks capable of reducing the fluids to precipitate copper are likely to be the organic-rich carbonate layers within both Kvenvik and Storviknes formation. In addition, a horizon of black shale identified in the field and by Melezhik et al. (2015) (Figure 10), has also been described by Mørk (1970), stretching along with the whole Kvenvik formation, may also have contributed to the reduction of ore-forming fluids. The graphite identified at locality Henning (Figure 32) is supposed to be a part of the black shale sequence according to Mørk (1970).

Low- and high-grade zones

At locality Kåfjord bridge, there has been identified pyrite as sulfide in the quartz-carbonate veins. This locality at Kåfjord bridge can therefore correspond to the very low-grade zone of a sediment-hosted Cu deposit with pyrite located close to the source rock as according to Cox et al. (2003). However, Melezhik et al. (2015) found chalcopyrite in the veins hosted by this gabbro and there has also been identified chalcopyrite at locality Innerstrømmen, which also lie in the lower part of Kvenvik formation and is hosted by gabbro (Figure 4; Figure 10). Locally variations may occur and the appearance of these veins with pyrite only at Kåfjord bridge is one evident proof of this being the very low-grade zone.

At locality Wilson, Carl Johan, Mitchell and Henning which lie approximately in the upper part of Kvenvik formation (Figure 10), all mineralization related to quartz-carbonate veins here contains both pyrite and chalcopyrite, which corresponds to a higher grade but still in the low-grade zone (Cox et al., 2003).

The sediment-hosted localities within Storviknes formation at Anna and Lundstrøm correspond to the high-grade zone as digenite and bornite have been found here (Cox et al., 2003). The locality Anna could correspond to a lower grade zone than locality Lundstrøm as bornite+chalcopyrite (and accessory covellite) is the copper-richest minerals found at Anna while bornite+digenite is the copper-richest minerals found at Lundstrøm. The zonation from lower Cu grade zone to the higher Cu grade zone in the Zambian type of sediment-hosted Cu

deposits, is characterized by pyrite to chalcopyrite to chalcopyrite+bornite to bornite+digenite+chalcocite (Cailteux et al., 2005). This corresponds to the differentiation between the locality Anna and Lundstrøm, and also for the differentiation in the low-grade zone.

A schematic figure of the whole ore-forming system is presented in Figure 71 below.

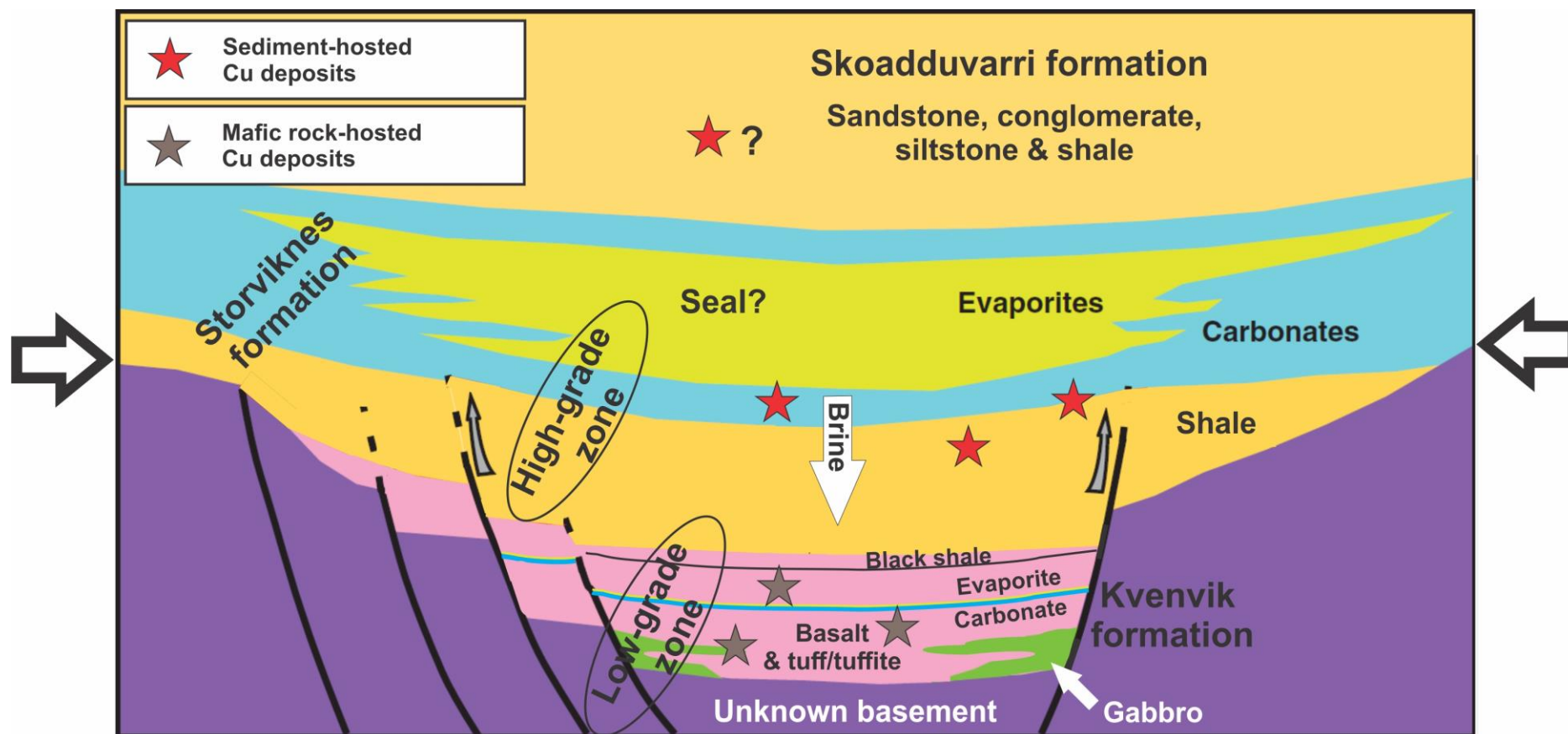


Figure 71: Schematic ore-forming model for the Cu deposits in the Kvenvik and Storviknes formation within the Kåfjord area, AKTW. Mafic rock-hosted mineralization occurs within the Kvenvik formation, while sediment-hosted mineralization occurs within the Storviknes formation. Locality Kåfjord bridge and Innerstrømmen (samples 060 & 0051; Type 2) are associated with the lowermost Cu mineralization (grey star), followed by locality Wilson, Carl Johan, Mitchell and Henning represented by the upper Cu mineralization within Kvenvik formation (e.g. samples 013, 014, 057, 0571, 051; Type 3). The lowermost mineralization in Storviknes formation (red star) is associated with sample 040 (Type 5) from locality Anna, while the following mineralization (in between the shale and the carbonate) is associated with the brecciated area (e.g. sample L2; Type 6) at locality Lundstrøm. The uppermost mineralization in Storviknes formation is associated with samples 032, 0221 and 0222 (Type 4.1 & 4.2) at locality Anna and Lundstrøm. The thickness of the layers are not correct and the non-depositional break between the Kvenvik and Storviknes formation (Melezhik et al., 2015) is not shown. The regional folding is also not shown (Bergh & Torske, 1988). Modified from Hitzman et al. (2010).

Relative timing of mineralization

The epigenetic mineralization in the Kvenvik and Storviknes formation can as described, be assigned to one event of fluid circulation, mainly based on the fluid inclusion study but also as it fits with the accepted sediment-hosted Cu deposit model (Hitzman et al., 2005), with mafic rocks as a source of Cu (MacKevett et al., 1997; Cox et al., 2003). This event is most likely to have occurred after the deposition of (at least the lower part) the Skoadduvarri sandstone formation as one barren quartz-carbonate veins located in the lower part of the Skoadduvarri formation, suggest the same type of fluid as the mineralized quartz-carbonate veins in the Kvenvik and Storviknes formation. Mineralization is also most likely to have occurred before deposition of the Bossekop formation as there have been done ore prospecting in the western part of AKTW, in Kvænangen by Laux (1972). By his report, mineralization was only identified in the Raipas Supergroup while the overlaying Bossekop Group was barren. Reitan (1960) within Laux (1972) suggested that mineralization occurred in Precambrian time before the deposition of Bossekop, as Bossekop is thought to be of late Precambrian age.

6 Conclusion and further work

6.1 Conclusion

This thesis, as a part of the MinExTarget project, has the aim to provide a better understanding of the sediment- and mafic rock-hosted Cu mineralization within the Storviknes and Kvenvik formations of AKTW. The main focus has been given to the mineral, geochemical and stable isotope characteristics of the ore mineralization, host rocks, and alteration products. Fluid inclusion study has also provided temperature and salinity conditions of the ore-bearing fluid. The main conclusions of this study are:

- A total of six different types of mineralization have been identified within the Kvenvik and Storviknes formation in the area of Kåfjord. One type of the mineralization has a syngenetic stratiform character, while the five others are related to epigenetic quartz-carbonate veins.
- The syngenetic stratiform mineralization has been classified as a VMS mineralization (Type 1 mineralization). It is hosted in basaltic tuff and tuffite in the Kvenvik formation, with pyrite as the major ore mineral, and accessory amounts of chalcopyrite, pyrrhotite and pentlandite. It also contains bedding parallel rutile-ilmenite bands. By the use of trace elements in chalcopyrite and pyrite, this VMS mineralization corresponds more or less to the range of the mafic rock-hosted Cu mineralized veins, while trace elements in rutile show dissimilarities to all other oxides, with some exceptions. Chalcopyrite and pyrite may be affected by hydrothermal overprint, while the rutile-ilmenite bands could be primary. A slight enrichment of Cr in chalcopyrite, pyrite and rutile compared to mafic rock-hosted Cu mineralization and oxides have been observed. Negative $\delta^{34}\text{S}$ reveals an influence of sulfate-reducing bacteria during deposition.
- Mafic rock-hosted Cu mineralization in Kvenvik formation occurs mainly in the form of epigenetic quartz-carbonate veins with chalcopyrite and pyrite as the major ore minerals. Minor amounts of sphalerite have been found as well. This mineral assemblage corresponds to the low-grade zone in a classical sediment-hosted Cu deposit. The mineral zonation from pyrite (Type 2 mineralization) to chalcopyrite and pyrite (Type 3 mineralization) indicates a transition from the very low-grade zone

towards the low-grade zone. Two types of chalcopyrite within Type 3 mineralization may occur:

- 1) Chalcopyrite in the form of exsolutions within anhedral-shaped pyrite crystals
- 2) Chalcopyrite that cements brecciated anhedral to subhedral-shaped pyrite crystals

Type 1 chalcopyrite is enriched in Se, but depleted in Ag and Pb compared to Type 2 chalcopyrite. Chalcopyrite disseminated in gabbro and basalt, thought to be primary mineralization, can not be clearly differentiated from chalcopyrite hosted in quartz-carbonate veins by the use of trace elements. Euhedral pyrite disseminated in gabbro may be primary or a later replacement, but further research needs to be done. The isotope study reveals that the positive $\delta^{13}\text{C}$ values in the quartz-carbonate veins hosted in mafic rocks within the Kvenvik formation, have been influenced by carbonate layers formed during the Lomagundi-Jatuli Event. The $\delta^{34}\text{S}$ values indicate a general enrichment in ^{34}S for most of sulfide samples in the Kvenvik formation. This enrichment suggests evaporites as a potential source of sulfur.

- Sediment-hosted Cu mineralization occurs as four types of epigenetic quartz-carbonate veins in the Storviknes formation with a mineral assemblage of digenite, bornite and chalcopyrite as major ore minerals, and accessory amounts of covellite, Se-rich galena, Se-Ag-Cu-rich galena, galena, molybdenite, wittichenite, tennantite and wulfenite. Cu-rich minerals as digenite and bornite correspond to the high-grade zone in a classic sediment-hosted Cu deposit model. The noticeable lack of pyrite in sediment-hosted Cu-deposits may reflect its replacement by copper sulfides. Most samples from the sediment-hosted Cu deposits suggest a marine origin of carbonates, with some samples showing an influence of organic carbon. The two ranges of $\delta^{34}\text{S}$ suggest different bond-strengths in different ore minerals.
- Trace elements in chalcopyrite and oxides in the sediment-hosted Cu mineralization are characterized by an enrichment of Se compared to mafic rock-hosted Cu mineralization, indicating the sedimentary rocks, in particular shales, in the Storviknes formation may be a source of Se. Lead, As, Ag and Mo may also be hosted by the Storviknes formation. Trace elements in mafic rock-hosted mineralization are enriched in Zn, Cr and Ni compared to sediment-hosted mineralization, indicating the source of these elements are the mafic rocks in Kvenvik formation.

- Whole rock geochemistry reveals that the four samples analyzed within Kvenvik formation can be classified as monzogabbro, picrobasalt, basalt, and basaltic tuff/tuffite. This study also confirms earlier studies (e.g. Bergh & Torske, 1988), with a tholeiitic composition and MORB origin of the mafic rocks. A slight depletion in Ce indicates concentration of Ce in ferromanganese nodules on the seafloor.
- A stratigraphically controlled relationship between quartz and carbonate in the epigenetic veins has been observed. Carbonate-rich veins are associated with stratigraphically lower formation (e.g. Kvenvik formation), while quartz-rich veins are associated with stratigraphically upper formations (e.g. Storviknes and Skoadduvarri formation).
- The Cu mineralization has most likely occurred during a single event of fluid circulation which lasted for a longer period. Fluid inclusion study reveals that this fluid had a highly saline and a low to moderate temperature. Such fluids have a good capability to transport Cu in forms of chloride complexes. Trace element behavior also suggests one fluid, and the alteration of ilmenite to rutile and titanite within magnetite can be linked to this same ore-forming fluid.

6.2 Further work

Further work is needed in both the Kvenvik and Storviknes formations, as well as in the Skoadduvarri formation. The epigenetic Cu mineralization seems to be structurally controlled, and therefore a detailed structural geology study is essential for the proper interpretation of the ore-forming processes in the Kåfjord area of AKTW. Mineral exploration in the Skoadduvarri formation should also be carried out, concentrated around conglomerates and potential organic-rich sequences (Appendix I).

References

- Abrahamsen, A. K. H., & Veiseth, A. (1997). *Nordkalottens første storindustri: kobberverket i Kåffjord, Alta*. Finnmark fylkeskommune i samarbeid med Alta kommune, mai 1997.
- Abramov, B. N. (2008). Petrochemistry of the Paleoproterozoic Udokan copper-bearing sedimentary complex. *Lithology and Mineral Resources*, 43, 37–43. <https://doi.org/10.1134/S0024490208010033>
- Achterberg, V. E., Ryan, C., Jackson, S. E., & Griffin, W. L. (2001). Data reduction software for LA-ICP-MS. In S. P. (Ed.), *Laser-Ablation-ICPMS in the Earth Sciences- Principles and Applications, Short Course Series 29* (pp. 239–243). Mineralogical Association of Canada.
- Agrawal, S., Guevara, M., & Verma, S. P. (2008). Tectonic discrimination of basic and ultrabasic volcanic rocks through log-transformed ratios of immobile trace elements. *International Geology Review*, 50(12), 1057–1079. <https://doi.org/10.2747/0020-6814.50.12.1057>
- Åhäll, K.-I., & Larson, S. Å. (2001). Growth-related 1.85-1.55 Ga magmatism in the Baltic Shield; a review addressing the tectonic characteristics of Svecofennian, TIB 1-related, and Gothian events - A reply. *GFF*, 123(1), 59–61. <https://doi.org/10.1080/11035890101231059>
- Archer, D. G. (1992). Thermodynamic Properties of the NaCl+H₂O System. II. Thermodynamic Properties of NaCl(aq), NaCl*2H₂(cr), and Phase Equilibria. *Journal of Physical and Chemical Reference Data*, 21, 793–829. <https://doi.org/10.1063/1.555915>
- Bachan, A., & Kump, L. R. (2015). The rise of oxygen and siderite oxidation during the Lomagundi Event. *Proceedings of the National Academy of Sciences of the United States of America*, 112(12), 6562–6567. <https://doi.org/10.1073/pnas.1422319112>
- Banner, J. L., & Hanson, G. N. (1990). Calculation of simultaneous isotopic and trace element variations during water-rock interaction with application to carbonate diagenesis. *Geochimica et Cosmochimica Acta*, 54, 3123–3137. [https://doi.org/10.1016/0016-7037\(90\)90128-8](https://doi.org/10.1016/0016-7037(90)90128-8)
- Barthelmy, D. (2012). *Web mineral*. (14.11.2020). <http://webmineral.com/>
- Bekker, A., & Holland, H. D. (2012). Oxygen overshoot and recovery during the early Paleoproterozoic. *Earth and Planetary Science Letters*, 317–318, 295–304. <https://doi.org/10.1016/j.epsl.2011.12.012>
- Bergh, S. G., & Torske, T. (1986). The Proterozoic Skoadduvarri Sandstone Formation, Alta, Northern Norway: A tectonic fan-delta complex. *Sedimentary Geology*, 47(1–2), 1–25. [https://doi.org/10.1016/0037-0738\(86\)90068-0](https://doi.org/10.1016/0037-0738(86)90068-0)
- Bergh, S. G., & Torske, T. (1988). Palaeovolcanology and Tectonic Setting of a Proterozoic Metatholeiitic Sequence Near the Baltic Shield margin, Northern Norway. *Precambrian Research*, 39, 227–246.
- Bodnar, R. J. (2003a). Chapter 1: Introduction to fluid inclusions. In I. Samson, A. Anderson,

- & D. Marshall (Eds.), *Fluid inclusions: Analysis and Interpretation* (Vol. 32, pp. 1–8). Mineral. Assoc. Canada.
- Bodnar, R. J. (2003b). Chapter 4: Introduction to aqueous-electrolyte fluid systems. In I. Samson, A. Anderson, & D. Marshall (Eds.), *Fluid Inclusions: Analysis and Interpretation* (pp. 81–99). Mineral. Assoc. Canada.
- Bodnar, R. J. (2003c). Chapter 8: Reequilibration of fluid inclusion. In I. Samson, A. Anderson, & D. Marshall (Eds.), *Fluid inclusions: Analysis and Interpretation* (Vol. 32, pp. 213–230). Mineral. Assoc. Canada. <https://doi.org/10.1201/b12744>
- Bodnar, R. J., Lecumberri-Sanchez, P., Moncada, D., & Steele-MacInnis, M. (2014). Fluid Inclusions in Hydrothermal Ore Deposits. In *Treatise on Geochemistry: Second Edition* (2nd ed., Vol. 13, Issue December). Elsevier Ltd. <https://doi.org/10.1016/B978-0-08-095975-7.01105-0>
- Bodnar, R. J., Sterner, S. M., & Hall, D. L. (1989). SALTY: a FORTRAN program to calculate compositions of fluid inclusions in the system NaCl-KCl-H₂O. *Computers and Geosciences*, 15(1), 19–41. [https://doi.org/10.1016/0098-3004\(89\)90053-8](https://doi.org/10.1016/0098-3004(89)90053-8)
- Bodnar, R. J., & Vityk, M. O. (1994). Interpretation of Microthermometric Data for H₂O-NaCl Fluid Inclusions. *Fluid Inclusions in Minerals: Methods and Application*, 117–130.
- Bogdanova, S., Gorbatshev, R., Skridlaite, G., Soesoo, A., Taran, L., & Kurlovich, D. (2015). Trans-Baltic Palaeoproterozoic correlations towards the reconstruction of supercontinent Columbia/Nuna. *Precambrian Research*, 259, 5–33. <https://doi.org/10.1016/j.precamres.2014.11.023>
- Borisenko, A. S. (1977). Cryometric technique applied to studies of the saline composition of solution in gaseous fluid inclusions in minerals. *Geologija i Geofizika, AN SSSR, SO*, 8, 16–27.
- Boynton, W. V. (1984). Cosmochemistry of the Rare Earth Elements: Meteorite Studies. In P. Henderson (Ed.), *Rare Earth Element Geochemistry* (Vol. 2, pp. 63–114). Elsevier B.V. <https://doi.org/10.1016/B978-0-444-42148-7.50008-3>
- Brown, A. C. (1997). World-class sediment-hosted stratiform copper deposits: Characteristics, genetic concepts and metallotects. *Australian Journal of Earth Sciences*, 44(3), 317–328. <https://doi.org/10.1080/08120099708728315>
- Cailteux, J. L. H., Kampunzu, A. B., Lerouge, C., Kaputo, A. K., & Milesi, J. P. (2005). Genesis of sediment-hosted stratiform copper-cobalt deposits, central African Copperbelt. *Journal of African Earth Sciences*, 42, 134–158. <https://doi.org/10.1016/j.jafrearsci.2005.08.001>
- Clark, I. D., & Fritz, P. (1997). Environmental Isotopes in Hydrogeology. In *Environmental Isotopes in Hydrogeology* (2nd ed.). CRC Press. <https://doi.org/10.1201/9781482242911>
- Cox, D. P., Lindsey, D. A., Singer, D. A., Moring, B. C., & Diggles, M. F. (2003). *Sediment-Hosted Copper Deposits of the World: Deposit Models and Database*. <http://pubs.usgs.gov/of/2003/of03-107>

- Craig, H. (1957). Isotopic standards for carbon and oxygen and correction factors for mass-spectrometric analysis of carbon dioxide. In *Geochimica et Cosmochimica Acta* (Vol. 12). [https://doi.org/10.1016/0016-7037\(57\)90024-8](https://doi.org/10.1016/0016-7037(57)90024-8)
- Craig, H. (1961). Isotopic Variations in Meteoric Waters. *Science*, 133, 1702–1703. <https://doi.org/10.1126/science.133.3465.1702>
- Dare, S. A. S., Barnes, S.-J., Beaudoin, G., Méric, J., Boutroy, E., & Potvin-Doucet, C. (2014). Trace elements in magnetite as petrogenetic indicators. *Mineralium Deposita*, 49(7), 785–796. <https://doi.org/10.1007/s00126-014-0529-0>
- Donald, J. B. (1969). Bond strength and sulfur isotopic fractionation in coexisting sulfides. *Economic Geology*, 64, 56–65. <https://doi.org/10.2113/gsecongeo.64.8.934>
- EIT RawMaterials. (2020a). *About us*. (10.10.2020). <https://eitrawmaterials.eu/about-us/>
- EIT RawMaterials. (2020b). *Vision and mission*. (10.10.2020). <https://eitrawmaterials.eu/about-us/vision-mission/>
- Fall, A., & Bodnar, R. J. (2018). How Precisely Can the Temperature of a Fluid Event be Constrained Using Fluid Inclusions ? *Economic Geology*, 8, 1817–1843. <https://doi.org/10.5382/econgeo.2018.4614>
- Fossen, H., Perdersen, R.-B., Bergh, S., & Andresen, A. (2013). En fjellkjede blir til. In I. B. Ramberg, I. Bryhni, A. Nøttvedt, & K. Rangnes (Eds.), *Landet blir til - Norges geologi* (2nd ed., p. 656). Norsk geologisk forening.
- Fryer, B. J., Jackson, S. E., & Longerich, H. P. (1995). The design, operation and role of the laser-ablation microprobe coupled with an inductively coupled plasma-mass spectrometer (LAM-ICP-MS) in the earth sciences. *The Canadian Mineralogist*, 33, 303–312.
- Gaal, G., & Gorbatshev, R. (1987). An Outline of the Precambrian Evolution of the Baltic Shield. *Precambrian Research*, 35, 15–62.
- Garmin. (2020a). *GPS Accuracy*. (23.11.2020). <https://support.garmin.com/en-US/?faq=aZc8RezeAb9LjCDpJpITY7>
- Garmin. (2020b). *GPSMAP®64st*. (23.11.2020). <https://buy.garmin.com/nb-NO/NO/p/140024#overview>
- Gautier, A. M., Gulacar, F., & Dalaloye, M. (1979). K-Ar age determinations of the Alta-Kvaenangen window rocks, northern Norway. *Norsk Geologisk Tidsskrift*, 59(2), 155–159.
- Giesemann, A., Jäger, H. J., Norman, A. L., Krouse, H. R., & Brand, W. A. (1994). On-Line Sulfur-Isotope Determination Using an Elemental Analyzer Coupled to a Mass Spectrometer. *Analytical Chemistry*, 66(18), 2816–2819. <https://doi.org/10.1021/ac00090a005>
- Goldstein, R. H. (2001). Fluid inclusions in sedimentary and diagenetic systems. *Lithos*, 55(1–4), 159–193. [https://doi.org/10.1016/S0024-4937\(00\)00044-X](https://doi.org/10.1016/S0024-4937(00)00044-X)

- Goldstein, R. H. (2003). Petrographic analysis of fluid inclusions. In I. Samson, A. Anderson, & D. Marshall (Eds.), *Fluid Inclusions: Analysis and Interpretation* (Vol. 32, pp. 9–43). Mineral. Assoc. Canada.
- Goldstein, R. H., & Reynolds, T. J. (1994). Systematics of Fluid Inclusions in Diagenetic Minerals. In *SEPM Short Course* (Vol. 31). <https://doi.org/10.2110/scn.94.31.0087>
- Gorbatshev, R., & Bogdanova, S. (1993). Frontiers in the Baltic Shield. *Precambrian Research*, 64(1–4), 3–21. [https://doi.org/10.1016/0301-9268\(93\)90066-B](https://doi.org/10.1016/0301-9268(93)90066-B)
- GTK. (2021). *Finnish Geosciences Research Laboratory*. (04.04.2021). <https://www.gtk.fi/en/research-infrastructure/finnish-geosciences-research-laboratory/>
- Günther, D., & Hattendorf, B. (2005). Solid sample analysis using laser ablation inductively coupled plasma mass spectrometry. *Trends in Analytic Chemistry*, 24(3), 255–265. <https://doi.org/10.1016/j.trac.2004.11.017>
- Hall, D. L., Sterner, S. M., & Bodnar, R. J. (1988). Freezing point depression of NaCl-KCl-H₂O solutions. *Economic Geology*, 83, 197–202.
- Heijlen, W., Banks, D. A., Muchez, P., Stensgard, B. M., & Yardley, B. W. D. (2008). The nature of mineralizing fluids of the Kipushi Zn-Cu deposit, Katanga, Democratic Republic of Congo: Quantitative fluid inclusion analysis using laser ablation ICP-MS and bulk crush-leach methods. *Economic Geology*, 103, 1459–1482. <https://doi.org/10.2113/gsecongeo.103.7.1459>
- Hilmo, J. B. (2021). *The geochemical signature of Cu mineralisation preserved in stream sediments from the Alta-Kvænangen Tectonic Window, Northern Norway*. UiT - The Arctic University of Norway, Master thesis.
- Hitzman, M., Kirkham, R., Broughton, D., Thorson, J., & Selley, D. (2005). The Sediment-Hosted Stratiform Copper Ore System. *Economic Geology*, 100th, 609–642. <https://doi.org/10.5382/av100.19>
- Hitzman, M. W. (2000). Source basins for sediment-hosted stratiform Cu deposits: Implications for the structure of the Zambian Copperbelt. *Journal of African Earth Sciences*, 30(4), 855–863. [https://doi.org/10.1016/S0899-5362\(00\)00056-7](https://doi.org/10.1016/S0899-5362(00)00056-7)
- Hitzman, Murray W., Selley, D., & Bull, S. (2010). Formation of sedimentary rock-hosted stratiform copper deposits through earth history. *Economic Geology*, 105(3), 627–639. <https://doi.org/10.2113/gsecongeo.105.3.627>
- Hoefs, J. (2018). *Stable Isotope Geochemistry* (8th ed.). Springer International Publishing AG. <https://doi.org/https://doi.org/10.1007/978-3-319-78527-1>
- Hollocher, K., Robinson, P., Walsh, E., & Roberts, D. (2012). American Journal of Science. *American Journal of Science*, 312(April), 357–416. <https://doi.org/10.2475/04.2012.01>
- Ilton, E. S., & Eugster, H. P. (1989). Base metal exchange between magnetite and a chloride-rich hydrothermal fluid. *Geochimica et Cosmochimica Acta*, 53(2), 291–301. [https://doi.org/10.1016/0016-7037\(89\)90381-5](https://doi.org/10.1016/0016-7037(89)90381-5)

- Irvine, T. N., & Baragar, W. R. A. (1971). A Guide to the Chemical Classification of the Common Volcanic Rocks. *Canadian Journal of Earth Sciences*, 8, 523–548.
- Ivanyuk, G. Y., Kalashnikov, A. O., Pakhomovsky, Y. A., Bazai, A. V., Goryainov, P. M., Mikhailova, J. A., Yakovenchuk, V. N., & Konopleva, N. G. (2017). Subsolidus Evolution of the Magnetite-Spinel-Ulvöspinel Solid Solutions in the Kovdor Phoscorite-Carbonatite Complex, NW Russia. *Minerals*, 7(11), 28. <https://doi.org/10.3390/min7110215>
- Janoušek, V., Farrow, C. M., & Erban, V. (2006). Interpretation of Whole-rock Geochemical Data in Igneous Geochemistry: Introducing Geochemical Data Toolkit (GCDkit). *Journal of Petrology*, 47(6), 1255–1259. <https://doi.org/10.1093/petrology/egl013>
- Karhu, J. A. (1993). Paleoproterozoic evolution of the carbon isotope ratios of sedimentary carbonates in the Fennoscandian Shield. In *Bulletin - Geological Survey of Finland* (Vol. 371). Geological tutkimuskeskus.
- Kirkham, R. V. (1989). Distribution, setting, and genesis of sediment-hosted stratiform copper deposits. *Geological Association of Canada, Special paper*, 3–38.
- Koch, J., & Günther, D. (2011). Review of the State-of-the-Art of Laser Ablation Inductively Coupled Plasma Mass Spectrometry. *Applied Spectroscopy*, 65(5), 155–162. <https://doi.org/10.1366/11-06255>
- Koistinen, T., Stephens, M. ., Bogatchev, V., Nordgulen, Ø., Wennerstrøm, M., & Korhonen, J. (2001). *Geological map of the Fennoscandian Shield; 1:2 mill.*
- Koziy, L., Bull, S., Large, R., & Selley, D. (2009). Salt as a fluid driver, and basement as a metal source, for stratiform sediment-hosted copper deposits. *Geology*, 37(12), 1107–1110. <https://doi.org/10.1130/G30380A.1>
- Lahtinen, R., Korja, A., & Nironen, M. (2005). Palaeoproterozoic tectonic evolution. In *Precambrian Geology of Finland - Key to the Evolution of the Fennoscandian Shield* (Vol. 14, Issue January, pp. 481–532). Elsevier B.V.
- Lahtinen, R., Korja, A., Nironen, M., & Heikkinen, P. (2009). Palaeoproterozoic accretionary processes in Fennoscandia. *Geological Society, London, Special Publications*, 318, 237–256. <https://doi.org/10.1144/SP318.8>
- Lambrecht, G., & Diamond, L. W. (2014). Morphological ripening of fluid inclusions and coupled zone-refining in quartz crystals revealed by cathodoluminescence imaging: Implications for CL-petrography, fluid inclusion analysis and trace-element geothermometry. *Geochimica et Cosmochimica Acta*, 141, 381–406. <https://doi.org/10.1016/j.gca.2014.06.036>
- Laurence, R. (2020). *Introduction to Ore-Forming Processes* (2nd ed.). Wiley-Blackwell.
- Laux, S. J. (1972). *Report of mapping done in the Kvænangen window, near Baddern. N. Troms.*
- Lawler, J. P., & Crawford, M. L. (1983). Stretching of fluid inclusions resulting from a low-temperature microthermometric technique. *Economic Geology*, 78(4), 527–529.

- Lesnov, S. P. (2010). *Rare Earth Elements in Ultramafic and Mafic Rocks and their Minerals*. Taylor & Francis Group.
- Lydon, J. W. (1998). Volcanogenic massive sulphide deposits. Part 2: Genetic models. *Geoscience Canada*, 15, 43–65.
- MacKevett, E. M. J., Cox, D. P., Potter, R. W. I., & Silberman, M. L. (1997). Kennecott-Type Deposits in the Wrangell Mountains, Alaska: High-Grade Copper Ores near a Basalt-Limestone Contact. In R. J. Goldfarb & L. D. Miller (Eds.), *Mineral Deposits of Alaska* (pp. 68–89). Economic Geology. <https://doi.org/doi.org/10.5382/Mono.09>
- Melezhik, V. A., Bingen, B., Sandstad, J. S., Pokrovsky, B. G., Solli, A., & Fallick, A. E. (2015). Sedimentary-volcanic successions of the Alta–Kvænangen Tectonic Window in the northern Norwegian Caledonides: Multiple constraints on deposition and correlation with complexes on the Fennoscandian Shield. *Norsk Geologisk Tidsskrift*, 95(3), 1–40. <https://doi.org/10.17850/njg95-3-01>
- Melezhik, V. A., & Fallick, A. E. (2010). On the Lomagundi-Jatuli carbon isotopic event: The evidence from the Kalix Greenstone Belt, Sweden. *Precambrian Research*, 179(1–4), 165–190. <https://doi.org/10.1016/j.precamres.2010.03.002>
- Melezhik, V. A., Huhma, H., Condon, D. J., Fallick, A. E., & Whitehouse, M. J. (2007). Temporal constraints on the Paleoproterozoic Lomagundi-Jatuli carbon isotopic event. *Geology*, 35(7), 655–658. <https://doi.org/10.1130/G23764A.1>
- Melezhik, V. A., Prave, A. R., Hanski, E. J., Fallick, A. E., Lepland, A., Kump, L. R., & Strauss, H. (2013). Volume 1: The Palaeoproterozoic of Fennoscandia as Context for the Fennoscandian Arctic Russia - Drilling Early Earth Project. In *Reading the Archive of Earth's Oxygenation*.
- Middlemost, E. A. K. (1994). Naming materials in the magma / igneous rock system. *Earth-Science Reviews*, 37, 215–224.
- MinExTarget. (2020). *Enhanced Use of Heavy Mineral Chemistry in Exploration Targeting*. <http://projects.gtk.fi/minextarget/index.html>
- Moberg, A. (1968). *Kopparverket i Kåfjord. Ett bidrag til Nordkalottens historia*. Norbottens Museum, 1968.
- Mørk, K. J. (1970). *Bergvesenet Rapportarkivet; En geologisk undersøkelse av området omkring Kåfjord kobbergruve, Kåfjord i Alta, Finnmark*.
- Mun, Y., Palinkaš, S. S., Kullerud, K., Nilsen, K. S., & Bekker, A. (2020). Evolution of metal-bearing fluids at the Nussir and Ulveryggen sediment-hosted Cu deposits, Repparfjord Tectonic Window, northern Norway. *Norwegian Journal of Geology*, 53. <https://doi.org/https://dx.doi.org/10.17850/njg100-2-5>.
- Nath, N. B., Roelandts, I., Sudhakar, M., Plüger, W. L., & Balaram, V. (1994). Cerium anomaly variations in ferromanganese nodules and crusts from the Indian Ocean. *Marine Geology*, 120(3–4), 385–400. [https://doi.org/10.1016/0025-3227\(94\)90069-8](https://doi.org/10.1016/0025-3227(94)90069-8)
- Neikov, O. D., & Yefimov, N. A. (2018). Chapter 1 - Powder Characterization and Testing.

- In S. Naboychenko (Ed.), *Handbook of Non-Ferrous Metal Powders: Technologies and Applications* (2nd ed., p. 1972). Elsevier.
- Neumann, U. (2019). *Guide for the microscopical identification of ore and gangue minerals*. Tübingen University Press 2019. <https://doi.org/http://dx.doi.org/10.15496/publikation-31274>
- NGU. (2021a). *1:250 000 bedrock map*. (19.01.2021). https://geo.ngu.no/kart/berggrunn_mobil/
- NGU. (2021b). *1:50 000 bedrock map*. (19.01.2021). https://geo.ngu.no/kart/berggrunn_mobil/
- NGU. (2021c). *Geophysical map*. (23.01.2021). <https://geo.ngu.no/geoscienceportalopen/>
- NGU. (2021d). *Mineralressurser*. (27.01.2021). https://geo.ngu.no/kart/mineralressurser_mobil/
- Nironen, M. (1997). The Svecofennian Orogen: a tectonic model. *Precambrian Research*, 86, 21–44.
- Nordgulen, Ø., & Andresen, A. (2013). De eldste bergartene dannes. In I. B. Ramberg, I. Bryhni, A. Nøttvedt, & K. Rangnes (Eds.), *Landet blir til - Norges geologi* (2nd ed., p. 656). Norsk Geologisk Forening.
- Norge i bilder. (2021). *Orthophoto*. (19.01.21). <https://www.norgebilder.no/>
- Outridge, P. M., Doherty, W., & Gregoire, D. C. (1997). Ablative and transport fractionation of trace elements during laser sampling of glass and copper. *Spectrochimica Acta Part B*, 52, 2093–2102.
- Pat Shanks III, W. C. (2014). Stable Isotope Geochemistry of Mineral Deposits. In *Treatise on Geochemistry* (2nd ed., Vol. 13, pp. 59–85). Elsevier Ltd. <https://doi.org/10.1016/B978-0-08-095975-7.01103-7>
- Perello, J., Sillitoe, R. H., Yakubchuk, A. S., Victor, A. V., & Cornejo, P. (2016). The Udokan Cu – Ag deposit in Transbaikalian Russia is one of the largest individual SC. *Ore Geology Reviews*, 46. <https://doi.org/10.1016/j.oregeorev.2016.11.004>
- Révész, K. M., & Landwehr, J. M. (2002). $\delta^{13}\text{C}$ and $\delta^{18}\text{O}$ isotopic composition of CaCo_3 measured by continuous flow isotope ratio mass spectrometry: Statistical evaluation and verification by application to Devils Hole core DH-11 calcite. *Rapid Communications in Mass Spectrometry*, 16(22), 2102–2114. <https://doi.org/10.1002/rcm.833>
- Roedder, E. (1984). Fluid inclusions. In P. H. Ribbe (Ed.), *Reviews in Mineralogy* (Vol. 12). Mineralogical Society of America.
- Sandstad, J. S., & Torgersen, E. (2019). Sediment-Hosted Cu-Deposits. *NGU Focus*, 2, 2.
- Sawkins, F. J. (1976). Massive sulphide deposits in relation to geotectonics. In D. F. Strong (Ed.), *Metallogeny and Plate Tectonics* (pp. 221–240). Geological Association of Canada.

- Scott, S. D. (1997). Submarine hydrothermal systems and deposits. In H. L. Barnes (Ed.), *Geochemistry of Hydrothermal Ore Deposits* (3rd ed., pp. 797–875). Wiley.
- Seal, R. R. (2006). Sulfur Isotope Geochemistry of Sulfide Minerals. *Reviews in Mineralogy and Geochemistry*, 61, 633–677. <https://doi.org/10.2138/rmg.2006.61.12>
- Shau, Y.-H., Torii, M., Horng, C.-S., & Peacor, D. R. (2000). Subsolidus evolution and alteration of titanomagnetite in ocean ridge basalts from Deep Sea Drilling Project/Ocean Drilling Program Hole 504B, Leg 83: Implications for the timing of magnetization. *Journal of Geophysical Research*, 105(B10), 23,635–23,649. <https://doi.org/10.1029/2000jb900191>
- Shepherd, T. J., Rankin, A. H., & Alderton, D. H. M. (1985). *A practical Guide to Fluid Inclusion Studies*. Blackie & Son Limited.
- Shervais, J. W. (1982). Ti-V plots and the petrogenesis of modern ophiolitic lavas. *Earth and Planetary Science Letters*, 59, 101–118. [https://doi.org/10.1016/0012-821X\(82\)90120-0](https://doi.org/10.1016/0012-821X(82)90120-0)
- Stakes, D. S., & O'Neil, J. R. (1982). Mineralogy and stable isotope geochemistry of hydrothermally altered oceanic rocks. *Earth and Planetary Science Letters*, 57(2), 285–304. [https://doi.org/10.1016/0012-821X\(82\)90151-0](https://doi.org/10.1016/0012-821X(82)90151-0)
- Steele-MacInnis, M., Bodnar, R. J., & Naden, J. (2011). Numerical model to determine the composition of H₂O-NaCl-CaCl₂ fluid inclusions based on microthermometric and microanalytical data. *Geochimica et Cosmochimica Acta*, 75(1), 21–40. <https://doi.org/10.1016/j.gca.2010.10.002>
- Steele-MacInnis, M., Han, L., Lowell, R. P., Rimstidt, J. D., & Bodnar, R. J. (2012). The role of fluid phase immiscibility in quartz dissolution and precipitation in sub-seafloor hydrothermal systems. *Earth and Planetary Science Letters*, 321–322, 139–151. <https://doi.org/10.1016/j.epsl.2011.12.037>
- Sterner, S. M., Hall, D. L., & Bodnar, R. J. (1988). Synthetic fluid inclusions. V. Solubility relations in the system NaCl-KCl-H₂O under vapor-saturated conditions. *Geochimica et Cosmochimica Acta*, 52(5), 989–1005. [https://doi.org/10.1016/0016-7037\(88\)90254-2](https://doi.org/10.1016/0016-7037(88)90254-2)
- Sverjensky, D. A. (1987). The Role of Migrating Oil Field Brines in the Formation of Sediment-Hosted Cu-Rich Deposits. *Economic Geology*, 82, 1130–1141. <https://doi.org/10.2113/gsecongeo.82.5.1130>
- Tiwari, M., Singh, A. K., & Sinha, D. K. (2015). Stable isotopes: tools for understanding past climatic conditions and their applications in chemostratigraphy. In M. Ramkumar (Ed.), *Chemostratigraphy: concepts, techniques, and applications* (p. 516). Elsevier Inc.
- Veizer, J., & Hoefs, J. (1976). The nature of O¹⁸/O¹⁶ and C¹³/C¹² secular trends in sedimentary carbonate rocks. *Geochimica et Cosmochimica Acta*, 40(11), 1387–1395. [https://doi.org/10.1016/0016-7037\(76\)90129-0](https://doi.org/10.1016/0016-7037(76)90129-0)
- Vik, E. (1985). *En geologisk undersøkelse av kobbermineraliseringene i Alta-Kvænangenvinduet, Troms og Finnmark*. Universitetet i Trondheim, Norges Tekniske Høgskole.

- Weihed, P., Arndt, N., Billström, K., Duchesne, J.-C., Eilu, P., Martinsson, O., Papunen, H., & Lahtinen, R. (2005). 8: Precambrian geodynamics and ore formation: The Fennoscandian Shield. *Ore Geology Reviews*, 27(1–4), 273–322. <https://doi.org/10.1016/j.oregeorev.2005.07.008>
- Whitney, D. L., & Evans, B. W. (2010). Abbreviations for names of rock-forming minerals. *American Mineralogist*, 95(1), 185–187. <https://doi.org/10.2138/am.2010.3371>
- Yongsheng, L., Zhaochu, H., Ming, L., & Shan, G. (2013). Applications of LA-ICP-MS in the elemental analyses of geological samples. *Chinese Science Bulletin*, 58(32), 3863–3878. <https://doi.org/10.1007/s11434-013-5901-4>
- Zwaan, K. B., & Gautier, A. M. (1980). *Alta og Gargia Beskrivelse til de berggrunnsgeologiske kart 1834 I og 1934 IV -M 1:50000 (Med fargetrykte kart)*. 357.

Appendices

Appendix A: Mineral abbreviations

Table A1: Mineral abbreviations obtained from Whitney and Evans (2010).

Symbol	Mineral name	Symbol	Mineral name
Ab	Albite	Ilm	Ilmenite
Afs	Alkali feldspar (Group)	Kfs	K-feldspar
Amp	Amphibole (Group)	Mag	Magnetite
Ank	Ankerite	Mol	Molybdenite
Bt	Biotite (Group)	Ms	Muscovite
Bn	Bornite	Ol	Olivine
Cal	Calcite	Opx	Orthopyroxene
Cb	Carbonate mineral (Group)	Pn	Pentlandite
Cct	Chalcocite	Pl	Plagioclase
Ccp	Chalcopyrite	Py	Pyrite
Chl	Chlorite (Group)	Po	Pyrrhotite
Cpx	Clinopyroxene (Group)	Qt	Quartz
Cv	Covellite	Rt	Rutile
Dg	Digenite	Sp	Sphalerite
Dol	Dolomite	Tnt	Tennantite
Gn	Galena	Ttn	Titanite
Hem	Hematite		

Appendix B: Additional isotope drill marks

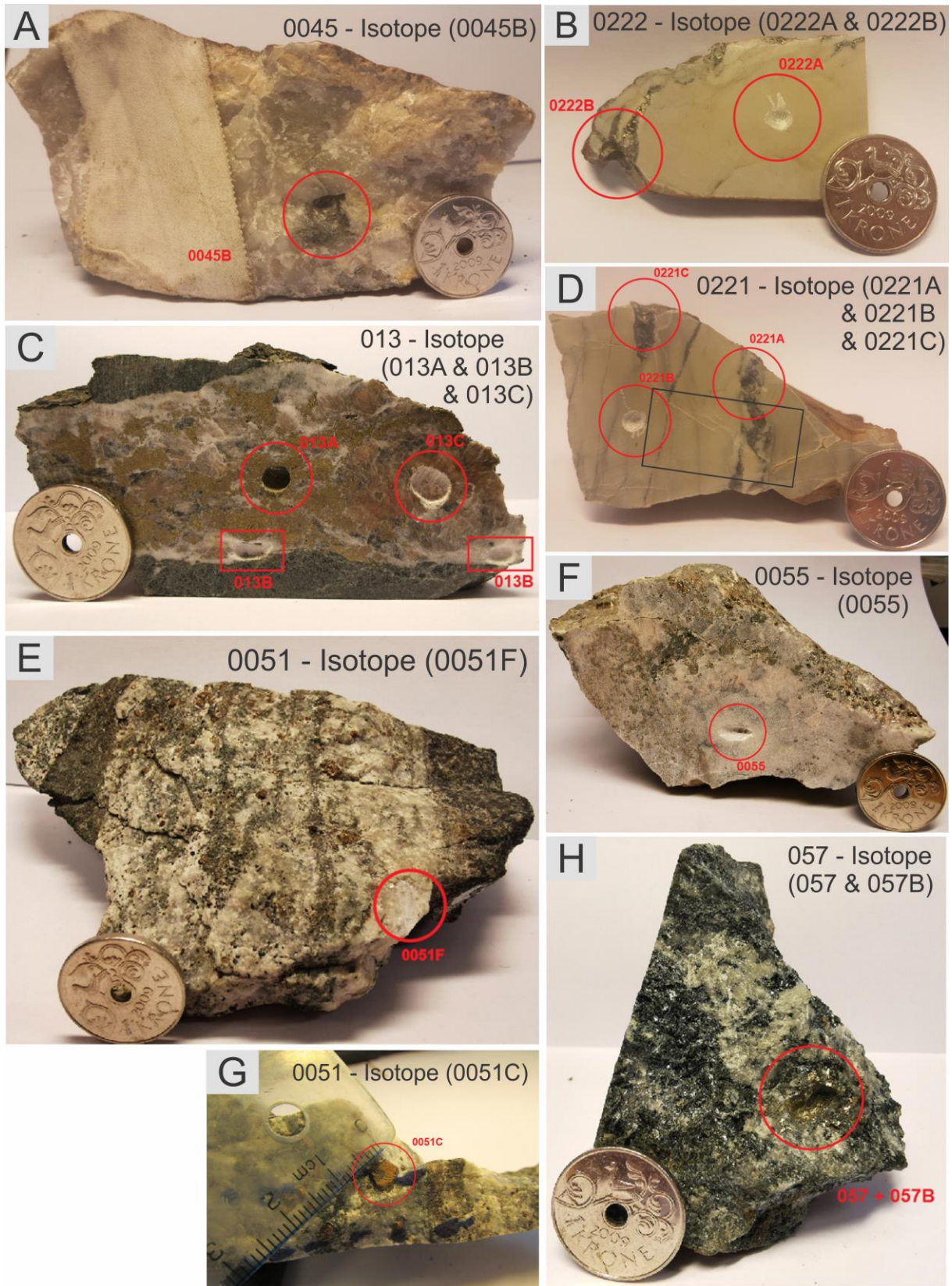


Figure D1: (A) Hand sample 0045 with sulfur isotope sample 0045B marked within the red circle; (B) Hand sample 0222 with carbonate isotope samples 0222A and sulfur isotope 0222B marked; (C) Hand sample 013 with sulfur isotope sample 013A and carbonate isotope samples 013B & 013C marked; (D) Hand sample 0221 with sulfur isotope samples 0221A & 0221C and carbonate isotope sample 0221B indicated by three red circles. The

approximately location of thin section 0221 is marked by the black rectangle; (E) Hand sample 0051 with carbonate isotope sample 0051F marked; (F) Hand sample 0055 with carbonate isotope sample 0055; (G) Hand sample 0051 with sulfur isotope sample 0051C marked; (H) Hand sample 057 with sulfur isotope sample 057 and 057B marked, drilled from the same spot.

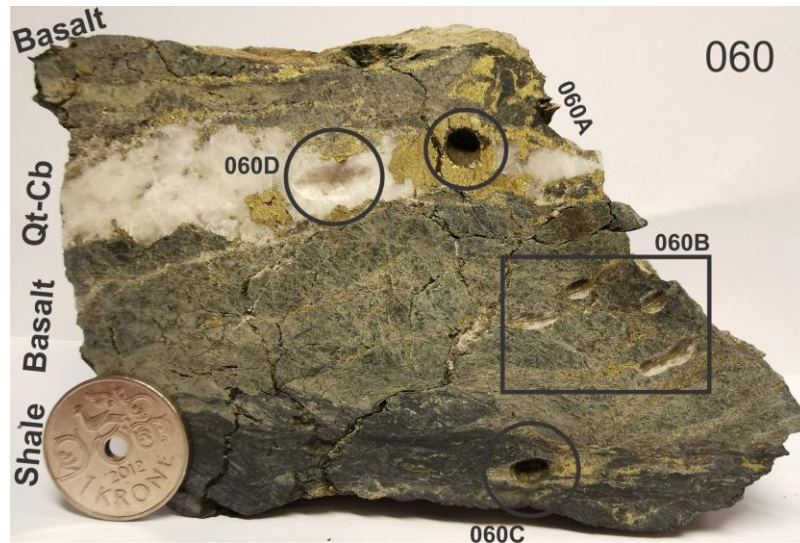


Figure D2: Sample 060 with three circles and one rectangle indicating the four isotope samples; 060A: Sulfur isotope within quartz-carbonate vein; 060B: Sulfur isotope within basalt; 060C: Sulfur isotope within shale; 060D: Carbonate isotope within quartz-carbonate vein. Abbreviations: Qt-Cb: Quartz-Carbonate.

Note: One sample from each of the four carbonate layers at locality Anna was supposed to be analyzed by carbonate isotope, but as sample 036 from the first layer most probably was held back in the custom, it was not analyzed in the first batch. A second batch with nine carbonate and two sulfur isotope samples, including a new sample 036 was then delivered to the Stable Isotope Laboratory at CAGE, UiT, for analysis in January. Only the two sulfur isotope samples were analyzed before the machine at the lab broke down. The nine carbonate samples were then sent to the lab in Switzerland to be analyzed there, but no results have come back yet (Mid-May) and will therefore be excluded from this thesis. Drill marks for all those nine samples are marked on the figures within the locality descriptions and some here in the Appendix, which includes following isotope samples; 036, 051C, 057C, 060D, 0051D, 0051E, 0051F, 0052B and 0055. The reason it has been added to the thesis is the thought that it can be used by others.

Appendix C: Mineral composition from literature

Table C1: Ideally composition of different minerals from Barthelmy (2012). Have been used to compare with SEM-EDS data.

<u>Ideal composition of minerals</u>	
Pyrite	Fe: 46,55% S: 53,45%
Chalcopyrite	Fe: 30,43% Cu: 34,63% S: 34,94%
Magnetite	Fe: 72,35% O: 27,64%
Titanite	Ca: 19,25% REE: 3,64% Ti: 18,16% Al: 2,73 Fe: 1,41 Si: 14,20 O: 39,64% F: 0,96%
Rutile	Ti: 59,94% O: 40,06%
Ilmenite	Ti: 31,56% Fe: 36,81% O: 31,63%
Bornite	Fe: 11,13 Cu: 63,31 S: 25,56
Digenite	Cu: 78,10% S: 21,90%
Chalcocite	Cu: 79,85% S: 20,15%
Djurleite	Cu: 79,34% S: 20,66%
Galena	Pb: 86,60% S: 13,40%
Wittichenite	Cu: 38,45% Bi: 42,15% S: 19,40%
Tennantite	Fe: 3,80% Cu: 47,51% As: 20,37% S: 28,33%
Pyrrhotite	Fe: 62,33% S: 37,67%
Pentlandite	Fe: 32,56% Ni: 34,21% S: 33,23%
Molybdenite	Mo: 59,94% S: 40,06%
Wulfenite	Mo: 26,13% Pb: 56,44% O: 17,43%
Covellite	Cu: 66,46% S: 33,54%

Table C1: Continued

Dolomite	Ca: 21,7% Mg: 13,18% C: 13,03% O: 52,06%
Ankerite	Ca: 19,42% Mg: 3,53% Mn: 2,66% Fe: 16,24% C: 11,64% O: 46,51
Calcite	Ca: 40,04% C: 12,00% O: 47,96%
Sphalerite	Zn: 64,04% Fe: 2,88% S: 33,06
Albite	Na: 8,30% Ca: 0,76% Al: 10,77% Si: 31,50% O: 48,66%

Appendix D: LA-ICP-MS spots

The quality of the following pictures are low as the total file size approached the limits. The scale is hard to see but it is 100 μm for all pictures. Spots not ablated are marked with a cross, and the reason for not ablating these spots are due to these mineral phases contained too much lead for LA-ICP-MS.

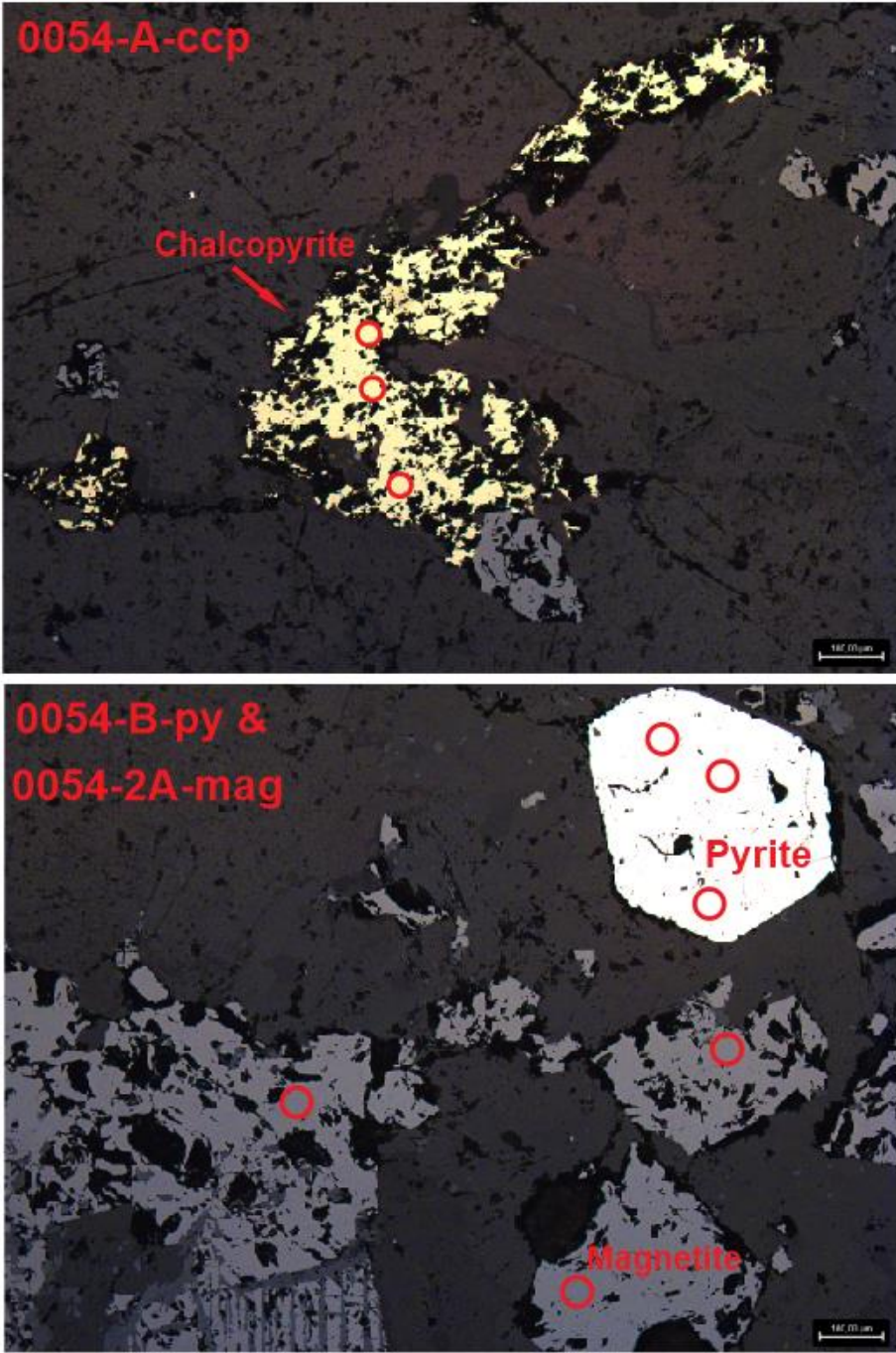


Figure D1: RLM PPL pictures of the ablated spots (LA-ICP-MS) in different mineral phases.

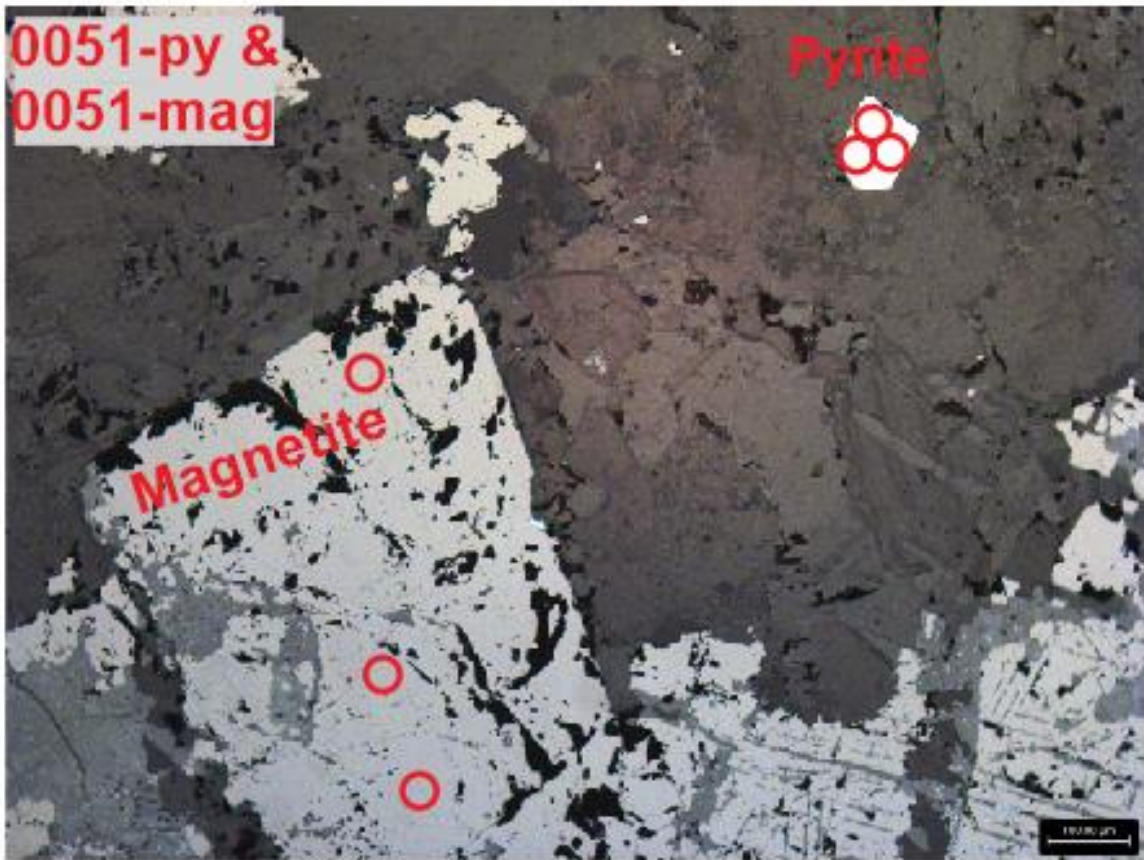
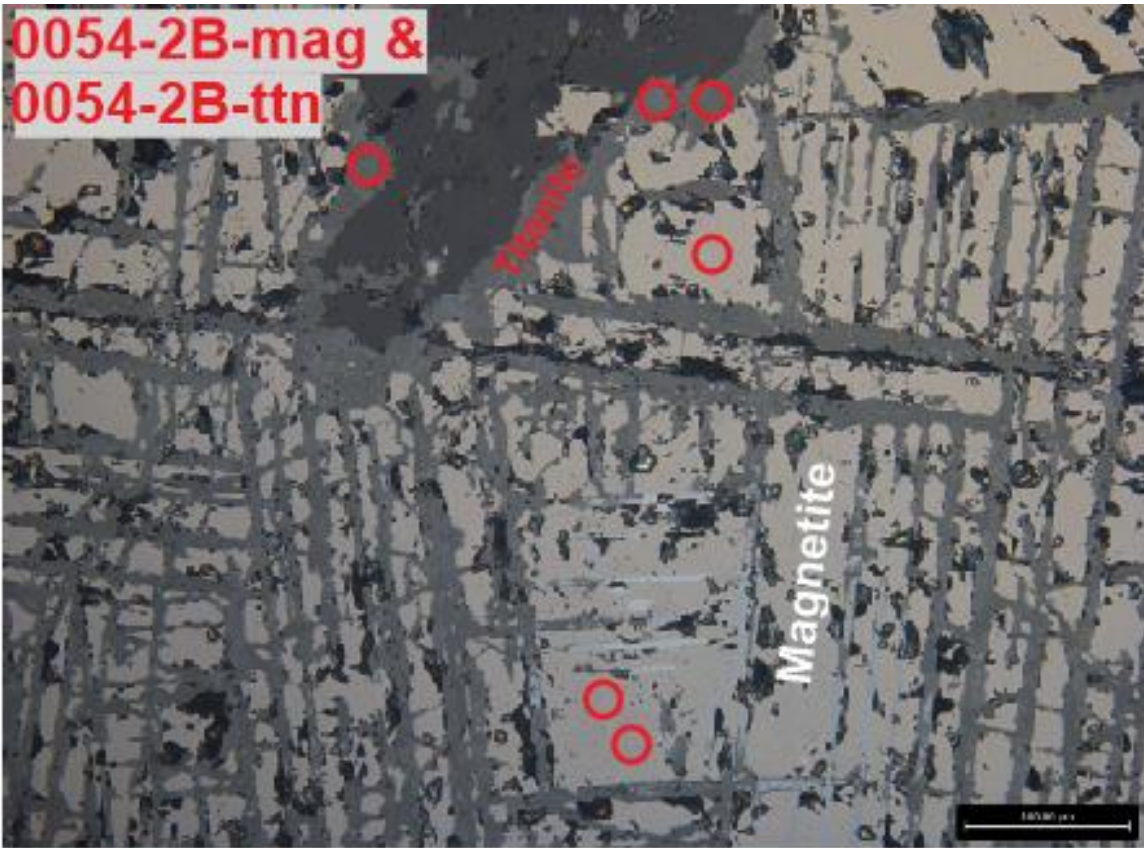


Figure D1: Continued.

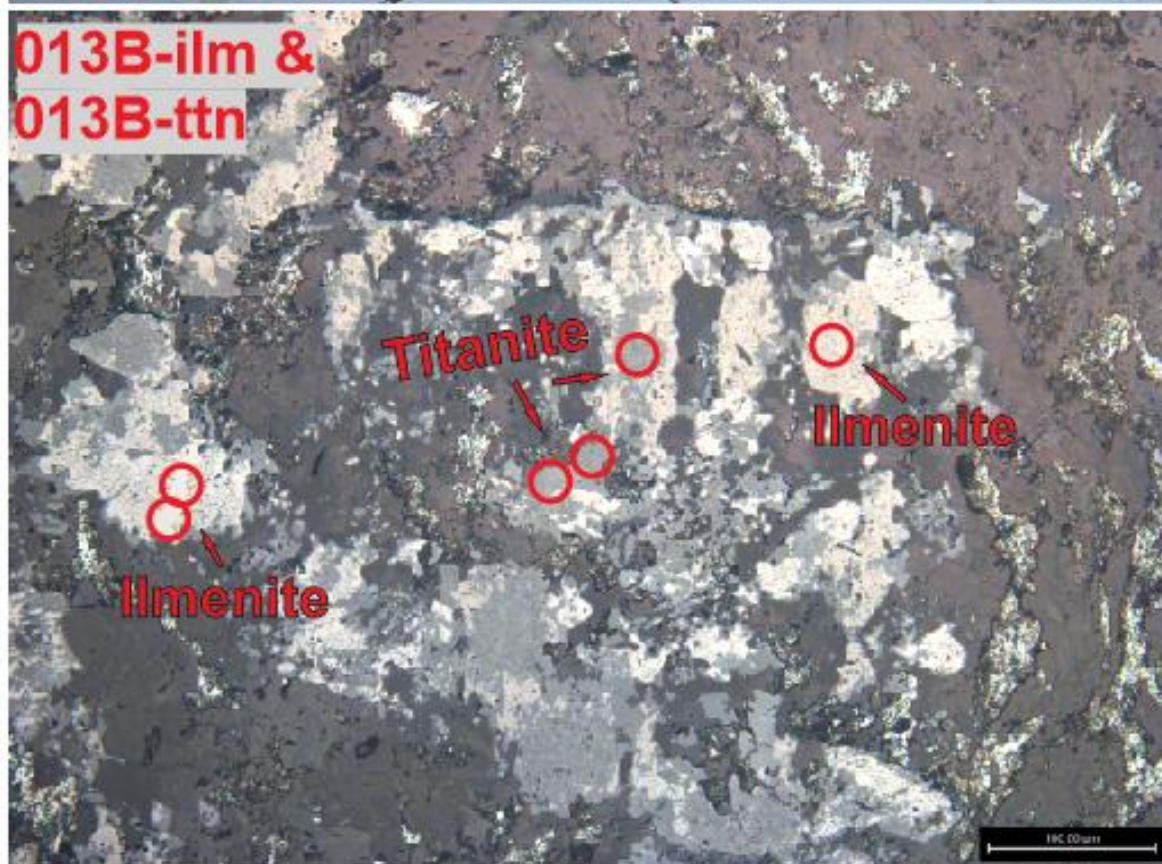
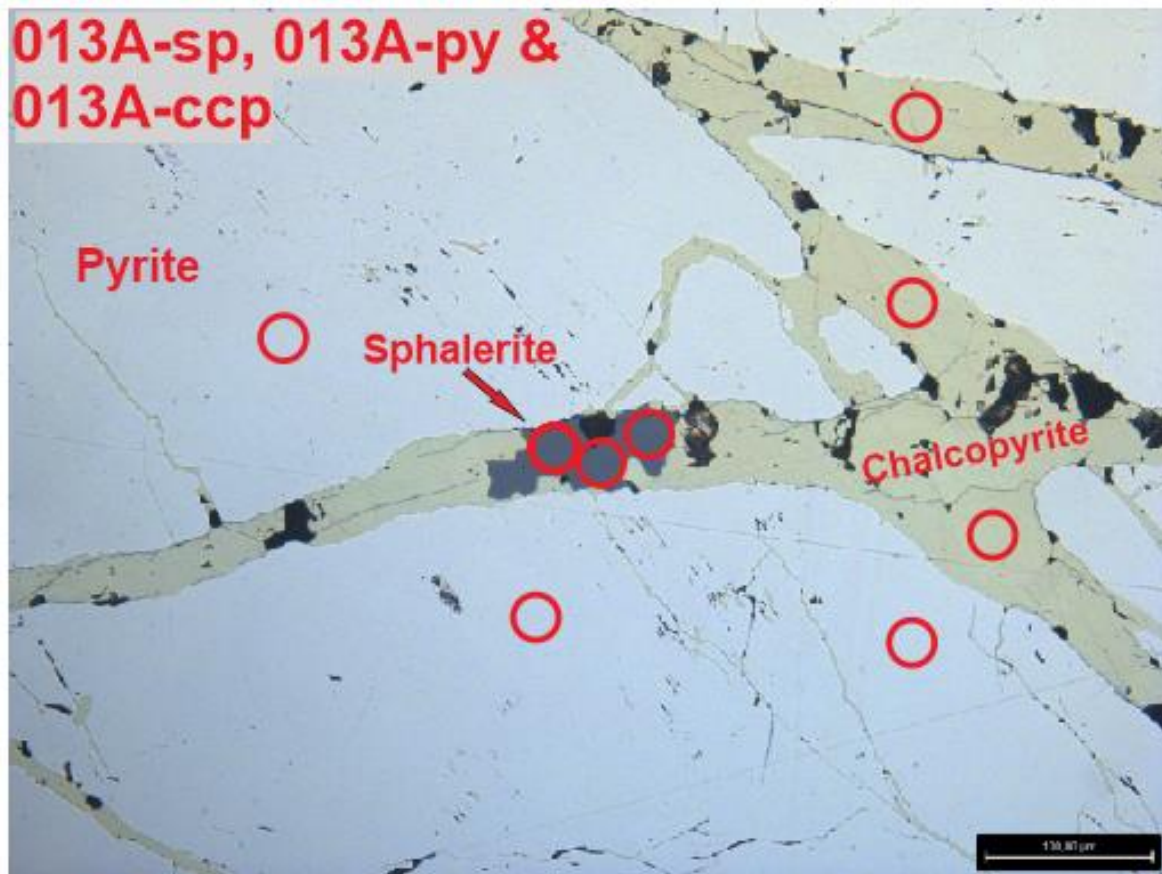


Figure D1: Continued.

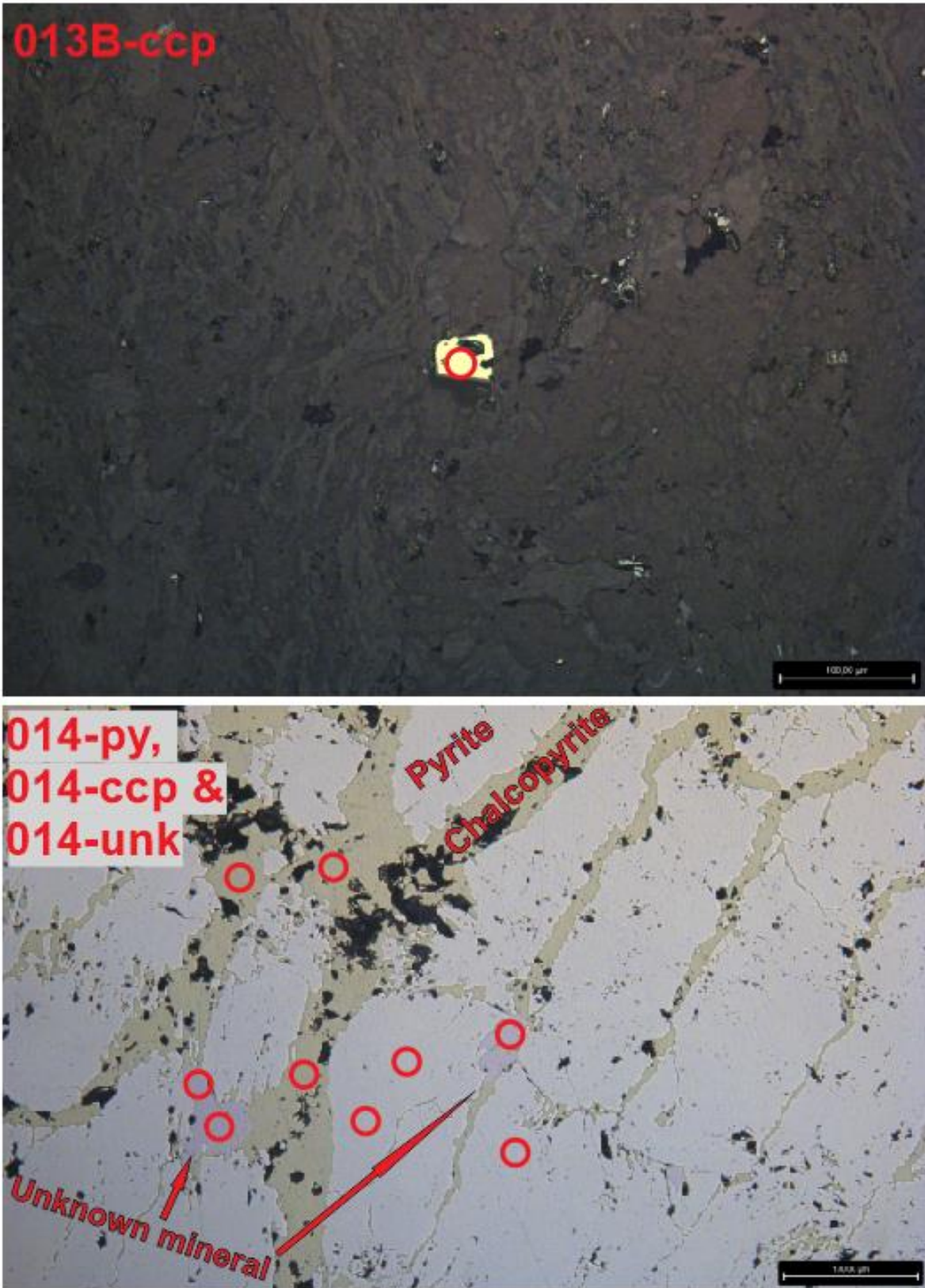


Figure D1: Continued. Only two of the three spots in the unknown mineral have been ablated.

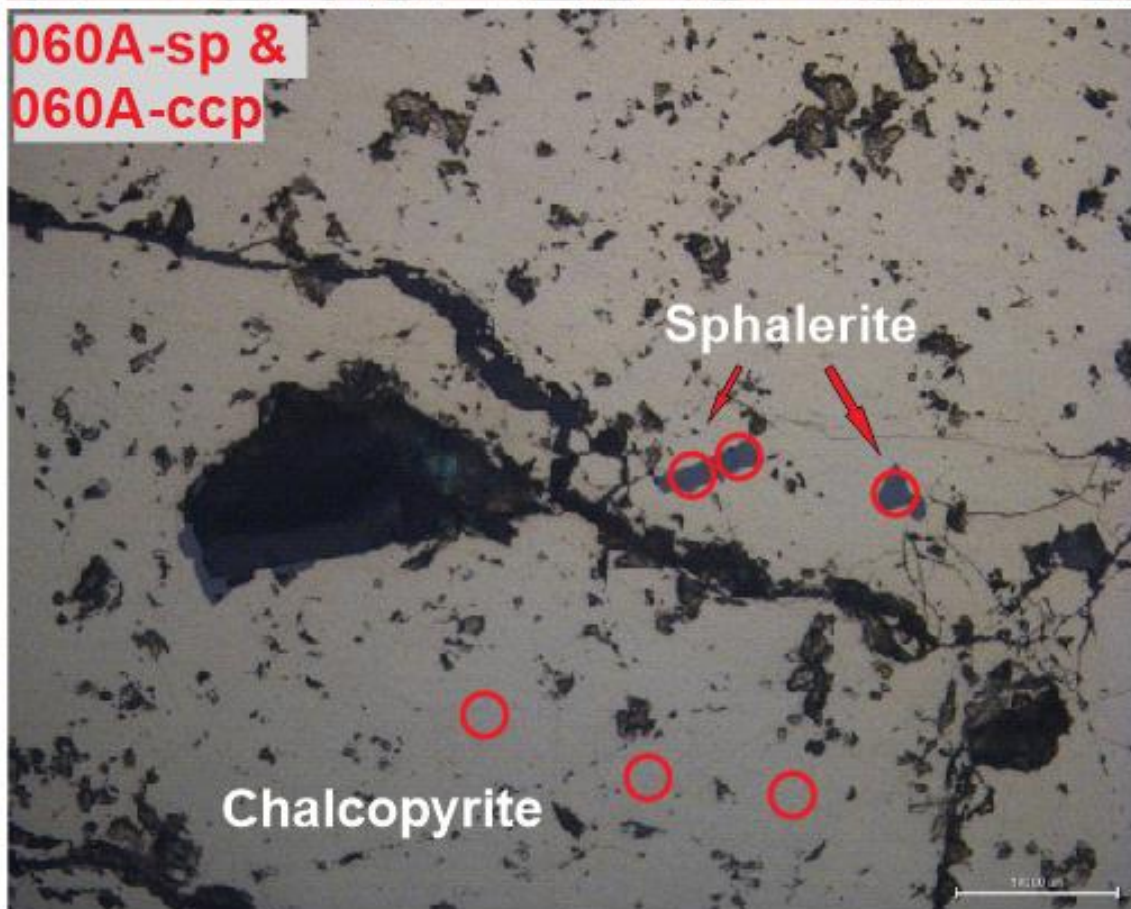
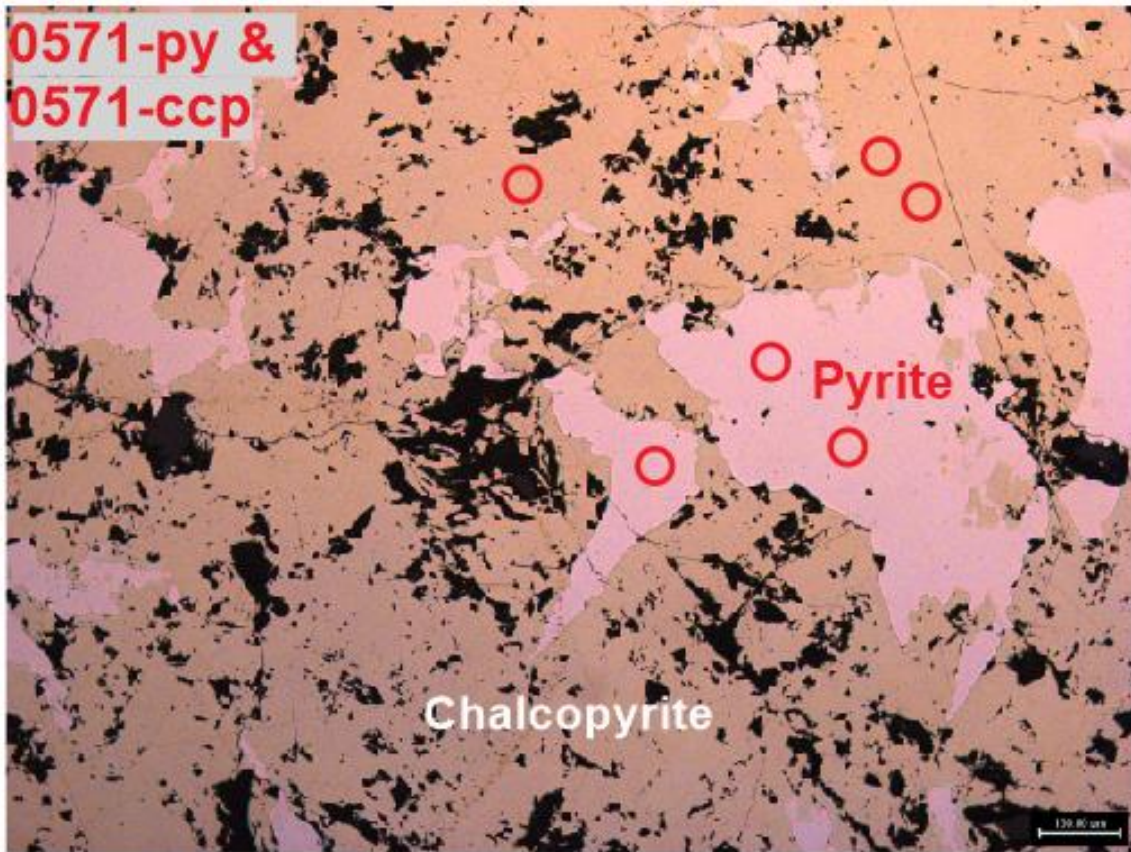


Figure D1: Continued.

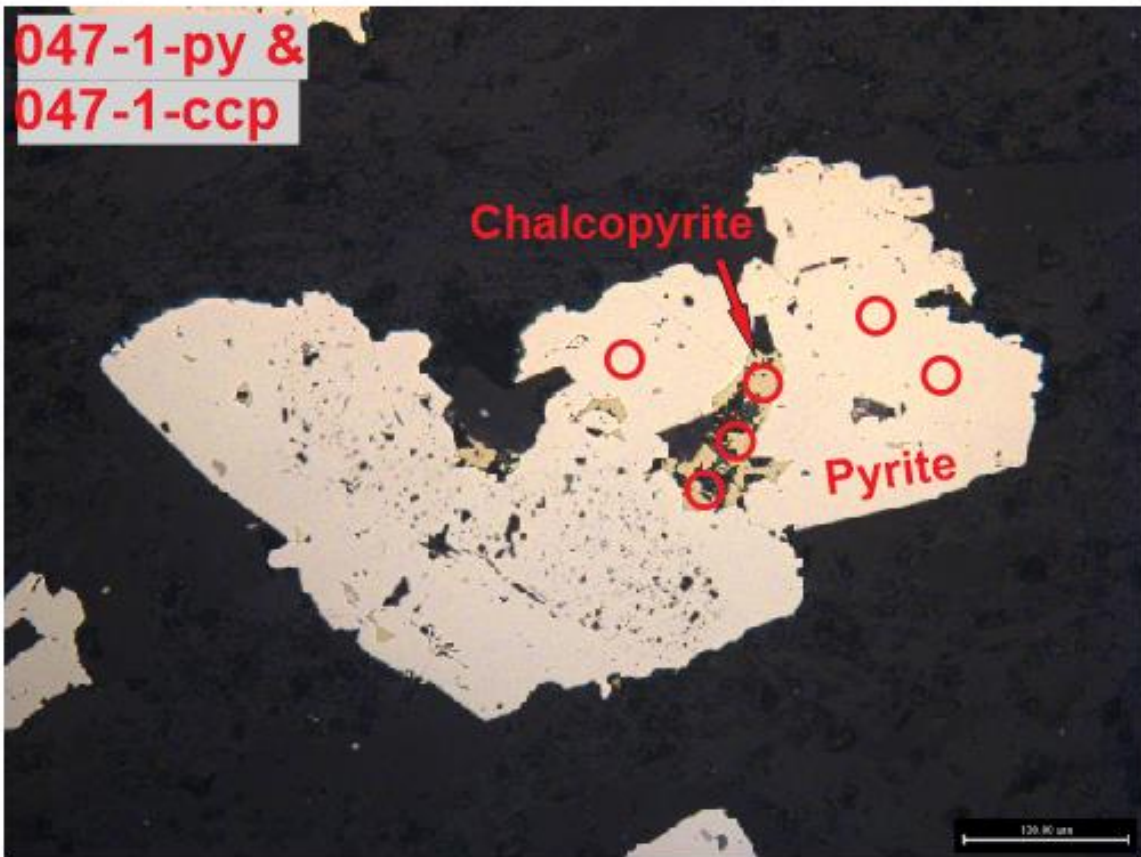
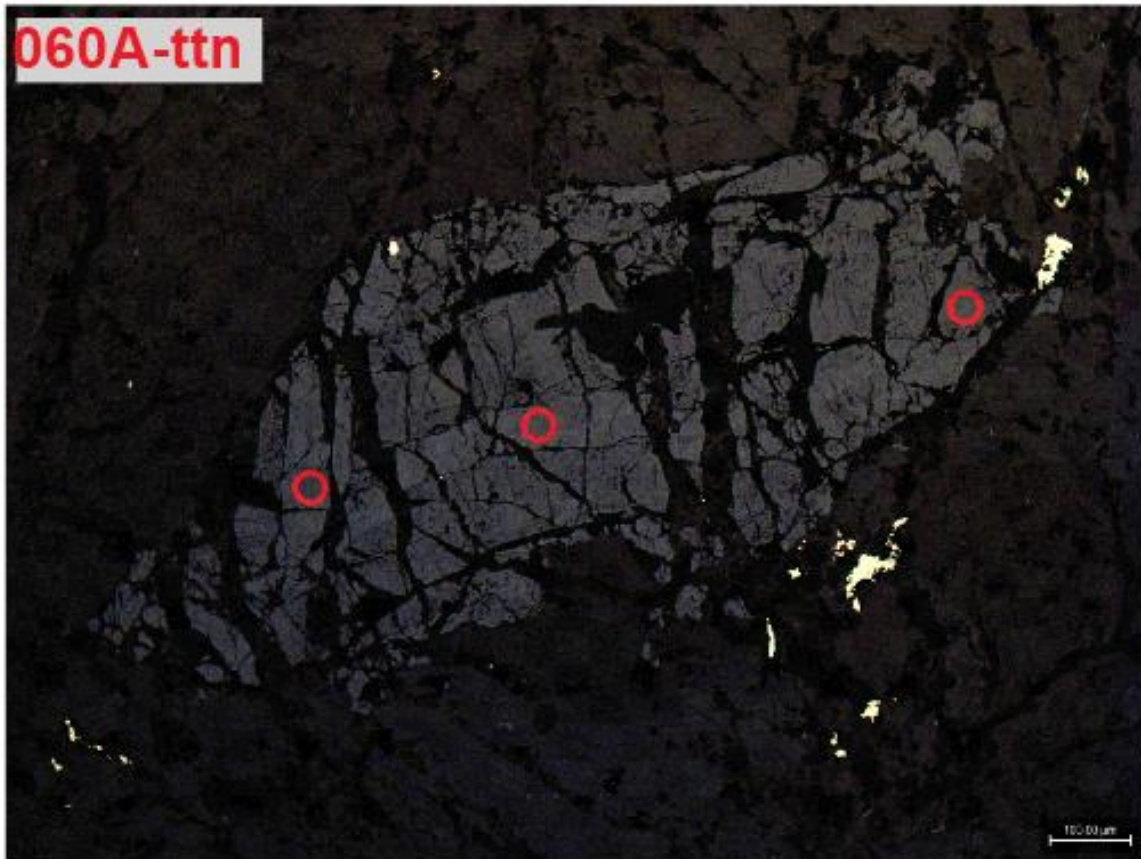


Figure D1: Continued.

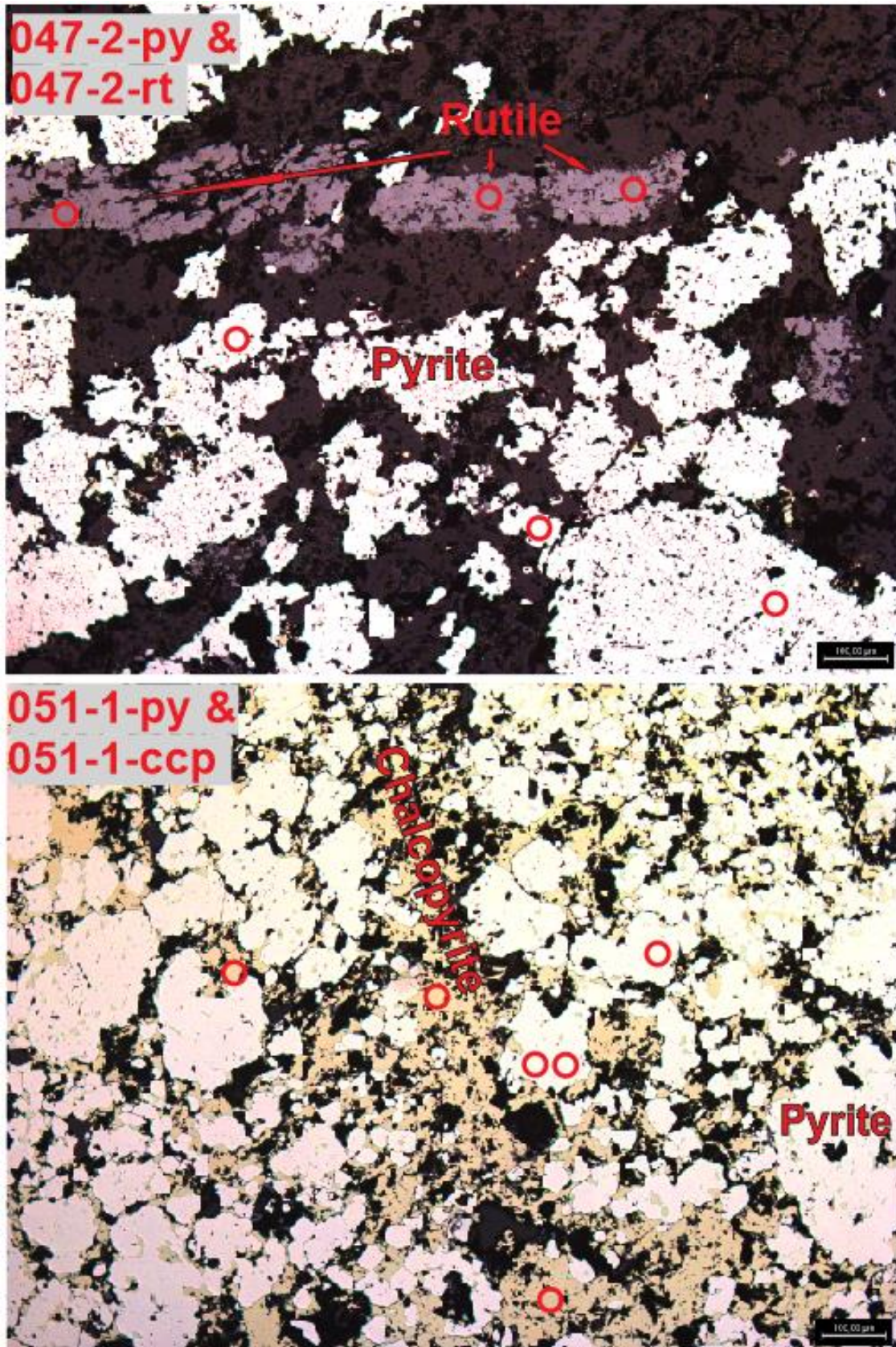


Figure D1: Continued. What should be marked here is that two spots in the pyrite and four spots in the rutile (in sample 047, 047-2-py and 047-2-rt) have been ablated, even though three spots in each mineral were marked.

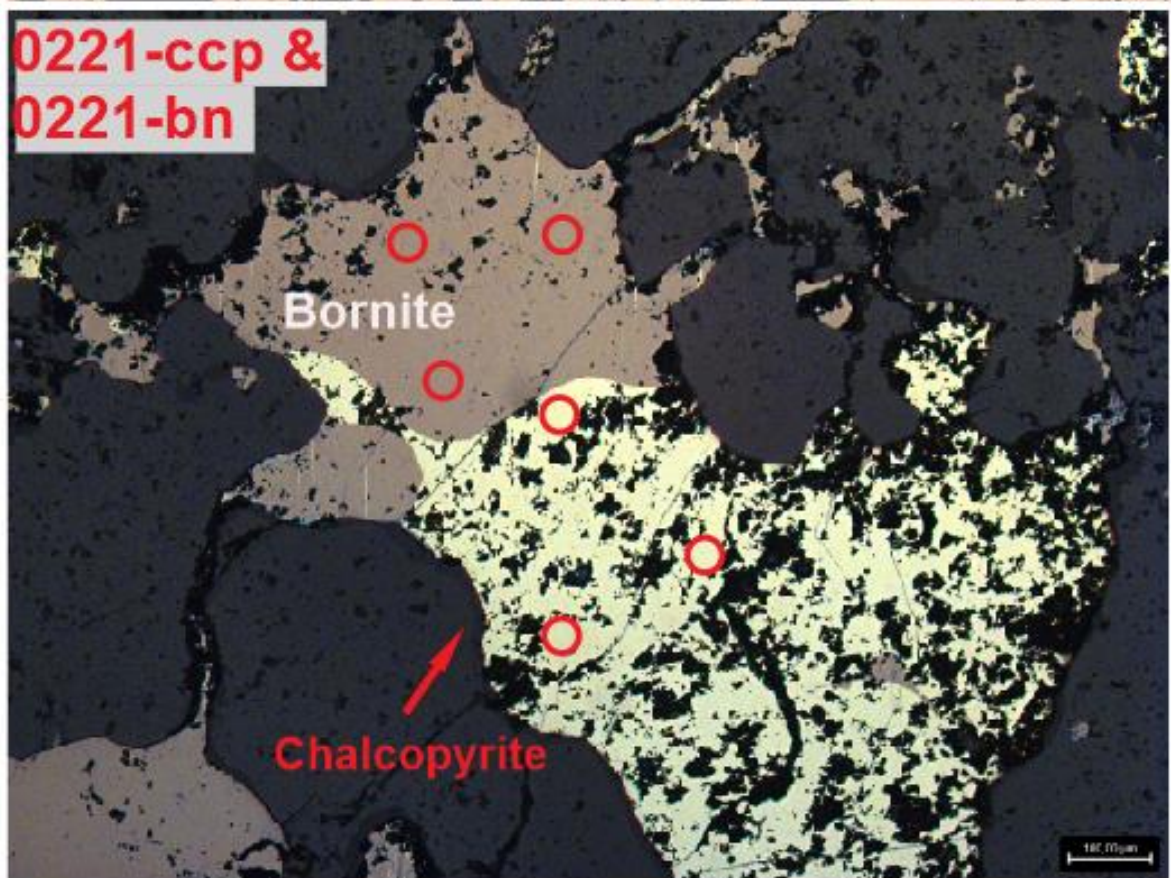
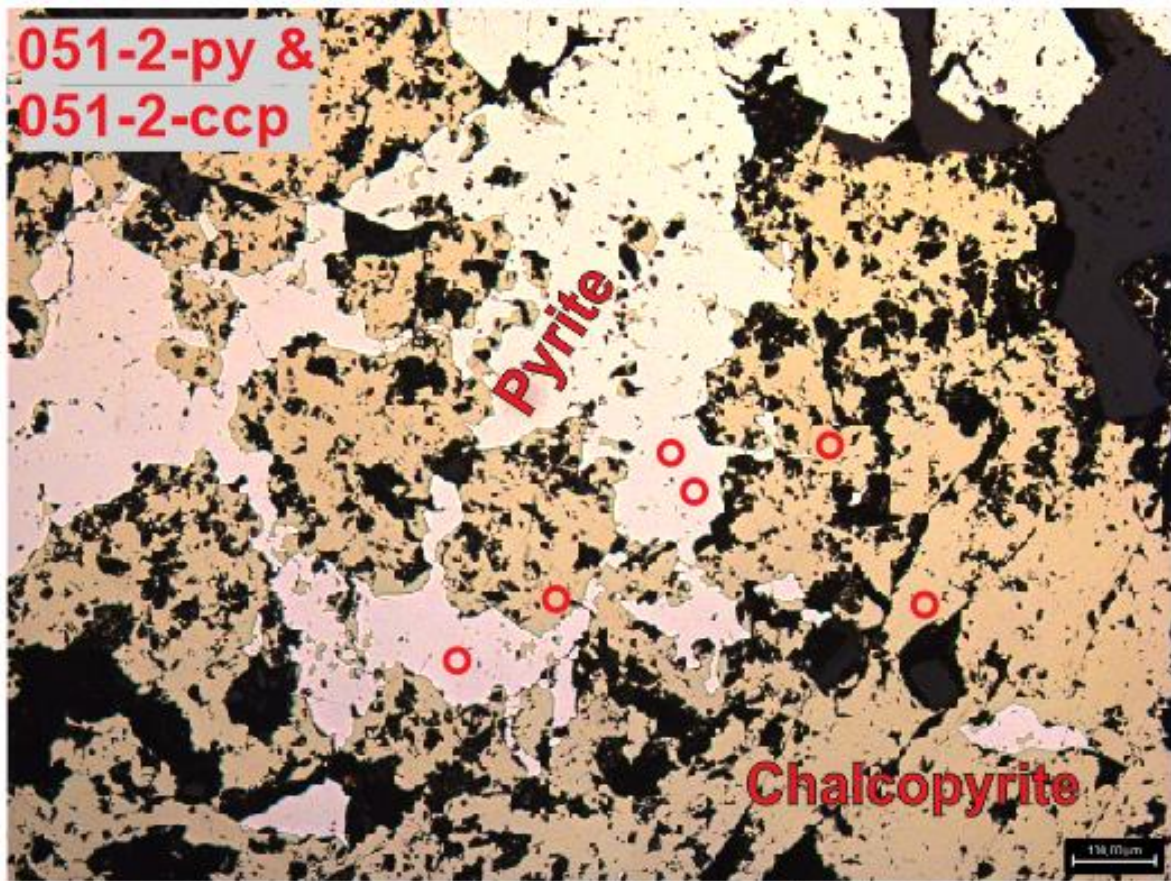


Figure D1: Continued.

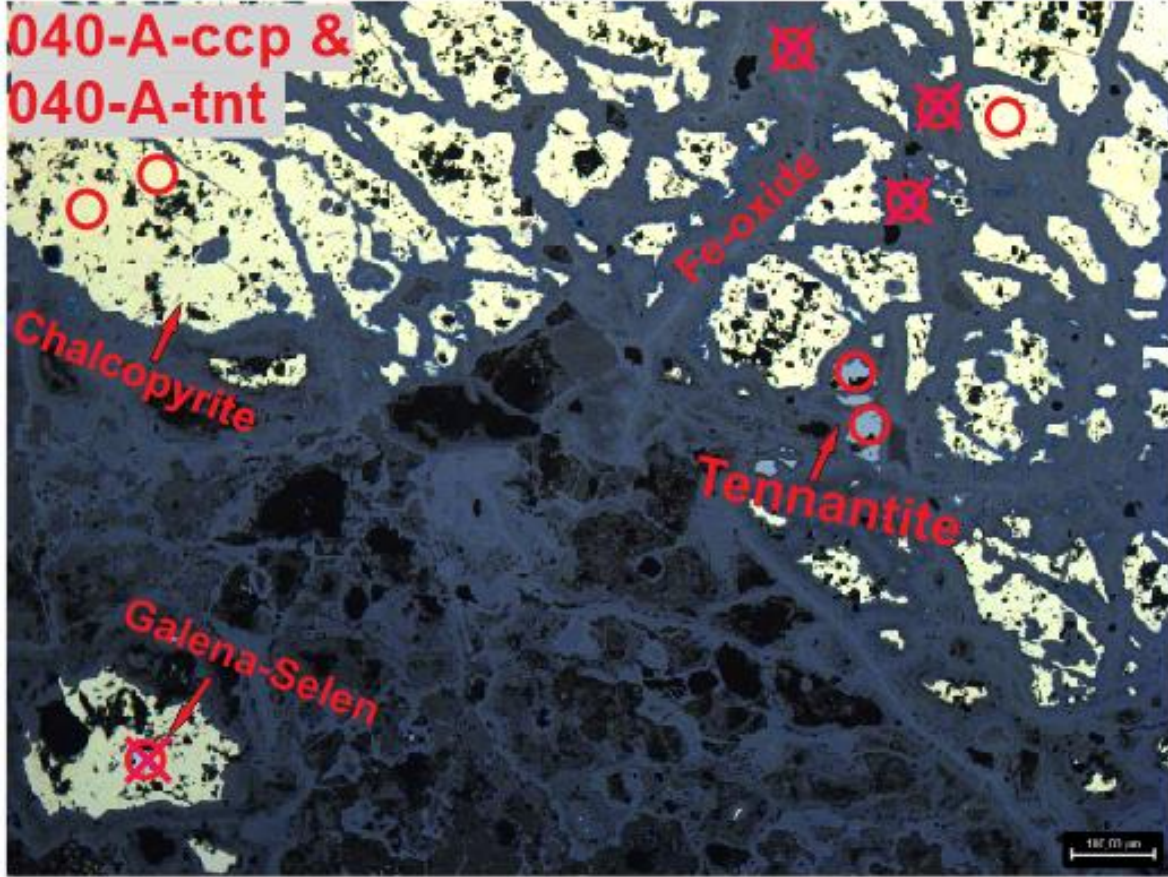
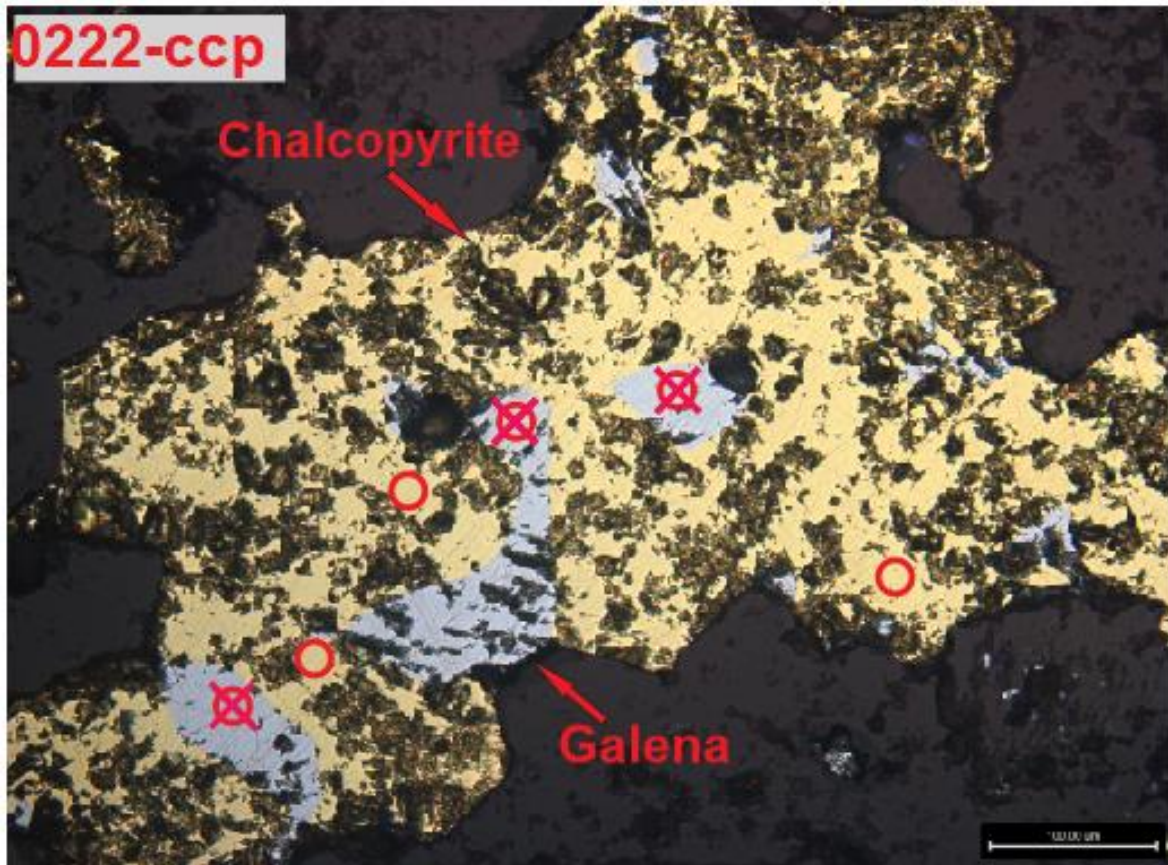


Figure D1: Continued. Wulfenite is also not spotted as it contains lead (not shown in the figure).

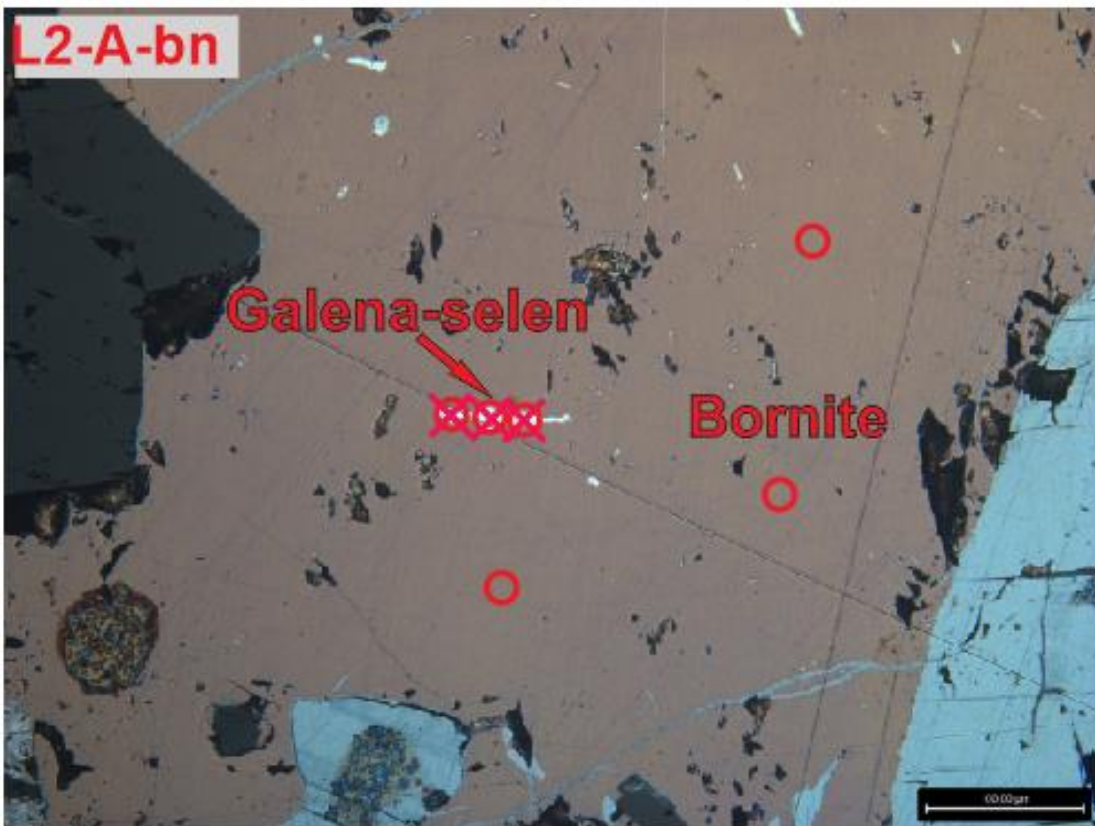


Figure D1: Continued.

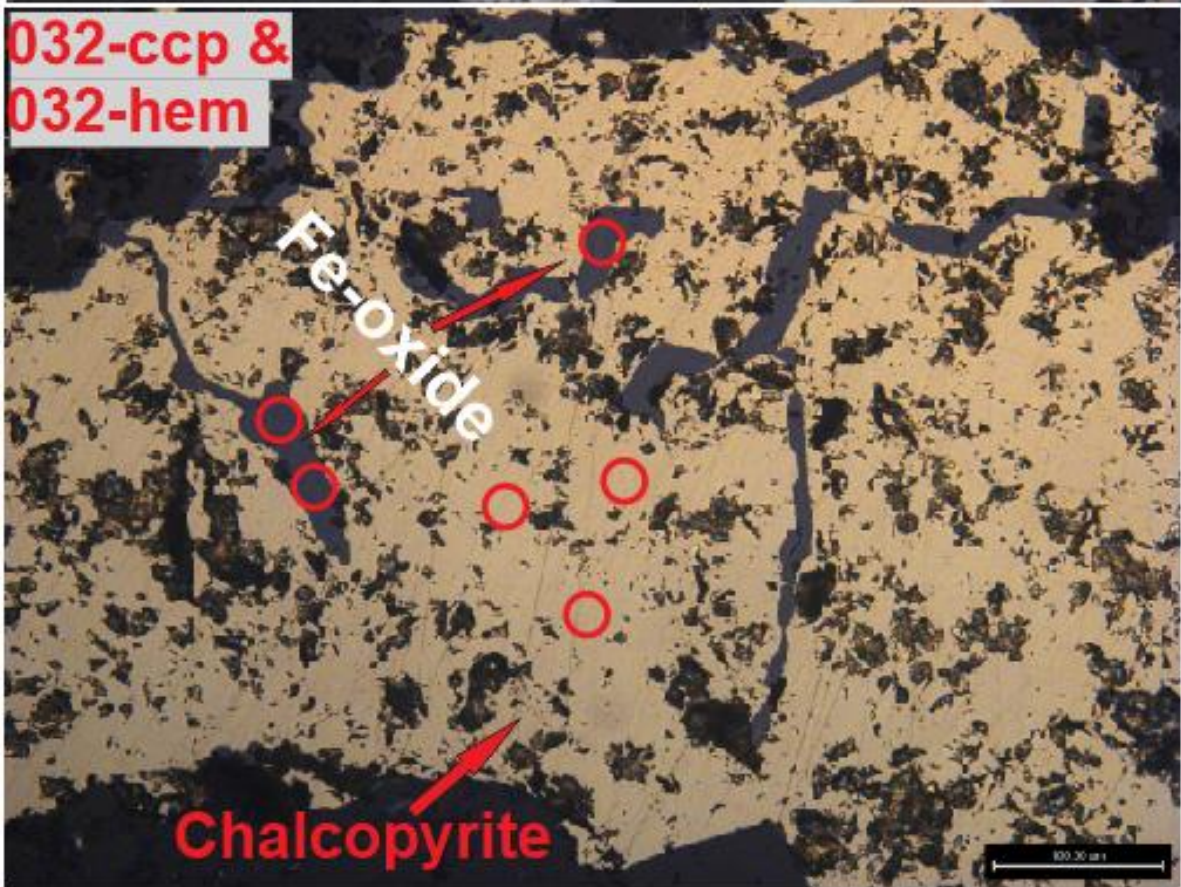
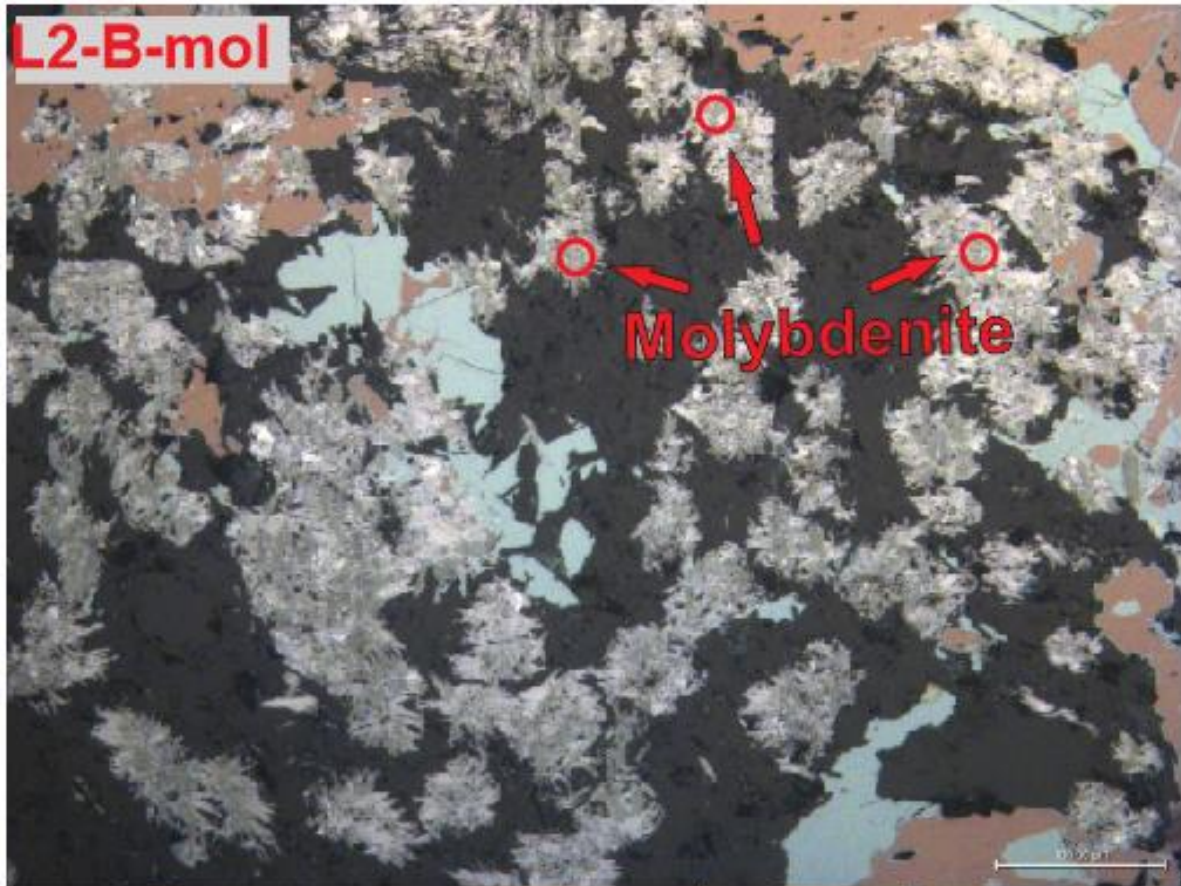


Figure D1: Continued.

Appendix E: Deviations from ideal composition

For most SEM-EDS data presented in this thesis, there are some deviations from minerals ideally composition. This deviation can be caused by several factors that will be discussed with some relevant examples.

Mafic rock-hosted oxides

SEM-EDS data from thin section 0054 corresponds in general well to the ideal composition of the different minerals with only some minor deviations as 3 wt.% higher Fe content in the massive magnetite, an influx of Fe in rutile and variation in the composition of titanite (Table 2). The lamellae-rich magnetite has some bigger deviations with a lower Fe content but has still been identified as magnetite by optical properties.

In thin section 0051, more minerals differ from their ideal composition from literature, which also is expected as this is identified as a part of a hydrothermal vein. A mineral identified to be titanite (Table 3) misses Fe, F and REE, and Al should be higher while Ti should be lower to correspond to the ideal composition. Although it has been identified as titanite due to this deviation is not too far from the ideal composition, only deviating with some few wt.%, and no other similar minerals with such a composition could be identified. The lack of Fe and F could be due to element exchanges or the detection limits of SEM-EDS, as they are only supposed to constitute 1.41 and 0.96 wt.% of titanite, respectively.

Ilmenite occurs as exsolution lamellar within the magnetite and deviates more from its ideal composition with an elevated Fe content and a reduced Ti content. It also contains 6 wt.% Mn, which is not in the ideal formula but could come from substitution between Fe^{2+} and available Mn^{2+} . It has still been identified as ilmenite as any other similar minerals with the same chemistry could not be found. It is also likely that the surrounding magnetite has some implies on these small ilmenite grains.

This deviation from ideal composition, especially in thin section 0051 is likely to come from hydrothermal alteration, affecting the elemental composition in minerals. Seritization found in thin section 0054 could be one evidence of hydrothermal alteration. Another source of this mineralogical deviation could be due to many of the minerals are very small, down to only a few microns in diameter, which can cause influx from the side laying mineral as the electron beam may also hit these surrounding minerals. Error in the calculation of the elemental

composition in the SEM-EDS itself could also occur and what also must be mentioned is that failure in the processing of the elemental data may also have happened.

Sediment-hosted sulfides

The selenium-rich galena at Lundstrøm (Thin section L2) could correspond to Olsacherite, but then the Pb content should have been much lower and the O content higher. Optical properties of this mineral including the lead value, suggest that it is galena as it is anisotropic, constant black in XPL and white in PPL. Wittichenite, identified in thin section L1 should have changed the Cu and Bi amount to correspond to its ideal composition. The selenium and copper-rich galena (thin section L1) could have its high copper value due to influxes of bornite. The selenium-, silver- and copper-rich galena, also in thin section L1 could be munakataite, but oxygen is missing which constitutes 21.1 wt.% of munakataite.

CuS minerals

In the same thin section L2, there has also been identified a CuS-mineral within bornite which is identified to be digenite by light microscopy properties. Digenite consists ideally of 78.10 wt.% Cu and 21.90 wt.% S while chalcocite consists of 79.85 wt.% Cu and 20.15% Fe. From the SEM-EDS data presented in Table 12, with Cu varying between 78.80 to 79.30 wt.%, it lays in between the composition of digenite and chalcocite, slightly towards chalcocite. In thin section L1, digenite has also been identified by the same optical properties as digenite in thin section L2. SEM-EDS data presented in Table 13 shows that the copper amount is varying between 79.80 to 79.90 wt.%. This place the digenite here very well into the elemental composition of chalcocite but have still been identified as digenite, as the optical properties are the same and the copper amount is only about 1.7 wt.% off the ideal composition of digenite.

In the two brecciated samples L1 and L2, a mineral called digenite has been identified as already mentioned. The reason it has been identified as digenite rather than chalcocite or djurleite is its distinguishing optical properties. According to Neumann (2019, p. 84, 108 & 110), digenite is a greyish blue mineral in PPL with no anisotropism (constantly black) in XPL, while djurleite has grey color with a blue tint and an extremely weak anisotropism and chalcocite have a whitish-grey color with a blue tint and a very weak anisotropism.

Distinguishing the minerals by their color in PPL has not been done as the variation in the blue color is hard to separate, but the digenite mineral in both thin sections shows roughly the same blue color. The reason it has been identified as digenite in both thin sections is that it

does not show any anisotropism at all in XPL when rotating the stage. This approach is very fragile as chalcocite and specially djurleite shows a very weak anisotropism and it could therefore be hard to determine if anisotropism is occurring or not. Based on the SEM-EDS data, djurleite with an ideal composition of 79.34 wt.% Cu would fit best in thin section L2 (78.80-79.30 wt.% Cu) while chalcocite with an ideal composition of 79.85 wt.% would fit best in this section L1 (79.80-79.90 wt.% Cu). Digenite has an ideal composition of 78.10 wt.% Cu, which does not differ too much from the measured composition in SEM-EDS. SEM-EDS do also have some limits in the accuracy but should on the other hand, be quite precisely as it is a FE-SEM.

What also should be mentioned is that the fractured digenite in thin section L2 (Figure 45B) shows some “lines” that have a darker blueish color than the rest of the digenite that could potentially be chalcocite or djurleite. These lines have been spotted by SEM-EDS and did not show any significant differences in the concentration of Cu and S relative to the main blue color. These lines could come from the presence of Cu-oxides in the fractures, disturbing the stability of digenite. The digenite in thin section L1 does not show this feature (Figure 47B), which could be due to it is not fractured and could therefore support the theory as it probably has not been affected by Cu-oxides in the same way. Cu-oxides in L1 has only been identified at the edges of bornite.

Carbonate layers in Storviknes formation

What also should be discussed is the elemental composition of the carbonate layers alternating at Anna and Lundstrøm in Storviknes formation. There has not been done any detailed investigation of these layers, but as seen in Table 10 from thin section 0221 at Anna, the host rock has been spotted by SEM-EDS which indicated the presence of O, Ca, Mg, Fe and Mn. Pure dolomite contains only O, Ca, Mg and C, while ankerite contains O, Ca, Mg, Fe, Mn and C. Carbon are however not detected as the samples were carbon-coated. The elements present in the carbonate mineral in Table 10 suggest then Ankerite as carbonate mineral. But when looking at the concentrations of the different elements, this is not as clear as the iron, manganese and oxygen content should have been higher, and magnesium and calcium content lower. In this case, the concentrations of elements in dolomite fits better as the oxygen, calcium and magnesium content is closer to the ideal composition of dolomite. What could be the case is that the carbonate is dolomite, but as the spots are taken close to the mineralized quartz-carbonate vein, hydrothermal alteration is most likely to have altered this carbonate and could be the reason for at least the influx of iron from the ore minerals. This

would be in accordance with previous work, but if ankerite was the original host rock, then it could have contributed with iron in the formation of the sulfides. The carbonate is also very fine-grained, and those three spots that were taken are most likely not to be representative of the whole carbonate rock. What also is interesting is that the carbonate clast spotted in thin section L2 from the brecciated sample L2 at Lundstrøm seen in Table 12, has the approximately same composition of elements as described.

Appendix F: LA-ICP-MS raw data

Notes: *The spots “L2-dig1” and “L2-dig2” have not been used in the boxplots for sulfides as there seems like these two spots are incorrect. Spot “L2-dig1” has concentrations that are way too high. For instance, sulfur is reported as 1 295 075 456 ppm, meaning nearly 1300% which is impossible. There may have been some problem with the data reduction in this spot, but it could not be figured out. Spot “L2-dig2” has problems with the elemental concentrations being reported as negative values below the detection limit, even though the detection limit is 0 for all elements, which could not be figured out. There may be some problems with the determination of detection limits for this spot. The two remaining spots in the digenite have been used in the following diagrams, but there is suspicion that both spots, “L2-dig3” and “L2-dig4” may also have some problems with data reduction as the sulfur value is too high. These two spots have been interpreted with caution. Four spots from the sphalerite have also been excluded, these spots includes all spots from sample 060 and one spot from sample 013 as the zinc value from LA-ICP-MS was too low which may have been caused by influxes of the side lying chalcopyrite. Two other spots from the unknown mineral in sample 014 have also been excluded from the boxplots. This mineral has been excluded as it needs to be analyzed in SEM-EDS to get a correct internal standard to determine trace elemental composition. By the LA-ICP-MS data presented here (Appendix F), it is very enriched in nickel, above 100 percent in one spot meaning the internal standard of 50 wt.% FeO could be wrong. The hematite used in the boxplots of oxides has only been identified to be hematite by light microscopy properties, and the internal standard used for data processing is the iron content of hematite. The true iron content should have been determined in SEM-EDS before the laser ablation, but this was unfortunately not done.*

Ti48 is plotted in the boxplots of oxides.

The detection limits for elements within minerals are different for each ablation, even though the same mineral is ablated. These detection limits vary between being reported as 0 and >0. Many elements are reported below detection limits, which gives a problem for those elements with a detection limit >0. The true concentration of these elements in this case, can be 0 or in between 0 and the detection limit. Presentations of these unknown concentrations are debated. The way it has been done in this thesis is to multiply by 0.5 to show all possible concentrations. Concentrations reported at detection limits (>0) are then getting half the value of the detection limit. but the detection limit line has not been added to the plots, because as mentioned, the detection limit varies from spot to spot and mineral to mineral.

Table F1: Elemental concentrations of sulfides and oxides from LA-ICP-MS (in ppm) including internal standards (in wt. %).

Int. std. (FeO)	39.15			59.18			59.89			3.86			59.89			40.1			39.15
Element	0054-A-ccp1	0054-A-ccp2	0054-A-ccp3	0054-B-py1	0054-B-py2	0054-B-py3	0051-py1	0051-py2	0051-py3	013A-sp1	013A-sp2	013A-sp3	013A-py1	013A-py2	013A-py3	013A-ccp1	013A-ccp2	013A-ccp3	013B-ccp
Si29	713.13	<321.29	<346.32	<144.83	<163.55	<152.11	<120.05	849.22	<126.81	449.61	10144.33	445.72	<120.07	<126.94	<128.88	7487.93	14547.5	<392.91	380.19
S34	390190.44	327375.44	327048.41	460346	522713.31	458918.22	424820.03	401830.84	449833.81	370058.47	288815.53	315003.34	359744.97	384512.81	341374.78	379987.72	397690.69	337302.22	340300.53
Ti48	27.93	22.9	23.85	38.3	44.11	39.63	33.69	35.28	35.7	29.29	31.01	22.23	30.66	36.47	34.82	34.68	51.42	31.55	141.86
Ti49	<5.64	<3.62	<5.56	4.09	4.23	4.58	4.1	3.25	4.27	<3.61	6.71	3.57	3.74	5.2	4.15	8.44	11.71	<6.49	7.29
V51	<0.65	<0.39	<0.52	<0.224	<0.27	<0.232	<0.195	1.99	<0.172	<0.31	<0.61	<0.31	<0.197	<0.246	<0.248	<0.65	<0.80	<0.75	1.95
Cr53	<22.42	<15.54	<18.23	<7.50	<7.98	<7.07	<5.93	<5.90	<5.93	<10.53	<15.84	<7.78	<5.97	<5.86	<6.09	<18.45	<24.43	<18.25	<17.38
Mn55	<4.88	<3.15	<3.38	<1.48	<1.64	<1.50	<1.17	2.64	<1.18	239.69	191.14	240.38	3.79	3.44	3.2	8.18	12	11.77	244.5
Fe57	304317.31	304317.31	304317.31	460012.78	460012.75	460012.75	465531.66	465531.66	465531.66	30004.21	30004.21	30004.21	465531.63	465531.63	465531.63	311002.16	311002.13	311002.13	304317.28
Co59	<1.23	<0.96	<1.04	18181.37	28830.52	9676.01	2809.32	2103.18	1347.21	1148.63	914.73	1193.29	1104.48	681.1	996.86	<1.12	7.12	<1.37	<1.33
Ni60	<23.86	<16.21	<17.58	20.1	21.3	21.52	26.34	31.46	47.95	<11.24	<18.40	<10.31	5482.4	3626.11	5867.69	<22.30	73.94	<22.27	<22.75
Cu65	382263.09	353105.63	345532.22	<2.49	<2.66	<2.54	<2.07	2.92	<2.16	8416.97	22196.07	12348.92	70.05	39.49	40	396674.06	356866.88	358752.06	359341.78
Zn67	<21.27	12.15	14.96	<5.72	<5.42	<5.77	<4.72	<5.00	<3.82	746469.19	376678.5	616890.75	<5.06	<5.24	<5.76	91.85	78.33	209.31	53.85
Ga71	<0.31	<0.14	<0.15	<0.066	<0.104	0.017	<0.053	0.121	<0.079	<0.00	<0.32	0.033	<0.076	<0.080	0.014	<0.34	0.09	<0.24	1.62
Ge73	<12.66	<6.34	<8.24	<2.93	<4.59	<3.72	<3.31	<3.36	<3.65	<5.36	<8.99	<3.99	<3.35	<3.05	<3.81	<11.38	<11.23	<8.37	<9.60
As75	<4.34	<3.01	<2.84	79.84	158.31	37.29	13.13	6.12	6.13	<1.89	33.37	2.21	88.51	72.67	106.33	18.87	35.82	<4.20	<3.88
Se77	58.31	59.95	44.62	10.57	25.72	11.17	<4.14	<3.78	<3.82	22.77	17.98	21.49	51.3	41.95	51.94	17.62	21.26	19.72	41.14
Nb93	0.029	<0.091	<0.102	<0.087	<0.098	<0.088	<0.098	<0.060	<0.051	<0.082	0.14	<0.156	<0.109	<0.073	<0.037	<0.24	<0.26	<0.36	<0.110
Mo95	<2.67	<1.61	<0.95	<0.33	<0.27	<0.27	<0.52	<0.28	<0.59	<0.82	1.35	<0.87	0.66	0.42	0.43	<1.85	<0.82	<1.79	<1.55
Ru99	<3.08	<2.20	<2.29	9.5	14.98	6.61	1.43	0.98	1.13	<1.22	<2.26	1.11	<0.85	<0.98	<0.92	<3.09	<4.09	<3.06	<3.70
Ru101	<3.30	<1.47	<2.16	<0.78	<0.98	<1.11	<0.58	<0.41	<0.67	<0.99	<2.57	<0.85	<0.57	<0.90	<0.68	<2.32	<2.70	<2.29	<3.02
Rh103	52.74	48.32	47.7	<0.188	<0.193	<0.141	<0.147	<0.122	<0.147	1.02	3.16	1.52	<0.181	<0.083	<0.172	51.38	46	44.26	44.4
Pd106	<1.71	<1.58	<2.29	<0.59	<0.62	<0.94	<0.62	<0.39	<0.67	562.13	231.95	476.28	<0.56	<0.84	<0.55	<2.16	<2.76	<2.20	<1.99
Ag109	2.86	2.2	1.83	<0.146	0.085	<0.180	<0.151	<0.132	<0.114	6.52	19.33	10.33	1.65	1.09	1.88	10.08	8.56	9.75	9.3
Cd111	<2.37	<2.01	<1.62	<0.47	<0.84	<0.81	<0.52	<0.86	0.26	4230.97	1589.59	3831.42	0.73	<1.04	<0.90	5.41	<3.11	4.09	3.17
In115	5.1	5.1	4.99	<0.046	<0.070	<0.033	<0.022	<0.0306	<0.023	11.46	10.72	10.29	<0.023	<0.045	0.0014	2.55	2.73	2.38	10.99
Sn120	<2.51	<1.75	<1.82	<0.63	<0.76	<0.75	<0.63	<0.67	<0.62	<1.00	<1.64	<0.88	<0.57	<0.61	<0.66	<2.03	<2.24	<2.03	<1.82
Sb123	0.023	<0.00	0.062	<0.00	<0.073	<0.00	<0.074	<0.00	<0.00	3.86	3.73	3.23	16.39	12.97	20.44	0.39	0.42	3.57	0.31
Te126	<1.87	<1.02	<1.24	<0.51	<0.71	<0.63	<0.43	<0.44	<0.53	<0.83	<0.98	<0.76	<0.49	<0.48	<0.43	<1.27	<1.85	<1.71	<1.85
Ba137	<0.36	<0.39	<0.41	<0.206	<0.142	<0.169	<0.152	0.21	<0.149	<0.26	5.97	<0.201	<0.181	<0.164	<0.157	5.4	10.64	<0.57	0.43
W183	<0.00	<0.00	<0.00	<0.00	<0.00	<0.00	<0.00	<0.00	<0.00	<0.00	0.36	<0.00	<0.00	0.12	<0.00	<0.00	<0.00	<0.00	<0.00
Re187	<0.00	<0.00	<0.00	<0.00	<0.00	<0.00	<0.00	0.017	0.03	<0.00	<0.00	<0.00	<0.00	<0.00	<0.00	<0.140	<0.00	<0.00	<0.00
Os190	<0.00	<0.00	<0.00	<0.00	<0.00	<0.00	<0.00	<0.00	<0.00	<0.00	<0.00	<0.00	<0.00	<0.00	<0.00	<0.00	<0.00	<0.00	<0.00
Ir193	<0.00	<0.00	<0.00	<0.00	<0.00	<0.00	<0.00	<0.00	<0.00	<0.00	<0.00	<0.00	<0.00	<0.00	<0.00	<0.00	<0.00	<0.00	<0.00
Pt195	<0.00	<0.00	<0.00	<0.00	<0.00	<0.00	<0.00	<0.00	<0.00	<0.00	<0.00	<0.00	<0.00	<0.00	<0.00	<0.00	<0.00	<0.00	<0.00
Au197	<0.00	<0.00	<0.00	<0.00	<0.00	<0.00	<0.00	<0.00	<0.00	0.18	0.2	0.2	0.092	0.057	<0.00	<0.00	<0.00	0.14	<0.00
Hg202	<6.17	<3.77	<3.80	<1.40	<1.56	<1.62	<1.05	<1.45	<1.20	335.38	396.26	349.15	<5.19	<3.66	<3.02	<8.78	<9.85	<7.75	<7.66
Tl203	<0.58	<0.163	<0.00	<0.112	0.024	0.007	0.044	0.009	<0.00	<0.160	1.49	0.4	9.42	5.8	6.95	0.027	0.28	0.027	<0.57
Pb208	2.15	0.58	0.66	<0.042	<0.048	<0.00	<0.035	2.15	<0.00	33.89	23.14	21.25	29.05	24.23	39.87	9.46	3.23	31.42	0.089
Th232	<-NaN	<-NaN	<-NaN	<-NaN	<-NaN	<-NaN	<-NaN	<-NaN	<-NaN	<-NaN	<-NaN	<-NaN	<-NaN	<-NaN	<-NaN	<-NaN	<-NaN	<-NaN	<-NaN
U238	<0.00	<0.00	<0.00	<0.00	<0.00	<0.00	<0.00	0.0128	<0.00	<0.00	0.015	<0.00	0.0026	0.0013	0.0008	0.0053	0.0033	0.0018	0.03

Table F1: Continued.

Int. std. (FeO)	50		59.89			39.15			59.89			39.15		
Element	014-unk	014-unk	014-py1	014-py2	014-py3	014-ccp1	014-ccp2	014-ccp3	0571-py1	0571-py2	0571-py3	0571-ccp1	0571-ccp2	0571-ccp3
Si29	5425.65	111.32	<7.63	33.29	84.56	135.98	789.02	62.4	53.04	31.64	99.7	199.94	321.24	417.94
S34	1631281.5	1319655	338160.31	355064.47	349288.63	299223.22	304057.19	300028.41	450377.31	479343.81	460613.97	326049.13	337150.84	324303.25
Ti48	198.9	154.11	40.17	41.99	39.41	32.48	34.31	32.05	45.64	46.18	41.41	29.89	28.31	28.51
Ti49	23.32	18.67	3.47	4.4	3.6	0.79	1.29	1.98	3.54	2.05	7.27	4.64	0.36	3.93
V51	0.486	0.2	<0.0091	0.0531	<0.0112	<0.0145	0.0527	<0.0180	0.0361	0.0136	<0.012	0.141	0.213	<0.023
Cr53	<2.37	<1.88	3.18	<0.33	2.51	3.29	<0.65	<0.65	1.71	2.9	1.62	2.75	3.37	4.2
Mn55	93.19	37.51	3.05	3.68	3.78	6.28	103.78	23.93	0.87	0.82	0.9	1.87	1.09	1.82
Fe57	388655.44	458613.41	465531.47	465531.5	465531.47	304317.19	304317.22	304317.22	465531.5	465531.5	465531.47	304317.22	304317.22	304317.22
Co59	12045.34	385174.16	933.61	1431.27	2208.7	191.52	495.4	949.73	5322.83	8007.62	8856.63	0.89	0.407	0.623
Ni60	1045720.19	728306.63	1484.04	1768.78	2317.84	771.31	449.12	1050.82	1060.92	559.29	284.75	<0.82	<0.78	1.02
Cu65	54923.34	34134.32	431.33	175.82	345.43	117033.55	139443.98	135349.69	45.59	2.3	1.97	363229.84	359434.88	325924.5
Zn67	65.85	5.42	<0.21	0.63	1.52	24.42	25.57	266.97	1.17	<0.187	0.75	132.53	166.61	173.97
Ga71	<0.028	<0.0158	0.0151	0.0105	<0.0043	<0.0069	0.0171	0.0337	<0.0030	0.0312	0.0381	0.0423	<0.0049	<0.010
Ge73	1.7	0.98	<0.098	<0.085	0.45	1.15	0.5	0.49	0.56	<0.109	0.89	<0.23	<0.19	2.53
As75	802.49	241.57	200.81	244.16	457.92	94.87	176.5	384.45	22.69	<0.046	0.39	<0.096	0.3	<0.096
Se77	722.39	482.6	23.22	17.02	18.67	21.92	24.99	21.61	42.32	56.09	47.63	34.32	27.43	32.66
Nb93	0.127	<0.020	0.0049	0.003	0.0195	0.053	<0.009	0.0231	0.0235	0.0313	<0.0024	<0.0077	<0.013	0.037
Mo95	228.05	1.13	1.38	0.351	0.467	0.13	0.512	0.487	<0.021	0.064	0.0266	0.03	0.15	<0.091
Ru99	479.93	320.18	0.155	0.722	0.873	<0.067	1.56	0.798	2.08	4.33	5.29	2.26	2.49	0.636
Ru101	12.83	10.02	<0.041	<0.045	0.185	0.606	<0.081	0.164	<0.027	0.103	<0.036	0.466	0.84	0.2
Rh103	6.87	3.98	0.0619	0.0497	0.0597	14.44	18.55	16.39	<0.008	<0.0082	<0.0073	44.94	46.32	43.68
Pd106	0.281	<0.114	0.078	<0.021	0.205	0.178	<0.046	1.03	0.156	<0.027	<0.027	<0.063	0.51	<0.057
Ag109	63.04	32	4.94	3.81	3.05	9.85	10.04	11.18	0.559	<0.0099	<0.0066	1.19	1.25	1.38
Cd111	2.9	2.71	<0.024	0.24	0.089	1.93	0.92	5.84	<0.036	<0.037	<0.03	0.6	0.62	2.32
In115	1.55	0.401	0.147	0.167	0.139	1.55	2.19	2.25	<0.0018	<0.0020	<0.00142	4.49	6.11	4.79
Sn120	1.6	0.88	0.023	<0.021	0.192	0.37	0.46	0.72	<0.021	0.035	<0.020	0.19	0.106	<0.046
Sb123	122.37	19.38	52.84	73	106.36	14.62	26.34	70.42	0.63	0.096	<0.00	<0.0095	<0.00	0.0085
Te126	272.58	95.94	5.59	20.06	87.53	6.16	15.56	79.86	1.106	0.442	0.155	<0.050	<0.057	0.419
Ba137	0.158	<0.072	0.05	<0.0150	<0.0149	<0.024	0.455	<0.030	0.0232	0.069	<0.0147	<0.030	0.241	0.381
W183	<0.00	<0.00	<0.00	<0.00	<0.00	<0.00	<0.00	<0.00	<0.00	<0.00	<0.00	<0.00	<0.00	<0.00
Re187	0.0447	<0.00	<0.00	<0.00	<0.00	<0.00	<0.00	0.0101	<0.00	0.0085	<0.00	<0.00	<0.00	<0.00
Os190	<0.00	<0.00	<0.00	<0.00	<0.00	<0.00	<0.00	<0.00	<0.00	<0.00	<0.00	<0.00	<0.00	<0.00
Ir193	<0.00	<0.00	<0.00	<0.00	<0.00	<0.00	<0.00	<0.00	<0.00	<0.00	<0.00	<0.00	<0.00	<0.00
Pt195	<0.00	<0.00	<0.00	<0.00	<0.00	<0.00	<0.00	<0.00	<0.00	<0.00	<0.00	<0.00	<0.00	<0.00
Au197	2.18	0.287	0.71	1.34	1.81	0.0532	0.216	1.15	0.262	<0.00	<0.00	<0.00	<0.00	<0.00
Hg202	30.67	15.5	1.25	2.19	3.91	2.06	1.64	4.63	0.58	0.21	<0.07	<0.14	2.06	1.26
Tl203	43.49	8.83	35.38	47.17	53.31	4.52	18.14	27.62	0.0054	0.0151	<0.006	0.033	0.081	<0.007
Pb208	393.16	95.73	229.46	218.13	257.35	84.29	73.11	157.15	3.13	0.91	<0.00	1.69	0.68	0.49
Th232	<-NaN	<-NaN	<-NaN	<-NaN	<-NaN	<-NaN	<-NaN	<-NaN	<-NaN	<-NaN	<-NaN	<-NaN	<-NaN	<-NaN
U238	0.0112	<0.00	0.0014	0.0033	0.00252	<0.00	<0.00	<0.00	<0.00	<0.00	<0.00	<0.00	<0.00	<0.00

Table F1: Continued.

Int. std. (FeO)	7.08			39.15			59.89			39.15			59.89	
Element	060A-sp1	060A-sp2	060A-sp3	060A-ccp1	060A-ccp2	060A-ccp3	047-1-py1	047-1-py2	047-1-py3	047-1-ccp1	047-1-ccp2	047-1-ccp3	047-2-py1	047-2-py2
Si29	1844.26	1543.02	252.67	372.72	3762.92	318.05	200.76	372.08	113.16	497.46	14402.88	2003.33	2440.46	150.63
S34	90729.43	99241.25	107566.66	331763.78	367352	353549.97	471267.38	407106.63	482347.5	356253.13	361937.16	393744.63	478647.56	439168.41
Ti48	10.88	10.26	9.58	28.61	34.7	26.71	47.61	40.48	45.92	28.55	29.01	44.27	88.5	39.37
Ti49	2.02	1.99	1.18	3.71	6.12	3.8	5.98	6.96	5.07	3.04	8.63	18.06	50.13	3.27
V51	1.84	1.9	1.23	0.133	0.85	<0.029	0.071	1.6	<0.0136	<0.024	0.359	2.77	36.61	0.164
Cr53	1.59	3.49	0.86	<1.08	1.74	2.94	3.52	<0.52	5.22	6.19	<1.42	16.39	51.19	1.31
Mn55	37.65	31.03	54.5	0.83	3.06	1.24	0.398	1.96	0.77	1.91	14.76	2.5	12.79	0.54
Fe57	55033.61	55033.61	55033.61	304317.22	304317.22	304317.22	465531.47	465531.47	465531.5	304317.19	304317.19	304317.22	465531.5	465531.5
Co59	145.18	131.83	231.74	1.56	1.55	1.1	141.86	198.36	304.3	1.28	0.275	8.38	344.89	575.5
Ni60	31.46	38.73	7.28	3.7	<1.16	<1.03	318.12	2802.54	83.46	23.9	24.05	46.82	83.23	131.87
Cu65	55300.26	58587.4	53636.26	335033.28	359946.53	372777.5	174.08	13.2	2.73	277956.97	350306.09	219669.45	8.47	3.94
Zn67	64849.88	70946.13	109376.04	497	277.7	447.22	8.5	<0.31	0.5	92.09	146.61	102.32	7.88	1.64
Ga71	0.0066	0.0133	0.0087	0.0239	<0.015	0.0233	0.0234	0.051	<0.008	0.0224	0.05	0.13	0.49	<0.0052
Ge73	<0.056	0.94	0.074	<0.25	<0.27	1.11	<0.123	<0.14	0.45	1.5	<0.33	<0.28	<0.14	0.76
As75	6.87	5.07	1.24	0.41	9.66	0.377	52.39	63.3	102.94	28.59	<0.153	23.48	61.28	67.17
Se77	55.48	63.09	72.23	290.97	222.84	224.84	16.05	14.49	25.15	91.14	96.92	80.76	39.32	45.74
Nb93	0.0231	0.0134	0.0106	<0.0163	0.1	0.0175	0.052	<0.0045	<0.0054	<0.010	0.087	<0.018	0.051	0.0115
Mo95	0.213	0.092	0.088	<0.067	<0.064	0.506	<0.046	<0.040	<0.048	<0.08	0.484	0.356	<0.047	<0.045
Ru99	<0.044	0.403	0.453	1.23	0.76	1.83	0.249	<0.070	<0.063	0.304	2.54	1.76	0.166	<0.080
Ru101	<0.032	<0.035	0.109	<0.16	0.62	0.298	<0.058	<0.06	<0.060	<0.104	<0.18	<0.17	0.112	0.093
Rh103	7.05	7.54	7.09	43.39	45.97	45.43	0.048	<0.0102	<0.0108	35.38	43.57	28.5	<0.014	<0.013
Pd106	48.14	50.81	73.66	0.41	1.22	<0.085	<0.036	0.198	<0.028	0.071	0.7	<0.086	<0.038	0.199
Ag109	139.65	163.85	202.09	23.07	25.1	24.08	<0.0112	0.209	0.0187	4.34	23.79	3.56	0.0321	<0.012
Cd111	686.24	768.9	1103.18	10.93	8.41	11.99	0.76	0.63	0.51	2.61	4.39	3.84	<0.10	0.54
In115	0.74	0.462	0.94	0.282	0.281	0.323	<0.0029	0.077	<0.00176	13.58	15.9	11.25	0.0264	0.00265
Sn120	0.038	<0.0156	0.112	0.58	<0.07	0.19	0.28	0.16	<0.030	2.85	8.65	2.55	0.15	<0.03
Sb123	2.17	1.26	1.19	0.04	1.6	<0.010	0.09	0.23	0.115	0.7	0.3	0.74	1.65	1.3
Te126	0.36	0.173	0.405	0.871	1.16	0.73	0.445	1.19	0.809	1.25	<0.078	0.467	2.08	0.458
Ba137	1.67	1.53	17.07	0.234	2.48	0.143	<0.035	0.095	<0.023	0.242	3.82	0.69	1.79	<0.025
W183	<0.00	<0.00	<0.00	<0.00	<0.00	<0.00	<0.00	<0.00	<0.00	<0.00	<0.00	<0.00	<0.00	<0.00
Re187	<0.00	<0.00	<0.00	<0.00	<0.00	<0.00	<0.00	<0.00	<0.00	<0.00	<0.00	<0.00	0.00488	<0.00
Os190	<0.00	<0.00	<0.00	<0.00	<0.00	<0.00	<0.00	<0.00	<0.00	<0.00	<0.00	<0.00	<0.00	<0.00
Ir193	<0.00	<0.00	<0.00	<0.00	<0.00	<0.00	<0.00	<0.00	<0.00	<0.00	<0.00	<0.00	<0.00	<0.00
Pt195	<0.00	<0.00	<0.00	<0.00	<0.00	<0.00	<0.00	<0.00	<0.00	<0.00	<0.00	<0.00	<0.00	<0.00
Au197	0.149	0.0073	<0.00	0.078	<0.00	0.106	<0.00	<0.00	<0.00	<0.00	0.042	<0.00	<0.00	<0.00
Hg202	13.39	13.2	18.34	8.3	4.75	4.4	<0.07	<0.06	<0.06	0.13	1.43	1.01	<0.06	<0.04
Tl203	1.75	0.29	0.21	<0.0083	0.5	<0.021	<0.0074	0.0119	<0.009	<0.0067	0.068	<0.018	0.022	<0.0052
Pb208	25.21	9.6	8.15	1.99	11.69	3.67	0.82	6.69	0.64	11.63	8.33	16.72	4.77	7.61
Th232	<-NaN	<-NaN	<-NaN	<-NaN	<-NaN	<-NaN	<-NaN	<-NaN	<-NaN	<-NaN	<-NaN	<-NaN	<-NaN	<-NaN
U238	0.0163	0.0184	0.0235	<0.00	<0.00	0.00075	0.00096	<0.00	<0.00	0.021	0.29	0.29	0.57	0.00133

Table F1: Continued.

Int. std. (FeO)	59.89			39.15			59.89			39.15			39.15		
Element	051-1-py1	051-1-py2	051-1-py3	051-1-ccp1	051-1-ccp2	051-1-ccp3	051-2-py1	051-2-py2	051-2-py3	051-2-ccp1	051-2-ccp2	051-2-ccp3	0221-ccp1	0221-ccp2	0221-ccp3
Si29	<14.24	10.72	268.12	978.62	489.71	190.37	<7.01	<11.52	41.85	901.56	110.83	901.79	870.19	734.84	124.84
S34	500606.28	462741.44	426896.59	353618.19	390744.94	452659.84	374468.44	441602.38	467405.5	364410.56	355622.47	368595.75	336513.66	347525.47	335254.44
Ti48	72.44	58.15	64.27	50.45	48.28	60.09	44.57	61.7	58.2	43.27	40.1	44.11	42.15	42.75	39.71
Ti49	9.72	7.3	7.54	4.56	9.66	6.71	6.3	7.93	6.31	6.03	6.42	8.25	7.3	5.64	2.14
V51	0.0497	0.0451	0.097	7.59	3.5	1.08	<0.0059	<0.012	<0.0095	0.125	0.106	<0.0191	0.038	0.113	0.077
Cr53	2.5	0.68	<0.43	10.21	4.35	<0.80	<0.22	1.74	0.97	10.79	8.57	3.73	<0.85	4.48	3.52
Mn55	0.58	0.61	4.34	205.28	74.86	2.58	0.67	<0.066	0.53	0.89	0.216	4.56	4.74	1.4	0.238
Fe57	465531.59	465531.59	465531.59	304317.28	304317.28	304317.31	465531.63	465531.63	465531.63	304317.31	304317.31	304317.31	304317.31	304317.28	304317.31
Co59	9.33	0.96	13.37	0.69	1.03	67.15	1.15	1.12	1.01	<0.069	0.083	0.393	0.414	0.283	<0.064
Ni60	2841.63	2188.99	2341.13	274.72	228.77	466.7	303.43	370.53	515.5	43.93	77.71	71.66	<0.81	<0.84	<0.78
Cu65	192.93	4.22	10407.83	340062.31	379870.25	92810.8	0.87	0.8	2.03	364173.5	354111.88	372201.44	330933.63	352294.47	340707.97
Zn67	2.04	<0.33	272.49	268.72	14024.55	38.31	<0.23	<0.37	1.5	265	149.65	210.53	2.92	3.95	1.63
Ga71	0.0225	<0.0020	0.185	0.0327	0.0283	<0.00	<0.00	<0.00	<0.0042	<0.00	<0.00	<0.00	0.0316	0.042	<0.00
Ge73	0.99	0.89	0.57	1.19	3.19	1.1	0.45	1.52	0.98	<0.19	<0.135	0.81	1.43	<0.158	0.31
As75	3.15	<0.044	6.42	2.81	1.58	24.78	<0.029	<0.050	0.342	2.49	<0.121	1.26	1.56	2.1	<0.108
Se77	123.18	93.36	76.18	123.59	162.48	99.46	128.84	180.22	155.57	84.05	103.26	95.55	176.11	172.55	134.49
Nb93	0.0071	<0.00	0.0075	<0.012	<0.00	<0.0044	<0.00	<0.0039	0.0119	<0.009	0.0158	0.0143	<0.00	<0.00	<0.0056
Mo95	<0.00	0.058	<0.00	0.423	0.441	0.236	<0.00	<0.021	0.053	0.401	0.183	<0.00	0.109	<0.00	<0.00
Ru99	<0.00	0.069	0.086	0.92	1.04	0.121	<0.0120	<0.020	<0.0128	0.7	0.64	0.516	0.568	0.251	1.2
Ru101	0.071	0.0479	0.048	<0.066	0.182	<0.00	<0.0119	<0.00	0.0441	0.606	0.453	0.362	0.584	0.94	0.479
Rh103	0.0112	0.0104	1.85	59.8	65.09	15.86	<0.0017	<0.00	<0.0027	61.2	60.31	62.3	58.41	61.69	59.01
Pd106	0.114	<0.00	0.239	<0.043	14.86	0.238	<0.013	<0.0127	0.014	0.201	0.297	0.57	<0.028	0.05	<0.025
Ag109	0.145	<0.00	2.01	19.38	21.41	3.34	<0.00	<0.00	0.011	11	13.06	22.61	10.31	2.35	5.39
Cd111	<0.00	<0.022	2.13	7.92	143.72	0.98	<0.0087	<0.029	<0.023	5.12	8.74	4.86	<0.047	<0.046	<0.031
In115	0.0241	<0.00080	1.11	19.58	24.39	5.5	0.00354	<0.00	0.00261	13.41	12.52	14.05	8.72	8	7.74
Sn120	0.14	<0.029	0.9	11.52	7.3	1.96	<0.018	<0.028	0.036	11.65	11.18	10.8	0.93	1.1	0.61
Sb123	0.363	<0.0057	2.37	4.45	8.02	1.57	<0.0025	0.0121	0.05	<0.00	0.6	0.118	0.0293	<0.00	<0.00
Te126	4.77	0.641	1.41	1.95	1.22	2.49	0.328	0.211	1.72	0.9	0.89	0.125	<0.059	0.368	<0.066
Ba137	<0.0083	<0.0062	1	1.13	0.247	1.22	<0.0060	0.0112	0.139	0.76	0.027	0.318	0.435	0.212	0.102
W183	<0.00	<0.00	<0.00	<0.00	<0.00	<0.00	<0.00	<0.00	<0.00	<0.00	<0.00	<0.00	<0.00	<0.00	<0.00
Re187	<0.00	<0.00	<0.00	<0.00	<0.00	<0.00	<0.00	<0.00	<0.00	<0.00	<0.0092	<0.00	<0.00	<0.00	<0.00
Os190	<0.00	<0.00	<0.00	<0.00	<0.00	<0.00	<0.00	<0.00	<0.00	<0.00	<0.00	<0.00	<0.00	<0.00	<0.00
Ir193	<0.00	<0.00	<0.00	<0.00	<0.00	<0.00	<0.00	<0.00	<0.00	<0.00	<0.00	<0.00	<0.00	<0.00	<0.00
Pt195	<0.00	<0.00	<0.00	<0.00	<0.00	<0.00	<0.00	<0.00	<0.00	<0.00	<0.00	<0.00	<0.00	<0.00	<0.00
Au197	0.0107	<0.00	0.0219	0.208	0.216	0.138	<0.00	<0.00	<0.00	<0.00	<0.00	<0.00	<0.00	<0.00	<0.00
Hg202	0.99	<0.08	1.46	5.76	7.77	1.24	0.29	<0.08	<0.08	1.44	0.58	2.03	1.85	0.88	1.11
Tl203	<0.009	0.036	0.057	4.39	2.91	0.037	<0.00	0.043	<0.008	<0.015	<0.014	0.3	0.027	<0.013	0.051
Pb208	2.5	0.0965	59.3	65.15	74.71	13.77	<0.00	0.0108	0.491	0.799	15.03	2.68	0.392	0.306	0.439
Th232	<-NaN	<-NaN	<-NaN	<-NaN	<-NaN	<-NaN	<-NaN	<-NaN	<-NaN	<-NaN	<-NaN	<-NaN	<-NaN	<-NaN	<-NaN
U238	0.00086	<0.00	<0.00	5.52	3.62	0.00187	<0.00	<0.00	<0.00	<0.00	<0.00	5.71	<0.00	<0.00	<0.00

Table F1: Continued.

Int. std. (FeO)	14.32			39.15			39.88			6.43	
Element	0221-bn1	0221-bn2	0221-bn3	0222-ccp1	0222-ccp2	0222-ccp3	040-A-ccp1	040-A-ccp2	040-A-ccp3	040-A-tnt1	040-A-tnt2
Si29	2935.47	601.12	732.25	843.02	950.9	168.48	148.83	313.84	607.03	1208.63	1052.72
S34	283769.81	267856.56	276003.56	355398.59	360519.97	328870.56	370434.44	347951.28	361023.72	9940.07	185871.56
Ti48	105.79	34.19	38.67	42.01	41.88	36.61	43.01	38.18	44.53	1.75	23.3
Ti49	88.63	3.79	5.22	6.5	7.01	6.94	4.17	2.01	4.31	<0.027	2.89
V51	0.7	0.183	0.52	<0.021	0.045	0.165	<0.024	<0.022	<0.033	0.47	0.45
Cr53	16.96	<0.86	11.1	4.64	2.82	<0.73	<0.93	<0.77	<0.99	0.64	0.64
Mn55	5.19	3.31	6.67	0.6	0.4	1.58	0.3	0.33	1.97	172	128.09
Fe57	111310.96	111310.95	111310.95	304317.31	304317.31	304317.31	304317.31	304317.31	304317.31	49981.11	49981.11
Co59	0.65	0.429	0.78	<0.062	0.261	<0.057	<0.076	0.254	0.192	22.12	76.39
Ni60	<0.79	8.44	1.69	<0.79	3.44	<0.70	<0.91	<0.76	<1.00	13.82	11.29
Cu65	549926.56	589140.25	557471.06	356893.53	368015.25	344668.31	354654.56	334137.63	370551.34	42702.64	309136.13
Zn67	2.22	<0.94	1.55	4.98	5.05	3.35	12.03	12	8.51	1209.25	30054.77
Ga71	0.0299	<0.00	0.073	<0.00	0.084	0.036	<0.008	<0.007	0.0237	0.028	0.064
Ge73	1.78	1.68	0.74	1.43	0.26	0.23	<0.24	2.52	<0.25	0.154	1.17
As75	18.33	0.82	0.77	2.19	1.63	1.1	18.41	0.95	2.31	8073.27	112914.45
Se77	392.44	259.34	451.19	321.62	437.4	566	556.8	718.92	591.37	327.63	1476.06
Nb93	0.139	0.038	0.0144	<0.0071	<0.0102	<0.0089	0.045	0.06	0.19	0.0029	0.036
Mo95	3.57	0.356	12.05	<0.00	<0.00	0.122	0.326	<0.00	<0.033	48.25	35.59
Ru99	2.1	2.18	1.18	0.65	1.13	1.16	0.73	0.81	0.54	0.149	1.21
Ru101	0.67	0.93	0.6	<0.051	0.6	0.25	<0.00	0.092	0.397	0.045	0.412
Rh103	108.45	108.02	110.83	60.33	61.55	55.39	56.47	57.96	60.6	7.01	53.42
Pd106	<0.030	0.033	<0.034	<0.029	<0.023	<0.035	0.087	<0.036	<0.042	2.53	59.71
Ag109	615.26	498.73	454.16	0.47	1.77	76.41	1.58	0.119	0.18	58.36	1004.2
Cd111	0.137	0.134	0.24	0.103	<0.073	0.137	0.25	<0.00	0.71	43.19	1052.88
In115	0.045	0.105	0.105	1.71	1.82	1.78	0.68	0.7	0.59	0.269	1.09
Sn120	0.194	<0.07	0.58	3.78	5.6	3.84	0.39	0.97	0.53	0.072	0.095
Sb123	0.052	<0.00	0.0378	<0.00	<0.00	0.083	0.194	0.046	0.033	167.52	2415.99
Te126	1.75	0.277	4.77	0.307	1.11	0.59	<0.072	0.318	<0.080	1.67	10.12
Ba137	1.86	0.49	0.42	0.58	0.61	0.139	0.52	0.159	0.64	7.53	22.14
W183	<0.00	<0.00	<0.00	<0.00	<0.00	<0.00	<0.00	<0.00	0.25	<0.00	<0.00
Re187	<0.00	<0.00	<0.00	<0.00	<0.00	<0.00	0.0262	0.0227	<0.00	0.00203	<0.00
Os190	<0.00	<0.00	<0.00	<0.00	<0.00	<0.00	<0.00	<0.00	<0.00	0.105	<0.00
Ir193	<0.00	<0.00	<0.00	<0.00	<0.00	<0.00	<0.00	<0.00	<0.00	<0.00	<0.00
Pt195	<0.00	<0.00	<0.00	<0.00	<0.00	<0.00	<0.00	<0.00	<0.00	<0.00	0.104
Au197	<0.00	<0.00	<0.00	<0.00	<0.00	<0.00	<0.00	<0.00	<0.00	0.00213	<0.00
Hg202	19.18	1.35	2.17	3.41	1.94	5.66	1.19	1.02	0.58	56.88	894.71
Tl203	0.044	0.058	0.026	<0.0081	<0.0055	<0.0074	0.0154	<0.008	<0.00	0.0024	<0.0032
Pb208	0.751	0.297	1.14	10.19	3.12	3912.51	37.09	2.6	29.12	3320.67	3512.51
Th232	<-NaN	<-NaN	<-NaN	<-NaN	<-NaN	<-NaN	<-NaN	<-NaN	<-NaN	<-NaN	<-NaN
U238	0.1	<0.00	<0.00	<0.00	<0.00	0.0044	0.0224	<0.00	<0.00	9.2	7.44

Table F1: Continued.

Int. std.	20.95 (S)				14.32 (FeO)			59.5 (Mo)			39.15 (FeO)		
Element	L2-dg1	L2-dg2	L2-dg3	L2-dg4	L2-A-bn1	L2-A-bn2	L2-A-bn3	L2-B-mol1	L2-B-mol2	L2-B-mol3	032-ccp1	032-ccp2	032-ccp3
Si29	<37910.78	<-13582.76	15846.77	14045.83	217.62	115.2	141.61	4204.58	3331.85	2383.01	153.64	2774.4	15731.88
S34	1295075456	<-43826.08	15652248	6453072	249302.59	252719.64	257094.13	94250.39	123421.27	127527.63	363857.81	353167.31	363087.72
Ti48	125581.63	<-127.91	1134.01	509.41	20.52	19.97	19.98	444.4	126.31	146.87	27.34	31.29	38.49
Ti49	15749.2	<-168.18	150.15	108.68	2.8	3.84	2.4	453.93	98.83	167.95	3.6	6.87	7.28
V51	<39.02	<-9.12	0.46	3.78	0.113	0.0501	<0.0070	20.82	17.73	14.66	0.016	0.0285	0.282
Cr53	<1386.13	<-503.02	<15.40	41.03	1.52	1.23	1.41	17.02	12.05	10.8	2.7	<0.32	1.58
Mn55	<280.83	5.88	120.33	157.99	2.44	1.5	1.41	17.38	21.35	10.94	0.98	1.64	3.08
Fe57	7773.11	7773.11	7773.11	7773.11	111310.95	111310.96	111310.95	3886.56	3886.56	3886.56	304317.28	304317.28	304317.28
Co59	<65.88	<-21.00	10.05	3.67	0.0505	0.045	0.081	881.02	1314.83	1057.13	0.0161	0.0475	0.117
Ni60	<1142.83	803.15	<12.06	62.34	<0.199	<0.18	<0.19	255.22	298.37	308.91	0.43	1.84	0.54
Cu65	2666123776	<-160.12	169.91	13121105	485909.5	520304.13	550082.56	4549.25	10777	15665.21	290559.88	290222.38	284679.47
Zn67	16754.52	<-275.08	541.04	98.44	4.44	1.99	3.56	10.03	8.05	5.73	9.49	8.42	14.59
Ga71	20.79	<-0.00	2.9	0.42	<0.0027	0.0237	0.00526	1.02	0.684	0.549	0.0179	0.0385	0.077
Ge73	2285.95	<-70.15	5.57	<1.34	0.824	0.311	0.508	0.319	0.0648	0.353	0.855	0.787	0.335
As75	2403.12	<-79.37	41.52	29.7	0.685	0.651	0.85	109.75	142.71	139.86	0.19	7.21	36.39
Se77	2920733.5	<-295.72	34301.64	14945.56	328.38	649.69	321.5	754.5	936.11	962.14	246.16	236.62	244.07
Nb93	131.08	13.25	2.4	1.28	0.015	0.0308	0.0089	1.71	0.49	0.69	<0.0048	<0.00250	0.0186
Mo95	817.09	<-13.35	133.82	47.89	0.519	0.41	1.9	71024.44	88056.58	86095.67	0.0387	<0.0175	0.063
Ru99	15402.93	<-64.50	182.8	75.47	2.03	2.11	2.02	1.21	1.88	1.71	0.622	1.15	0.649
Ru101	8801.4	<-36.81	87.47	35.78	0.669	0.935	1.07	0.224	0.248	0.273	0.661	0.579	0.351
Rh103	841866	<-8.14	8223.02	3581.46	101.53	100.83	102.71	0.886	2.03	2.87	54.17	51.13	50.33
Pd106	<81.90	184.69	<0.76	<0.47	<0.0134	<0.016	0.0288	0.087	0.096	0.092	0.272	0.156	0.42
Ag109	759016.31	<-11.38	7364.13	4464.83	35.48	86.93	28.85	126.66	210.84	153.89	44.28	48.94	46.78
Cd111	638.49	283.97	6.75	<0.39	<0.026	0.088	0.057	0.64	0.68	0.66	1.54	1.63	2.01
In115	15.76	16.13	<0.099	<0.026	0.1944	0.117	0.147	0.0511	0.1491	0.0895	2.271	2.303	2.226
Sn120	985.3	19.13	<1.20	<0.59	0.218	0.393	0.166	0.444	0.51	0.306	0.372	0.457	0.48
Sb123	806.48	<-0.00	1.13	1.66	0.00329	0.527	0.00347	55.6	66.67	61.63	0.0159	<0.00	0.0531
Te126	47766.19	<-46.21	81.92	20.8	0.139	23.54	0.155	35.16	64.56	46	<0.035	<0.031	<0.033
Ba137	193.58	20.75	9.6	9.67	0.136	0.119	0.119	21.22	12.87	12.62	0.091	2.21	11.49
W183	<0.00	<-0.00	<0.00	<0.00	<0.00	<0.00	<0.00	0.328	0.0193	0.104	<0.00	<0.00	<0.00
Re187	<0.00	<-0.00	<0.00	<0.00	<0.00	<0.00	0.00429	0.631	1.06	0.96	<0.00	<0.00	<0.00
Os190	<0.00	<-0.00	<0.00	<0.00	<0.00	<0.00	<0.00	<0.00	<0.00	<0.00	<0.00	<0.00	<0.00
Ir193	<0.00	<-0.00	<0.00	<0.00	<0.00	<0.00	<0.00	<0.00	<0.00	<0.00	<0.00	<0.00	<0.00
Pt195	<0.00	<-0.00	<0.00	<0.00	<0.00	<0.00	<0.00	0.07	0.0463	0.0341	<0.00	<0.00	<0.00
Au197	699.9	<-0.00	5.8	4.92	0.36	0.062	0.24	3.98	5.82	5.93	<0.00	<0.00	<0.00
Hg202	41908.71	<-90.49	302.75	198.47	0.56	0.36	0.49	8.67	10.33	11.43	2.01	2.66	2.36
Tl203	73.82	1.59	<0.160	<0.041	0.0135	0.0232	0.0147	2.05	2.33	2.42	<0.0024	<0.0033	0.0114
Pb208	3136.62	<-0.00	131.74	67.6	0.9	270.13	1.75	4918.94	5766.61	5724.88	0.288	0.339	2
Th232	<-NaN	<-NaN	<-NaN	<-NaN	<-NaN	<-NaN	<-NaN	<-NaN	<-NaN	<-NaN	<-NaN	<-NaN	<-NaN
U238	<0.00	<-0.00	0.272	0.0377	0.00089	0.00047	0.01604	0.1716	0.957	0.26	<0.00	0.00556	0.0955

Table F1: Continued.

Int. std. (FeO)	96.42			86.2			95.84			39.88			89.98			
Element	0054-2A-mag1	0054-2A-mag2	0054-2A-mag3	0054-2b-mag1	0054-2b-mag2	0054-2b-mag3	0051-mag1	0051-mag2	0051-mag3	013B-ilm1	013B-ilm2	013B-ilm3	032B-hem1	032B-hem2	032B-hem3	032B-hem4
Mg24	29.97	61.27	138	214.87	393.38	275.19	201.75	322.93	361.15	8476.27	7060.57	6070.21	524.01	362.94	256.38	284.03
Al27	72.55	71.51	78.79	37.86	163.05	120.78	79.49	84.72	79.19	6605.33	7158.37	5039.31	859.06	64.86	41.85	36.98
Si29	<54.31	89.04	1581.26	1170.49	1767.42	4044.64	1831.82	2193.74	2392.34	127474.73	65693.19	63483.55	44263.95	42298.48	31420.02	12124.65
P31	8.43	48.73	42.94	34.83	51.8	54.05	37.07	35.84	43.54	108.26	86.38	61.33	58.01	73.38	52.53	111.31
Ca44	<28.61	<28.93	<27.17	<24.43	149.51	2087.04	<26.55	<29.27	271.68	148871.17	71481.03	48127.18	4033.93	3753.5	2701.66	1335.1
Sc45	0.31	<0.171	<0.154	0.474	0.97	8.14	<0.160	1.51	2.46	148.91	105.58	82.51	1.02	1.63	0.83	0.88
Ti49	19.59	62.95	22.93	31110.49	87526.02	107862.62	32.41	58984.78	63362.42	505857.78	443520.41	439903.94	951.66	12.93	4.51	9.58
V51	1128.27	1226.32	1159.97	1015.22	1035.45	1232.07	593.79	558.24	541.51	321.47	180.63	213.16	5.37	0.76	<0.0227	0.286
Cr53	2.14	<0.82	<0.82	1.99	3.74	<1.00	<0.87	<0.97	1.7	432.49	331.53	150.77	7.79	10.53	3.16	8.7
Mn55	422.55	420.97	422.8	7108.21	17157.72	3711.34	482.03	15437.62	16674.26	89400.09	93052.42	86574.98	90.56	80.53	84.09	31.79
Fe57	749483.38	749483.38	749483.44	670042.19	670042.19	670042.25	744975	744975	744975	309991.69	309991.69	309991.72	699424.69	699424.69	699424.75	699424.75
Co59	11.4	13.34	12.82	11.73	13.77	12.16	0.295	0.256	0.821	29.81	25.93	43.15	6.84	1.64	0.203	0.224
Ni60	17.14	15.19	13.83	11.17	14.68	10.18	16.36	16.73	17.72	7.95	9.93	5.78	6.15	8.03	2.49	9.33
Cu63	<0.060	0.122	<0.054	2.15	62.86	4.3	0.275	<0.080	0.907	7.77	4.47	4.19	346996.81	345240.03	355217.22	463859.38
Zn66	3.2	6.05	5.65	10.22	17.67	15.75	5.69	21.27	17.94	119.85	117.02	151.41	89.24	74.15	33.09	47.21
Ga71	23.51	22.41	23.49	19.49	20	21.99	16.05	17.13	17.46	2.26	2.36	1.65	0.607	0.3	0.137	0.076
Ge73	2.64	3.14	3.3	0.75	1.59	1.038	4.11	0.48	2.64	7.51	9.63	4.88	0.188	1.16	0.46	1.72
As75	1.5	6.53	6.8	4.62	15.11	9.41	1.93	7.38	10.54	17.64	18.57	21.99	146.98	65.88	15.1	28.83
Se77	<0.44	<0.50	<0.45	1.27	<0.44	3.37	<0.39	<0.44	<0.50	<0.81	<0.57	2.79	392.77	404.16	465.28	451.57
Y89	<0.00	0.146	0.00552	1.57	2.76	8.4	<0.00	0.236	1.24	436.68	779.55	352.41	3.33	1.03	0.629	<0.00
Zr90	<0.00	0.0417	<0.00	0.833	0.867	60.83	<0.00	0.174	0.5	18.64	7.23	19.44	0.755	0.0623	1.246	0.164
Nb93	<0.0049	0.043	<0.0094	2.15	22.64	32.81	0.0234	23.78	40.39	82.62	102.78	50.58	1.112	0.0345	0.0175	0.0273
Mo95	<0.00	0.0426	0.151	3.94	4.52	3.61	0.0962	9.87	12.44	17.58	17.49	15.31	341.78	272.36	917.89	219.44
Ag107	<0.0047	<0.0097	0.0245	<0.0044	0.0364	0.022	<0.0112	<0.0077	<0.0092	0.0671	<0.00	<0.023	48.58	53.88	62.3	147.08
Sn118	<0.109	0.476	<0.113	<0.097	0.371	0.961	0.538	0.55	0.73	2.82	4.7	4.03	0.644	0.461	0.859	0.149
Sb121	0.157	0.0705	<0.023	0.228	0.466	2.09	<0.027	0.1118	0.261	4.07	5.68	3.69	23.79	17.35	14.55	3.81
La139	0.00231	<0.00	<0.00	0.0094	0.246	0.621	0.00479	<0.0036	0.0148	7.78	7.91	5.38	1.36	0.331	0.143	0.052
Sm147	<0.00	<0.00	0.0106	0.038	0.0392	0.559	<0.00	<0.00	0.0346	13.11	27.71	16.35	0.128	0.0631	0.0575	0.0219
Yb172	<0.00	0.0083	<0.00	0.0903	0.321	0.788	<0.00	0.1401	0.237	59.76	68.44	37.07	0.0363	<0.00	<0.00	0.0685
Hf178	<0.00	<0.00	<0.00	0.0566	0.0136	4.08	<0.00	<0.00	0.0903	0.624	0.204	0.881	<0.00	<0.00	<0.00	<0.00
Ta181	0.00552	0.00513	<0.0062	2.66	3.25	5.28	<0.00	1.89	2.04	1.43	1.62	0.748	0.119	<0.00	0.0089	<0.00
W182	<0.00	<0.00	<0.00	0.1344	0.291	3.78	<0.00	<0.00	0.551	0.942	7.97	12.05	4.88	0.142	<0.00	<0.00
Au197	<0.00	<0.00	<0.00	<0.00	<0.00	<0.00	<0.00	<0.00	<0.00	<0.00	<0.00	<0.00	0.02	0.038	<0.00	0.0095
Pb208	0.0234	0.0126	<0.0040	0.0431	0.0827	0.424	<0.0057	<0.0056	0.0125	2.73	3.8	1.051	278.08	124.84	0.832	38.26

Table F1: Continued.

Int. std. (CaO)	30.78			27.94			27.94		
Element	0054-2B-ttn1	0054-2B-ttn2	0054-2B-ttn3	013B-ttn1	013B-ttn2	013B-ttn3	060A-ttn1	060A-ttn2	060A-ttn3
Mg24	1273.26	5339.79	53493.23	434.01	525.45	770.09	5899.76	871.65	3631.26
Al27	9171.17	7482.14	13461.42	4806.87	5433.81	5156.27	13531.32	5286.12	8304.7
Si29	144218.7	147145.33	253684.64	127184.66	138717.86	121801.48	150915.13	140577.25	133848.59
P31	82.31	66.47	93.83	103.32	116.46	112.15	61.66	64.96	63.69
Ca44	219984.94	219984.92	219984.92	199973.33	199973.33	199973.33	199973.33	199973.33	199973.33
Sc45	16.32	22.25	135.67	212.73	254.97	252.13	8.94	5.95	4.78
Ti49	214377.61	203809.38	160143.73	220125.92	219106.28	185154.33	204087.48	206714.48	181910.33
V51	772.02	826.24	982.14	306.81	337.03	353.63	2296.67	234.3	508.59
Cr53	<0.73	<0.54	<0.76	328.06	452.2	384.94	73.85	25.47	40.19
Mn55	247.97	344.14	1843.86	7962.68	4078.12	1557.04	268.86	342.78	219.78
Fe57	97906.76	12162.57	71490.88	33574.31	17298.06	9070.31	14362.86	3613.4	8462.21
Co59	3.29	2.39	29.16	4.07	1.72	1.65	5.58	0.78	3.16
Ni60	5.26	3.58	11.45	1.95	1.39	3.41	28.66	7.17	13.67
Cu63	4.06	3.13	3.64	3.15	3	2.29	63.37	35.01	34.79
Zn66	10.63	7.63	28.91	17.83	10.86	8.42	18.18	6.92	11.82
Ga71	8.9	7.26	13.37	4.73	4.92	5.41	3.47	0.96	1.8
Ge73	11.81	12.07	12.15	19.47	16.69	19.3	7.51	5.16	3.67
As75	12.7	6.4	7.29	4.13	6.74	7.28	5.2	5.29	8.59
Se77	<0.43	4.04	0.52	2.4	4.44	1.1	<0.29	<0.26	<0.27
Y89	400.48	1070.01	440.11	1825.71	2318.08	1865.31	66.8	54.56	55.35
Zr90	940.25	208.86	227.84	34.17	35.61	46.86	145.56	405.63	259.69
Nb93	131.94	164.78	100.41	86.64	86.15	77.93	51.87	125.36	93.02
Mo95	0.252	0.203	0.637	0.88	0.82	0.109	0.498	0.504	0.093
Ag107	0.0093	0.00355	<0.0044	0.0084	<0.0095	<0.00	0.0151	0.0119	0.0259
Sn118	9.71	19.6	10.04	8.05	9.6	9.12	7.02	2.86	3.67
Sb121	0.9	0.801	0.93	3.83	3.86	3.13	1.64	0.93	0.8
La139	3.83	1.49	2.5	9.36	9.82	10.08	2.81	1.44	1.065
Sm147	20.29	46.97	33.82	98.96	118.25	107.08	4.68	3.47	2.47
Yb172	46.92	97.78	43.64	162.53	203.25	169.82	10.98	12	11.35
Hf178	29.92	17.35	13.21	1.58	2.15	2.36	8.08	9.92	8.88
Ta181	6.07	5.16	3.94	1.53	1.44	1.14	2.42	5.65	4.59
W182	2.32	0.89	0.601	31.7	35.39	39.47	2.2	3.61	1.15
Au197	<0.00	<0.00	<0.00	<0.00	<0.00	<0.00	<0.00	0.0017	<0.00
Pb208	2.78	1.28	0.943	1.41	1.53	1.5	1.24	1.1	1.2

Table F1: Continued.

Int. std. (TiO2)	99.5			
Element	047-2 rt1	047-2 rt2	047-2 rt3	047-2 rt4
Mg24	440.45	709.36	415.85	515.24
Al27	656.81	850.33	186.73	918.08
Si29	16441.35	10247.39	6973.7	16430.45
P31	248.23	239.59	203.78	102.67
Ca44	36.2	345.06	169.66	205.61
Sc45	15.69	49.49	26.67	25.39
Ti49	596510.88	596510.88	596510.88	596510.88
V51	6372.8	8521.29	9203.06	6548.07
Cr53	3296.66	3415.92	5746.13	4527.42
Mn55	646.68	992.73	1576.16	2711.35
Fe57	28256.39	40780.07	62564.61	99111.3
Co59	<0.110	0.472	0.168	<0.122
Ni60	10.29	8.59	15.75	26.87
Cu63	70.93	7.2	10.64	10.09
Zn66	24.4	25.92	194.06	39.42
Ga71	0.864	0.596	0.966	0.645
Ge73	0.75	0.67	3.55	3.43
As75	19.64	13.21	13.48	16.98
Se77	<0.67	<0.80	5.92	1.3
Y89	10.83	7.16	11.94	18.96
Zr90	28.95	140.25	102.18	50.11
Nb93	827.13	2937.28	2481.46	1357.1
Mo95	0.417	0.213	0.414	<0.099
Ag107	0.0542	<0.00	<0.0199	<0.026
Sn118	169.18	321.11	333.07	151.73
Sb121	24.99	13.15	12.82	27.22
La139	14.6	8.52	16.17	17.09
Sm147	2.71	1.92	3.58	3.66
Yb172	0.397	0.476	1.13	2.86
Hf178	1.57	19.71	5.61	3.45
Ta181	66.48	151.97	78.15	67.99
W182	268.75	390.89	309.04	510.56
Au197	<0.00	<0.00	<0.00	<0.00
Pb208	18.58	10.77	15.19	19.73

Detection limits LA-ICP-MS

Table F2: Detection limits for sulfides and oxides from LA-ICP-MS (all in ppm) with 99% confidence.

Element	0054-A-ccp1	0054-A-ccp2	0054-A-ccp3	0054-B-py1	0054-B-py2	0054-B-py3	0051-py1	0051-py2	0051-py3	013A-sp1	013A-sp2	013A-sp3	013A-py1	013A-py2	013A-py3	013A-ccp1	013A-ccp2	013A-ccp3	013B-ccp
Si29	494.46	321.29	346.32	144.83	163.55	152.11	120.05	120.07	126.81	204.07	323.67	177.71	120.07	126.94	128.88	389.65	488.78	392.91	379.35
S34	1562.47	1036.59	1096.23	458.28	515.84	479.85	369.99	373.58	397.69	664.52	1053.09	576.65	391.61	412.57	420.37	1264.65	1566.36	1250.47	1197.49
Ti48	5.42	3.71	3.99	1.75	2.38	2.43	1.9	1.99	2.1	3.41	5.09	2.67	1.97	2.2	2.28	7.26	8.05	6.05	6.02
Ti49	5.64	3.62	5.56	2.19	3.05	2.91	0.917	1.95	2.67	3.61	5.26	2.9	1.4	2.73	2.56	7.66	6.09	6.49	4.18
V51	0.648	0.391	0.521	0.224	0.267	0.232	0.195	0.199	0.172	0.309	0.606	0.313	0.197	0.246	0.248	0.647	0.799	0.75	0.772
Cr53	22.42	15.54	18.23	7.5	7.98	7.07	5.93	5.9	5.93	10.53	15.84	7.78	5.97	5.86	6.09	18.45	24.43	18.25	17.38
Mn55	4.88	3.15	3.38	1.48	1.64	1.5	1.17	1.15	1.18	2.02	3.21	1.77	1.18	1.29	1.23	3.83	4.79	3.76	3.75
Fe57	139.44	86.59	101.16	40.04	48.14	43.47	35.03	35.16	36.33	57.66	97.45	54.15	35.51	37.16	38.05	111.05	139.03	109.6	120.55
Co59	1.23	0.965	1.04	0.412	0.439	0.461	0.361	0.369	0.358	0.658	1.03	0.58	0.382	0.436	0.389	1.12	1.41	1.37	1.33
Ni60	23.86	16.21	17.58	7.67	8.59	7.96	6.34	6.53	6.94	11.24	18.4	10.31	6.87	7.29	7.29	22.3	27	22.27	22.75
Cu65	6.92	5.11	5.5	2.49	2.66	2.54	2.07	1.84	2.16	3.39	5.27	2.87	1.86	2.14	2.04	6.49	7.98	6.47	6.69
Zn67	21.27	11.31	13.47	5.72	5.42	5.77	4.72	5	3.82	9.63	14.32	6.61	5.06	5.24	5.76	12.27	22.74	15.5	14.58
Ga71	0.308	0.137	0.154	0.0656	0.104	<0.00000	0.0531	0.106	0.0786	<0.00000	0.32	<0.00000	0.0761	0.0805	<0.00000	0.335	<0.00000	0.241	<0.00000
Ge73	12.66	6.34	8.24	2.93	4.59	3.72	3.31	3.36	3.65	5.36	8.99	3.99	3.35	3.05	3.81	11.38	11.23	8.37	9.6
As75	4.34	3.01	2.84	1.25	1.3	1.29	0.923	0.933	1.08	1.89	2.85	1.63	1.14	1.17	1.22	3.55	5.22	4.2	3.88
Se77	15.52	11.64	10.13	4.34	4.43	4.75	4.14	3.78	3.82	5.76	9.25	4.53	3.91	3.42	3.15	9.51	9.7	13.31	9.3
Nb93	<0.00000	0.0914	0.102	0.087	0.0975	0.0881	0.0984	0.0598	0.0511	0.0821	<0.00000	0.156	0.109	0.0727	0.0367	0.238	0.264	0.357	0.11
Mo95	2.67	1.61	0.953	0.334	0.268	0.734	0.517	0.277	0.586	0.824	1.21	0.869	0.357	0.38	0.223	1.85	0.82	1.79	1.55
Ru99	3.08	2.2	2.29	1.08	0.94	0.74	0.961	0.83	0.874	1.22	2.26	0.977	0.854	0.977	0.917	3.09	4.09	3.06	3.7
Ru101	3.3	1.47	2.16	0.778	0.983	1.11	0.581	0.411	0.671	0.991	2.57	0.854	0.571	0.903	0.68	2.32	2.7	2.29	3.02
Rh103	0.653	0.453	0.41	0.188	0.193	0.141	0.147	0.122	0.147	0.216	0.413	0.202	0.181	0.0828	0.172	0.396	0.565	0.389	0.528
Pd106	1.71	1.58	2.29	0.587	0.624	0.94	0.616	0.389	0.668	0.894	1.22	0.975	0.563	0.843	0.552	2.16	2.76	2.2	1.99
Ag109	0.641	0.278	0.448	0.146	0.0834	0.18	0.151	0.132	0.114	0.264	0.327	0.212	0.117	0.26	0.117	0.636	0.551	0.603	0.646
Cd111	2.37	2.01	1.62	0.466	0.839	0.807	0.517	0.857	0.209	1.08	1.83	0.63	0.474	1.04	0.9	0.967	3.11	2.25	2.44
In115	0.22	0.086	0.0972	0.0457	0.0699	0.0333	0.0217	0.0306	0.0229	0.0525	0.073	0.0477	0.0226	0.0449	<0.00000	0.0713	0.141	0.0518	0.13
Sn120	2.51	1.75	1.82	0.633	0.762	0.752	0.625	0.665	0.623	0.995	1.64	0.883	0.566	0.612	0.656	2.03	2.24	2.03	1.82
Sb123	<0.00000	<0.00000	<0.00000	<0.00000	0.0734	<0.00000	0.0738	<0.00000	<0.00000	<0.00000	<0.00000	0.0775	<0.00000	<0.00000	<0.00000	0.223	<0.00000	0.159	0.281
Te126	1.87	1.02	1.24	0.507	0.711	0.63	0.434	0.445	0.527	0.828	0.978	0.759	0.491	0.482	0.432	1.27	1.85	1.71	1.85
Ba137	0.359	0.386	0.413	0.206	0.142	0.169	0.152	0.17	0.149	0.256	0.364	0.201	0.181	0.164	0.157	0.468	0.656	0.575	0.405
W183	<0.00000	<0.00000	<0.00000	<0.00000	<0.00000	<0.00000	<0.00000	<0.00000	<0.00000	<0.00000	<0.00000	<0.00000	<0.00000	<0.00000	<0.00000	<0.00000	<0.00000	<0.00000	<0.00000
Re187	<0.00000	<0.00000	<0.00000	<0.00000	<0.00000	<0.00000	<0.00000	<0.00000	<0.00000	<0.00000	<0.00000	<0.00000	<0.00000	<0.00000	<0.00000	0.14	<0.00000	<0.00000	<0.00000
Os190	<0.00000	<0.00000	<0.00000	<0.00000	<0.00000	<0.00000	<0.00000	<0.00000	<0.00000	<0.00000	<0.00000	<0.00000	<0.00000	<0.00000	<0.00000	<0.00000	<0.00000	<0.00000	<0.00000
Ir193	<0.00000	<0.00000	<0.00000	<0.00000	<0.00000	<0.00000	<0.00000	<0.00000	<0.00000	<0.00000	<0.00000	<0.00000	<0.00000	<0.00000	<0.00000	<0.00000	<0.00000	<0.00000	<0.00000
Pt195	<0.00000	<0.00000	<0.00000	<0.00000	<0.00000	<0.00000	<0.00000	<0.00000	<0.00000	<0.00000	<0.00000	<0.00000	<0.00000	<0.00000	<0.00000	<0.00000	<0.00000	<0.00000	<0.00000
Au197	<0.00000	<0.00000	<0.00000	<0.00000	<0.00000	<0.00000	<0.00000	<0.00000	<0.00000	<0.00000	<0.00000	<0.00000	<0.00000	<0.00000	<0.00000	<0.00000	<0.00000	<0.00000	<0.00000
Hg202	6.17	3.77	3.8	1.4	1.56	1.62	1.05	1.45	1.2	3.63	12.69	7.22	5.19	3.66	3.02	8.78	9.85	7.75	7.66
Tl203	0.579	0.163	<0.00000	0.112	<0.00000	<0.00000	<0.00000	<0.00000	<0.00000	0.16	<0.00000	<0.00000	0.0978	<0.00000	<0.00000	<0.00000	<0.00000	<0.00000	0.57
Pb208	<0.00000	<0.00000	<0.00000	0.0423	0.0481	<0.00000	0.0354	<0.00000	<0.00000	<0.00000	<0.00000	0.0401	<0.00000	0.05	<0.00000	<0.00000	0.109	<0.00000	<0.00000
Th232	<0.00	<0.00	<0.00	<0.00	<0.00	<0.00	<0.00	<0.00	<0.00	<0.00	<0.00	<0.00	<0.00	<0.00	<0.00	<0.00	<0.00	<0.00	<0.00
U238	<0.00000	<0.00000	<0.00000	<0.00000	<0.00000	<0.00000	<0.00000	<0.00000	<0.00000	<0.00000	<0.00000	<0.00000	<0.00000	<0.00000	<0.00000	<0.00000	<0.00000	<0.00000	<0.00000

Table F2: Continued.

Element	014-unk	014-unk	014-py1	014-py2	014-py3	014-ccp1	014-ccp2	014-ccp3	0571-py1	0571-py2	0571-py3	0571-ccp1	0571-ccp2	0571-ccp3
Si29	54.51	43.48	7.63	7.48	7.84	12.93	14.93	13.87	7.45	8.18	7.49	18.04	17.38	17.58
S34	173.56	136.98	24.52	24.52	24.63	41.82	47.57	45.2	23.78	26.04	24	57.7	54.84	55.9
Ti48	0.738	0.553	0.106	0.123	0.0861	0.181	0.198	0.178	0.101	0.111	0.105	0.231	0.199	0.197
Ti49	0.588	0.911	0.0984	0.0914	0.134	0.265	0.26	0.223	<0.00000	0.155	0.0633	0.253	0.299	0.3
V51	0.0616	0.0447	0.00911	0.00927	0.0112	0.0145	0.0148	0.018	0.0102	0.00809	0.0118	0.0231	0.0198	0.0229
Cr53	2.37	1.88	0.322	0.327	0.338	0.551	0.653	0.646	0.347	0.365	0.345	0.804	0.824	0.795
Mn55	0.367	0.286	0.053	0.0517	0.0529	0.09	0.104	0.0955	0.0527	0.0588	0.053	0.12	0.125	0.126
Fe57	11.21	8.82	1.56	1.5	1.61	2.64	2.99	2.88	1.48	1.74	1.64	3.7	3.76	3.53
Co59	0.126	0.113	0.0213	0.0202	0.0187	0.0326	0.0327	0.0318	0.0163	0.0205	0.0198	0.0483	0.0456	0.0443
Ni60	2.19	1.82	0.323	0.338	0.323	0.539	0.633	0.621	0.341	0.388	0.351	0.819	0.782	0.806
Cu65	0.541	0.449	0.0773	0.0818	0.0807	0.13	0.151	0.165	0.0902	0.0931	0.0724	0.203	0.192	0.207
Zn67	0.99	0.968	0.211	0.17	0.152	0.319	0.336	0.331	0.139	0.187	0.165	0.502	0.446	0.331
Ga71	0.0284	0.0158	<0.00000	0.00211	0.00428	0.00689	0.0058	<0.00000	0.00301	0.00239	<0.00000	<0.00000	0.00493	0.0104
Ge73	0.579	0.391	0.0978	0.0846	0.0864	0.131	0.137	0.161	0.0866	0.109	0.0812	0.232	0.191	0.153
As75	0.238	0.205	0.0355	0.0349	0.0357	0.0665	0.0723	0.0661	0.04	0.0462	0.0399	0.0958	0.0982	0.0963
Se77	1.16	0.875	0.151	0.167	0.158	0.25	0.203	0.19	0.12	0.113	0.128	0.344	0.335	0.282
Nb93	<0.00000	0.0195	<0.00000	0.00215	<0.00000	0.00251	0.00853	0.00403	0.00224	0.0031	0.00243	0.00768	0.0125	0.00801
Mo95	<0.00000	0.11	0.00909	<0.00000	0.0188	0.0261	0.0475	0.0377	0.0208	0.0147	0.0141	0.0221	0.0481	0.0907
Ru99	0.314	0.233	0.0444	0.0526	0.0416	0.0669	0.0563	0.0892	0.0517	0.0276	0.0485	0.0583	0.108	0.0927
Ru101	0.255	0.145	0.0413	0.0451	0.0344	0.0445	0.0813	0.0634	0.0274	0.0443	0.0362	0.105	0.0685	0.0824
Rh103	0.0263	0.032	0.00562	0.00539	0.00664	0.011	0.0154	0.0112	0.00754	0.00816	0.00734	0.016	0.0153	0.0145
Pd106	0.127	0.114	0.0194	0.0215	0.0283	0.0258	0.0464	0.0362	0.0218	0.027	0.0266	0.0625	0.0443	0.0572
Ag109	0.0557	0.0496	0.00898	0.0039	0.00593	0.0131	0.0161	0.0155	0.0044	0.00986	0.00665	0.0187	0.00645	0.0152
Cd111	0.207	0.188	0.024	0.0286	0.0477	0.045	0.0895	0.0732	0.0364	0.0375	0.0342	0.0946	0.105	0.0871
In115	<0.00000	0.0105	0.00193	0.00197	0.0018	0.00273	0.00199	0.00305	0.00179	0.002	0.00142	0.00244	0.00275	0.00383
Sn120	0.144	0.112	0.0187	0.0208	0.02	0.0344	0.0395	0.0348	0.0207	0.0199	0.0201	0.0458	0.0436	0.046
Sb123	<0.00000	0.0137	0.00181	<0.00000	<0.00000	<0.00000	<0.00000	<0.00000	<0.00000	<0.00000	<0.00000	0.00948	<0.00000	0.007
Te126	0.13	0.102	0.0219	0.0169	0.0185	0.0416	0.0401	0.0396	0.0252	0.0194	0.0185	0.0497	0.0571	0.0481
Ba137	0.0809	0.072	0.0115	0.015	0.0149	0.0241	0.027	0.0298	0.0143	0.0176	0.0147	0.0297	0.0332	0.028
W183	<0.00000	<0.00000	<0.00000	<0.00000	<0.00000	<0.00000	<0.00000	<0.00000	<0.00000	<0.00000	<0.00000	<0.00000	<0.00000	<0.00000
Re187	<0.00000	<0.00000	<0.00000	<0.00000	<0.00000	<0.00000	<0.00000	<0.00000	<0.00000	<0.00000	<0.00000	<0.00000	<0.00000	<0.00000
Os190	<0.00000	<0.00000	<0.00000	<0.00000	<0.00000	<0.00000	<0.00000	<0.00000	<0.00000	<0.00000	<0.00000	<0.00000	<0.00000	<0.00000
Ir193	<0.00000	<0.00000	<0.00000	<0.00000	<0.00000	<0.00000	<0.00000	<0.00000	<0.00000	<0.00000	<0.00000	<0.00000	<0.00000	<0.00000
Pt195	<0.00000	<0.00000	<0.00000	<0.00000	<0.00000	<0.00000	<0.00000	<0.00000	<0.00000	<0.00000	<0.00000	<0.00000	<0.00000	<0.00000
Au197	<0.00000	<0.00000	<0.00000	<0.00000	<0.00000	<0.00000	<0.00000	<0.00000	<0.00000	<0.00000	<0.00000	<0.00000	<0.00000	<0.00000
Hg202	0.573	0.505	0.0813	0.0802	0.0653	0.113	0.129	0.106	0.0479	0.0674	0.0657	0.144	0.0841	0.0983
Tl203	0.0223	0.0246	0.00452	0.00559	<0.00000	<0.00000	0.00864	<0.00000	0.00312	<0.00000	0.00567	<0.00000	<0.00000	0.00729
Pb208	<0.00000	<0.00000	<0.00000	<0.00000	<0.00000	<0.00000	<0.00000	<0.00000	<0.00000	<0.00000	<0.00000	<0.00000	<0.00000	0.00246
Th232	<0.00	<0.00	<0.00	<0.00	<0.00	<0.00	<0.00	<0.00	<0.00	<0.00	<0.00	<0.00	<0.00	<0.00
U238	<0.00000	<0.00000	<0.00000	<0.00000	<0.00000	<0.00000	<0.00000	<0.00000	<0.00000	<0.00000	<0.00000	<0.00000	<0.00000	<0.00000

Table F2: Continued.

Element	060A-sp1	060A-sp2	060A-sp3	060A-ccp1	060A-ccp2	060A-ccp3	047-1-py1	047-1-py2	047-1-py3	047-1-ccp1	047-1-ccp2	047-1-ccp3	047-2-py1	047-2-py2
Si29	5.18	5.76	5.69	20.97	25.14	21.95	11.07	10.08	10.42	17.26	26.24	22.27	10.26	9.52
S34	18.09	20.33	19.59	71.19	86.44	74.79	37.24	34.12	34.86	58.53	90.41	75.86	34.92	32.4
Ti48	0.0604	0.0683	0.0625	0.216	0.261	0.24	0.115	0.116	0.125	0.21	0.307	0.232	0.11	0.113
Ti49	0.0698	0.088	0.0721	0.331	0.393	0.271	0.101	0.165	0.163	0.26	0.338	0.261	0.198	0.167
V51	0.0063	0.00431	0.00835	0.0184	0.0308	0.0287	0.0135	0.0133	0.0136	0.0237	0.0344	0.0311	0.0169	0.0109
Cr53	0.248	0.263	0.27	1.08	1.25	1.08	0.541	0.521	0.506	0.887	1.42	1.05	0.558	0.503
Mn55	0.0399	0.0451	0.0437	0.155	0.183	0.159	0.0842	0.0774	0.0782	0.127	0.205	0.178	0.0828	0.0726
Fe57	1.08	1.22	1.25	4.35	5.42	4.52	2.35	2.15	2.1	3.46	5.76	4.8	2.11	2.06
Co59	0.0131	0.0153	0.0143	0.0492	0.0575	0.0533	0.029	0.025	0.0273	0.0433	0.0623	0.0547	0.0292	0.0218
Ni60	0.249	0.283	0.261	0.987	1.16	1.03	0.526	0.495	0.512	0.886	1.33	1.14	0.521	0.48
Cu65	0.0658	0.0723	0.0708	0.244	0.316	0.261	0.151	0.13	0.13	0.231	0.364	0.294	0.143	0.117
Zn67	0.141	0.177	0.165	0.494	0.795	0.691	0.323	0.314	0.301	0.499	0.826	0.763	0.373	0.271
Ga71	0.00341	<0.00000	0.0038	<0.00000	0.0147	0.00935	<0.00000	0.00308	0.00784	0.00921	0.0117	0.0145	0.00462	0.0052
Ge73	0.0563	0.0642	0.0612	0.246	0.266	0.276	0.123	0.135	0.117	0.185	0.329	0.283	0.136	0.109
As75	0.0272	0.0338	0.0333	0.115	0.147	0.118	0.0611	0.0597	0.0597	0.104	0.153	0.12	0.0575	0.0566
Se77	0.107	0.0755	0.102	0.254	0.462	0.46	0.215	0.222	0.154	0.265	0.426	0.396	0.162	0.177
Nb93	0.00211	0.00143	<0.00000	0.0163	<0.00000	0.00777	0.00687	0.00451	0.00544	0.0102	0.00716	0.0179	0.00813	0.00266
Mo95	0.00937	0.0133	0.0148	0.0672	0.0638	0.0406	0.046	0.0401	0.048	0.0797	0.0801	<0.00000	0.0468	0.0449
Ru99	0.0442	0.0327	0.0246	0.137	0.18	0.0955	0.0725	0.0703	0.0631	0.101	0.0941	0.116	0.0574	0.0804
Ru101	0.0318	0.0351	0.031	0.156	0.112	0.106	0.0581	0.0638	0.0603	0.104	0.182	0.165	0.049	0.042
Rh103	0.00406	0.00505	0.00499	0.0181	0.0205	0.0202	0.00941	0.0102	0.0108	0.0168	0.0358	0.0193	0.014	0.0125
Pd106	0.0189	0.0196	0.0238	0.07	0.0758	0.0847	0.0359	0.0293	0.0275	0.0683	0.0673	0.0858	0.0376	0.0334
Ag109	0.00467	0.00518	0.00272	0.0234	0.0192	0.00612	0.0112	0.00755	0.00837	0.0225	0.0265	0.0259	0.00907	0.0118
Cd111	0.0228	<0.00000	0.0357	0.158	0.108	0.16	0.0399	0.053	0.0795	0.123	0.165	0.216	0.0964	0.0343
In115	0.00112	0.0012	0.00124	0.00349	0.00497	0.00182	0.00292	0.00208	0.00176	0.00207	0.00851	0.00595	0.00155	0.00142
Sn120	0.0138	0.0156	0.0153	0.0527	0.0687	0.0601	0.0282	0.0279	0.0303	0.0468	0.0721	0.0608	0.0261	0.0272
Sb123	<0.00000	<0.00000	<0.00000	<0.00000	<0.00000	0.00976	<0.00000	<0.00000	<0.00000	0.00999	<0.00000	<0.00000	<0.00000	<0.00000
Te126	0.0142	0.0217	0.0175	0.0597	0.0499	0.0622	0.0303	0.0319	0.033	0.0316	0.0785	0.0765	0.0302	0.0329
Ba137	0.0092	0.00958	0.0143	0.0352	0.0545	0.0474	0.0346	0.0258	0.0234	0.0353	0.0562	0.0715	0.0154	0.0251
W183	<0.00000	<0.00000	<0.00000	<0.00000	<0.00000	<0.00000	<0.00000	<0.00000	<0.00000	<0.00000	<0.00000	<0.00000	<0.00000	<0.00000
Re187	<0.00000	<0.00000	<0.00000	<0.00000	<0.00000	<0.00000	<0.00000	<0.00000	<0.00000	<0.00000	<0.00000	<0.00000	<0.00000	<0.00000
Os190	<0.00000	<0.00000	<0.00000	<0.00000	<0.00000	<0.00000	<0.00000	<0.00000	<0.00000	<0.00000	<0.00000	<0.00000	<0.00000	<0.00000
Ir193	<0.00000	<0.00000	<0.00000	<0.00000	<0.00000	<0.00000	<0.00000	<0.00000	<0.00000	<0.00000	<0.00000	<0.00000	<0.00000	<0.00000
Pt195	<0.00000	<0.00000	<0.00000	<0.00000	<0.00000	<0.00000	<0.00000	<0.00000	<0.00000	<0.00000	<0.00000	<0.00000	<0.00000	<0.00000
Au197	<0.00000	<0.00000	<0.00000	<0.00000	<0.00000	<0.00000	<0.00000	<0.00000	<0.00000	<0.00000	<0.00000	<0.00000	<0.00000	<0.00000
Hg202	0.0304	0.049	0.0429	0.173	0.171	0.164	0.075	0.0649	0.06	0.0952	0.142	0.0858	0.0633	0.044
Tl203	<0.00000	0.00237	0.00503	0.00831	0.0192	0.021	0.00745	<0.00000	0.00904	0.00666	0.0146	0.0179	<0.00000	0.00515
Pb208	<0.00000	<0.00000	0.00082	<0.00000	<0.00000	<0.00000	0.00234	0.00153	<0.00000	<0.00000	<0.00000	<0.00000	<0.00000	<0.00000
Th232	<0.00	<0.00	<0.00	<0.00	<0.00	<0.00	<0.00	<0.00	<0.00	<0.00	<0.00	<0.00	<0.00	<0.00
U238	<0.00000	<0.00000	<0.00000	<0.00000	<0.00000	<0.00000	<0.00000	<0.00000	<0.00000	<0.00000	<0.00000	<0.00000	<0.00000	<0.00000

Table F2: Continued.

Element	051-1-py1	051-1-py2	051-1-py3	051-1-ccp1	051-1-ccp2	051-1-ccp3	051-2-py1	051-2-py2	051-2-py3	051-2-ccp1	051-2-ccp2	051-2-ccp3	0221-ccp1	0221-ccp2	0221-ccp3
Si29	14.24	10.61	13.37	34.03	35.3	24.82	7.01	11.52	10.7	27.89	27.02	28.44	26.18	26.72	24.88
S34	35.34	26.81	33.77	84.84	87.7	62.09	18.08	29.5	27.06	70.18	67.17	71.4	65	65.74	61.32
Ti48	0.0883	0.0811	0.111	0.276	0.266	0.174	0.0522	0.0966	0.0909	0.232	0.21	0.213	0.196	0.185	0.171
Ti49	0.0889	0.0667	0.118	0.295	<0.00000	0.262	<0.00000	0.168	0.173	0.256	0.142	0.301	0.308	0.331	0.232
V51	0.0101	0.00844	0.0102	0.0227	0.03	0.0234	0.00592	0.0123	0.00945	0.0213	0.0199	0.0191	0.0163	0.0172	0.015
Cr53	0.418	0.321	0.426	0.993	1.11	0.803	0.222	0.34	0.342	0.786	0.787	0.899	0.848	0.81	0.77
Mn55	0.0794	0.058	0.0727	0.191	0.19	0.138	0.0398	0.0659	0.0594	0.155	0.15	0.154	0.142	0.147	0.14
Fe57	2.1	1.52	1.89	4.63	5.09	3.5	1.02	1.6	1.56	4.15	3.67	4.01	3.69	3.8	3.59
Co59	0.0379	0.0261	0.0346	0.0824	0.0862	0.0636	0.0179	0.0288	0.0287	0.0695	0.0671	0.0692	0.0655	0.0686	0.0643
Ni60	0.434	0.329	0.426	1.03	1.08	0.767	0.222	0.378	0.352	0.901	0.851	0.892	0.815	0.839	0.784
Cu65	0.0855	0.056	0.0712	0.179	0.218	0.156	0.0445	0.0725	0.0607	0.184	0.166	0.176	0.171	0.186	0.157
Zn67	0.419	0.328	0.403	0.963	1.11	0.803	0.232	0.369	0.33	0.818	0.787	0.911	0.84	0.887	0.789
Ga71	<0.00000	0.00201	<0.00000	0.00886	<0.00000	<0.00000	<0.00000	<0.00000	0.00424	<0.00000	<0.00000	<0.00000	<0.00000	<0.00000	<0.00000
Ge73	0.0196	0.0257	0.0374	0.142	0.05	0.0832	0.0405	0.0368	0.0587	0.186	0.135	0.137	0.126	0.158	0.112
As75	0.0547	0.0438	0.0521	0.142	0.147	0.108	0.029	0.0503	0.0425	0.109	0.121	0.117	0.119	0.107	0.108
Se77	0.256	0.185	0.215	0.5	0.63	0.501	0.111	0.206	0.176	0.507	0.457	0.498	0.418	0.458	0.285
Nb93	<0.00000	<0.00000	0.00215	0.0123	<0.00000	0.0044	<0.00000	0.00385	0.00207	0.00856	0.00755	<0.00000	<0.00000	<0.00000	0.00556
Mo95	<0.00000	<0.00000	<0.00000	<0.00000	<0.00000	0.025	<0.00000	0.0209	<0.00000	<0.00000	<0.00000	<0.00000	<0.00000	<0.00000	<0.00000
Ru99	<0.00000	<0.00000	<0.00000	<0.00000	<0.00000	<0.00000	0.012	0.02	0.0128	<0.00000	<0.00000	0.0468	<0.00000	<0.00000	<0.00000
Ru101	0.0163	<0.00000	0.0241	0.0659	<0.00000	<0.00000	0.0119	<0.00000	<0.00000	<0.00000	<0.00000	<0.00000	<0.00000	<0.00000	0.0294
Rh103	0.00345	<0.00000	0.0032	0.00977	<0.00000	<0.00000	0.00175	<0.00000	0.00266	0.0117	0.00795	<0.00000	0.0093	0.00901	<0.00000
Pd106	<0.00000	<0.00000	0.0175	0.0433	<0.00000	<0.00000	0.0132	0.0127	0.0114	<0.00000	0.0277	<0.00000	0.0277	0.0267	0.0251
Ag109	<0.00000	<0.00000	<0.00000	<0.00000	<0.00000	0.00485	<0.00000	<0.00000	<0.00000	<0.00000	0.0074	<0.00000	<0.00000	<0.00000	0.00693
Cd111	<0.00000	0.0219	0.0315	0.0557	<0.00000	<0.00000	0.00871	0.0293	0.0231	0.059	<0.00000	0.0347	0.0472	0.0459	0.0308
In115	<0.00000	0.0008	0.0007	<0.00000	<0.00000	<0.00000	0.00039	<0.00000	0.00084	0.00153	<0.00000	0.0022	<0.00000	0.00206	0.0024
Sn120	0.0367	0.029	0.0352	0.0925	0.0896	0.064	0.0181	0.0279	0.027	0.0748	0.0678	0.0759	0.0686	0.0651	0.0681
Sb123	0.00676	0.00567	<0.00000	<0.00000	0.0117	<0.00000	0.00247	<0.00000	<0.00000	<0.00000	0.00932	<0.00000	<0.00000	<0.00000	<0.00000
Te126	0.028	0.0222	0.0233	0.0779	0.0753	0.057	0.0158	0.0286	0.0263	0.0809	0.0643	0.0687	0.0586	0.0452	0.0657
Ba137	0.00828	0.00619	0.0109	0.0192	<0.00000	0.0147	0.00597	<0.00000	0.0091	0.0314	0.0223	<0.00000	0.0206	0.0219	0.024
W183	<0.00000	<0.00000	<0.00000	<0.00000	<0.00000	<0.00000	<0.00000	<0.00000	<0.00000	<0.00000	<0.00000	<0.00000	<0.00000	<0.00000	<0.00000
Re187	<0.00000	<0.00000	<0.00000	<0.00000	<0.00000	<0.00000	<0.00000	<0.00000	<0.00000	<0.00000	0.00923	<0.00000	<0.00000	<0.00000	<0.00000
Os190	<0.00000	<0.00000	<0.00000	<0.00000	<0.00000	<0.00000	<0.00000	<0.00000	<0.00000	<0.00000	<0.00000	<0.00000	<0.00000	<0.00000	<0.00000
Ir193	<0.00000	<0.00000	<0.00000	<0.00000	<0.00000	<0.00000	<0.00000	<0.00000	<0.00000	<0.00000	<0.00000	<0.00000	<0.00000	<0.00000	<0.00000
Pt195	<0.00000	<0.00000	<0.00000	<0.00000	<0.00000	<0.00000	<0.00000	<0.00000	<0.00000	<0.00000	<0.00000	<0.00000	<0.00000	<0.00000	<0.00000
Au197	<0.00000	<0.00000	<0.00000	<0.00000	<0.00000	<0.00000	<0.00000	<0.00000	<0.00000	<0.00000	<0.00000	<0.00000	<0.00000	<0.00000	<0.00000
Hg202	0.0832	0.0761	0.0738	0.209	0.211	0.178	0.0375	0.0775	0.0782	0.144	0.165	0.142	0.153	0.159	0.114
Tl203	0.00931	<0.00000	<0.00000	0.0199	0.0165	<0.00000	<0.00000	0.00382	0.00757	0.0146	0.0137	0.0116	0.00769	0.0127	0.00958
Pb208	<0.00000	<0.00000	<0.00000	<0.00000	<0.00000	<0.00000	<0.00000	<0.00000	<0.00000	<0.00000	<0.00000	<0.00000	<0.00000	<0.00000	<0.00000
Th232	<0.00	<0.00	<0.00	<0.00	<0.00	<0.00	<0.00	<0.00	<0.00	<0.00	<0.00	<0.00	<0.00	<0.00	<0.00
U238	<0.00000	<0.00000	<0.00000	<0.00000	<0.00000	<0.00000	<0.00000	<0.00000	<0.00000	<0.00000	<0.00000	<0.00000	<0.00000	<0.00000	<0.00000

Table F2: Continued.

Element	0221-bn1	0221-bn2	0221-bn3	0222-ccp1	0222-ccp2	0222-ccp3	040-A-ccp1	040-A-ccp2	040-A-ccp3	040-A-tnt1	040-A-tnt2
Si29	23.96	27.34	25.82	24.45	23.82	21.77	27.34	23.02	30.42	2.68	14.63
S34	59.53	67.79	63.58	63.67	61.53	56.69	69.7	58.77	76.5	6.71	36.49
Ti48	0.168	0.195	0.186	0.19	0.177	0.165	0.195	0.167	0.225	0.0197	0.103
Ti49	0.21	0.339	0.336	0.214	0.279	0.202	0.162	0.344	0.28	0.0274	0.162
V51	0.0204	0.0233	0.0201	0.021	0.0194	0.0183	0.0239	0.0217	0.0327	0.00283	0.0109
Cr53	0.741	0.856	0.767	0.743	0.699	0.728	0.933	0.768	0.986	0.0836	0.46
Mn55	0.136	0.154	0.14	0.137	0.129	0.115	0.153	0.128	0.158	0.0147	0.0788
Fe57	3.58	4.15	3.76	3.52	3.5	3.16	3.9	3.44	4.47	0.385	2.12
Co59	0.0646	0.0696	0.0644	0.0625	0.0612	0.0568	0.0763	0.0611	0.0772	0.007	0.035
Ni60	0.789	0.848	0.817	0.79	0.729	0.697	0.914	0.765	0.997	0.0864	0.459
Cu65	0.164	0.208	0.187	0.185	0.174	0.179	0.221	0.196	0.225	0.0214	0.118
Zn67	0.787	0.942	0.864	0.773	0.779	0.739	0.919	0.716	0.92	0.083	0.523
Ga71	<0.00000	<0.00000	<0.00000	<0.00000	<0.00000	<0.00000	0.00829	0.00689	<0.00000	<0.00000	<0.00000
Ge73	0.0844	0.169	0.12	0.115	0.192	0.159	0.237	0.112	0.249	0.0181	0.13
As75	0.0971	0.114	0.103	0.0993	0.0993	0.094	0.115	0.101	0.128	0.0117	0.096
Se77	0.361	0.435	0.412	0.399	0.336	0.355	0.496	0.347	0.554	0.0514	0.239
Nb93	0.00892	<0.00000	<0.00000	0.00713	0.0102	0.00887	0.00958	<0.00000	0.0113	0.0015	<0.00000
Mo95	<0.00000	0.0403	<0.00000	<0.00000	<0.00000	<0.00000	<0.00000	<0.00000	0.0327	<0.00000	<0.00000
Ru99	0.0404	<0.00000	<0.00000	<0.00000	<0.00000	<0.00000	<0.00000	<0.00000	<0.00000	<0.00000	<0.00000
Ru101	0.0459	0.0331	0.0518	0.0505	0.0401	<0.00000	<0.00000	<0.00000	<0.00000	<0.00000	<0.00000
Rh103	0.00838	0.00675	0.00942	0.00719	0.00569	0.011	0.00494	0.00708	0.0119	<0.00000	<0.00000
Pd106	0.0302	0.0279	0.0336	0.0289	0.0227	0.0346	<0.00000	0.036	0.0418	0.00415	<0.00000
Ag109	<0.00000	0.011	<0.00000	0.0069	0.0067	0.0065	<0.00000	0.0084	0.011	0.00057	0.00818
Cd111	0.0608	<0.00000	<0.00000	0.0533	0.0733	0.0503	<0.00000	<0.00000	<0.00000	<0.00000	0.0277
In115	<0.00000	<0.00000	0.00155	0.00311	0.00235	<0.00000	0.0041	0.00278	0.00316	0.00023	<0.00000
Sn120	0.0571	0.0716	0.0603	0.0622	0.0503	0.0554	0.0643	0.0486	0.0728	0.00627	0.0343
Sb123	<0.00000	<0.00000	<0.00000	<0.00000	<0.00000	<0.00000	<0.00000	<0.00000	<0.00000	<0.00000	<0.00000
Te126	0.0633	0.0602	0.0594	0.0488	0.0473	0.0502	0.0719	0.0516	0.0796	0.00648	0.031
Ba137	0.0118	0.0165	0.021	0.0144	0.0243	0.00783	0.0281	0.0202	0.0372	0.00166	0.0148
W183	<0.00000	<0.00000	<0.00000	<0.00000	<0.00000	<0.00000	<0.00000	<0.00000	<0.00000	<0.00000	<0.00000
Re187	<0.00000	<0.00000	<0.00000	<0.00000	<0.00000	<0.00000	<0.00000	<0.00000	<0.00000	<0.00000	<0.00000
Os190	<0.00000	<0.00000	<0.00000	<0.00000	<0.00000	<0.00000	<0.00000	<0.00000	<0.00000	<0.00000	<0.00000
Ir193	<0.00000	<0.00000	<0.00000	<0.00000	<0.00000	<0.00000	<0.00000	<0.00000	<0.00000	<0.00000	<0.00000
Pt195	<0.00000	<0.00000	<0.00000	<0.00000	<0.00000	<0.00000	<0.00000	<0.00000	<0.00000	<0.00000	<0.00000
Au197	<0.00000	<0.00000	<0.00000	<0.00000	<0.00000	<0.00000	<0.00000	<0.00000	<0.00000	<0.00000	<0.00000
Hg202	0.156	0.197	0.166	0.12	0.0964	0.137	0.179	0.128	0.172	0.0195	0.192
Tl203	<0.00000	<0.00000	<0.00000	0.00811	0.00547	0.00737	<0.00000	0.0075	<0.00000	0.00104	0.00322
Pb208	0.00273	<0.00000	0.00436	<0.00000	<0.00000	<0.00000	0.00573	<0.00000	<0.00000	<0.00000	0.0043
Th232	<0.00	<0.00	<0.00	<0.00	<0.00	<0.00	<0.00	<0.00	<0.00	<0.00	<0.00
U238	<0.00000	<0.00000	<0.00000	<0.00000	<0.00000	<0.00000	<0.00000	<0.00000	<0.00000	<0.00000	<0.00000

Table F2: Continued.

Element	L2-dg1	L2-dg2	L2-dg3	L2-dg4	L2-A-bn1	L2-A-bn2	L2-A-bn3	L2-B-mol1	L2-B-mol2	L2-B-mol3	032-ccp1	032-ccp2	032-ccp3
Si29	37910.78	<0.00000	395.8	188.68	6.94	6.3	6.65	1.32	1.58	1.87	6.98	7.64	8.88
S34	123618.21	<0.00000	1270.44	593.39	21.62	19.48	20.79	4.15	5.03	6.04	23.32	25.67	29.99
Ti48	334.72	<0.00000	3.81	1.76	0.0603	0.054	0.0568	0.0113	0.0122	0.0142	0.0533	0.0602	0.0687
Ti49	295.23	<0.00000	4.25	1.19	0.0858	0.0376	0.0746	0.00791	0.00854	0.018	0.0561	0.0715	0.114
V51	39.02	<0.00000	0.358	0.123	0.00541	0.00549	0.00696	0.00105	0.00107	0.0015	0.00561	0.00749	0.00581
Cr53	1386.13	<0.00000	15.4	6.65	0.251	0.224	0.238	0.0515	0.0624	0.071	0.278	0.318	0.366
Mn55	280.83	<0.00000	2.81	1.36	0.0467	0.042	0.0448	0.00905	0.0107	0.013	0.0488	0.0536	0.0629
Fe57	6193.67	<0.00000	67.66	30.9	1.12	1.04	1.07	0.21	0.257	0.309	1.08	1.25	1.58
Co59	65.88	<0.00000	0.684	0.342	0.013	0.0109	0.0106	0.00231	0.00269	0.00294	0.0123	0.0128	0.0152
Ni60	1142.83	<0.00000	12.06	5.32	0.199	0.183	0.192	0.0386	0.0471	0.0593	0.227	0.254	0.294
Cu65	308.18	<0.00000	5.43	2.6	0.0982	0.0925	0.101	0.0204	0.0245	0.0299	0.108	0.121	0.136
Zn67	734.94	<0.00000	9.35	4.16	0.152	0.162	0.162	0.0304	0.0305	0.0451	0.173	0.181	0.209
Ga71	8.54	<0.00000	0.138	<0.00000	0.00275	<0.00000	<0.00000	0.0003	0.00038	<0.00000	0.00254	<0.00000	0.00235
Ge73	276.84	<0.00000	2.66	1.34	0.0425	0.0448	0.0527	0.00849	0.0114	0.011	0.0561	0.0288	0.0819
As75	210.15	<0.00000	2.2	1.07	0.0386	0.0359	0.039	0.0079	0.00939	0.0124	0.0475	0.0486	0.0565
Se77	916.08	<0.00000	9.86	5.46	0.182	0.132	0.161	0.0315	0.0466	0.0584	0.244	0.197	0.262
Nb93	10.88	<0.00000	0.0874	<0.00000	0.00201	0.00217	0.00232	0.00038	0.00058	0.00058	0.00477	0.0025	0.00294
Mo95	51.73	<0.00000	0.592	0.266	<0.00000	0.0172	0.0146	<0.00000	0.00286	0.00288	0.0136	0.0175	0.0231
Ru99	151.65	<0.00000	1.54	0.859	0.0215	0.0165	0.0217	0.00544	0.00259	0.00678	0.0338	0.0257	0.0325
Ru101	112.84	<0.00000	1.15	0.597	0.0261	0.0199	0.0207	0.00402	0.0037	0.0058	0.0176	0.0196	0.0316
Rh103	27.64	<0.00000	0.123	0.0899	0.00519	0.00412	0.00469	0.00077	0.0004	0.00143	0.00267	0.00494	0.00704
Pd106	81.9	<0.00000	0.758	0.467	0.0134	0.0159	0.0172	0.00207	0.00288	0.00327	0.0161	0.0169	0.00758
Ag109	27.38	<0.00000	0.297	0.153	0.00603	0.00515	0.00433	0.00115	0.00095	0.00106	<0.00000	0.00612	0.00538
Cd111	58.63	<0.00000	0.546	0.386	0.0259	<0.00000	0.0103	0.00358	0.00425	0.00691	0.0213	0.0209	0.0295
In115	2.51	<0.00000	0.099	0.0256	0.00093	0.00101	0.00062	0.00012	0.00027	0.00031	0.00053	<0.00000	<0.00000
Sn120	110.02	<0.00000	1.2	0.585	0.0213	0.019	0.0208	0.00387	0.00489	0.00596	0.0202	0.0227	0.0271
Sb123	17.72	<0.00000	<0.00000	<0.00000	<0.00000	<0.00000	<0.00000	<0.00000	<0.00000	0.00056	<0.00000	<0.00000	<0.00000
Te126	98.85	<0.00000	1.2	0.623	0.0212	0.0141	0.0215	0.00408	0.00555	0.00862	0.0347	0.0308	0.0335
Ba137	41.85	<0.00000	0.605	0.325	0.0137	0.00977	0.0105	0.00225	0.00345	0.00262	0.0125	0.0113	0.0152
W183	<0.00000	<0.00000	<0.00000	<0.00000	<0.00000	<0.00000	<0.00000	<0.00000	<0.00000	<0.00000	<0.00000	<0.00000	<0.00000
Re187	<0.00000	<0.00000	<0.00000	<0.00000	<0.00000	<0.00000	<0.00000	<0.00000	<0.00000	0.00065	<0.00000	<0.00000	<0.00000
Os190	<0.00000	<0.00000	<0.00000	<0.00000	<0.00000	<0.00000	<0.00000	<0.00000	<0.00000	<0.00000	<0.00000	<0.00000	<0.00000
Ir193	<0.00000	<0.00000	<0.00000	<0.00000	<0.00000	<0.00000	<0.00000	<0.00000	<0.00000	<0.00000	<0.00000	<0.00000	<0.00000
Pt195	<0.00000	<0.00000	<0.00000	<0.00000	<0.00000	<0.00000	<0.00000	<0.00000	<0.00000	<0.00000	<0.00000	<0.00000	<0.00000
Au197	<0.00000	<0.00000	<0.00000	<0.00000	<0.00000	<0.00000	<0.00000	<0.00000	<0.00000	<0.00000	<0.00000	<0.00000	<0.00000
Hg202	254.27	<0.00000	3.18	1.16	0.0489	0.0385	0.0583	0.0113	0.0144	0.0208	0.0626	0.0678	0.0888
Tl203	11.4	<0.00000	0.16	0.0413	0.0015	0.00231	0.00143	0.0005	<0.00000	0.00063	0.00242	0.0033	<0.00000
Pb208	<0.00000	<0.00000	<0.00000	<0.00000	0.00091	<0.00000	<0.00000	<0.00000	0.00069	<0.00000	0.00412	0.00344	0.00302
Th232	<0.00	<0.00	<0.00	<0.00	<0.00	<0.00	<0.00	<0.00	<0.00	<0.00	<0.00	<0.00	<0.00
U238	<0.00000	<0.00000	<0.00000	<0.00000	<0.00000	<0.00000	<0.00000	<0.00000	<0.00000	<0.00000	<0.00000	<0.00000	<0.00000

Table F2: Continued.

Element	0054-2A-mag1	0054-2A-mag2	0054-2A-mag3	0054-2b-mag1	0054-2b-mag2	0054-2b-mag3	0051-mag1	0051-mag2	0051-mag3	013B-ilm1	013B-ilm2	013B-ilm3	032B-hem1	032B-hem2	032B-hem3	032B-hem4
Mg24	0.126	0.127	0.12	0.131	0.153	0.168	0.157	0.171	0.186	0.307	0.274	0.286	0.142	0.168	0.151	0.234
Al27	0.32	0.315	0.291	0.273	0.314	0.343	0.316	0.33	0.382	0.675	0.549	0.573	0.318	0.346	0.302	0.477
Si29	54.31	54.1	50.21	43.09	48.88	52.22	47.44	50.96	57.77	82.49	67.86	70.5	28.23	31.55	27.37	41.3
P31	1.5	1.51	1.48	1.37	1.56	1.75	1.62	1.78	2.05	2.91	2.38	2.52	1.27	1.4	1.2	1.79
Ca44	28.61	28.93	27.17	24.43	27.41	29.89	26.55	29.27	32.95	47.79	39.89	41.35	17.04	18.88	16.27	25.4
Sc45	0.157	0.171	0.154	0.139	0.169	0.176	0.16	0.161	0.184	0.274	0.23	0.247	0.104	0.105	0.0953	0.143
Ti49	0.228	0.18	0.138	0.395	0.557	0.613	0.338	0.384	0.675	0.902	1.09	1.11	0.6	0.681	0.54	0.864
V51	0.015	0.0159	0.0166	0.0137	0.022	0.0281	0.0219	0.0157	0.0243	0.0408	0.0299	0.0444	0.0208	0.0233	0.0227	0.0235
Cr53	0.804	0.818	0.822	0.734	0.839	0.997	0.874	0.974	1.09	1.75	1.43	1.47	0.771	0.794	0.753	1.14
Mn55	0.159	0.157	0.151	0.144	0.164	0.18	0.159	0.174	0.203	0.314	0.253	0.273	0.128	0.141	0.129	0.2
Fe57	6.53	6.4	5.75	5.53	6.23	6.69	5.99	6.51	7.54	10.98	9.43	9.6	4.39	4.94	4.43	6.69
Co59	0.0524	0.0512	0.0497	0.0563	0.0626	0.0656	0.0607	0.0685	0.0694	0.126	0.101	0.109	0.0604	0.0611	0.0598	0.0885
Ni60	0.475	0.486	0.483	0.492	0.557	0.633	0.589	0.626	0.73	1.17	1.01	1.07	0.63	0.71	0.637	0.984
Cu63	0.0599	0.0567	0.0545	0.0507	0.0684	0.0707	0.064	0.0804	0.0776	0.106	0.123	0.133	0.0753	0.088	0.0859	0.151
Zn66	0.469	0.449	0.442	0.421	0.493	0.515	0.484	0.511	0.605	0.885	0.747	0.786	0.387	0.419	0.365	0.545
Ga71	<0.00000	<0.00000	<0.00000	<0.00000	0.00694	0.0156	<0.00000	<0.00000	<0.00000	0.02	<0.00000	<0.00000	0.014	0.00689	<0.00000	0.00951
Ge73	0.0943	0.109	0.161	0.109	0.149	0.151	0.166	0.194	0.184	0.254	0.258	0.26	0.119	0.165	0.121	0.209
As75	0.473	0.479	0.473	0.446	0.493	0.567	0.523	0.573	0.644	0.929	0.777	0.798	0.434	0.478	0.413	0.604
Se77	0.438	0.496	0.449	0.332	0.439	0.42	0.391	0.437	0.499	0.807	0.569	0.543	0.306	0.377	0.367	0.495
Y89	<0.00000	<0.00000	<0.00000	<0.00000	<0.00000	<0.00000	<0.00000	<0.00000	<0.00000	0.0125	<0.00000	0.0149	<0.00000	<0.00000	<0.00000	<0.00000
Zr90	<0.00000	<0.00000	<0.00000	<0.00000	<0.00000	<0.00000	<0.00000	<0.00000	<0.00000	<0.00000	<0.00000	<0.00000	<0.00000	0.0136	<0.00000	<0.00000
Nb93	0.0049	0.00707	0.00937	0.0118	<0.00000	<0.00000	<0.00000	0.00556	<0.00000	0.0204	<0.00000	0.0193	0.00882	<0.00000	<0.00000	0.00943
Mo95	<0.00000	<0.00000	0.0273	0.0411	0.0416	0.0466	<0.00000	0.0228	0.0471	0.0593	0.0333	<0.00000	<0.00000	0.028	0.0304	<0.00000
Ag107	0.00473	0.00966	<0.00000	0.00435	<0.00000	<0.00000	0.0112	0.00771	0.00919	<0.00000	<0.00000	0.0226	0.01	0.00988	0.00618	0.00682
Sn118	0.109	0.109	0.113	0.0974	0.11	0.129	0.114	0.125	0.148	0.21	0.156	0.158	0.0886	0.0947	0.0798	0.12
Sb121	0.018	0.0217	0.023	0.0172	0.0156	0.0218	0.0275	0.00992	0.0193	0.0472	0.0145	0.0155	0.00929	0.00722	0.012	0.0141
La139	<0.00000	<0.00000	<0.00000	<0.00000	<0.00000	<0.00000	<0.00000	0.00356	0.00424	<0.00000	<0.00000	0.00952	<0.00000	<0.00000	0.00266	0.00293
Sm147	<0.00000	<0.00000	<0.00000	<0.00000	<0.00000	<0.00000	<0.00000	<0.00000	<0.00000	<0.00000	<0.00000	<0.00000	<0.00000	<0.00000	<0.00000	<0.00000
Yb172	<0.00000	<0.00000	<0.00000	<0.00000	<0.00000	<0.00000	<0.00000	<0.00000	<0.00000	<0.00000	<0.00000	<0.00000	<0.00000	<0.00000	<0.00000	<0.00000
Hf178	<0.00000	<0.00000	<0.00000	<0.00000	<0.00000	<0.00000	<0.00000	<0.00000	<0.00000	<0.00000	<0.00000	<0.00000	<0.00000	<0.00000	<0.00000	<0.00000
Ta181	<0.00000	<0.00000	0.00622	<0.00000	<0.00000	<0.00000	<0.00000	0.00525	<0.00000	<0.00000	0.00768	0.0082	<0.00000	<0.00000	<0.00000	<0.00000
W182	<0.00000	<0.00000	<0.00000	<0.00000	<0.00000	<0.00000	<0.00000	<0.00000	<0.00000	<0.00000	<0.00000	<0.00000	<0.00000	<0.00000	<0.00000	<0.00000
Au197	<0.00000	<0.00000	<0.00000	<0.00000	<0.00000	<0.00000	<0.00000	<0.00000	<0.00000	<0.00000	<0.00000	<0.00000	<0.00000	<0.00000	<0.00000	<0.00000
Pb208	0.00244	0.00352	0.00405	<0.00000	0.00505	0.004	0.00573	0.00555	0.00331	0.00722	<0.00000	0.00864	0.00221	0.00344	0.00215	0.00474

Table F2: Continued.

Element	0054-2B-ttn1	0054-2B-ttn2	0054-2B-ttn3	013B-ttn1	013B-ttn2	013B-ttn3	060A-ttn1	060A-ttn2	060A-ttn3
Mg24	0.115	0.0826	0.117	0.123	0.105	0.0859	0.112	0.0969	0.101
Al27	0.264	0.195	0.28	0.255	0.222	0.193	0.243	0.219	0.207
Si29	45.59	32.81	43.47	30.57	27.47	23.72	29.57	26.17	25.83
P31	1.4	1.02	1.37	1.08	0.993	0.898	1.15	1.02	1.03
Ca44	24.87	18.22	24.33	18.26	15.88	13.65	17.06	15.21	15.12
Sc45	0.138	0.102	0.146	0.105	0.0957	0.0795	0.0985	0.0852	0.0864
Ti49	0.153	0.317	0.457	0.436	0.43	0.425	0.518	0.469	0.554
V51	0.0137	0.0123	0.0187	0.0114	0.0149	0.00748	0.0173	0.0164	0.013
Cr53	0.727	0.541	0.76	0.645	0.591	0.5	0.659	0.601	0.57
Mn55	0.142	0.106	0.137	0.121	0.106	0.0928	0.114	0.101	0.0985
Fe57	5.6	4.15	5.55	4.2	3.69	3.21	4.24	3.76	3.65
Co59	0.0454	0.0338	0.0555	0.0467	0.0475	0.0391	0.0541	0.0499	0.051
Ni60	0.448	0.339	0.482	0.457	0.418	0.345	0.448	0.413	0.407
Cu63	0.0562	0.04	0.0571	0.0517	0.046	0.0437	0.0509	0.0492	0.0428
Zn66	0.409	0.322	0.417	0.332	0.301	0.25	0.33	0.3	0.294
Ga71	<0.00000	<0.00000	0.00867	0.0056	0.0125	<0.00000	0.0135	0.00656	<0.00000
Ge73	0.132	0.0963	0.14	0.109	0.123	0.0863	0.112	0.0798	0.0877
As75	0.448	0.326	0.44	0.366	0.33	0.289	0.374	0.333	0.329
Se77	0.432	0.238	0.35	0.316	0.247	0.255	0.286	0.257	0.265
Y89	0.00513	<0.00000	<0.00000	<0.00000	<0.00000	<0.00000	<0.00000	<0.00000	<0.00000
Zr90	<0.00000	<0.00000	<0.00000	<0.00000	<0.00000	<0.00000	<0.00000	<0.00000	<0.00000
Nb93	0.00738	<0.00000	0.00896	0.0107	0.00833	0.00417	<0.00000	0.00744	0.00577
Mo95	<0.00000	0.0131	<0.00000	0.0235	0.014	<0.00000	0.0229	0.0273	0.0274
Ag107	<0.00000	<0.00000	0.00437	<0.00000	0.00955	<0.00000	0.00555	0.00469	<0.00000
Sn118	0.0976	0.0742	0.0959	0.0728	0.0674	0.0591	0.0776	0.0722	0.0708
Sb121	0.0186	0.0146	0.0122	0.0126	0.0122	0.0102	0.00411	0.00849	0.00851
La139	<0.00000	<0.00000	0.00289	<0.00000	<0.00000	<0.00000	<0.00000	<0.00000	<0.00000
Sm147	<0.00000	<0.00000	<0.00000	<0.00000	<0.00000	<0.00000	<0.00000	0.0135	<0.00000
Yb172	<0.00000	<0.00000	<0.00000	<0.00000	<0.00000	<0.00000	<0.00000	<0.00000	<0.00000
Hf178	<0.00000	<0.00000	<0.00000	<0.00000	<0.00000	<0.00000	<0.00000	<0.00000	<0.00000
Ta181	<0.00000	<0.00000	<0.00000	0.00383	<0.00000	<0.00000	0.00531	<0.00000	<0.00000
W182	<0.00000	<0.00000	<0.00000	<0.00000	<0.00000	<0.00000	<0.00000	<0.00000	<0.00000
Au197	<0.00000	<0.00000	<0.00000	<0.00000	<0.00000	<0.00000	<0.00000	<0.00000	<0.00000
Pb208	0.00301	0.00276	0.00388	0.00202	0.00341	0.00148	<0.00000	0.00236	0.00374

Table F2: Continued.

Element	047-2 rt1	047-2 rt2	047-2 rt3	047-2 rt4
Mg24	0.286	0.282	0.342	0.315
Al27	0.602	0.602	0.751	0.722
Si29	55	55.95	70.77	69.22
P31	6.58	7.01	8.99	8.95
Ca44	33.26	33.55	41.09	40.79
Sc45	0.187	0.191	0.223	0.237
Ti49	0.721	0.804	1.29	1.74
V51	0.0192	0.0322	0.0373	0.0477
Cr53	1.27	1.32	1.63	1.6
Mn55	0.225	0.231	0.276	0.281
Fe57	8.3	7.82	10.21	10.05
Co59	0.11	0.102	0.116	0.122
Ni60	1	1.02	1.25	1.23
Cu63	0.126	0.127	0.157	0.156
Zn66	0.637	0.624	0.795	0.815
Ga71	<0.00000	0.0122	<0.00000	<0.00000
Ge73	0.186	0.239	0.232	0.206
As75	0.791	0.855	1.1	1.09
Se77	0.669	0.797	0.822	0.83
Y89	0.0114	<0.00000	<0.00000	<0.00000
Zr90	<0.00000	<0.00000	<0.00000	<0.00000
Nb93	0.00888	<0.00000	<0.00000	0.0167
Mo95	0.0527	0.0315	0.0682	0.0989
Ag107	<0.00000	<0.00000	0.0199	0.0263
Sn118	0.287	0.299	0.387	0.36
Sb121	0.0678	0.0764	0.0701	0.047
La139	<0.00000	<0.00000	<0.00000	<0.00000
Sm147	<0.00000	<0.00000	<0.00000	<0.00000
Yb172	<0.00000	<0.00000	<0.00000	<0.00000
Hf178	<0.00000	<0.00000	<0.00000	<0.00000
Ta181	0.00684	<0.00000	<0.00000	<0.00000
W182	<0.00000	<0.00000	<0.00000	<0.00000
Au197	<0.00000	<0.00000	<0.00000	<0.00000
Pb208	0.00411	0.00738	0.00753	<0.00000

Appendix G: Fluid inclusion study data

Table G1: Fluid inclusion data. Abbreviations: L: Liquid, V: Vapor, S: Solid, T_e : First melting temperature, T_{ice} : Final ice melting temperature, T_s : Final halite temperature, T_h : Homogenization temperature.

Sample	Host mineral	FIA#	FI type	T_e (°C)	T_{hyd} (°C)	T_{ice} (°C)	T_s (°C)	T_h (°C)	Homogenization mode	Composition	NaCl/(NaCl+CaCl2)	Salinity (wt.% NaCl eq.)	Density (g/cm ⁻³)	dP/dT (bar/°C)
Sample 030 , Skadduvarri sandstone, Barren quartz-carbonate vein associated with chlorites														
030a	Quartz	FIA#1	L+V	-52		-25.5	10.0	222	L+V→L	NaCl-CaCl2-H2O	0.6171	27.3	1.06	18.49
			L+V	-52		-24.8	15.0	215	L+V→L	NaCl-CaCl2-H2O	0.6618	27.3	1.07	18.86
			L+V	-52		-25.0	8.0	221	L+V→L	NaCl-CaCl2-H2O	0.6432	27.2	1.06	18.54
			L+V	-52		-25.2	10.0	221	L+V→L	NaCl-CaCl2-H2O	0.6306	27.3	1.06	18.54
			L+V	-52		-24.5	12.0	220	L+V→L	NaCl-CaCl2-H2O	0.6600	27.3	1.06	18.59
			L+V	-52		-25.4	16.0	218	L+V→L	NaCl-CaCl2-H2O	0.6211	27.5	1.07	18.71
			L+V	-52		-25.1	5.6	220	L+V→L	NaCl-CaCl2-H2O	0.6346	27.1	1.06	18.59
			L+V	-52		-25.2	8.0	222	L+V→L	NaCl-CaCl2-H2O	0.6346	27.1	1.06	18.48
		FIA#2	L+V	-21			15.0	127	L+V→L	NaCl-H2O	1.0000	26.3	1.13	24.16
			L+V	-21			5.0	125	L+V→L	NaCl-H2O	1.0000	26.3	1.14	24.30
			L+V	-21			6.0	122	L+V→L	NaCl-H2O	1.0000	26.3	1.14	24.50
			L+V	-21			12.0	130	L+V→L	NaCl-H2O	1.0000	26.3	1.13	23.96
		FIA#3	L+V	-21			10.0	200	L+V→L	NaCl-H2O	1.0000	26.3	1.07	19.66
			L+V	-21			5.0	195	L+V→L	NaCl-H2O	1.0000	26.3	1.08	19.94
L+V	-21				7.0	198	L+V→L	NaCl-H2O	1.0000	26.3	1.08	19.77		
030b	Quartz	FIA#4	L+V	-52		-25.0	11.5	218	L+V→L	NaCl-CaCl2-H2O	0.6455	27.3	1.07	18.70
			L+V	-52		-25.0	12.0	220	L+V→L	NaCl-CaCl2-H2O	0.6458	27.3	1.07	18.59
			L+V	-52		-25.0	12.0	220	L+V→L	NaCl-CaCl2-H2O	0.6458	27.3	1.07	18.59
		FIA#5	L+V	-52		-25.4	12.5	220	L+V→L	NaCl-CaCl2-H2O	0.6188	27.4	1.07	18.60
			L+V	-52		-25.0	13.7	223	L+V→L	NaCl-CaCl2-H2O	0.6468	27.3	1.06	18.44
			L+V	-52		-25.2	12.0	220	L+V→L	NaCl-CaCl2-H2O	0.6319	27.3	1.07	18.60
			L+V	-52		-25.2	15.0	225	L+V→L	NaCl-CaCl2-H2O	0.6338	27.4	1.06	18.34

Table G1: Continued.

Sample	Host mineral	FIA#	Fl type	T _e (°C)	T _{hyd} (°C)	T _{ice} (°C)	T _s (°C)	T _H (°C)	Homogenization mode	Composition	NaCl/(NaCl-CaCl ₂)	Salinity (wt. % NaCl equ)	Density (g/cm ⁻³)	dP/dT (bar/°C)	
Sample 034 , Sediment hosted Lundström deposit, Mineralized quartz-carbonate vein associated with bornite, digenite and chlorites.															
034a	Quartz	FIA#1	L+V	-21		-3.0		129	L+V→L	NaCl-H ₂ O	1.0000	5.0	0.97	19.35	
			L+V			-3.4		134	L+V→L	NaCl-H ₂ O	1.0000	5.6	0.97	19.33	
			L+V			-3.2		135	L+V→L	NaCl-H ₂ O	1.0000	5.3	0.97	19.17	
			L+V			-3.4		130	L+V→L	NaCl-H ₂ O	1.0000	5.6	0.98	19.54	
			L+V			-5.0		132	L+V→L	NaCl-H ₂ O	1.0000	7.9	0.99	20.37	
			L+V			-3.0		133	L+V→L	NaCl-H ₂ O	1.0000	5.0	0.97	19.16	
		L+V			-3.5		132	L+V→L	NaCl-H ₂ O	1.0000	5.7	0.97	19.50		
		FIA#2	L+V	-52		-25.0	3.5	217	L+V→L	NaCl-CaCl ₂ -H ₂ O	0.6402		27.1	1.06	18.70
			L+V	-52		-25.0	15.0	219	L+V→L	NaCl-CaCl ₂ -H ₂ O	0.6476		27.4	1.06	18.60
L+V	-52			-25.0	13.0	222	L+V→L	NaCl-CaCl ₂ -H ₂ O	0.6464		27.3	1.05	18.44		
034b	Quartz	FIA#3	L+V+S	-52			315.0	230	L+V+S→L+S→L	NaCl-CaCl ₂ -H ₂ O	-	40.2	1.17	-	
			L+V+S	-52			300.0	227	L+V+S→L+S→L	NaCl-CaCl ₂ -H ₂ O	-	39.0	1.17	-	
			L+V+S	-52			270.0	228	L+V+S→L+S→L	NaCl-CaCl ₂ -H ₂ O	-	36.5	1.15	-	
		FIA#4	L+V	-21		-3.5		130	L+V→L	NaCl-H ₂ O	1.0000	5.7	0.98	19.60	
			L+V	-21		-3.7		127	L+V→L	NaCl-H ₂ O	1.0000	6.0	0.98	19.88	
			L+V	-21		-4.1		125	L+V→L	NaCl-H ₂ O	1.0000	6.6	0.99	20.24	
034c	Quartz	FIA#5	L+V+S	-52			250.0	217	L+V+S→L+S→L	NaCl-CaCl ₂ -H ₂ O	-	35.1	1.14	-	
			L+V+S	-52			250.0	227	L+V+S→L+S→L	NaCl-CaCl ₂ -H ₂ O	-	34.9	1.13	-	
		FIA#6	L+V+S	-52			230.0	230	L+V+S→L	NaCl-CaCl ₂ -H ₂ O	-	33.5	1.11	18.40	
			L+V+S	-52			240.0	222	L+V+S→L+S→L	NaCl-CaCl ₂ -H ₂ O	-	34.2	1.13	-	
Sample 0221 , Sediment hosted Anna deposit, Mineralized quartz-carbonate vein associated with bornite, digenite and halite															
0221	Quartz	FIA#1	L+V+S	-52			153.0	207	L+V+S→L+V→L	NaCl-CaCl ₂ -H ₂ O	-	29.8	1.10	19.29	
			L+V+S	-52			150.0	212	L+V+S→L+V→L	NaCl-CaCl ₂ -H ₂ O	-	29.7	1.09	19.05	
			L+V+S	-52			145.0	192	L+V+S→L+V→L	NaCl-CaCl ₂ -H ₂ O	-	29.5	1.11	20.03	
			L+V+S	-52			145.0	200	L+V+S→L+V→L	NaCl-CaCl ₂ -H ₂ O	-	29.5	1.10	19.63	
		FIA#2	L+V+S	-52			157.0	209	L+V+S→L+V→L	NaCl-CaCl ₂ -H ₂ O	-	29.9	1.10	19.20	
			L+V+S	-52			155.0	212	L+V+S→L+V→L	NaCl-CaCl ₂ -H ₂ O	-	29.9	1.10	19.06	
			L+V+S	-52			150.0	212	L+V+S→L+V→L	NaCl-CaCl ₂ -H ₂ O	-	29.7	1.09	19.05	
		FIA#3	L+V+S	-52			160.0	210	L+V+S→L+V→L	NaCl-CaCl ₂ -H ₂ O	-	30.1	1.10	19.15	
			L+V+S	-52			158.0	210	L+V+S→L+V→L	NaCl-CaCl ₂ -H ₂ O	-	30.0	1.10	19.15	
			L+V+S	-52			155.0	210	L+V+S→L+V→L	NaCl-CaCl ₂ -H ₂ O	-	29.9	1.10	19.15	
		FIA#4	L+V	-21		-4.2		119	L+V→L	NaCl-H ₂ O	1.0000	6.7	0.99	20.64	
			L+V	-21		-4.1		118	L+V→L	NaCl-H ₂ O	1.0000	6.6	0.99	20.63	
			L+V	-21		-4.0		120	L+V→L	NaCl-H ₂ O	1.0000	6.4	0.99	20.45	
			L+V	-21		-4.2		120	L+V→L	NaCl-H ₂ O	1.0000	6.7	0.99	20.58	
			L+V	-21		-4.1		122	L+V→L	NaCl-H ₂ O	1.0000	6.6	0.99	20.40	

Table G1: Continued.

Sample	Host mineral	FIA#	Fl type	T _e (°C)	T _{hyd} (°C)	T _{ice} (°C)	T _s (°C)	T _H (°C)	Homogenization mode	Composition	NaCl/(NaCl+CaCl2)	Salinity (wt. % NaCl equ)	Density (g/cm ⁻³)	dP/dT (bar/°C)	
Sample 040 , Sediment hosted Anna deposit, Mineralized quartz-carbonate vein associated with bornite, digenite and halite															
040	Quartz	FIA#1	L+V+S	-52		-25.0	150.0	235	L+V+S→L+V→L	NaCl-CaCl2-H2O	0.7138	29.7	1.07	18.00	
			L+V+S	-52		-25.0	152.0	230	L+V+S→L+V→L	NaCl-CaCl2-H2O	0.7150	29.7	1.08	18.23	
			L+V+S	-52		-25.0	155.0	230	L+V+S→L+V→L	NaCl-CaCl2-H2O	0.7169	29.9	1.08	18.23	
	FIA#2	L+V	-23			25.0	212	L+V→L	NaCl-H2O	1.0000	26.5	1.07	18.99		
		L+V	-23			23.0	227	L+V→L	NaCl-H2O	1.0000	26.4	1.05	18.17		
		L+V	-23			23.5	225	L+V→L	NaCl-H2O	1.0000	26.4	1.05	18.28		
		L+V	-23			20.2	230	L+V→L	NaCl-H2O	1.0000	26.4	1.05	18.01		
	FIA#3	L+V	-23			12.0	212	L+V→L	NaCl-H2O	1.0000	26.3	1.06	18.98		
		L+V	-23			10.0	218	L+V→L	NaCl-H2O	1.0000	26.3	1.06	18.65		
		L+V	-23			11.5	218	L+V→L	NaCl-H2O	1.0000	26.3	1.06	18.65		
	FIA#4	L+V	-23			15.5	221	L+V→L	NaCl-H2O	1.0000	26.4	1.06	18.49		
		L+V	-23			15.0	215	L+V→L	NaCl-H2O	1.0000	26.3	1.06	18.82		
				L+V	-23			18.2	218	L+V→L	NaCl-H2O	1.0000	26.4	1.06	18.66
Sample 0052 , Kåfjord bridge, Gabbro-hosted mineralized carbonate vein associated with chalcopyrite and chlorite															
0052	Calcite	FIA#1	L+V+S	-52			245.0	220	L+V+S→L+S→L	NaCl-CaCl2-H2O	-	34.3	1.14	20.91	
							245.0	221	L+V+S→L+S→L		34.4	1.14	20.82		
							243.0	225	L+V+S→L+S→L		34.3	1.13	20.31		
							247.0	225	L+V+S→L+S→L		34.7	1.13	20.56		
							245.0	225	L+V+S→L+S→L		34.5	1.13	20.44		
		FIA#2	L+V+S	-52				220.0	218	L+V+S→L+S→L	NaCl-CaCl2-H2O		32.7	1.13	19.45
								223.0	218			32.9	1.13	19.69	
								225.0	215			33.1	1.13	20.17	
								225.0	215			33.1	1.13	20.17	
		FIA#3	L+V+S	-52				200.0	212	L+V+S→L+V→L	NaCl-CaCl2-H2O		31.9	1.11	19.06
								205.0	222			32.1	1.11	18.66	
								208.0	220			32.3	1.11	18.75	
								210.0	220			32.4	1.11	18.75	
								205.0	219	L+V+S→L+V→L	NaCl-CaCl2-H2O		32.1	1.11	18.78
		FIA#4	L+V+S	-52				205.0	220				32.1	1.11	18.74
								210.0	220			32.4	1.11	18.75	
								210.0	220			32.4	1.11	18.75	
								210.0	220			32.4	1.11	18.75	

Appendix H: Correlation matrices of sulfides

Table H1: Correlation matrix for mafic rock-hosted sulfides in quartz-carbonate veins. $n=45$, $Df = n-2 \rightarrow 43$, Level of significance (p)= 0.05 = 5% \rightarrow 0.295. Values below detection limits are assigned "0". Green color: Positive significant correlation, Red color: Negative significant correlation, Py: Pyrite, Ccp: Chalcopyrite, Sp: Sphalerite. Based on LA-ICP-MS data.

	Py	Ccp	Sp	Si	S	Ti	V	Cr	Mn	Fe	Co	Ni	Cu	Zn	Ga	Ge	As	Se	Nb	Mo	Ru	Rh	Pd	Ag	Cd	In	Sn	Sb	Te	Ba	Au	Hg	Tl	Pb	U		
Py	1.00																																				
Ccp	-0.91	1.00																																			
Sp	-0.20	-0.21	1.00																																		
Si	-0.28	0.29	-0.03	1.00																																	
S	0.63	-0.57	-0.16	-0.02	1.00																																
Ti	0.14	-0.07	-0.19	0.03	0.31	1.00																															
V	-0.22	0.24	-0.07	0.01	-0.07	0.26	1.00																														
Cr	-0.28	0.34	-0.14	-0.07	-0.15	0.02	0.46	1.00																													
Mn	-0.36	0.07	0.69	-0.01	-0.28	0.31	0.48	0.07	1.00																												
Fe	0.85	-0.57	-0.68	-0.18	0.56	0.21	-0.13	-0.14	-0.63	1.00																											
Co	0.40	-0.38	-0.04	-0.12	0.55	-0.02	-0.11	-0.17	-0.12	0.31	1.00																										
Ni	0.49	-0.44	-0.12	-0.16	0.01	0.05	-0.13	-0.16	-0.17	0.43	-0.11	1.00																									
Cu	-0.85	0.92	-0.18	0.35	-0.50	-0.06	0.25	0.38	0.07	-0.53	-0.37	-0.45	1.00																								
Zn	-0.20	-0.21	1.00	-0.03	-0.15	-0.18	-0.06	-0.13	0.68	-0.68	-0.04	-0.12	-0.18	1.00																							
Ga	-0.12	0.14	-0.03	0.01	-0.10	0.81	0.21	-0.11	0.49	-0.08	-0.07	-0.08	0.17	-0.03	1.00																						
Ge	-0.11	0.17	-0.13	-0.12	0.07	0.15	0.35	0.31	0.02	-0.01	-0.18	-0.06	0.10	-0.13	-0.09	1.00																					
As	0.20	-0.16	-0.11	-0.08	-0.23	-0.11	-0.14	-0.13	-0.09	0.21	0.17	0.33	-0.31	-0.11	-0.09	-0.10	1.00																				
Se	-0.18	0.24	-0.15	-0.05	0.04	0.11	0.20	0.24	-0.08	-0.05	-0.26	-0.07	0.29	-0.14	-0.07	0.36	-0.31	1.00																			
Nb	-0.19	0.23	-0.10	0.07	-0.13	-0.12	-0.07	0.15	-0.17	-0.09	-0.09	-0.09	0.17	-0.11	-0.09	0.12	0.08	0.25	1.00																		
Mo	0.07	-0.02	-0.13	-0.14	-0.34	-0.11	0.14	0.27	0.00	0.13	-0.16	0.43	-0.10	-0.13	-0.10	0.06	0.53	-0.02	-0.07	1.00																	
Ru	0.29	-0.26	-0.07	-0.13	0.49	-0.07	-0.07	-0.08	-0.12	0.24	0.97	-0.22	-0.24	-0.07	-0.09	-0.14	0.11	-0.19	-0.09	-0.17	1.00																
Rh	-0.83	0.91	-0.18	0.31	-0.47	-0.05	0.34	0.49	0.09	-0.52	-0.36	-0.44	0.98	-0.18	0.12	0.16	-0.31	0.30	0.14	-0.06	-0.24	1.00															
Pd	-0.20	-0.21	1.00	-0.03	-0.15	-0.18	-0.06	-0.13	0.69	-0.68	-0.04	-0.12	-0.18	1.00	-0.03	-0.12	-0.11	-0.14	-0.10	-0.13	-0.07	-0.18	1.00														
Ag	-0.65	0.62	0.06	0.22	-0.44	-0.06	0.37	0.38	0.28	-0.52	-0.30	-0.27	0.63	0.06	0.06	0.21	-0.07	0.57	0.33	0.17	-0.20	0.65	0.07	1.00													
Cd	-0.21	-0.20	1.00	-0.03	-0.15	-0.18	-0.06	-0.13	0.69	-0.69	-0.04	-0.12	-0.18	1.00	-0.03	-0.12	-0.11	-0.14	-0.11	-0.13	-0.07	-0.17	1.00	0.07	1.00												
In	-0.60	0.49	0.27	0.02	-0.29	0.14	0.61	0.59	0.56	-0.60	-0.25	-0.30	0.54	0.28	0.18	0.36	-0.26	0.13	-0.13	0.06	-0.18	0.65	0.28	0.52	0.29	1.00											
Sn	-0.35	0.38	-0.08	-0.02	-0.12	0.07	0.50	0.82	0.15	-0.22	-0.16	-0.16	0.42	-0.08	-0.06	0.24	-0.16	0.24	-0.05	0.16	-0.10	0.56	-0.08	0.51	-0.08	0.77	1.00										
Sb	0.17	-0.15	-0.06	-0.11	-0.33	-0.09	-0.08	-0.05	-0.04	0.16	-0.07	0.36	-0.26	-0.06	-0.07	-0.05	0.94	-0.25	0.08	0.59	-0.12	-0.26	-0.06	-0.01	-0.06	-0.16	-0.10	1.00									
Te	0.04	-0.01	-0.07	-0.08	-0.26	-0.06	-0.07	-0.03	-0.04	0.06	-0.04	0.17	-0.15	-0.07	-0.05	0.02	0.88	-0.17	0.15	0.32	-0.07	-0.16	-0.06	0.03	-0.07	-0.12	-0.06	0.86	1.00								
Ba	-0.26	0.29	-0.07	0.99	0.01	0.08	0.04	-0.06	-0.02	-0.15	-0.13	-0.14	0.33	-0.07	0.03	-0.10	-0.08	-0.04	0.04	-0.12	-0.14	0.29	-0.07	0.20	-0.07	0.02	-0.01	-0.12	-0.08	1.00							
Au	0.13	-0.13	0.02	-0.11	-0.28	-0.08	-0.01	-0.01	0.02	0.08	-0.06	0.21	-0.21	0.02	-0.07	-0.01	0.88	-0.19	0.06	0.49	-0.10	-0.21	0.02	0.04	0.02	-0.08	-0.06	0.96	0.86	-0.11	1.00						
Hg	-0.21	-0.20	1.00	-0.03	-0.17	-0.19	-0.05	-0.13	0.69	-0.69	-0.05	-0.12	-0.17	0.99	-0.04	-0.12	-0.10	-0.13	-0.10	-0.12	-0.07	-0.17	0.99	0.09	1.00	0.28	-0.07	-0.05	-0.06	-0.07	0.03	1.00					
Tl	0.21	-0.17	-0.08	-0.10	-0.31	-0.08	-0.06	-0.02	-0.04	0.20	-0.07	0.33	-0.26	-0.08	-0.07	-0.07	0.89	-0.24	0.04	0.63	-0.11	-0.25	-0.08	-0.02	-0.08	-0.17	-0.09	0.98	0.76	-0.11	0.94	-0.08	1.00				
Pb	0.13	-0.12	-0.02	-0.11	-0.35	-0.07	0.06	0.06	0.04	0.11	-0.11	0.29	-0.22	-0.01	-0.07	0.04	0.84	-0.21	0.08	0.68	-0.16	-0.20	-0.01	0.08	-0.01	-0.04	-0.01	0.94	0.72	-0.10	0.91	-0.01	0.95	1.00			
U	-0.25	0.27	-0.06	0.01	-0.08	0.08	0.68	0.47	0.27	-0.16	-0.11	-0.11	0.32	-0.05	-0.03	0.42	-0.13	0.22	-0.05	0.10	-0.06	0.43	-0.05	0.52	-0.05	0.69	0.71	-0.07	-0.06	0.01	-0.02	-0.04	-0.05	0.04	1.00		

Appendix I: Magnetic anomaly and Skoadduvarri

The mines that were active in Kåfjord produced copper with a very high Cu grade as described in the mining history, but the main limits of the mining have been the quantities of the material, as the high copper grade is restricted to these relatively small quartz-carbonate veins (Moberg, 1968). New geophysical maps provided by NGU (NGU, 2021c) by the MINN program (Mineralressurser I Nord-Norge) can be used in the field of mineral exploration. As seen in Figure 5, the copper-poor (in quantity) localities Innerstrømmen and Henning producing copper in a minor scale lies approximately at the southern and northern limits of the big positive magnetic anomaly in Kåfjord, respectively. The copper-rich (in quantity) localities Carl Johan, Wilson and Mitchell that have been a subject of mining in a bigger scale, lies inside the big positive anomaly (Figure 5), which also includes the biggest mine “old mine” and other historical mines in Kåfjord. By this, it seems like the magnetic map corresponds to the major sources of copper lying within the positive magnetic anomaly. Locality Kåfjord bridge is also located within this big positive anomaly, but it has not been a subject of mining and hosts only minor accessory copper in the gabbro and pyrite in the quartz-carbonate veins. What could explain the positive magnetic anomaly in the Kvenvik formation of Kåfjord, is the strong magnetic property magnetite exhibits as magnetite is identified in major amounts in the gabbro at Kåfjord bridge. Copper itself does not produce such anomalies.

In Storviknes formation, the two mines Anna and Lundstrøm lie in differences from the mines in Kvenvik formation within a negative magnetic anomaly (Figure 5). Cu mineralization here is related to smaller quartz-carbonate veins intruding the sedimentary host rock. This type of host rock is most likely the source of the negative magnetic anomaly.

As described in Cox et al. (2003), sediment-hosted Cu-deposits can be found hosted in sandstones and conglomerates if a reductant (often organic debris) is present. Skodduvarri formation consists mostly of sandstone but also conglomerate (Bergh & Torske, 1986), which potentially can be a host rock. A Conglomerate containing jasper was identified within the sandstone of the Skoadduvarri formation, close to the water intake dam at Lundstrømvannet during the fieldwork. Both the sandstone and this conglomerate should have been inspected in more detail in the scope of a potential host rock to Cu-mineralization (Figure 71). Maybe an even higher Cu grade zone enriched in CuS minerals has been deposited within Skoadduvarri formation.

